TEHNIČKI GLASNIK / TECHNICAL JOURNAL

TEHNIČKI GLASNIK / TECHNICAL JOURNAL – GODIŠTE / VOLUME 11 – BROJ / NUMBER 4

PROSINAC 2017 / DECEMBER 2017 – STRANICA / PAGES 143-229

/

SVEUČILIŠTE SJEVER / UNIVERSITY NORTH – CROATIA – EUROPE

ISSN 1846-6168 (PRINT) / ISSN 1848-5588 (ONLINE)

TEHNIČKI GLASNIK / TECHNICAL JOURNAL

ISSN 1846-6168 (Print) ISSN 1848-5588 (Online)

TEHNIČKI GLASNIK - TECHNICAL JOURNAL

Scientific-professional journal of University North

Volume 11 Number 4
Varaždin, October-December 2017 Pages 143–229

Editorial Office:
Sveučilište Sjever – Tehnički glasnik
Sveučilišni centar Varaždin
104. brigade 3, 42000 Varaždin, Hrvatska
Tel. ++385/ 42/ 493 328, Fax.++385/ 42/ 493 333
E-mail: tehnickiglasnik@unin.hr
http://tehnickiglasnik.unin.hr
http://www.unin.hr/djelatnost/izdavastvo/tehnicki-glasnik/
http://hrcak.srce.hr/tehnickiglasnik

Founder and Publisher:
Sveučilište Sjever / University North

Print:
Centar za digitalno nakladništvo, Sveučilište Sjever

All manuscripts published in journal have been reviewed.
Manuscripts are not returned.

The journal is free of charge and four issues per year are published.
Circulation: 100 copies

Journal is indexed and abstracted in:
Web of Science Core Collection (Emerging Sources Citation Index - ESCI), EBSCOhost Academic Search Complete, EBSCOhost – One Belt, One Road Reference Source Product,
ERIH PLUS, CITEFACTOR – Academic Scientific Journals, Hrčak - Portal znanstvenih časopisa RH

Registration of journal:
The journal "Tehnički glasnik" is listed in the HGK Register on the issuance and distribution of printed editions on the 18th October 2007 under number 825.

Preparation ended:
December 2017

Note from the Editor-in-Chief

Dear readers,

It is my great pleasure to present you with this year's last issue of **Tehnički Glasnik-Technical Journal**, number 4, year 11. This is our 11th year of the regular publishing process and it might be the right time to analyze what we have been doing this year. This year we have not been able to reach the planned publication of four issues per year; however, with exceptional efforts, we have managed to publish three issues (one double and two single issues). We did not see this as a failure since we tried to maintain the quality of the published works at a level that would enable us to include the journal in significant databases. This decision has shown to be the right one: in August this year, we were informed that Tehnički Glasnik-Technical Journal had been selected for inclusion in the services provided by the company Clarivate Analytics. Since January 2017, our journal has been indexed and abstracted in the Emerging Sources Citation Index (ESCI) under the Web of Science Core Collection (WoS), even though the entire 2016 is included in the ESCI. Of course, maintaining the quality and working on citations will still be needed in order to obtain the journal's first impact factor (IF) in Journal Citation Reports (JCR) for 2018.

With great efforts of the authors, reviewers and the editorial team, we have managed to complete this last journal issue with fourteen selected papers. Following the reviewers' remarks, the authors edited the papers in the form in front of you.

In the end, as always, we welcome you, our dear readers, to use your input to contribute to our joint work and permanent endeavor to retain the quality of our joint journal. Due to the fact that this issue is published in December, I use the opportunity to wish you all a happy and successful New Year.

Best regards,

Full. Prof. Milan Kljajin, Ph.D.
Editor-in-Chief
Tehnički Glasnik-Technical Journal

ISSN 1846-6168 (Print), ISSN 1848-5588 (Online)
ID: TG-20171101192113

Original scientific paper

OPTIMIZATION OF ABRASIVE WATERJET MACHINING PROCESS PARAMETERS

Miroslav DUSPARA, Valnea STARČEVIĆ, Ivan SAMARDŽIĆ, Marko HORVAT

Abstract: Currently, more than 50 000 different construction materials are available on the market and that number is increasing. Many new materials are often difficult to machine with conventional methods that are currently dominating in production facilities, so the industry is more and more turning to non–traditional machining processes such as abrasive waterjet cutting (AWJC). With the exceptional capabilities that it provides, abrasive waterjet cutting has disadvantages such as surface roughness and striation marks on the cutting surface, which represents a limitation for further application in production. The experimental part of the paper focuses on the verification of the thesis whether conventional material process technologies can be replaced with the abrasive waterjet cutting technology under certain conditions, while maintaining the required quality of the machined surface and productivity. An analysis of the influence of the selected cutting parameters and an optimization of the model was performed on the specimens from the AISI 316L steel on the cutting depth of 25 mm. The results obtained by optimization showed that abrasive waterjet cutting can replace conventional technologies and achieve the required values of the machined surface.

Keywords: Abrasive waterjet cutting; optimisation; cutting parameters; centra lcomposite design; AISI 316L

1 INTRODUCTION

The major target of metal cutting is to ensure high productivity with the high quality of a product and low machining costs. What exerts the greatest influence on the choice of treatment are the type of material and the geometry of a specimen. Those two factors usually determine the way of processing, and after the selection of the process, it is necessary to determine the operating conditions. The surface finish produced by conventional machining is generally uniform. Therefore, the surface finish of the machined surface can simply be characterized by measuring the surface roughness of any point of the machined surface. The abrasive waterjet cutting technology (AWJC) represents a relatively new, emerging non-conventional way of cutting almost all sorts of materials and shapes.

Due to the numerous advantages such as the narrow kerf, no heat effect zone in the material, reduction of waste disposal costs, minimal force compared to other conventional machining methods and so on, abrasive waterjet cutting has been used in various industrial applications. Despite numerous advantages over many other ways of conventional processing, there are two major obstacles, which limit further application for industrial purposes: relatively high costs of machining and the formation of striation marks on the surface of the material on higher cutting depths.

2 RELATED AND PREVIOUS WORK

The topography characteristic of the surface generated by the abrasive waterjet cutting technology has been an aim of the research of many scientists since the early 1980s. Hashish and Kovacevic are considered to be the pioneers in the area of metal machining with AWJC. Based on the flow visualization study, Hashish has proposed a theory that surfaces created by the abrasive waterjet cutting technology (AWJC) can be divided into main two zones: the upper smooth zone where the primary irregularity on a machined surface is roughness and the lower rough zone that is characterized by wavy striations (as shown in Fig. 1). [1]

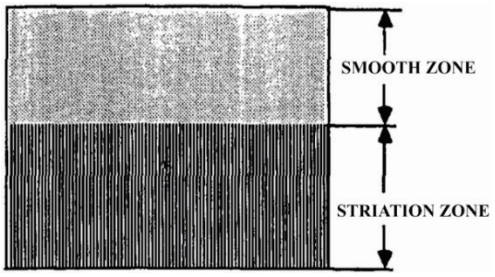

Figure 1 Division of the abrasive waterjet cut surface [1]

Based on Hashish's study, Tan has proposed a kinematics/geometry model of the cutting process in order to explain the striation forming mechanism. Souda, Matsui et al. reported that striation marks can be suppressed by adjusting the entrance angle of a water stream with multi pass cutting and with lower values of the jet traverse speed [1÷4].

There are other studies on waterjet generated surfaces that were aimed primarily at qualifying surface roughness as a function of the cutting parameters. In an experimental study for the abrasive waterjet cutting surfaces involving striations, the scientists Kim, Reuber and Hunt noticed that the values of surface roughness approximately increase with the increase of the cutting speed and cutting depth. Neusen et al. made a similar conclusion in the cutting of metal matrix composites. Kovacevic used a second-order mathematical model to characterize the surface roughness across the cut's depth as a function of several AWJ operation parameters. [1, 2,]

Striation marks represent a common phenomenon on the surfaces generated with beam-cutting technologies, such as waterjets, lasers or plasmas [4, 5, 6]. The formation of periodic wavy patterns (or striation marks) has drawn much

attention in abrasive waterjet cutting on the higher cutting depth because it strongly affects the quality of the finished surface and the dimensional accuracy of the machined surface. [1]

An example of the surface created with abrasive waterjet cutting with a typical wavy structure in a lower zone of the specimen (cutting depth 25 mm) from AISI 316L steel is shown in Fig. 2.

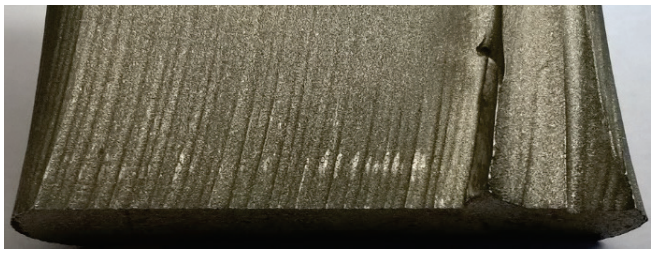

Figure 2 AISI 316L surface irregularities created by the AWJC technology

The mechanisms of forming striation marks on a surface of the material are not fully clarified and are still far from being qualitatively described. There are several different theories related to the striation marks forming mechanism, but generally, scientists agree that there are three categories with regard to the source of striations: as consequences of the machining system vibration, due to the dynamic behaviour of the waterjet and the dissipation of energy, and as a result of the characteristics inherent to the abrasive waterjet cutting (i.e. the process of material removal). [1]

3 EXPERIMENTAL SET-UP

In the experimental part of the paper, an influence of the selected cutting parameters was shown on the quality of surface roughness, or a mathematical model that will, depending on the input parameter, predict the quality-machined surface. The experiments were conducted on the TENKING 23020 abrasive waterjet cutting system with the ultra high-pressure pump capable of providing a pressure of water of 400 MPa. The examined material of specimens (dimension of specimens 40 × 30 × 10 mm) is the austenitic corrosion resistant steel X2CrNiMo17-12-2(AISI 316L) whose chemical composition is shown in Tab. 1.

Table 1 Chemical composition range for the AISI 316L stainless steel [7]

Grade		Cr	Mn	Si	P	S	Cr	Mo	Ni	N
AISI 316L	Min.	-	-	-	-	-	16.0	2.0	10.0	-
	Max.	0.03	2.0	0.75	0.045	0.03	18.0	3.0	14.0	0.1

In order to increase the cutting power of water stream, the Barton garnet MESH 120 abrasive particles were added in the mixing chamber of the waterjet cutter. Garnet abrasive offers the best combination of the cutting rate, consumable parts wear, availability, acquisition cost, and disposal cost. The most common grades used are #80 and #120. Fine grit abrasive particles (such as MESH 120) cut slower compared to MESH 80, but the finish on the machined surface is of more quality.

Three independent variables have been selected to analyze their influence on the roughness of the machined surface and they varied on two levels ($+\alpha$ and $-\alpha$). The variables include the jet traverse speed, pressure of water stream and flow rate of abrasive particles. The level and range of input variables used for the experimental design in the paper are listed in Tab. 2.

Table 2 Levels and ranges of input variables (cutting parameters) used for the experimental design

Levels of parameters	Pressure, MPa	Jet traverse speed, mm/min	Flow rate, kg/min
−1.682	300	22	0.3
−1	310	25	0.35
0	325	30	0.4
1	340	35	0.45
1.682	350	38	0.5

4 DESIGN OF EXPERIMENT (DOE)

After the cutting operation, the control and surface roughness measurement is carried out on the observed surface of the specimen. The surface roughness was measured with a portable surface roughness test Mitutoyo SJ 301 SurfTest on the cutting depth of 25 mm according to the standard ISO 4287:1997 (Figure 3b). In the mentioned cutting zone, it is pronounced that striations are forming on the surface of the material, and the attention of many researchers is focused on the research of the striation formation mechanism and improving the quality in the observed zone.

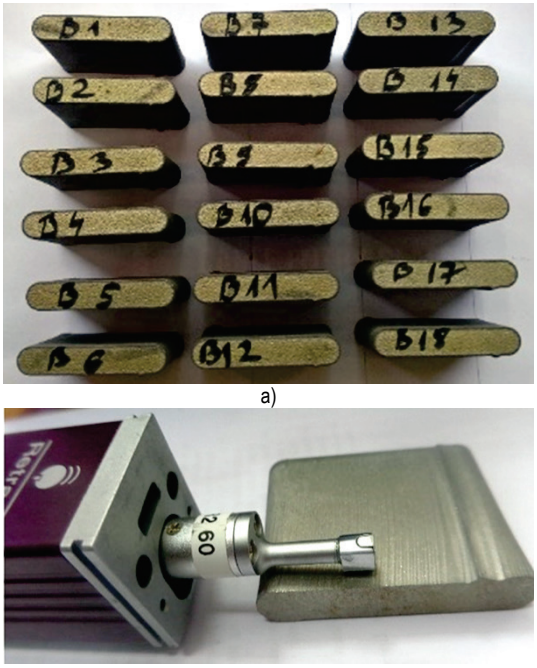

a)

b)

Figure 3 a) AISI 316L steel specimens used for experimental work, b) surface roughness measurement by the Mitutoyo SJ 301 Surf Test.

From all types of available parameters for describing the surface quality, *Ra* parameter was chosen, which defines the arithmetic mean deviation of the surface profile. The measurement is simple, standardized and generally applied [7].

Table 3 Values of surface roughness on the cutting depth of 25 mm

Number of runs	Process parameters			Response surface roughness *Ra*
	A: Pressure *p*	B: Jet traverse speed v_f	C: Flow rate m_a	
	MPa	mm/min	kg/min	μm
1	325	30	0.40	7.1
2	340	35	0.35	15.7
3	325	30	0.50	8.19
4	300	30	0.40	15.66
5	340	25	0.45	5.94
6	340	35	0.45	14.52
7	325	30	0.40	7.7
8	310	25	0.35	6.57
9	310	35	0.35	17.84
10	325	22	0.40	5.54
11	325	30	0.40	8.35
12	325	30	0.30	13.23
13	340	25	0.35	6.64
14	350	30	0.40	7.54
15	325	38	0.40	18.47
16	325	30	0.40	8.5
17	310	25	0.45	6.98
18	310	35	0.45	15.92

In order to obtain the independent and higher order effects on different process variables on the values of surface roughness, the experiment was performed by using the central composite design (CCD). The adequacy of the selected model for every level of cutting was tested by using the analysis of variance. [8]

The values of surface roughness for all levels were analyzed with a statistical software package Design Expert (version DX9, 9.0.6, Stat – Ease, Inc. Minneapolis 2014). The design of the experiment was 2^3 factorials with four central points, which requires 18 test runs (Fig. 3b). The design matrix (the number of experiments and the order of the run) with a surface roughness model as a response is shown in Tab. 3.

5 ANALYSIS OF VARIANCE (ANOVA)

The first step in the statistical analysis is to determine whether there is a need for the transformation of data. The range of values of surface roughness on the examined cutting depth is 5.54 ÷ 18.47 μm. Based on the response range of the data in the experiment, which is less than ten (3.334), the software suggests that there is no need for the transformation of data. The next step represents the selection of an adequate regression model for the observed cutting depth. The best model is the most fitted function to the experimental data. In this paper, checking the model adequacy is conducted with the analysis of variance (ANOVA) technique.

The model was tested in relation to mean square deviations, the deviations from the model and determination coefficients [8, 9].

The results obtained by ANOVA recommended that the quadratic regression model is statistically the best fit. The *P* – value for all zones obtained by the conducted statistical analysis showed that the value of models is lower than 0.05, which indicates that the models are statistically significant. With a backward elimination based on *p* – values, all insignificant terms are eliminated in order to adjust the fitted model. [9] The analysis of the variance for the regression model Ra_{25} is shown in Tab. 4.

Table 4 Values of surface roughness on the cutting depth of 25 mm

Source	Sum of square	Degree of freedom	Mean square	*F*-value	*p*-value
Model	324.35	5	64.87	26.08	< 0.0001
A - pressure	24.02	1	24.02	9.66	0.0091
B – trav. speed	126.32	1	261.18	105.1	< 0.0001
C – flow rate	11.34	1	11.34	4.56	0.0540
A^2	13.61	1	13.61	5.47	0.0374
B^2	18.37	1	18.37	7.38	0.0187
Residual	29.85	12	2.49	-	-
Lack of fit	28.61	9	3.18	7.68	0.0603
Pure error	1.24	3	0.41	-	-
Total	354.19	17	-	-	-

From Tab. 4 it is visible that the *F* – value of the model amounts to 26.08, which implies that the selected model has a significant value. There is less than 0.1 % probability that the *F* - value is that high due to noise. Moreover, from the above-mentioned table it can be concluded that the factor B - jet traverse speed represents the most significant factor, and the *p*-value for the variable *F*-value (105.1) is less than the probability error type (< 0.01 %).

The influence of the pressure of water stream on the quality of the machined surface is also important: as the pressure of stream increases, the surface of the machined material becomes smoother. Due to an increase in jet pressure, the kinetic energy of the particles increases, which results in a smoother machined surface [11, 12, 13].

The mass flow rate of abrasive particles did not show prominent influence on the quality of the machined surface (i.e. not a significant cutting parameter), with the *value of F* = 4.56. Having in mind that even though the fact that with the addition of the abrasive particles' cutting power, the ability of the water stream increases, the quality of the machined surface decreases when an amount of abrasive particles in a stream increases. Abrasive particles collide with themselves in the water stream, and the result of that is a loss of kinetic energy and an uneven machined surface [13, 14]. Fig. 5 gives a graphical representation of the comparison of the predicted values and the data experimentally obtained (in other word the real values).

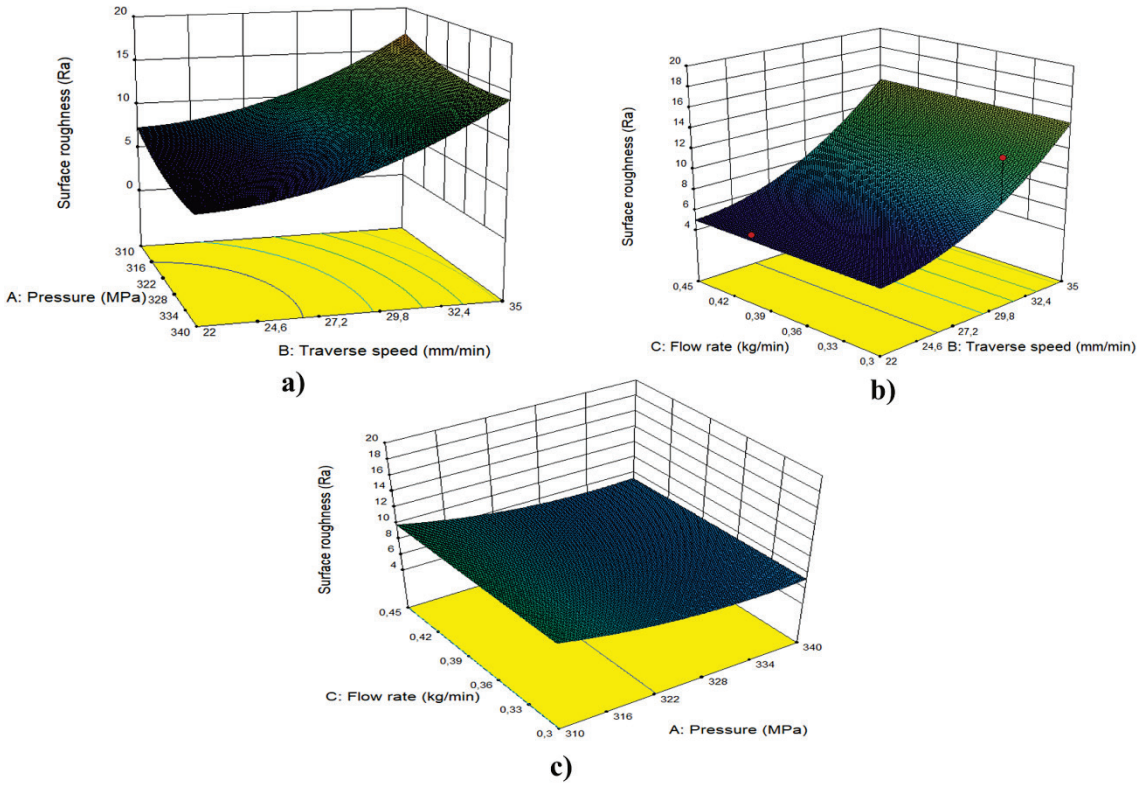

Figure 4 Response surface of surface roughness vs. a) jet traverse speed and water pressure, b) jet traverse speed and flow rate, c) water pressure and flow rate

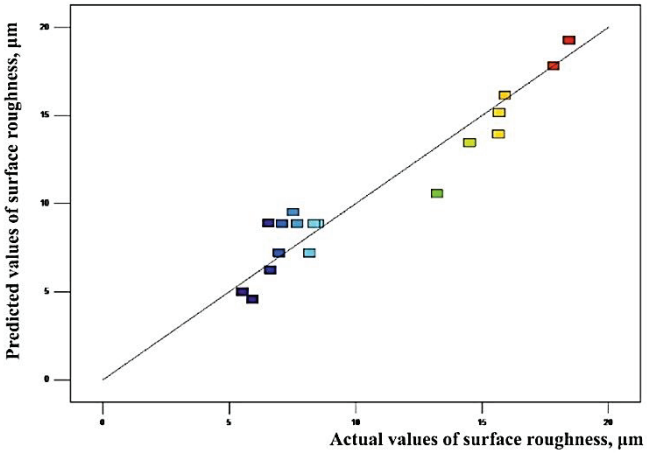

Figure 5 Values of the surface roughness *Ra* created by the model – predicted (Eq. (1)) vs. the actual values of surface roughness (Eq. (2))

The curve of the diagram is a straight line (i.e. Henry's line), as a proof that the data result from the normal distribution. All the effects that lie along the line are negligible, and there is no significant deviation from the line (i.e. there are no outliers). The plot appears satisfactory, so there is no reason to suspect that there are any problems with the validity of the conclusion.

6 REGRESSION ANALYSIS

The term regression analysis denotes a statistical modeling and an analysis method for mathematically modeling the relationship between thedependent and independent variables. The statistical analysis includes a correlation degree measurement between the selected variables and the estimation performance related to the independent variables. Additionally, the regression analysis compares the data obtained experimentally with the estimated data in order to understand the reliability of the regression model. In this paper, the jet traverse speed, waterjet pressure and the flow rate of abrasive particles are independent variables, and the values of surface roughness are estimated and dependent variable [9].

The mathematical model in terms of the coded (Eq. 1) and actual factors (Eq. 2) for an independent and dependent variables and the degree of the relations between the variables are as follows:

The mathematical model in terms of coded factors:

$$Ra_{25} = 8.07 - 1.33A + 4.80\,B - 1.26\,C + 1.03A^2 + 2.16B^2 \quad (1)$$

The mathematical model in terms of factual factors:

$$Ra_{25} = 545.19 - 3.0542A - 2.17056B - 16.83C + 4.56229 \cdot 10^{-3}\,A^2 + \ 0.051048\,B^2 \quad (2)$$

Values R^2 and $R^2_{adj.}$ are used in order to show the power of the relationship between the dependent and independent variables in the paper. Value R^2 is computed as 88.37 %, $R^2_{adj.}$ as 84.79 %. The obtained values of R show that the relationship among the data obtained from the mathematical model and the data obtained experimentally is very strong [9, 10].

7 OPTIMIZATION MODEL

According to the classification of the cut surface machined by the abrasive waterjet proposed by Hashish [1, 4], the cutting depth of 25 mm is defined as a deformation wear zone because of the pronounced striation marks on the surface of the material. Surface roughness in the observed zone is moving within the range of 5.54 ÷ 18.47 μm, thus there is a need for additional treatment due to the weak surface quality that causes the increase of machining costs.

During the machining of the above-mentioned steel on the classical milling machine, it is possible to achieve values of surface roughness in the range of 3.2 ÷ 6.34 μm. That range of surface values fulfills most of the exploitation requirements. Besides the cutting parameters, the economic feasibility of the process is taken into account (i.e. the maximum allowable cutting speed and minimum consumption of abrasive grains). During the process of optimization, it is necessary to take into account the costs that arise during the cutting. Considering the fact that abrasive grains have a great share in the total costs (approximately 55 ÷ 60 %), it is necessary to find a combination of cutting parameters that will ensure a minimum consumption of abrasive particles while maintaining the quality of the machined surface in the required range [13, 14].

The success of the conducted numerical optimization in the Design Expert is estimated through the objective function called desirability. The overall desirability (D) is a geometric (multiplicative) mean of all individual desirabilities (d_i) that range from 0 (least) to 1 (most) with the highest level of importance (5+):

$$D = (d_1 \times d_2 \times \dots d_n)^{\frac{1}{n}} = (\prod_{i=1}^{n} d_i)^{\overline{n}} \quad (3)$$

where n is the number of responses.

For the case analyzed in paper, target optimization is chosen in the range of values of 5.54 ÷ 18.47 μm (Fig. 7), and the levels of the parameter for numerical optimization are shown in Tab. 6

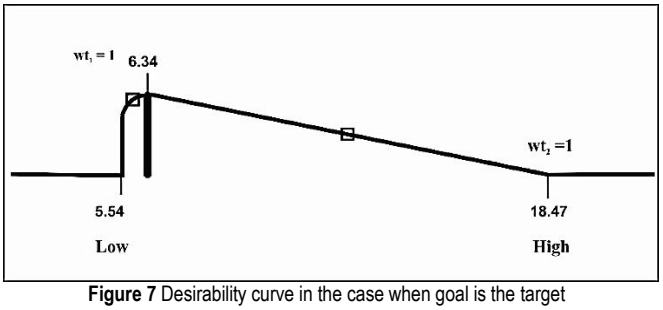

Figure 7 Desirability curve in the case when goal is the target

Table 6 Optimization of the Abrasive Waterjet Cutting parameters for the AISI 316L machining

Parameters	Low level	Center level	High level
Jet traverse speed, mm/min	22	28.50	35
Water pressure, MPa	310	325	340
Flow rate, kg/min	0.3	0.38	0.45

8 ESTIMATION AND VALIDATION OF EXPERIMENTAL RESULTS

Based on the set criteria, the software has created 100 potential combinations of parameters which are considered to be the optimal (i.e. desirability $d_i = 1$). In other words, it is possible to achieve the regression model which will be considered the optimal within required conditions, in 100 combinations according to the limitations of optimization.

Table 6 Potential solutions for the numerical analysis of the regression model Ra_{25}

Number of runs	Process parameters			Values of surface roughness Ra	Desirability
	A: Pressure p	B: Jet traverse speed v_f	C: Flow rate m_a		
	MPa	mm/min	kg/min	μm	
1	327.763	27.283	0.416	6.340	1.000
2	332.345	26.979	0.394	6.340	1.000
3	327.425	25.176	0.354	6.340	1.000
4	325.993	26.520	0.398	6.340	1.000
5	325.832	26.580	0.401	6.340	1.000
6	326.737	26.415	0.391	6.340	1.000
7	326.744	26.864	0.406	6.340	1.000
8	323.243	26.561	0.414	6.340	1.000
9	323.955	26.573	0.410	6.340	1.000
10	318.781	22.297	0.365	6.34	1.0
⋮	⋮	⋮	⋮	⋮	⋮
98	321.624	27.246	0.448	6.34	1.0
99	328.591	25.900	0.369	6.34	1.0
100	334.597	22.848	0.301	6.34	1.0

The first solution generated by the software was selected as an optimal combination of the cutting parameters: v_f = 27.283 mm/min, p = 327.763 MPa and m_a = 0.416 kg/min. The results obtained by optimization also can be displayed in a graphical form. In order to determine the optimal levels of each variable for the required value of surface roughness, 3D and contour plots were constructed by plotting the response against each of the two selected variables (pressure of water stream and traverse jet speed), while the third variable (flow rate of abrasive particles) is maintained at a zero (fixed) level.

What is chosen as the optimal solution is the solution that suggests the smallest possible flow rate of abrasive particles to achieve the required values of surface roughness. The reason for this is the price of abrasive particles (app. 4.05 euros per kilo), which is the largest item in the share of the cutting costs. If the amount of abrasive particles is reduced to the minimal required amount, with an optimal combination of the main parameters (jet traverse speed and water pressure), the price of cutting with the abrasive jet will be lower, which represents another way of competing with conventional technologies.

The results of optimization (the optimal combination of parameters) can be displayed in graphic form by using the 3D and contour plot. The first 14 optimal combinations of parameters are shown in Fig. 8.

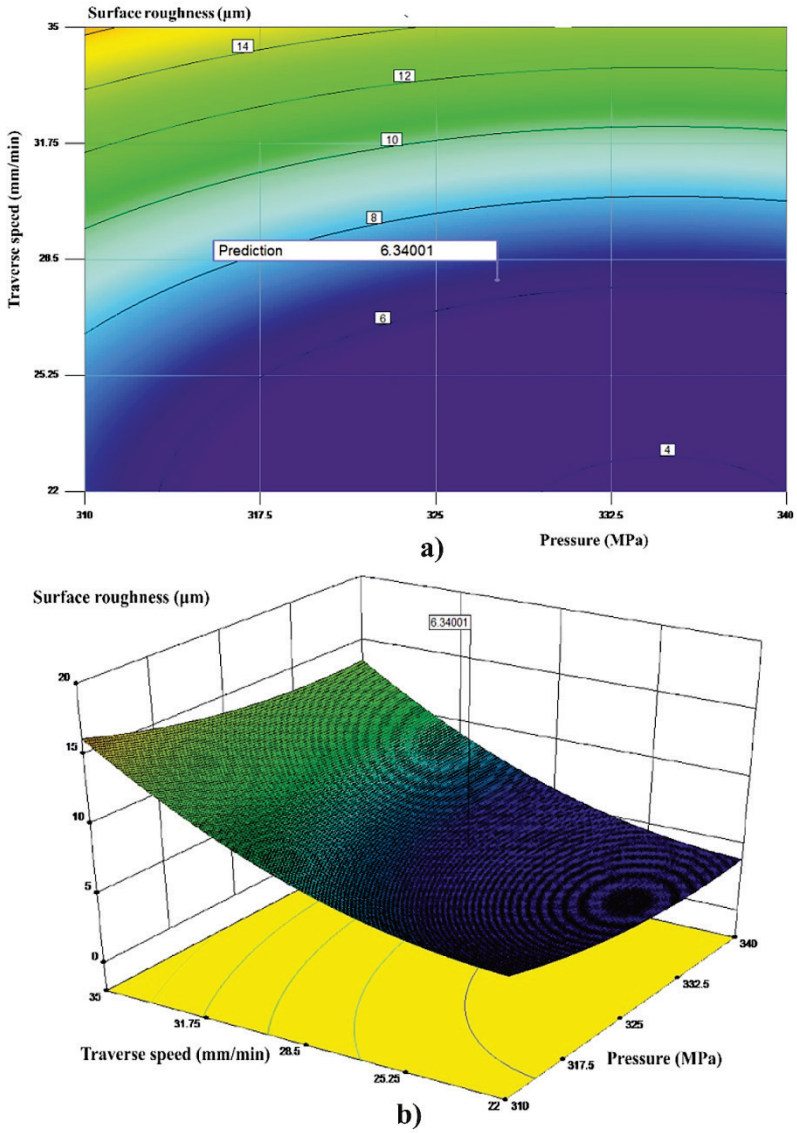

Figure 8 Graphical display of optimization for the analyzed cutting depth: a) 3D surface, b) contour

Graphical optimization is based on the overlapping of the two-dimensional responses of the obtained values. In the experimental space, when points with the same value of desirability are connected, the surface with optimal values is obtained (where values of desirability that are 1 or lower are acceptable). The response surface for *Ra* in terms of the waterjet pressure and jet traverse speed is shown in Fig. 8. From the above-mentioned figure, it can be concluded that the values of *Ra* increase with an increase of jet the traverse speed and pressure of water, while the value of the abrasive flow rate has a constant value (m_a = 0,4 kg/min). With the graphical display, the results of the numeric analysis are confirmed.

By comparing the results obtained by ANOVA (with the probability of 95 %) and optimization, it can be concluded that the quality of the machined surface obtained with abrasive waterjet cutting and with milling (as a representative of the conventional technology) can be compared.

9 CONCLUSION

The aim of this paper is to determine whether it is possible to compare the quality of machined surface created with an abrasive water jet (as a representative of the non-conventional technology) with conventional technology (in this case milling was chosen) which is currently dominating in the industry. The examination was conducted on specimens from the austenitic corrosion resistant steel AISI 316L.

In this paper, the data for the experiment were obtained by the central composite design (CCD) with three factors (jet traverse speed, the flow rate of abrasive particles and the pressure of the water stream) at two levels. The input variable is the surface roughness at a cutting depth of 25 mm.

Based on the analysis of variance on the selected cutting depth, it has been established that jet traverse speed, the pressure of the water stream and the interaction of those two factors are significant. With the increase of the cutting speed, the resulting cut has the smaller width and poor quality. In order to examine the hypothesis about the comparability of the surface roughness machined by abrasive waterjet cutting and milling, it was necessary to find the maximum cutting speed a with minimum consumption of abrasive grains that will ensure the value of surface roughness of 6.34 μm or less.

The results of optimization have shown that the abrasive waterjet cutting technology can compare and replace traditional technologies (such as milling). The highest cutting speed for achieving a required roughness of the surface is 27.283 mm/min, pressure is 327.763 MPa and the flow rate is 0.416 kg/min (Fig. 8). With that combination of parameters, the cost of cutting is reduced, and thw demand for the quality of thw-machined surface is successfully achieved.

Note: This research was presented at the International Conference MATRIB 2017 (29 June - 2 July 2017, Vela Luka, Croatia).

10 REFERENCES

[1] Chen, F. L et al. The mechanism of surface striation formation in abrasive waterjet machining, Journal of Material Processing Technology, 141, (2003), pp. 213-218.
[2] Hashish , M. A modeling study of metal cutting with abrasive waterjets, Journal of Engineering Material Technology, 106, (1984), pp. 88-100.
[3] Matsui S. et al. High precision Cutting Method for Metallic Materials by Abrasive Waterjet, Proceedings of 10th International Symposium on Jet Cutting Technology, Amsterdam, Vol. 93F, (1990), pp. 398-407.
[4] Majumdar, A.; Bhushan B. Role of Fractal Geometry in Roughness Characterization and Contact Mechanics of Surface, ASME Journal of Tribology, Vol. 112, (1990), pp. 205-216.
[5] Toenshoff, H. K.; Emmelmann, C. Laser cutting of advanced ceramics, Ann. CIRP, 38/1 (1989), pp. 377-390.
[6] Henderson, I. Precios profile cutting of structural materials using waterjet and high power laser cutting, Journal of Australasian Welding, 41, 2(1996), pp. 27-28.
[7] Duspara, M. Istraživanje rezljivosti korozijski postojanog čelika AISI 316 L mlazom vode, PhD theesis, pp. 135-138, 2014.
[8] Alsoufi, M. et al. Influence of abrasive waterjet machining parameters on the surface texture quality of Carrara marble, Journal of surface engineered materials and advanced technology, 7(2007), pp. 535-544.
[9] Kartal, F. et al. Optimization of Abrasive Water Jet Turning Parameters for Machining of Low - Density Polyethane Material based on Experimental Design Method, International Polymer Process Journal of Polymer Processing Society, 29, 4(2014), pp. 535-544.
[10] Montgomery, D. C. Design and Analysis of Experiment, 8th Edition, 2012, John Wiley & Sons.
[11] Glogović, Z. Utjecaj parametara plinskog naštrcavanja na svojstva nanešenog sloja, Ph.D. theesis, pp. 212-213, 2010
[12] Gyliene, V. et al. Investigation of abrasive waterjet cutting parameters influence on 6082 aluminium alloy surface roughness, Mechanika, 20(6), pp. 602-606,
[13] Kovacevic, R. Surface texture in Abrasive Waterjet cutting, Journal of Manufacturing Systems, 10, 1(1991), pp. 32-39.
[14] Chitrirai pon Selvan, M. et al. Effects of process parameters on surface roughness in abrasive waterjet cutting of aluminium, Frontiers of Mechanical Engineering, 7, (2012), pp. 439-444.

Authors' contacts:

Miroslav DUSPARA
Valnea STARČEVIĆ, Corresponding author
Ivan SAMARDŽIĆ
J. J. Strossmayer University of Osijek,
Mechanical Engineering Faculty in Slavonski Brod,
Trg I. B. Mažuranić 2, 35 000 Slavonski Brod, Croatia
vstarcevic@sfsb.hr

Marko HORVAT
University North - University Center Varaždin,
104. brigade 3, 42 000 Varaždin, Croatia

ISSN 1846-6168 (Print), ISSN 1848-5588 (Online)
ID: TG-20171104195702

Original scientific paper

DEVELOPING A MODEL OF A STRAIN (DEFORMATION) OF A DAMAGED REINFORCED CONCRETE PILLAR IN RELATION TO A LINEAR LOAD CAPACITY

Željko KOS, Lovorka GOTAL DMITROVIĆ, Evgenij KLIMENKO

Abstract: Most research is mainly focused on the border load strength of a reinforced concrete pillar made of a high strength concrete, but what about the bearing capacity of the damaged AB columns of concrete with a normal strength from the last century. In this article, an experiment of a strain test (deformation) was described in relation to the amount of the axial eccentric load, to the breakdown of the damaged reinforced concrete pillar. Through real values, a model has been developed which can predict the straining of the deflection in relation to the size of the axial eccentric load. After testing the function of strain stress dependence and the axial eccentric load, a correlation test using the $\chi 2$ test was performed. Through testing, it was found that there was no statistically significant difference between the real values and the values obtained by the mathematical model.

Keywords: load; strain; reinforced concrete pillar

1 INTRODUCTION

A pillar as a support structural element of a construction has a very important impact on the ductile effect and the combined effectiveness of the whole construction, which is why it is essential to know its performance completely. There has been much behavioural research of reinforced concrete pillars in the last few decades for different types of strain, together with the research of the aspect and limitations of armature given to cracking and the pillar's load capacity. All previous research was primarily focused on the linear load capacity of a construction element. Due to the greater demands of load capacity and a longer lifetime, together with the endurance of pillars, especially in the seismological unstable areas, research is conducted mainly on reinforced steel pillars made from high strength concrete ($\geq$50 MPa). There is an open question of damaged reinforced pillar load capacity on the buildings built in the last century from the normal strength concrete (<50 MPa) [7]. The question is what threatens the building structure as a whole, what the remaining time of service of the damaged pillars is and whether there is a possible and payable way for the recovery of the damaged pillars. Based on the above-mentioned questions, what was approached was the planning and realization of the experiment of exploring the strain stress (deformation) in relation to the size of the axial eccentric load, all the way to the breakdown of the damaged reinforced concrete pillar. Through real values, a model has been developed which can predict the straining (deformation) of the deflection in relation to the size of the axial eccentric load. The model development process has no strict rules, thus, modelling is first and foremost art. The only rule is that the model must provide a realistic picture of the structure and functions of the actual system and show the behaviour of the system in different states, all the way from working under normal conditions to testing its work in critical situations, respectively examining the system's adaptability to the changes in key parameters.

Modelling can be explained as a process of building a representative of a real system and its use to solve the perceived problem, where only those characteristics of the real system that contribute to the problem solving are important. The use of a well-designed model provides valuable information about the problem-solving possibilities, as well as about all variants of a possible solution, and about the possible adverse impacts and states in which the actual system can be found by changing certain features of the system [2].

The contemporary modelling of complex systems assumes the use of computers in defining the requirements and model building, although the entire modelling process is still based on the knowledge, logic, abilities and experience of the modelling person and cannot be fully automated. The use of computers in the modelling process applies primarily to the mathematical calculations of the value of individual characteristics, because the complexity and the amount of such calculations is increasing with the geometric progression in dependence on the increase in the number of elements of the model [3].

The purpose of the model developed for this work is prediction. It involves evaluating the value (quantitatively or qualitatively) of system variables over a given time, based on the knowledge of other systems, respectively changes in the value of their variables in the same period. Models are often developed to anticipate the effect of changing the system's driving factors or system results. Prediction models can be very simple (often empirical) but may be more complicated. They must have a certain level of accuracy in the reproduction of previous measurements and thus require calibration data and other independent verification data [1].

The prediction is based mainly on quantitative data, although qualitative data can be used with them. Quantitative data refer to the measurable characteristics or flows across the system and can be collected as time series, as parts of a given area, or by surveying a particular

population. Qualitative data or information include professional opinions, beliefs, or information obtained from surveys and conversations. This information can be categorized (yes/no, high/middle/low ...), but may also be descriptive or specific by regulation.

Almost every model development relies on quantitative and qualitative information. However, models based on quantitative data rely mainly on the theory or knowledge gained by the iterations in the development of their conceptual model.

2 PREPAIRING OF A RESEARCH

2.1 Research of the damaged reinforced concrete pillar

The choice of an experimental pattern for measuring the strain-deformation stress at the deflection is largely dependent on the area of the slenderness of the reinforced concrete pillar, which depends on the geometric size of the model (Fig. 1) and on the way of fixing of the ends of the pillar of the so-called edge conditions (Fig. 2).

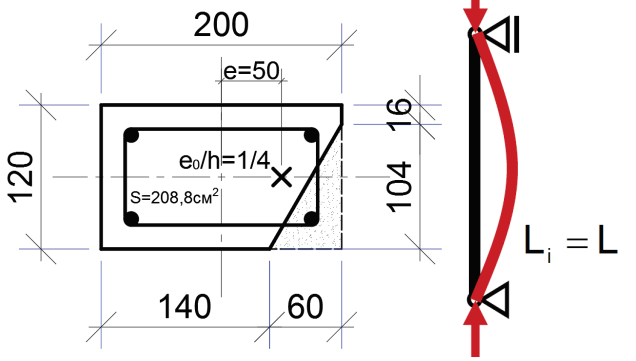

Figure 1 Cross section

Figure 2 Edge conditions

According to the European norms (EC-2, EN) [5], pillars are considered short and no budget is required for the theory of the 2nd order if the increase of the bending moment determined by the 1st order theory due to the deformation is not greater than 10%. This is fulfilled when the condition is met:

$$\lambda = 25(\omega + 0.9) \cdot \left(2 - \frac{M_{01}}{M_{02}} \right), \qquad (1)$$

where:

$\omega = \frac{A_s \cdot f_{yd}}{A_s \cdot f_{cd}}$ - If A_s is unknown, ω is taken 0.1

A_s - The surface of the armature in the transverse section of the element

λ - Coefficient of the element slenderness

M_{01}, M_{02} - First-order moments at the ends - if moments are 0, ratios are taken 1.0.

Review of slenderness of the reinforced concrete pillar length of 175 cm, cross section 20 ×12 cm.

$$\lambda = \frac{l_0}{i} \le \lambda_{max}, \qquad (2)$$

where:

l_0 - Element deflection length

$i = \sqrt{\frac{I}{A_c}}$ - The radius of the inertia in the direction of the smaller deflection resistance

I - Moment of inertia

A_c - Cross-section surface.

What is selected is a 20 × 12 cm cross section, 175 cm long research form (pillar) with the length of the damaged part of 40 cm in the middle of the height of the pillar, i.e. the damage is in the range of 67.5 cm to 107.5 cm height of the research form. The research form is made of concrete C 25/30 with longitudinal bars of B500 4 × 10 mm and forks B360 of 6 mm / 15 cm (/ 10 cm at both ends of the research form). By setting the basic parameters of the selected reinforced concrete pillar, not taking into account the damage of the cross section of the research form, the slenderness was λ = 50.52, which is more than the calculated λ_{max} = 29.61 limit. Therefore, the reinforced concrete pillar for the analysis has slenderness greater than the boundary and a calculation is required by the 2nd order theory (calculation for slender pillars).

2.2 Research form reinforced concrete pillar cross-section damage

According to the investigations of the undamaged samples of the pillar [6] after the breakdown, what was noticed was a localized type of damage of the examined samples, "wedged" shape approximately at the centre of the column, the depth of damage of 1/4 to 1/2 of the horizontal section length and the damage length of 20÷30 % of the total column length. This type of damage also occurs on the buildings of the last century; thus, for the experiment, a similar damage was made in the shape of the rectangular triangle cross section which was placed in one of the corners of the rectangular cross section. The cathetus of the triangle are given by the *b* side of the cross section 10.4 cm and by the *h* side 6 cm (Fig. 1).

2.3 Eccentric axial force

Since the eccentric loading of columns is often in the constructed structures, and because of the assumption of increasing the deformation of the deflection in the direction of the larger inertia torque of the cross section, the eccentricity of 1/4 h of the axial force is determined on the half section of the column where damage is present. In the direction of the lower inertia torque of the cross-sectional area, the position of the axial force action was determined with no eccentricity (Fig. 3) for the reason that the impact of the damage to the pillar curvature would be more noticeable.

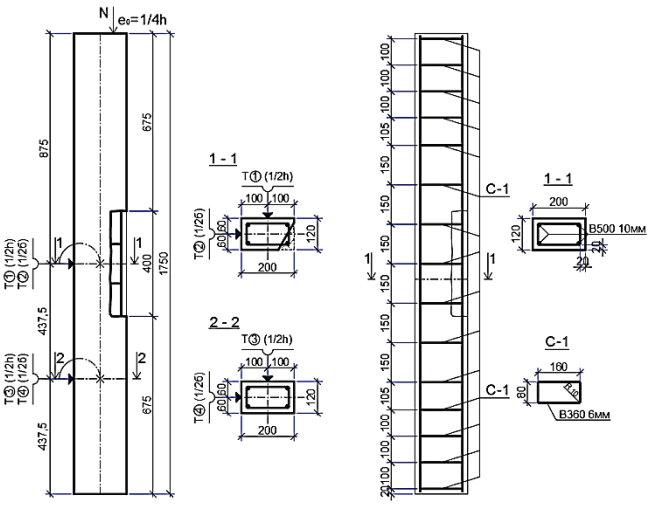

Figure 3 Research form

3 DESCRIPTION OF MEASURING AND RESULTS

The load on both ends of the research form is applied by a hydraulic press over a metal plate with a surface of a half-size of the cross-section ($h/2 \times b$) of the research form, located on the cross section at which damage is present. Thus, the axial force, eccentric to the height (h) of the cross section of the research form, was gradually applied and the research of the research form was measured every 50 kN at four measurement points using a 0.01 mm precision measuring instruments.

The measuring points shown in Figure x were placed on two undamaged sides of the research form, with a right angle between, two placed at the centre and two in a quarter of the height of the research pattern, planar on the half of the "b" and h sections of the research pattern. The expected deflection of the b and h sides outwards, relative to the vertical axis of the research form was achieved. Because of the eccentric loading and damage on the opposite side of the measurement, a significant bending of the side b was noted, i.e. a larger deflection was recorded in the direction of the maximum inertia torque of the cross section, while in the direction of the minimum inertia torque moment of the cross section was markedly less deflection but in the expected direction, or side h opposite to the damage, it is also moved outward in relation to the vertical axis of the research form. The results obtained are shown in Tab. 1.

Table 1 Result of stress strain changes

F/Fult	ε_1	ε_2	ε_3	ε_4
0	0	0	0	0
0.122	0	0.043	0	0
0.244	0.180	0.011	0.126	0
0.366	0.460	0.057	0.320	0
0.488	0.586	0.140	0.406	0.006
0.610	0.666	0.286	0.469	0.103
0.732	0.754	0.549	0.509	0.234
0.854	0.891	1.286	0.514	0.571
0.976	1.071	2.971	0.520	1.183

With the ver. 8st Stat Soft Inc. application *Statistica*, the stress dependency function (ε) is tested at each load point (F). According to the results obtained, in the T_1 and T_3 functions the strain corresponded to the logarithmic function (Fig. 4 and Fig. 5) and this:

$$T_1: \ f(x) = 0.962 + 1.1422 \cdot \log x, \tag{3}$$

$$T_3: \ f(x) = 0.5723 + 0.634 \cdot \log x. \tag{4}$$

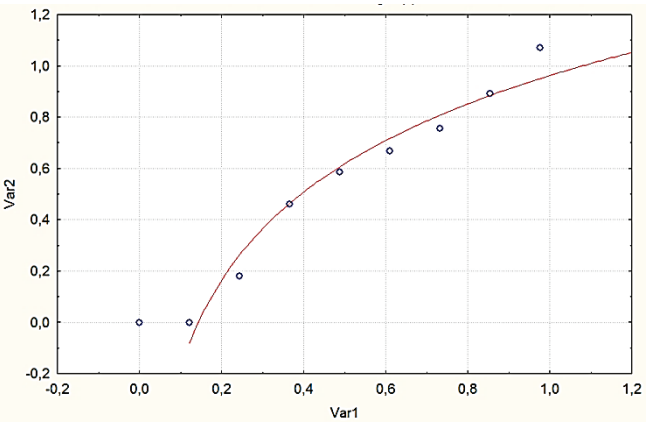

Figure 4 Load stress dependence in item 1

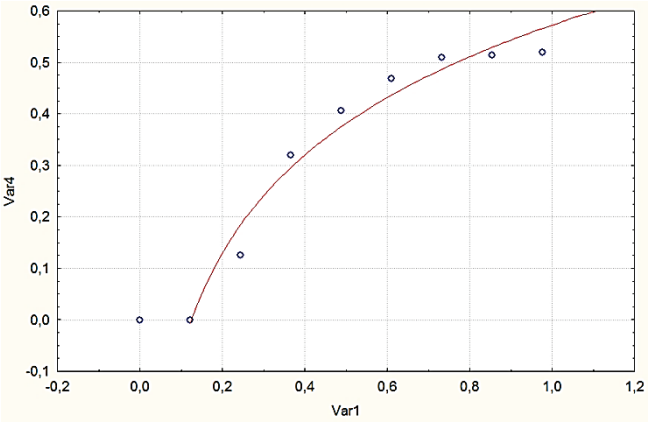

Figure 5 Load stress dependence in item 3

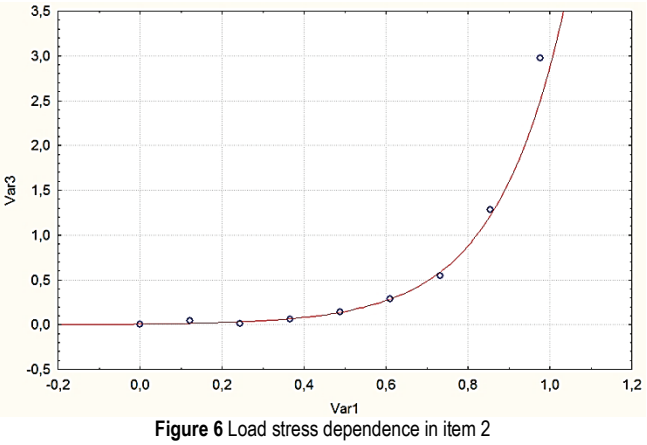

Figure 6 Load stress dependence in item 2

Unlike in the points 1 and 3, in the points 2 and 4 the functions of the reluctance were exponential functions (Fig. 6 and Fig. 7):

$$T_2:\ f(x) = 0.0075 \cdot e^{5.9489 \cdot x}, \quad (5)$$

$$T_4:\ f(x) = 9.9514 \times 10^{-5} \cdot e^{10.0662 \cdot x}. \quad (6)$$

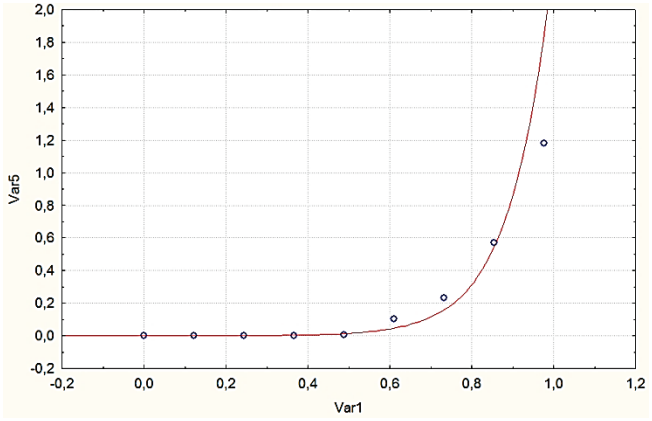

Figure 7 Load stress dependence in item 4

With the χ^2 test, the existence of statistically significant correlations in the actual frequency and value of the computed ones was calculated. This test is used to test the significance of the difference between the obtained (f_d) and expected (f_0) frequencies. Defined by the formula [4]:

$$T_2:\ \chi^2 = \sum \frac{(f_d - f_0)^2}{f_0}. \quad (7)$$

Table 2 Values derived from dependency functions

F/Fult	ε_1	ε_2	ε_3	ε_4
0	-	0.0075	-	0.000099514
0.122	-0.0816	0.0155	-0.0069	0.000339806
0.244	0.26228	0.03202	0.18391	0.00116032
0.366	0.46341	0.06617	0.29555	0.003962092
0.488	0.60611	0.13672	0.37476	0.013529178
0.610	0.7168	0.28252	0.4362	0.046197471
0.732	0.80724	0.58376	0.4864	0.157748416
0.854	0.88371	1.20624	0.52884	0.538656383
0.976	0.94995	2.49247	0.56561	1.839325595

χ^2 test results are shown in Tab. 3.

Table 3 Values of the χ2 test

	Function 1	Function 2	Function 3	Function 4
χ2	0.026	0.374	0.017	0.136
Degrees of freedom	6	8	6	8
P	0.99999964	0.99995611	0.9999999	0.99999916
Conclusion	There is no statistically significant difference	There is no statistically significant difference	There is no statistically significant difference	There is no statistically significant difference

The differential equation system is used to show the change of tension (dε) of the load change (dF):

$$T_1:\ d\varepsilon = 0.962 + 1.1422 \cdot \log(dF), \quad (8)$$

$$T_2:\ d\varepsilon = 0.0075 \cdot e^{5.9489 \cdot dF}, \quad (9)$$

$$T_3:\ d\varepsilon = 0.5723 + 0.634 \cdot \log(dF), \quad (10)$$

$$T_4:\ d\varepsilon = 9.9514 \times 10^{-5} \cdot e^{10.0662 \cdot dF}. \quad (11)$$

4 CONCLUSION

The experiment showed that at the linear increase of the load on the research form, due to the eccentric position of the axial force and the damage on the opposite side of the measurement, a significant curvature of side *b* was recorded, that is, the larger deflection was recorded in the direction of the maximum moment of inertia. The action of the eccentric axial force is applied perpendicularly to the part of the cross section where damage is present. The assumption of the experiment is that, in such an unfavourable position of the axial force, a significant role in the curvature other than eccentricity also has a damage of the research form cross section. In the direction of the minimum moment of inertia, there was significantly less deflection, but in the expected direction, or side *h* opposite to the damage, it also turned outward in relation to the vertical axis of the research form.

The expected direction of the curvature of the research form in the direction of the minimum moment of inertia confirms the influence of cross-sectional defects, while the main cause of the significant curvature of the research form in the direction of the maximum moment of inertia is the eccentricity itself. In order to fully confirm the impact of the cross-sectional defects of the research form on bending, and most importantly determine the magnitude of that impact, it is necessary to extend the experiment to a larger number of research forms.

The test patterns should contain different sizes and geometric forms of cross-sectional defects. Finally, such an expanded experiment should result in finding out the method of calculating the remaining firmness of the reinforced concrete columns with the damaged cross-section.

Compared to the linear increase of the eccentric axial force, the deformation of the curvature took place in the form of the exponential function at the points T_2 and T_4 and according to the logarithmic function, at the points T_1 and T_3. Thus, the deflection of side *b*, although in the direction of the maximum inertia moment, takes place in the exponential function, while the deflection of the page *h* takes place according to the logarithmic function.

By performing a χ^2 test, it is proved that the functions describe the actual data statistically, that is, that there is no statistical difference between the actual data set and the number of data obtained by the function. The equations obtained were translated and merged into the differential equation system and a mathematical model of the behaviour of a damaged reinforced concrete pillar made of concrete of normal strength (<50 MPa) due to the axial eccentric load was conceived.

Note: This research was presented at the International Conference MATRIB 2017 (29 June - 2 July 2017, Vela Luka, Croatia).

5 REFERENCES

[1] Gotal Dmitrović, L.; Dušak, V.; Milković, M.: Modeliranje informacijskih sustava za zaštitu površinskih voda, Sveučilište Sjever, Varaždin, 2017.
[2] Harell R. C.; Bateman E. R.; Gogg J. T.; Mott R. A. J.: System Improving Using Simulation; PROMODEL Corporation Orem Utah, 1996.
[3] Jain S.; Choong N. F.; Aye K. M.; Luo M.: Virtual factory: an integrated approach to manufacturing systems modeling; International Journal of Operations & Production Management, 21(5-6), 2001.
[4] Šošić, I.: Primijenjena statistika, Školska knjiga, Zagreb, 2006
[5] European Committee for Standardization Eurocode 2: Design of concrete structures Part 1: General rules and rules for buildings 2001.
[6] Němeček J.: Effect of Stirrups on Behavior of Normal and High Strength Concrete Columns, Acta Polytechnica Vol. 44 No. 5–6/2004.
[7] Rabie M.: Behavior of R.C Columns with Poor Concrete Strength at Upper Part, Life Science Journal 9 (2) 2012.

Authors' contacts:

Željko KOS, PhD student
University North, University Center Varaždin
104. brigade 3, 42000 Varaždin, Croatia
e-mail: zeljko.kos@unin.hr

Lovorka GOTAL DMITROVIĆ, PhD, Research Associate
(Corresponding author)
University North, University Center Varaždin
104. brigade 3, 42000 Varaždin, Croatia
e-mail: lgotaldmitrovic@unin.hr

Evgenij KLIMENKO, PhD, Full Professor
Odessa State Academy of Civil Engineering and Architecture
Didrihsona 4, 65029 Odessa, Ukraine
e-mail: klimenkoew57@gmail.com

ISSN 1846-6168 (Print), ISSN 1848-5588 (Online)
ID: TG-20171104203425

Original scientific paper

FREEZING POINTS OF PURE METALS AS DEFINING POINTS OF INTERNATIONAL TEMPERATURE SCALE ITS-90

Tomislav VELIKI

Abstract: Melting and freezing temperatures are one of the most important features of metals, both in production and application. For the extremely pure metals where purity higher than 99.9999% is reached, difference between the melting and the freezing temperature is less than 1 mK (1/1000 °C). This virtue has been used for establishment of the temperature fixed points, on which the Practical temperature scales were laid upon. Temperatures of the fixed points are determined on the basis of thermodynamics. The temperature fixed points are used for the calibration of thermometers, which are then in turn used for interpolation between the fixed points. Every realization of the Practical temperature scale is an independent experiment. In this sense, this paper describes mathematical modeling and equipment used for the realization of the temperature scale in the Republic of Croatia in the range from −0 °C to 660 °C, accompanied with the measurement uncertainties.

Keywords: international temperature scale; melting and freezing temperatures; pure petals

1 INTRODUCTION

To achieve the uniformity in measurement of temperature in a way that was achieved in length measurements with *Meter Convention* and the unique standard for length established in 1875, it was needed to invent the practical standard for temperature. The first International Temperature Scale was adopted in 1927 to overcome the practical difficulties of the direct realization of thermodynamic temperatures by gas thermometry and to unify existing temperature scales. It was introduced by the Seventh General Conference on Weights and Measures (CIPM) with the intention of producing a practical scale of temperature which would be easily and accurately reproducible and which would give the best approximation of thermodynamic temperatures. The Scale was revised in 1948, amended in 1960, and revised again in 1968 and 1990. The International Temperature Scale of 1990, known as ITS-90 [1], was adopted by the International Committee for Weights and Measures (BIPM) at its meeting in 1989. However, this scale prescribes numerical values of the temperature at the temperature fixed points, interpolation function and instrument between fixed points while the physical realization is left to the user of the scale. This paper will describe the independent realization of the ITS-90 as primary standard in the Republic of Croatia in the range where freezing points of the pure metal are used, accompanied with description of equipment and uncertainties achieved.

2 DEFINITION OF THE INTERNATIONAL TEMPERATURE SCALE ITS-90

International Temperature Scale ITS-90[1] extends upwards from 0.65 K to the highest temperature practicably measurable in terms of the Planck radiation law using monochromatic radiation. The ITS-90 comprises a number of ranges and sub-ranges throughout each of which temperatures T_{90} are defined. Definition prescribes thermometric fixed points which are based on melting, freezing or triple points of pure substances to which precise values of temperature were measured by thermodynamic thermometers. An excerpt from [1] is presented in Tab. 1.

Table 1 Defining temperature points of International Temperature Scale ITS-90 assigned to the specific phase transitions of pure substances, [1]

Equilibrium state	T_{90} /K	t_{90} /°C
Triple point of hydrogen	13.8033	−259.3467
Boiling point of hydrogen at a pressure of 33321.3 Pa	17.035	−256.115
Boiling point of hydrogen at a pressure of 101292 Pa	20.27	−252.88
Triple point of neon	24.5561	−248.5939
Triple point of oxygen	54.3584	−218.7916
Triple point of argon	83.8058	−189.3442
Triple point of mercury	234.3156	−38.8344
Triple point of water	273.16	0.01
Melting point of gallium	302.9146	29.7646
Freezing point of indium	429.7485	156.5985
Freezing point of tin	505.078	231.928
Freezing point of zinc	692.677	419.527
Freezing point of aluminum	933.473	660.323
Freezing point of silver	1234.93	961.78
Freezing point of gold	1337.33	1064.18
Freezing point of copper	1357.77	1084.62

The comparison of fixed-point temperatures and the interpolation of the scale between fixed points in the temperature range between about 0 °C and 962 °C is by definition of ITS-90 carried out by platinum resistance thermometry. In this range, defining temperatures are phase transitions of metallic fixed points materials (Ga, Sn, Zn, Al, Ag) having nominal purity in-between 99.9999 % and 99.99999%. Thermometers calibrated per ITS–90 use prescribed mathematical formulas to interpolate between its defined points. ITS–90 also draws a distinction between "freezing" and "melting" points. The distinction depends on whether heat is going into (melting) or out of (freezing) the sample when the measurement is made. Only gallium is

measured while melting; all the other metals are measured while the samples are freezing.

Temperature T_{90} in this range is expressed through ratio of resistances of platinum resistance thermometer $R(T_{90})$ and the resistance of the same thermometer at temperature of triple point of water $R(273,16)$:

$$W(T_{90}) = R(T_{90}) / R(273,16) \tag{1}$$

Reference function at this range of ITS-90 is defined according to [1]:

$$W_r(T_{90}) = C_0 + \sum_{i=1}^{9} C_i \left[\frac{T_{90} / K - 754,15}{481} \right]^i \tag{2}$$

and numerical values of the coefficients c_0 to c_9 are available in [1] .

Deviation function of the thermometer which after calibration in defining fixed points is used for interpolation across the range has the following form:

$$\begin{aligned} &W(T_{90}) - W_r(T_{90}) = a\left[W(T_{90}) - 1\right] + \\ &+ b\left[W(T_{90}) - 1\right]^2 + c\left[W(T_{90}) - 1\right]^3 + \\ &+ d\left[W(T_{90}) - W(660,323°C)\right]^2 \end{aligned} \tag{3}$$

Thus, after measuring resistance of the thermometer in the temperature fixed points and immediate measuring of the resistance in the triple point of water during calibration, coefficients *a* to *d* from Eq. (3) can be calculated for specific thermometer. That thermometer is then used for the interpolation of the temperature according to ITS-90 with calculated measurement uncertainty.

3 DEVELOPMENT OF THE INDEPENDENT REALIZATION OF THE ITS-90

Realization of the International Temperature Scale ITS-90 was performed in the Laboratory for Process Measurement located at the Faculty of Mechanical Engineering and Naval Architecture, University of Zagreb, in the period from 2002 to 2011. As the definition of the ITS-90 described in the previous chapter does not stipulate technical details but offers general recommendations elaborated in [2] and [3], every national laboratory is obliged to design and purchase equipment and devise a method adequate for the experiment. For the establishment of the freezing point of tin, zinc and aluminum the open type of fixed point was chosen, with quartz envelope and pure graphite parts delivered by company Isotech. Materials required for filling the points were acquired by the producer Johnson Matthey. Dimensions and specifications are given in Tab. 2.

The main purpose of the open fixed-point cells is the ability to regulate pressure of argon gas during phase transition, thus lowering the uncertainties. The second benefit comes into play in the case of the rupture of the quartz envelope during melting and freezing of the fixed-point material, when overpressure of argon can prevent volatile oxidation of graphite container containing pure metal, as well as contamination of the pure metal with impurities from atmosphere.

Table 2 Specifications of the fixed points used for realization of the ITS-90

Type	ITL-M-17669	ITL-M-17671	ITL-M-17672
Material	Sn	Zn	Al
Producer	Johnson Matthey	Johnson Matthey	Johnson Matthey
Outer diameter	50 mm	50 mm	50 mm
Thermometer tube	8 mm	8 mm	8 mm
Height	520 mm	520 mm	610 mm
Height of molten material	200 mm	200 mm	200 mm
Nominal Purity	99.9999 %	99.9999 %	99.9999 %

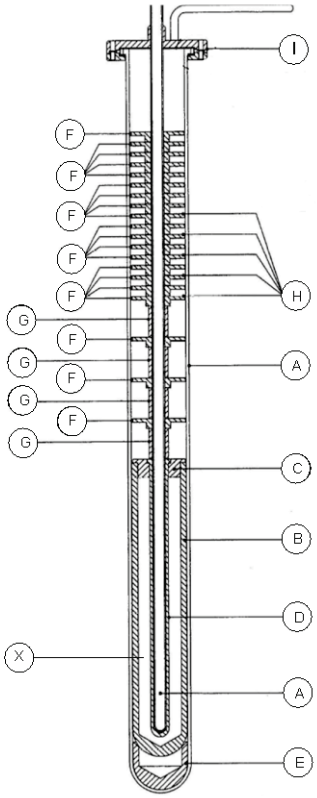

Figure 1 Cross section of the open temperature fixed point. Height of the cell is approximately 520 mm. Description of the labels on the figure are given in text.

Fig. 1 depicts cross section and main parts of the physical realization of the fixed point which is to be inserted into thermometric three zone controlled furnace. Quartz envelope (A) is used to separate the interior filled with argon from the surroundings, thus preventing oxidation, while allowing thermometer to be inserted into the middle of the material going through phase transition. A graphite container (B) is used to hold pure metal (X) both in molten and solidified state. It is sealed by the graphite top (C) and the graphite re-entrance tube for thermometer (D), and is positioned on the graphite cushioning insert (E). The graphite rings (E) with accompanying bushings (G) are used

to decrease heat transfer toward the top of the fixed point. In the area where largest temperature gradients are expected, additional platinum foil plates are applied for lower radiation losses. The top of the fixed point is sealed with a flange connecting quartz tube for thermometer and quartz envelope, and contains connection for argon gas installation.

During a regular course of calibration, material would be left overnight on temperature 2÷5 °C over phase transition. Then temperature of the furnace would be set to approximately 2 °C under phase transition. When thermometer would reach that temperature, it would be removed and a pre-cooled quartz tube would be inserted to start crystallization since pure metals have pronounced supercooling effect, as described in [4]. Once the phase transition front would start from both outside and the thermometer entrance, thermometer would be reinserted into the fixed point and the measurement could commence after the stabilization phase, as described in [5] .

4 MATHEMATICAL MODEL OF MEASUREMENT

The values of the resistance of the thermometer $R(T_{90})$ during phase transition on defining temperature T_{90} and resistance $R(273{,}16)$ on temperature of the triple point of water are obtained from readings from resistance thermometry, X_t and $X_{273,16}$. The reading of the bridge X_t is the ratio of unknown resistance of the thermometer $R_i(T_{90})$ and resistance of known standard resistor, R_{s1}.

$$R(T_{90}) = X_t \cdot R_{S1} \tag{4}$$

Similarly, the reading of the bridge $X_{273,16}$ corresponds to the ratio of the resistance of the thermometer inserted into triple point of water and resistance of the standard resistor R_{s2}. The resistance of the thermometer at the triple point of water is determined from the following:

$$R(273{,}16) = X_{273,16} \cdot R_{s2} \tag{5}$$

At each temperature, the minimum of 32 readings from the bridge are taken at two different electrical excitation currents, usually 1 mA and √2 mA, to allow extrapolation to the ideal value of 0 mA, as elaborated in [6].

However, the reading of the bridge is influenced by the various phenomena whose effects are to be corrected and uncertainties of the corrections estimated. Firstly, the values of the standard resistor have drifted from the time of calibration by $C_{RS1/1}$ and $C_{RS2/1}$. Secondly, corrections have to be made due to deviation of the temperature of the oil bath in which standard resistors are kept $C_{RS1/2}$, $C_{RS2/2}$. Thirdly, temperatures of the phase transitions in fixed points are to be corrected due to dissolved impurities in the metals and the water used for the triple point, deviation of temperature due to hydrostatic head from free surface to thermometer, effect of self-heating of the thermometer due to passing current, stray heat fluxes, and effect of argon pressure during realization. Lastly, corrections in the measurement system such as nonlinearity of the resistance bridge, electromagnetic disturbances and loss of isolation in the thermometer are to be estimated. After taking into account all known corrections, the mathematical model of the measurement has a form:

$$W(T_{90}) = \frac{R_{0s1} + C_{RS1/1} + C_{RS1/2}}{R_{0s1} + C_{RS1/1} + C_{RS1/2}} \cdot \frac{X_t + \sum_{l=1}^{l} C_{xt/l}}{X_{273,16} + \sum_{k=1}^{k} C_{x273,16/k}} \tag{6}$$

where $\sum_{l=1}^{l} C_{xt/l}$ and $\sum_{k=1}^{k} C_{x273,16/k}$ are known corrections of the temperature of the phase transition in the fixed point and in the triple point of water.

The value of corrections described in Eq. (6) and their intrinsic uncertainties are the main challenge in realization of the International Temperature Scale. During the experiment, some of the corrections were estimated from the data available in available literature, others were measured experimentally, as described in [7]. For estimation of thermal stray fluxes numerical simulations were used, as described in [8]. The largest uncertainty contribution is the purity of the fixed-point material. In order to have confidence in its value, it is calculated, then measured experimentally, and then finally verified by the laboratory inter-comparisons with other National Laboratories [9, 10].

5 MEASUREMENT RESULTS

During the process of realization of the Temperature Scale, measurements are performed with twofold purpose: to characterize the experimental realization of the scale as standard, and to calibrate interpolating thermometers against standard.

The metals used for temperature fixed points are the purest commercially available (with nominal mass purity >99.9999 %), but the effects of dissolved impurities must not be taken for granted. All materials were purchased with chemical trace analysis conforming nominal purity. From this chemical analysis and using publicly available data such as [11], corrections of the temperature can be calculated. However, those corrections are to be checked experimentally since impurities stated in the analysis are on the edge of detection threshold and refer to the lot of the material and not to the purchased sample. The experimental verification of the impurities dissolved on the fixed point material is performed by continuous melting and freezing of pure metal and measurement of the duration and slope of temperature arrest during phase transition, [12].

For ideally pure metals melting and freezing temperature would be the same, while the presence of impurities changes the shape and lowers the values of the phase transition, as depicted in Fig. 2, where 5N material (mass purity 99.999 %) has substantially lower melting and freezing temperatures than 6N (mass purity 99.9999 %).

The temperatures of the phase transition and its slope are measured using the standard platinum thermometer.

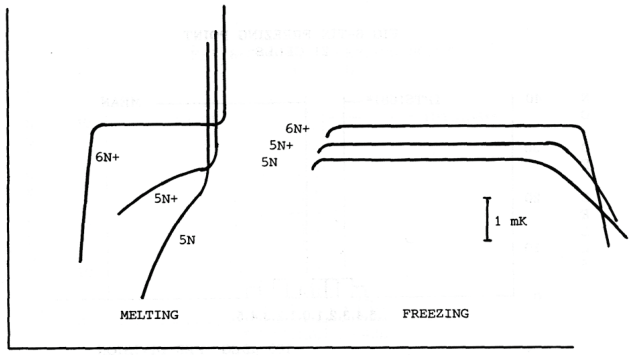

Figure 2 Typical melting and freezing behavior of a dilute binary alloy, [12]. Marks 6N and 5N stand for mass purity of 99.9999 % and 99.999 %.

As this correction accounts for the major attribution in the overall uncertainty, the measurements were performed for every fixed point used for realization of the ITS-90. To allow the analysis of measurement results, metrological furnace, in which fixed points were inserted, was controlled in such a way that melting and freezing would last for at least 3 hours.

The experimental results of the measurement of phase transitions in melting and freezing for fixed point filled with aluminum are shown in Fig. 3. The values measured during melting are shown in grey, while those measured during freezing are shown in black. For the ease of graphical explanation both processes are shifted to start at the same point.

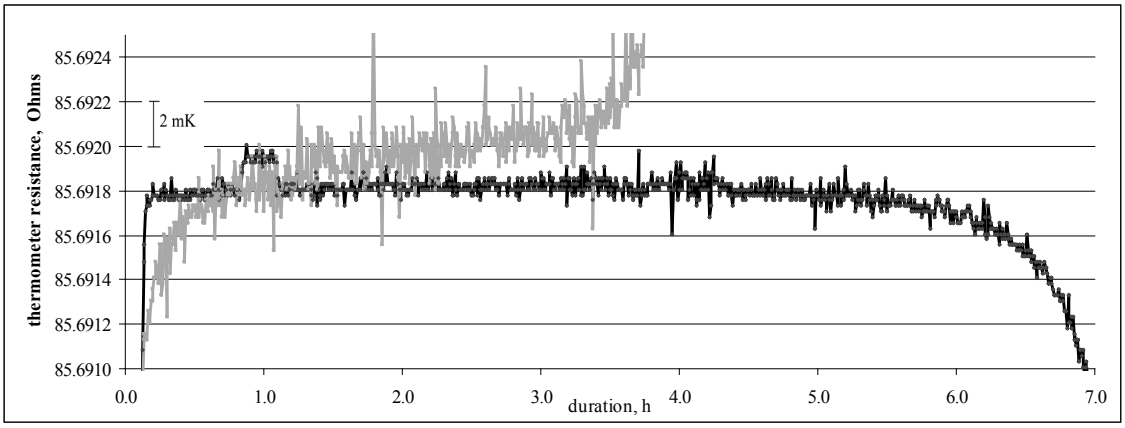

Figure 3 Measurement results showing resistance of the thermometer during melting and freezing for characterization of the aluminum fixed point. Melting process is shown in grey, while freezing is represented by black curve.

Table 3 Final values of the calculated temperature corrections due to impurities in the fixed point after laboratory inter-comparisons, and accompanying EURAMET projects from which they were calculated.

Fixed point	Correction, mK	Uncertainty, mK, k=2	Inter-laboratory comparison
Sn	0.0	0.5	EURAMET 1144, EURAMET 1167
Zn	−1.2	0.9	EURAMET 1144, EURAMET 1167
Al	−4.1	1.5	EURAMET 820 [9], LPM-PTB 2009

As the data obtained from the chemical analysis were inconclusive, for the realization of the ITS 90 corrections due to impurity are calculated based on measurements of melting and freezing behavior. In the first step, corrections are estimated to have value zero, with pertaining uncertainties being equal to the temperature span in which 80 % of the phase transition takes place. In the second step, the temperature during phase transition is compared using platinum resistance thermometer with realizations in different European National Institutes, enabling better calculation of the correction of temperature in every fixed point. For every fixed point several inter-comparison measurements were performed with other laboratories comprising European Association of National Metrology Institutes – EURAMET. Based on the analysis of those measurements, the final values of corrections due to impurities of the fixed points materials are calculated with their pertaining uncertainties as shown in Tab. 3.

The development of the independent experimental realization of the ITS-90 in the above-mentioned way has enabled calibration of the platinum resistance thermometers according to ITS-90. Those thermometers are then used as temperature standard in dissemination of the ITS-90 for all temperature measurements in scientific, industrial and legal metrology. However, when calibration of the platinum resistance thermometer is performed, new corrections are added upon those corrections due to impurities of the material in fixed points, and overall uncertainty is calculated. Tab. 4 shows overall uncertainties achieved with measurement setup for the calibration of the thermometers in fixed points.

Table 4 Overall calculated uncertainties for calibration of platinum resistance thermometers in the temperature fixed points

Fixed Point	Temperature, °C	Uncertainty of calibration, mK, k=2
Al FP	660.323	9.0
Zn FP	419.527	7.0
Sn FP	231.928	3.0
Ga MP	29.765	1.0

6 CONCLUSION

The freezing points of pure metals are the basis for realization of International Temperature Scale ITS-90 as standard for measurements in temperature. Limiting factors in achieving lower uncertainties in such experiments are impurities in the material of fixed point. In this paper, the method for estimation on the correction due to impurities is presented, with uncertainties achievable in the calibration of the platinum resistance thermometers, which are then used for dissemination of the ITS-90. Methods and values presented in the paper were not only achieved in laboratory environment, but were tested and verified by the German Accreditation Service DAkKS in 2009 and the Croatian Accreditation Agency HAA in 2013.

Note: This research was presented at the International Conference MATRIB 2017 (29 June - 2 July 2017, Vela Luka, Croatia).

7 REFERENCES

[1] H. Preston-Thomas, The International temperature scale of 1990 (ITS-90), Metrologia 27 (1990), no. 1, 3-10.
[2] Supplementary Information for the International Temperature Scale of 1990, BIPM, Sevres, 1990.
[3] B. Fellmuth, E. Tegeler and J. Fischer, Uncertainty of the Characteristics of SPRTs Calibrated According to the ITS-90, Proc. TEMPMEKO 2004, June 2004, Faculty of Mechanical Engineering and Naval Architecture, 2005, 1135-1140.
[4] D. Zvizdić, L. Grgec-Bermanec, T. Veliki, J. Zelko and A. Jurišinac, Realization of Temperature Scale ITS-90 in Republic of Croatia, Proc CROLAB-Kompetentnost laboratorija, CROLAB, Dubrovnik, 2007.
[5] D. Zvizdic, T. Veliki and L. Grgec Bermanec, Realization of the Temperature Scale in the Range from 234.3 K (Hg triple point) to 1084.62°C (Cu freezing point) in Croatia, International Journal of Thermophysics 29 (2008), no. 3, 984-990.
[6] T. Veliki, Development of the Primary Temperature Standard with New Method for Dissemination of Traceability, PHD Thesis, University Of Zagreb, Zagreb, 2011.
[7] D. Head, J. Gray and M. de Podesta, Current Work on Furnaces and Data Analysis to Improve the Uniformity and Noise Levels for Metal Fixed Points, International Journal of Thermophysics 30 (2009), no. 1, 296-305.
[8] S. Krizmanić, T. Veliki and D. Zvizdić, Modeling of Transient Heat Transfer in Zinc Fixed-Point Cell, International Journal of Thermophysics 32 (2011), no. 1, 326-336.
[9] D. Heyer, U. Noatsch, E. Tegeler, M. Anagnostou, E. Turzo-Andras, I. Antonsen, V. Augevicius, J. Bojkovski, A. Bronnum, V. Chimenti, S. Duris, E. Filipe, S. Gaita, J. Gray, D. Head, E. Grudniewicz, J. Ivarsson, M. Kalemci, O. Kerkhof, I. Lobo, S. Nemeth, A. Pokhodun, J. Ranostaj, E. Renaot, P. Rosenkranz, M. Smid, P. Steur, A. Steiner, M. Valin, T. Veliki and T. Weckstroem, Intercomparison of the Realization of the ITS-90 at the Freezing Points of Al and Ag among European NMIs, International Journal of Thermophysics 28 (2007), no. 6, 1964-1975.
[10] J. Bojkovski, T. Veliki, J. Drnovsek and D. Zvizdic, Bilateral comparison of Mercury and Gallium Fixed-points Cells Using Standard Platinum Resistance Thermometer, International Journal of Thermophysics 32 (2011), no. 7-8, 1544-1552.
[11] G. F. Strouse, NIST Methods of Estimating the Impurity Uncertainty Component for ITS-90 fixed-point cells from the Ar TP to the Ag FP, CCT 03/19, BIPM, Sevres, 2003.
[12] E. H. McLaren, The Freezing Points of High-purity Metals as Precision Temperature Standards, Temperature, Its Measurement and Control in Science and Industry 3 (1962), 185-198.

Author's contacts:

Tomislav VELIKI, Assistant Professor
University North
Ul. 104. brigade 3, 42000 Varaždin, Croatia
E-mail: tveliki@unin.hr

ISSN 1846-6168 (Print), ISSN 1848-5588 (Online)
ID: TG-20171112214636

Original scientific paper

MULTIPLE INFLUENCE OF SILICA-CONTAINING COMPONENT OF THE CHEMO-BIOGENIC ORIGIN ON THE STRUCTURE AND PROPERTIES OF COMPOSITES ON SILICATE MATRIX

Yevgen LUTSKIN, Olena SHYNKEVYCH, Aleksej ANISKIN

Abstract: A distinctive feature of the silicate matrix composites unlike silicate autoclaved concrete is that they are made on the basis of the ternary complex activated silicate concrete mixture modified by alkali and mineral additives, and harden at 85 °C and standard atmospheric pressure. Due to the implementation of a complete activation of highly mobile silicate concrete mixture, that is one of the technological features to obtain this type of composites, energy-saving modes of preparation were provided. The composites and products based on them are characterized by low density at high values of strength, water and crack resistance and heat capacity. Now there is clear idea about the functional role and impact on the structure and properties of silica-containing components chemo-biogenic genesis, which were previously used either as active mineral additives or fillers. The comparative analysis of the influence of the tripoli specific surface to the restructuring and silicate matrix properties and porous composites modified of alkali containing additives other additives were carried out. Based on this analysis the mechanism of formation of silicate matrix structure and properties was grounded and proposed. It is shown that the tripoli particles promoted "physical" seal structure of silicate matrix and the formation of capillaries' discontinuous structure, by means of their own micro-porosity.

Keywords: complex activation; silica-containing component; silicate matrix

1 INTRODUCTION

Conservation of the Earth's ecosystem is one of the main mankind tasks. Nowadays, the development strategy of many countries is impossible without environmental technologies or so-called "green" technologies. Their goals are blowout controls, resource-saving, waste management, increasing of productional energy efficiency, etc. The development and adaptation of new resource-saving technologies is one of the most advanced versions for always urgent issue solving of competitive enterprises. The cost of building materials depends on the raw materials they are made of and how energy-consuming their production technology is. Cutting the cost of building materials and construction totally will allow the production of building materials at the site of their using from the local raw materials and with using the non-autoclave [1÷6] and non-fire technologies. Therefore, in order to the conserve the Earth's ecosystem as a planet, optimization is necessary – it is the optimization of the system "man – eco- and energy-saving technologies – composite materials – environmental conditions". This approach will have a beneficial effect on the conservation of the planet's energy and material resources.

As technological methods progress, the possibility of using different types of activation should be noted. This contributes to the reduction of energy costs and allows the control of the structure formation process in such a way as to provide the required and predicted physical and mechanical properties of materials, products, and structures.

The development of new-generation materials is based on complex activated silicate mixtures, which are produced under casted technology with using of modern nanotechnological methods [1÷6].

These materials are characterized by reduced density with sufficiently high strength, high water-, frost-, crack-resistance and heat capacity.

2 NANOTECHNOLOGY RECEPTIONS OF PRODUCING THE COMPLEX ACTIVATED COMPOSITES ON SILICATE MATRIX

One of the research tasks is the identification of general mechanisms of structure and properties formation of the non-autoclaved hardening silicate composites.

Developed by the authors, the complex activation includes the continuous loop of the different types and methods of activation: mechanical, chemical, and thermal [1, 2].

Each type of activation is accompanied by effects which create the conditions for the possibility of subsequent type of activation.

The result of the complex activation is the formation of linear defects, dislocations, and point positions and substitutions. Furthermore, there may be angle change between the bonds and the appearance of dangling bonds, which leads to the formation of free radicals in the crystals with covalent bonds and the amorphization of molecular crystals.

Each type of activation will be caused by the prevalence of any type of deformations of the solid phase structure. The differences will be responsible for the nature and kind of dislocations with allowance for the extent and duration of external and internal influences.

2.1 Mechanical activation

Mechanical effects in the dispersion medium speed mixer activator provide mechanochemical activation of

crystalline quartz surface. The term "mechanochemical reaction" was introduced by W. Ostwald in 1891.

Mechanochemical activation is carried out on the special properties of the newly formed surfaces, especially changing the local chemical and phase content of solids, as well as their aggregate state of under the influence of mechanical effects of high intensity [7].

As with nanotechnology reception, the mechanochemical activation reduces the viscosity of 3 or more dispersed systems containing lime [1÷3]. This effect of viscosity reduction was used to compensate the increased water demand of the mixture introducing the composite porous opal-cristobalite rocks and using the activation of the binder together with the fine aggregate.

2.2 Thermal activation

Used as a binder, quicklime promotes the "inner activation" of dispersed system under an elevated temperature T= 40÷60°C. The formation of multiple point contacts in the dislocation fields appears and the conditions for the hydration hardening unrelated in hydrous calcium lime are created.

External thermal activation occurs in conditions of thermal-moisture treatment. In such conditions at T=85 °C contradiction is canceled, which relates to the increasing the quartz solubility and decreasing lime solubility with increasing its dissolution [8, 9]. In addition, the increase of pH system causes to create favorable conditions for longevity growths GSK during the operational phase when $11.5 \leq pH \leq 12.5$.

2.3 Chemical activation

According to E. Avvakumov's works [10], with the presence of water in the inorganic solid-phase system the "method of soft mechanochemical synthesis" is developed. Hydroxides are used as the starting components to obtain composite oxides from the simple oxide. One of these is characterized by acidic, the other one is characterized by basic properties. By means of the neutralization reaction the intensification of the processes takes place. In addition, in such system the conditions for the hydrothermal processes are created.

The acid activation occurs by introducing the amorphous-crystalline silica, alkaline activation – the introduction of increased amounts of lime; it raises pH. The replacement of ground quartz sand in the binder by opal-cristobalite rocks increases frost and water resistance of the silicate matrix while reducing its density matrix to 20÷25%.

Moreover, the presence of opal-cristobalite rock in the dispersion causes formation of nanoscale in the GSK pores of these rocks; in this case, they are "nanoreactor". Its walls restrict the growth of neoplasm [11]. Also, the presence of particles of porous rocks with different dispersion binder allows adjusting the speed and reaction kinetics of hydration [3].

The use of quicklime determines the possibility of using high modulus liquid glass as one of the alkali additions, so the temperature rise on the forming stage allows regulating rapid setting of such mixture.

Alkali and alkali-containing additives increase the thermodynamic instability of systems by shifting the equilibrium caused by the formation of additional defects on the surface of silica-containing components. Alkali-containing additives are capable for aeration of mixtures under certain conditions [12].

In this work, the low-temperature aeration of concrete during introduction of the activation to the mixture for the silicate matrix by liquid glass additives $Na_2O \cdot nSiO_2 + mH_2O$ and sodium hydroxide NaOH is provided.

3 EXPERIMENTAL

In this study, one of the objectives is to identify local laws of formation of structure and properties of the aerated complex activated composites on the silicate matrix of thermal-moisture hardening to establish and use in practice the most effective and cost-effective methods of nanotechnology in the production process.

The forming of informative base for the optimization of technological decisions is provided using the methods of the experimentally-statistical modeling. The multifactor experiment was carried out with the use of the mathematical theory of planning of the experiment [13÷15]. Two comparable complexes of six-factor experimentally-statistical models are calculated. ES models by type (1) describe the dependence "mixture-properties" and "mixture-structure". It allows studying the dependence "content-structure-properties".

To analyze the possibilities of the regulation of the structure and properties of the aerated composites on the silicate matrix six factorial field experiments according to the 24-point plan, such as "triangles on the cube" by type "mixture-technology-quality", were carried out [13÷15]. In the plan, three mixed factors and three independent of the content vary simultaneously. With three mixed factors the surface area of tripoli as the component of lime-silica binder at levels was fixed: υ_1 – S_{sp1}=400 m^2/kg, υ_2 – S_{sp2}=500 m^2/kg, υ_3 – S_{sp3}=600 m^2/kg. With three independent factors in the experiments the content of alkali-containing additives was varied: x_4 – NaOH – (0.5÷1)%, x_5 –$Na_2O \cdot nSiO_2 + mH_2O$ – (1÷5)% and gypsum additives x_6 – $CaSO_4 \cdot 2H_2O$ – (2÷4)%.

The data on the properties and characteristics of the structure of full-scale experiments carried out in each of the 24 points of the plan were the basis for the ES models' calculations.

According to the experiment results, ES model is calculated, which allowed to estimate the effect of alkali-containing additives and the specific surface area of tripoli on the properties and characteristics of the structure of aerated composites on silicate matrix.

The computation experiment has shown that the factor which has the greatest influence on the properties is the specific surface area of tripoli. Due to the synergistic action of alkali additives and liquid glass, taken in optimal ratios for each property and given S_{sp} of tripoli, the aeration of the

mixture is achieved. This lowers the density and high values of the properties: compressive strength R_b (MPa), bending strength R_{btb} (MPa), water resistance (coefficient of softening) k_s, crack resistance (critical coefficient of stress intensity) k_{Ic} (MPa·m$^{-0.5}$), heat conductivity (coefficient of heat conductivity) λ (Wt/m·K), frost resistance F (cycles). The introduction of additives of alkali and liquid glass increases the volume of the mixture to 1.2÷1.4 times. The density of the composite varies from 1300 to 1500 kg/m^3, which is 17÷23% lower than the density of the matrix material and 25÷30% lower than the density of autoclaved silicate brick.

4 RESULTS AND DISCUSSION

According to the experimental results, the experimental-statistical (ES) models were calculated. By ES models the optimal values of quality criteria and compositions of mixtures have been installed. Compressive strength R_b varies from 12 to 18.5 MPa, i.e. 1.5 times, and it is in the range of changing of the matrix material strength. Maximum strength is greater than 18 MPa and is obtained for compositions which contain 5% of liquid glass, 0.5% of alkali, and 4% of gypsum, S_{sp}=400 m^2/kg of Tripoli. The same strength of the silicate matrix is obtained on tripoli with S_{sp} = 500 m^2/kg.

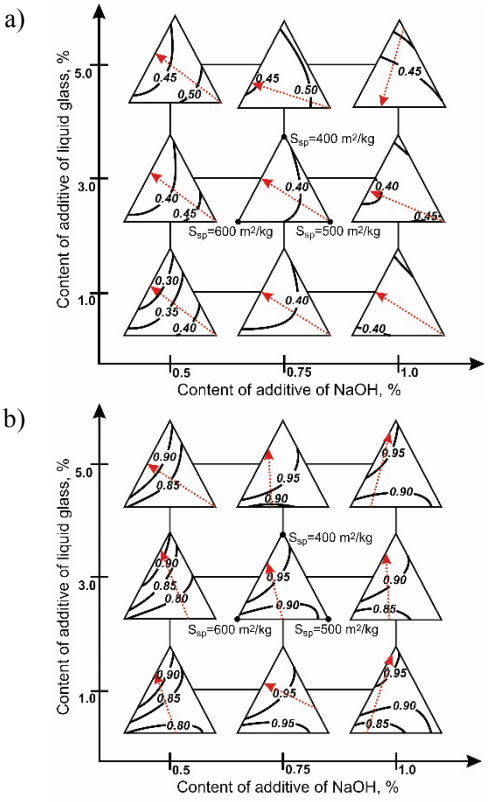

Figure 1 The influence of additives NaOH and liquid glass on coefficient of heat conductivity λ (a) and softening coefficient k_s (b) and for a fixed value additive of gypsum 4%

According to the ES model (1), the coefficient of heat conductivity λ of aerated composites under the influence of all six factors varies 1.9 times, from 0.28 to 0.54 Wt/m·K. The minimum value of the heat conductivity coefficient λ = 0.28 Wt/m·K is obtained on the contents which contain 0.5% NaOH and 1% liquid glass, a mixture of tripoli particles with a specific surface S_{sp}=400 and S_{sp}=600 m^2/kg in equal ratio and gypsum additive 4% (Fig. 1a).

Softening coefficient is varied by k_s 0.81÷1. The values k_s≥0.95 were obtained with the content 0.75% NaOH and 5% liquid glass on specific surface of tripoli S_{sp}=400 m^2/kg and the gypsum additive content of 4% (Fig. 1b).

Frost resistance of aerated materials is 25÷30 cycles that lay within the changes in frost resistance of matrix material – F25-50. The maximum value of the frost resistance of aerated composites was obtained on S_{sp}=400 m^2/kg, and the content of additives gypsum is 4%. The similar values of frost resistance of silicate matrix were obtained in the mixture of tripoli particles S_{sp}=400 and S_{sp}=600 m^2/kg in equal proportions and gypsum content 2.5%.

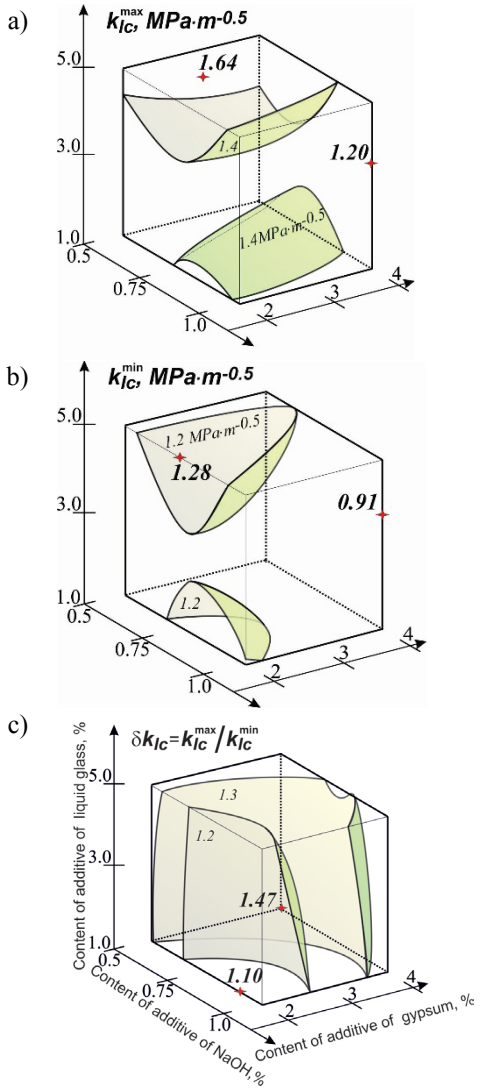

Figure 2 The changing the maximum (a) and minimum (b) values k_{Ic} under the influence of content and technological factors, taking into account the values of S_{sp} of tripoli determining the maximum and minimum values k_{Ic} respectively. Relative change ratio $\delta k_{Ic} = k_{Ic}^{max}/k_{Ic}^{min}$ (c) due to changes of S_{sp} of tripoli

The critical coefficient of stress intensity k_{Ic} under the influence of all factors varies by 1.8 times, from 0.91 to 1.64 MPa·m$^{-0.5}$ (Fig. 2, b). According to the ES models, taking into account the quantities of S_{sp} tripoli, which provide maximum and minimum values k_{Ic}, the ratio $\delta k_{Ic} = k_{Ic}^{max}/k_{Ic}^{min}$=1.1÷1.47 time was calculated (Fig. 2c).

The maximum values of the critical stress intensity factor k_{Ic}=1.64 MPa·m$^{-0.5}$ of aerated composites are equal to k_{Ic} of matrix material and the minimum value k_{Ic} = 0.91 MPa·m$^{-0.5}$ of aerated composites is twice the k_{Ic} of the matrix material [5]. In this case, the maximum and minimum values k_{Ic} for porous composite and the matrix material were obtained at the different values of tripoli S_{sp}. Thus, maximum k_{Ic} for aerated composites was obtained on S_{sp}=600 m^2/kg, and for the matrix material, on the mixture S_{sp}=400 and S_{sp}=600 m^2/kg with an equal ratio. It may be associated with different particles density in the volume and cramped conditions of aerated composites.

The visualization of ranges of property changes under the influence alkali-containing additives and the specific surface area of tripoli is shown in Fig. 3.

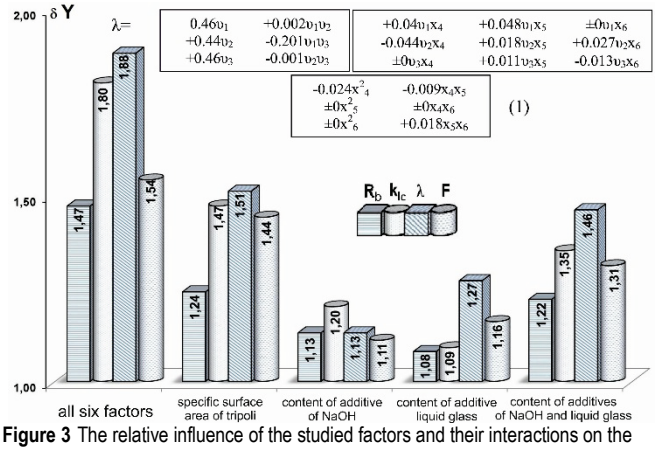

Figure 3 The relative influence of the studied factors and their interactions on the change of properties

Thus, the changed conditions of structure formation by introducing alkali-containing additives promoting aerated composites, predetermine the introduction of tripoli with a specific surface area. This may be connected, in this case, with the formation of the matrix structure in "straitened circumstances" of interporous partitions. For obtaining optimal compositions of porous composites, introducing alkali-containing additives they condition the necessity of changes S_{sp} of tripoli and adjustment of the content of gypsum additives compared with the optimal composition of the silicate matrix at constant quantitative content of other components for the mixture and the conditions of their hardening.

This change of the properties is associated with the change of structural parameters of porous composites under the influence of alkali-containing additives and S_{sp} of tripoli.

To analyze the impact of the structure characteristics on the properties the ES models of change of total, open and closed porosity and parameters of capillary porosity were calculated. The content of closed pores can be increased by reducing the content of open pores 1.7 times.

The total porosity can be increased to 30%. The average size of the capillaries d_k is changed in 4.3 times; the coefficient of distribution uniformity according to their size α_k in 2.3 times.

In the next phase of research using the computational experiments [14, 15] according to ES models, the comparative analysis of property changes and the structure characteristics of the silicate matrix and aerated composites based on the isoparametric conditions at the constant total porosity P_{tot}=const=40% was carried out.

It was found that at the constant total porosity P_{tot}=const=40% the aerated composites are characterized by k_{Ic}=1.2÷1.35 MPa·m$^{-0.5}$, that is 1.5÷1.7 times higher and the coefficient of heat conductivity is 1.8÷2.8 times lower than at the matrix material; the softening coefficient is $k_s \geq 0.95$ (Fig. 4a).

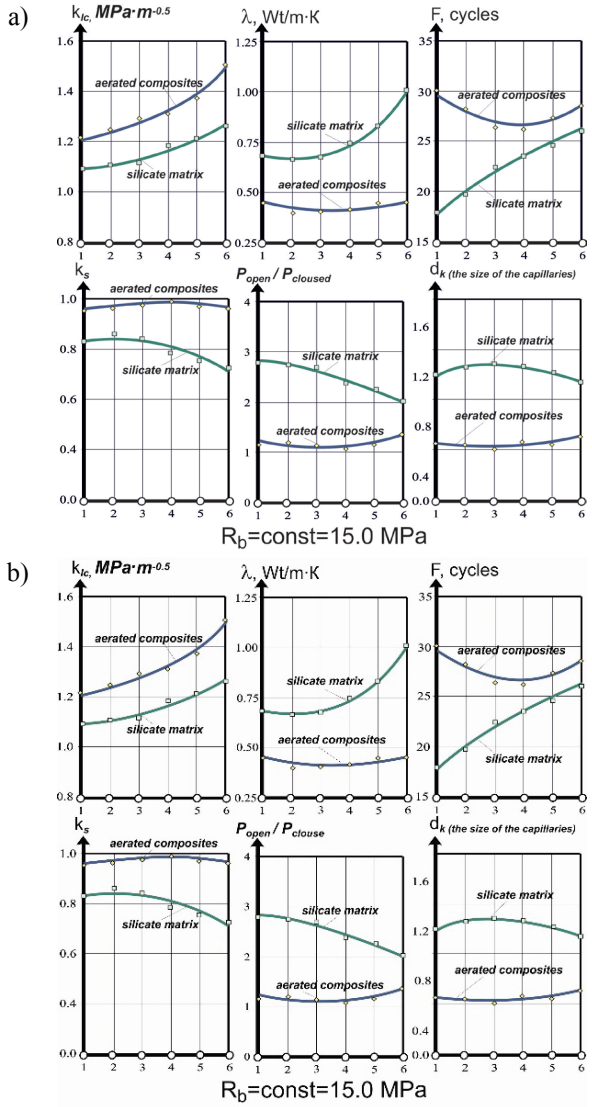

Figure 4 The comparative analysis of the changes in the properties and characteristics of the structure of the silicate matrix and of aerated composites based on isoparametric conditions: (a) P_{tot}=const=40% and (b) R_b=const=15.0 MPa

This improvement relates to the change of the structure parameters. Thus, at the aerated composites comparing with the silicate matrix the ratio of the open and closed pores is reduced 3.5 times; the average size of the capillaries relative d_k from 1.2 to 0.35 is reduced more than 3 times.

A similar comparative analysis of property changes and structure characteristics of the silicate matrix and aerated composites based on isoparametric conditions was carried out at R_b=const =15.0 MPa.

Under these conditions, the levels of the properties and their variation intervals vary: λ is decreased 1.5÷2 times, k_s=1.0, k_{Ic}=1.1÷1.45 MPa·m$^{-0.5}$, it confirms the ambiguous influence P_{tot} on R_b. R_b is determined not only by the total porosity, but also a variety of other characteristics of the structure.

The optimization problem was to obtain the aerated composites on the silicate matrix, whose physico-mechanical properties were above the properties of the silicate matrix.

The isoparametric analysis while retaining R_b=const=15 MPa and P_{tot}=const=40% showed that the ranges of other properties and structure parameters are significantly reduced: $\delta\lambda$=20%, δR_{btb}=18%, δk_s=6%, δk_{Ic}=7%, δP_{tot} – 10%, $\delta\alpha_k$ – 5% with aerated composites simultaneously with two properties of specified level (R_b and P_{tot}) (Tab. 1).

Table 1 The changing of the properties and structure parameters of aerated composites in isoparametric conditions P_{tot}=const=40% and R_b=const=15.0 MPa

	Main properties and structure parameters of aerated composites	Specific surface area of tripoli S_{sp} (m^2/kg)		
		S_{sp}=400	S_{sp}=500	S_{sp}=600
1	Compressive strength R_b (MPa)	constant 15 MPa		
2	Total porosity P_{tot} (%)	constant 40 %		
3	Bending strength R_{btb} (MPa)	2.45	2.75	2.98
4	Coefficient of softening k_s	1.00	0.94	0.94
5	Critical coefficient of stress intensity k_{Ic} (MPa·m$^{-0.5}$)	1.31	1.28	1.37
6	Coefficient of heat conductivity λ (Wt/m·K)	0.42	0.43	0.43
7	Frost resistance F (cycles)	28	27	29
8	Ration open and closed porosity P_{open}/P_{close}	1.47	1.24	1.48
9	Average size of the capillaries α_k	0.55	0.53	0.56
10	Coefficient of uniformity of distribution of capillaries size d_k	0.58	0.72	0.60

Changes of $\delta\lambda$, δR_{btb}, δk_s, δk_{Ic} are associated with the presence of a mixture of different specific surface of tripoli, which confirms its significant influence on the formation of the structure as a silicate matrix with aerated composites based on it. It allows regulating the properties and structure characteristics of the materials at the constant compressive strength and porosity by varying the specific surface of tripoli.

5 CONCLUSIONS

The mechanism of formation structure and properties of complex activated lime-silica mixture, modified by the filler in the form of tripoli on quicklime was proposed.

It is shown that the particles of tripoli contribute to seal structure of silicate matrix and the formation of discontinuous structure of capillaries, including its own microporosity. Furthermore, due to the high sorption capacity, the tripoli pores can be the matrix from ultrafine size hydrosilicates whose properties differ from the properties of the calcium hydrosilicates formed in the mixture free space. It contributes to obtaining the aerated composites with high physical and mechanical properties.

Thus, the structure modification of the silicate matrix by using quicklime, alkali-containing additives, and tripoli predetermined specific surface area, allows adjusting the levels of the properties and structure parameters of the aerated composites on silicate matrix in a wide range.

According to the results of optimization the recommended contents are those which allow to get aerated composites on the silicate matrix given grades of strength, heat conductivity and frost resistance: compressive strength R_b – 10 MPa, 12.5 MPa, density ρ=1300÷1400 kg/m^3, frost resistance F25, heat conductivity λ=0.30÷0.40 Wt/m·K, critical coefficient of stress intensity k_{Ic}≥1 MPa·m$^{-0.5}$, coefficient of softening k_s≥0.9.

Note: This research was presented at the International Conference MATRIB 2017 (29 June - 2 July 2017, Vela Luka, Croatia).

6 REFERENCES

[1] Shinkevich E.; Lutskin E.; Gnyp O.; Koichev A.; Dotsenko J.: The Influence of Modification of the Structure of Silicate Materials on Their Properties After Non-autoclaved Hardening, Proc. of the 8th Int. Symp. Brittle Matrix Composites 8, Warsaw, October 2006, 517-525

[2] Shinkevich E.; Sidorova N.; Lutskin E.; Sidorov V.; Politkin S.: Raw Mix for Obtain Modified Silicate Materials and Method of Its Prepare, Declared patent # 64603 A, 7 C04B28/20, Ukraine, 2004

[3] Shinkevich E.: Kinetic-mathematical model of hydration of lime-silica binder, which activated together with a fine-grained filler, Proc. of 13th Int. Congress on the Chemistry of Cement, Madrid, July 2011, 358

[4] Lutskin Y.; Shinkevich E.: Aerated Complex Activated Composites on Silicate Matrix of Thermal-moisture Hardening, Proc. of 14th Int. Congress on the Chemistry of Cement / Abstract Book, Volume 2, Beijing, October 2015, 632

[5] Shinkevich E.; Zaytsev Y.; Lutskin E.; Bondarenko G.; Tymnyak A.: Structural durability, deformation properties and fracture mechanics parameters of advanced silicate materials, Proc. of 2nd International conference on Microstructural-related Durability of Cementitious Composites, September 2013, 1462-1468.

[6] Vinnichenko V.; Krot A.; Vitsenko N.: Theoretical and experimental research into manufacturing of silicate products without thermal treatment, Eastern-European Journal of Enterprise Technologies. Technology organic and inorganic substances, Vol 5, No 6 (83) (2016), 29-36

[7] Butt Y. M.; Sychev M. M.; Timashev V. V.: Chemical technology of binders, Moscow, Higher School, 1980

[8] Babushkin V. I.; Matveev G. M.; Mchedlov-Petrosyan O.P.: Thermodynamics of silicates, Moskow, Stroyizdat, 1986

[9] Shtark J.; Viht B.: Durability of Concrete, Transl. from German ed. Krivenko P.V., Kiev, 2004
[10] Avvakumov E. G.; Senna M.; Kosova N.; Soft W.: Mechanochemical Synthesis a Basis for New Chemical Technologies, Netherlands, Kluwer Academic Publishers, 2001
[11] Poole C.; Owens F.: Nanotechnology, translation from English. ed. Golovey, Y. I., Moscow, Technosphere, 2005
[12] Gluhovskij V. D.; Runova R. F.; Maksunov S. E.: Binders and composite materials of contact hardening, Kiev, Budivelnik, 1991
[13] Voznesenskiy V.; Lyashenko T. et al.: Computer and optimization of composite materials, Kiev, Budyvelnik, 1989
[14] Lutskin E.; Shinkevich E.: Relationship between microstructure and properties of silicate composites on the basis of activated lime-silica binder, Proc. of 13th International Congress on the Chemistry of Cement, Madrid, July 2011, 359.
[15] Lutskin E.; Shinkevich E.: Analysis of the relationship between microstructure and properties of activated lime-silica composites on the basis of experimentally-statistical modelling, Tehnički glasnik-Technical Journal, Vol. 9, No. 1 (2015), 27-33.

Authors' contacts:

Yevgen LUTSKIN, Ph.D., Associate Professor
Odessa State Academy of Civil Engineering and Architecture
Didrikhson Street 4, Odessa, Ukraine, 65029
Tel. +38 (067) 923-91-82, e-mail: lutskin@ukr.net

Olena SHYNKEVYCH, D.Sc. in Eng., Professor
Odessa State Academy of Civil Engineering and Architecture
Didrikhson Street 4, Odessa, Ukraine, 65029
Tel. +38 (067) 767-17-24, e-mail: elena_shinkevich@ukr.net

Aleksej ANISKIN, Ph.D., Senior Lecturer
University North
104. brigade 3, 42000 Varaždin, Croatia
Tel. +38 (092) 304-94-06, e-mail: aaniskin@unin.hr

ISSN 1846-6168 (Print), ISSN 1848-5588 (Online)
ID: TG-20171127181040

Original scientific paper

MICROSTRUCTURAL CHANGES IN HEAT TREATMENT OF PM HIGH-SPEED STEELS

Sanja ŠOLIĆ, Zdravko SCHAUPERL, Matjaž GODEC, Vlado TROPŠA

Abstract: Properly performed heat treatment can significantly affect final properties of high-speed steels, so the heat treatment parameters are chosen depending on the specific properties of the particular tool. Deep cryogenic treatment is carried out at a temperature of -196 °C (liquid nitrogen). By combining deep cryogenic treatments and various austenitization temperatures, which affects the volume of retained austenite, it is possible to affect the hardness and fracture toughness of tools and other steel parts. However, it may also affect the increase in wear resistance regardless of the increase in hardness. In addition, dimensional stability is achieved by transformation of residual austenite into martensite, eliminating the change in volume by 4%. This paper investigated the effect of deep cryogenic treatment on microstructures in high-speed steel produced by powder metallurgy in comparison to vacuum heat treatment.

Keywords: deep cryogenic treatment; high-speed steel; microstructure

1 INTRODUCTION

Properly performed heat treatment can significantly influence the finite properties of high-speed steel, so the heat treatment parameters are chosen depending on the specific properties of the particular tool. The high-speed steel heat treatment consists of austenitization in a protective atmosphere, quenching and three high temperature tempering treatments. High temperature tempering treatments are conducted for the purpose of the elimination of residual austenite, which is present in the microstructure after quenching up to 40% (depending on the height of austenitization temperature). The austenitization temperature, which is usually around 50 °C below the solidus temperature, is a very important factor in the heat treatment of high-speed steels.

In an annealed condition, the ferrite matrix of high-speed steel is almost carbon-free and consists predominantly of iron and chromium. Carbon is bound to eutectic, eutectoid, and secondary carbides. Although, in high-speed steels the austenitic area starts at a temperature somewhat less than 900 °C, the carbon content in the matrix is low, and almost all the carbides are out of the solid solution. Very high austenitization temperatures allow for the dissolution of sufficient amount of carbide to obtain a sufficient amount of carbon and alloying elements in the austenite. At temperatures from 900 °C to 1100 °C, $M_{23}C_6$ carbide dissolves. M_6C carbides dissolve at an interval of 1150 °C to the solidus temperature, and the minor part will melt only at liquidus temperature. MC carbides dissolve very poorly and are still present in large amount at liquidus temperature. Partial dissolution of the M_6C carbides results in a partial entry of the vanadium into a solid solution resulting in stronger pronounced secondary hardening with tempering [1÷3]. Kinetics of carbide dissolution depends on the duration and height of the austenitization temperature and on the quenching technology, i.e. the duration of heating to the austenitization temperature.

The usual holding time at austenitization temperature is from 80 to 150 s [3], which is enough to dissolve sufficient amount of carbide and not affect the dimensions and mass of the tool. The austenitization temperature is also selected according to the properties of the tool. Higher austenitization temperatures are chosen for tools that will work at high temperatures, requiring primarily high hardness; lower austenitization temperatures are selected for cutting tools that will work in cold conditions and where the toughness of the tool is very important.

After quenching, in the microstructure of high-speed steel beside martensite there is 20% to 40% of the retained austenite present. Secondary and eutectic carbides are also present. The retained austenite may be transformed into martensite by deep cryogenic treatment at −196 °C or by destabilizing with tempering followed by rapid cooling to room temperature. The tempering is performed in two or three steps in the temperature range between 500÷600 °C. At the tempering temperature, carbon and alloying elements from martensite and the retained austenite form tempering carbides, which reduces the tetragonality of martensite and thus hardness. Partially decreased amount of carbon in the retained austenite leads to the increase of the martensite start temperature, and the austenite with the lower carbon content becomes less stable and starts to transform into martensite when cooling to room temperature.

With multiple tempering in quenched martensite multiple tempering carbides form followed by secondary martensite forming from the retained austenite. This significantly reduces the amount of the retained austenite. The result is an increase in tool hardness and increased wear resistance.

Tempering carbides form in martensite during the tempering at the temperatures around 500 °C and are M_3C type in HS 6-5-2 high-speed steel or $M_{23}C_6$ type in HS 18-0-1 high-speed steel [4]. Up to 400 °C only M_3C carbides form. Also, cementite formation is established at the same temperature interval. At 600 °C carbon is almost entirely bonded within the carbides [2].

At higher tempering temperatures there is no new carbide formation, but only transformation of one to another type of carbide, or the dissolution of one carbide type and the formation of the other. In case of the present vanadium in steel, in secondary hardening at 550 °C, the dominant carbide type is MC (VC, V_4C_3). It has higher crystal lattice parameter, and in the microstructure, it can be observed on the boundaries of martensitic needles [3].

1.1 Deep - cryogenic treatment

For the purpose of eliminating the retained austenite, experiments with cryogenic treatment started at the beginning of the 20th century. However, due to poor equipment and the inability to achieve temperatures below -80 °C, the results were not satisfactory. With the development of equipment and low-temperature techniques in the 70s of the 20th century, it was possible to achieve very low temperatures – up to −196 °C – enabling the intensification of the research on the influence of deep cryogenic treatment to the various steels properties.

Cold treatment at about −80 °C ("dry ice") to −120 °C is sufficient to transform the retained austenite from quenched steel to martensite (Fig. 1) and it is in wide commercial application, particularly for removal of the retained austenite in carburized and surface quenched parts. For high alloyed tool steels, deep cryogenic treatment improves dimensional stability because of the retained austenite transformation to martensite thus eliminating 4 % volume change [6÷11].

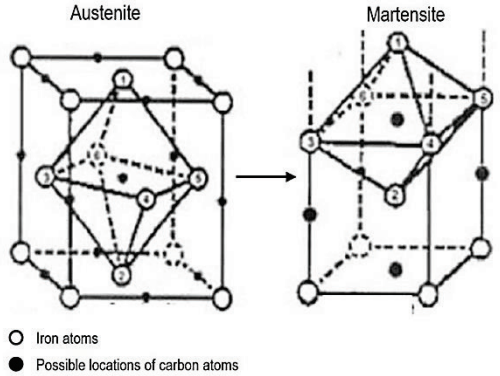

Figure 1 Transformation of the retained austenite into martensite [6]

Deep cryogenic treatment (DCT) is carried out at a temperature of −196 °C (liquid nitrogen). By combining DCT and various austenitization temperatures, affecting the volume of retained austenite, it is possible to affect the hardness and fracture toughness [12, 13] of certain components, but it can also affect the increase in wear resistance regardless of hardness. [11, 14]

In DCT two metallurgical phenomena occur: transformation of retained austenite into martensite with the start of nucleation for subsequent precipitation of very fine carbides from the martensite. It has been shown that the effect of DCT takes place in several stages. In the first stage, up to −130 °C, a transformation of the retained austenite to martensite occurs, resulting in increased hardness. Meng et al. [10] state that the martensite formed during DCT is not equivalent to the martensite formed by quenching and tempering. This transformation, as in classical heat treatment, is not time-dependent.

At the second stage, at about −196 °C, time-dependent decomposition of the primary martensite begins. This decomposition causes decrease of steel hardness, but there is a nucleation of a large number of fine-dispersed nanometer carbides. During the subsequent tempering, formation and precipitation of very fine nanometric η-carbides occurs (Fig. 2) [10, 11]. According to Hirotsu and Nagakura (1972) [15, 16] η-carbides are type M_2C with orthorhombic crystal lattice with the parameters a = 4.525 Å, b = 4.318 Å, c = 2.830 Å, with the following gaps between plane d_{101} = 0.242 nm, d_{020} = 0.215 nm, d_{121} = 0.161 nm. The number of these carbides has been shown to increase with the duration of the treatment (minimum 24 h) [15], a lower temperature (optimally −196 °C), and lower austenitization temperature (with the aim of formation as much primary martensite as possible). Meng et al. [10] have found that the dominant mechanism of increasing wear resistance in tool steels is the formation of these very small nanometric η-carbides.

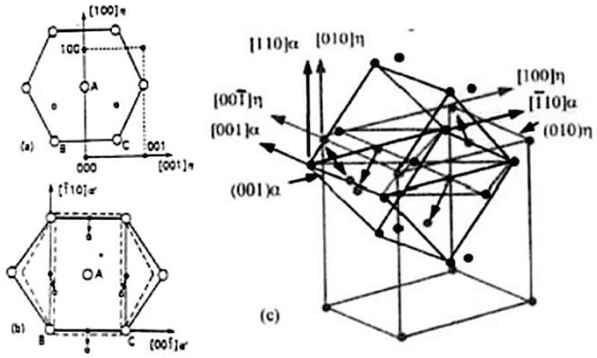

Figure 2 Formation of the η-carbides from martensite [10]

The purpose of this research was to examine the influence of deep cryogenic treatment on the microstructure in high-speed steel produced by powder metallurgy compared to classical heat treatment.

2 EXPERIMENTAL PROCEDURE

The material used in this study was a high-speed steel grade PM S390 MC produced by powder metallurgy. The chemical composition of steel is shown in Tab. 1.

Table 1 Chemical composition of the PM S390 MC high-speed steel

%C	%Si	%Mn	%Cr	%Mo	%V	%W	%Co	%Fe
1.64	0.60	0.30	4.80	2.00	4.80	10.40	8.00	rest

Heat treatment was conducted in an Ipsen vacuum furnace. Samples were preheated at the 650 °C / 30 min, 850 °C / 20 min, 1050 °C / 15 min before the heating to the austenitization temperature. Heating to the austenitization temperature of 1130 °C was 5 °C/min. Duration of the austenitization was 6 min. After that, the samples were

quenched in the nitrogen flow, p = 1050 mbar. The heat treatment parameters are shown in Tab. 2.

Table 2 Heat treatment parameters

Batch	Austenitization, °C/min	Deep cryogenic treatment, °C/h	Tempering, °C/h
1.	1130 / 6 min	-	520 / 520 / 490 / 2 h
2.	1130 / 6 min	-196 °C / 24 h	520 / 2 h

After quenching, the test samples were immersed in liquid nitrogen at controlled speed and left for 24 h. Other samples were tempered three times. After tempering and deep cryogenic treatment, the Rockwell hardness and HV 1were measured. On each sample hardness was measured ten times. The results represent the mean value of ten measurements. The test samples were excluded after each of the individual heat treatment phases and analyzed on the field-emission scanning electron microscope. For microstructure testing, the samples were prepared by a standard metallographic preparation procedure. The microstructure was tested on the FE SEM JEOL JSM6500F electron microscope. For microstructure testing, the samples were etched with 3% Nital solution.

3 RESULTS AND DISCUSSION

Tab. 3 shows hardness test results. For this research, the austenitization temperature and the tempering temperature were chosen for both batches of the heat treatment to obtain high hardness and wear resistance. Since it is recommended for deep cryogenic treatment to choose the lowest austenitization temperature to obtain as many primary martensite as possible and less retained austenite after quenching, the hardness test results show that in the classical heat treatment the highest hardness was achieved after quenching.

Table 3 Hardness of the test samples after conducted heat treatments

	Heat treatment	HRC	HV 1
1.	Austenitization (1130 °C / 6 min) + quenching	67.5	-
	1. tempering (520 °C / 2 h)	67	-
	2. tempering (520 °C / 2 h)	66	-
	3. tempering (490 °C / 2 h)	66	917
2.	Austenitization (1130 °C / 6 min) + quenching	67.5	
	Deep cryogenic treatment (−196 °C / 24 h)	68	
	1. tempering (520 °C / 2 h)	66.5	945

The microstructure of the tested HSS PM S390 MC samples in annealed condition and after quenching is shown in Fig. 3.

Figs. 4 and 5 show a comparison of the microstructural changes with the quenching and tempering and with the deep cryogenic treatment.

The microstructure analysis showed a characteristic microstructure of high-speed steel produced with powder metallurgy. Eutectic carbides of nodular shape with a diameter of less than 1 μm are evenly distributed over the martensitic matrix. EBSD and EDS analysis [1] identified two types of carbides, M_6C (Fe_3W_3C) and MC (VC) carbides. On the larger magnification of the microstructure shown in Figs. 4 and 5, secondary carbides of the M_3C type are also visible. MnS and complex sulfides $(Mn, Cr, Fe)_xS_y$ were also present in the microstructure.

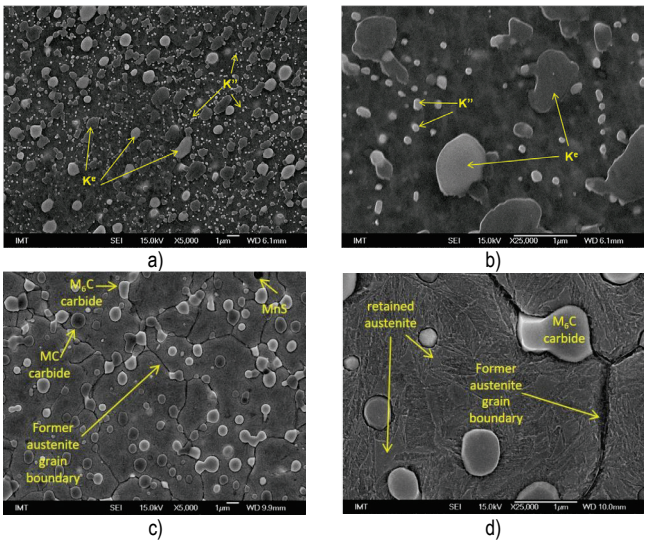

Figure 3 Microstructure of the PM S390 MC HSS [1]
a) annealed condition, b) annealed condition, higher magnification
c) quenched condition, d) quenched condition higher magnification

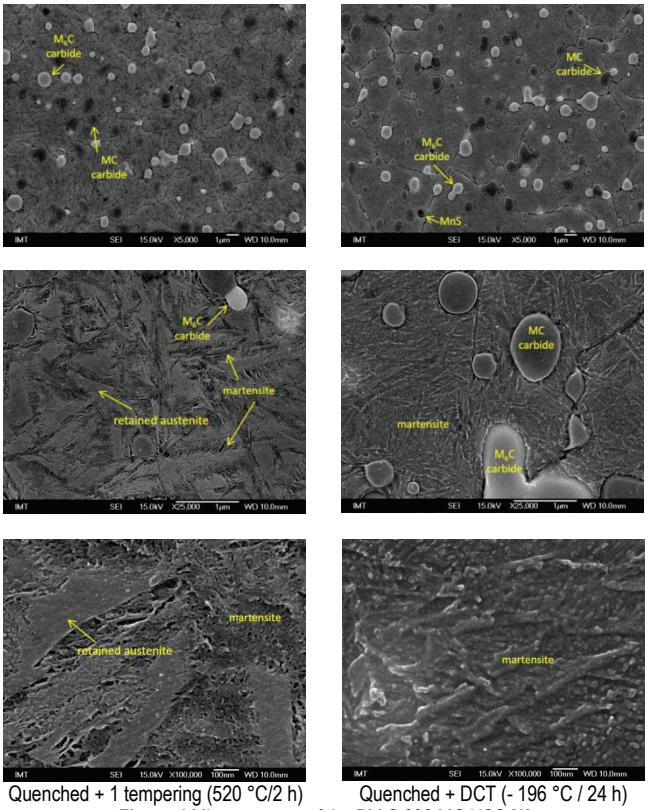

Quenched + 1 tempering (520 °C/2 h) Quenched + DCT (- 196 °C / 24 h)

Figure 4 Microstructure of the PM S 390 MC HSS [1]

In Fig. 5, at a large magnification, the martensitic matrix of a deep cryogenic treated sample appears to be finer, i.e. martensitic needles seem to be smaller than those in quenched and tempered samples.

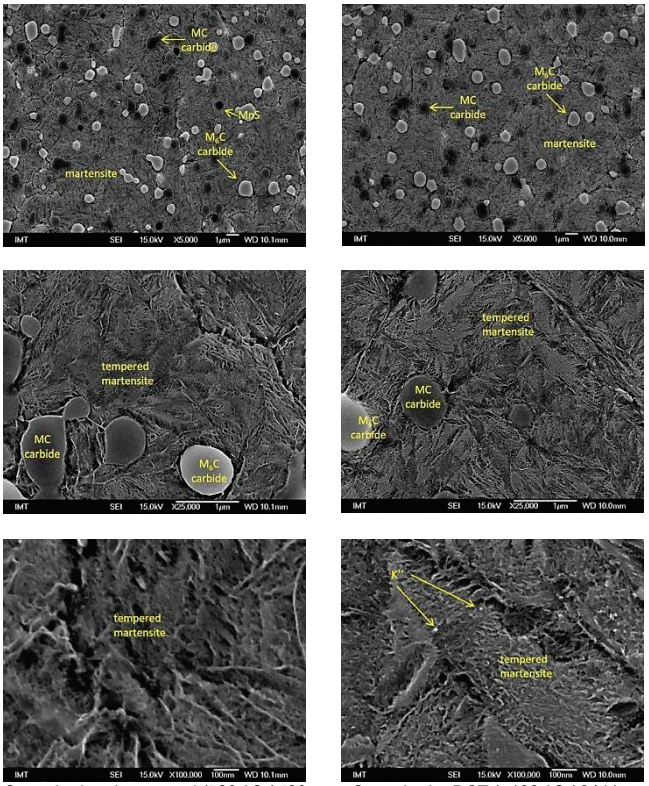

Quenched and tempered (520 °C / 520 °C / 490 °C / 2 h)

Quenched + DCT (- 196 °C / 24 h) + tempering (520 °C / 2h)

Figure 5 Microstructure of the PM S 390 MC HSS after heat treatments [1]

4 CONCLUSION

Properly conducted heat treatment can significantly influence the finite properties of high-speed steels, so the heat treatment parameters are chosen depending on the specific properties of the particular tool. By combining deep cryogenic treatment and various austenitization temperatures, affecting the volume of the retained austenite, it is possible to affect the hardness and fracture toughness of certain components. Moreover, it can increase wear resistance regardless of changes in hardness values. In this paper, the effect of deep cryogenic treatment on the microstructure changes in high-speed steel produced by powder metallurgy compared to classical heat treatment was investigated. Metallographic analysis of samples showed a characteristic microstructure of high-speed steel manufactured with powder metallurgy. The higher magnifications of the microstructure showed differences in morphology of the martensitic matrix between classically heat treated and deep-cryogenically treated samples. Based on the obtained results, it is possible to conclude that the deep cryogenic treatment mechanism has effect on the high-speed steel microstructure which cannot be characterized by conventional metallographic methods but requires more thorough and precise procedures.

Note: This research was presented at the International Conference MATRIB 2017 (29 June - 2 July 2017, Vela Luka, Croatia).

5 REFERENCES

[1] Šolić, S. Influence of the microstructure on the tribological properties of cutting tools. // Doctoral Thesis, Zagreb, UniZg, FAMENA, 2011. (in Croatian)
[2] Leskovšek, V. Optimization of the vacuum heat treatment parameters of high-speed steels. // Doctoral Thesis, Zagreb, UniZg, FAMENA, 1999. (in Croatian)
[3] Dobrzanski, L. A. Structure and properties of high-speed steels with wear resistant cases or coatings. // Journal of Materials Processing Technology 109, 2001, 44-51. https://doi.org/10.1016/S0924-0136(00)00774-3
[4] Horn, E. High-speed steels, Atlas of Precipitate sin Steels, Verlag Stahleisen mbH Dusseldorf, 1983, 143-159.
[5] Colombier, L. Les aciers na coupe rapide. // Traitement Thermique, 51, 1970, 33-42.
[6] Kamody, D. J. Using deep cryogenics to advantage. // Advanced Materials & Properties, 10, 1998, 215-218.
[7] Wurzbach, R. N.; DeFelice, W. Improving component wear performance through cryogenic treatment. // Maintenance Reliability group, Brogue, Pennsylvania.
[8] Akbarizadeh, A.; Shafyei, A.; Golozar, M. A. Effect of cryogenic treatment on wear behavior of D6 tool steel. // Materials and Design, 2008.
[9] Lasky, R. C. The effect of cryogenic tempering on tool steels. / The cryogenic institute of New England.
[10] Meng, F.; Tagashira, K.; Azuma, R.; Sohma, H. Role of eta-carbide precipitation's in the wear resistance improvements Fe-12Cr-Mo-V-1,4C tool steel by cryogenic treatment. // ISIJ International 34, 2(1994), pp. 205-210. https://doi.org/10.2355/isijinternational.34.205
[11] Stratton, P. F. Process optimisation for deep cold treatment of tool steels. // 1st International conference on heat treatment and surface engineering of tools and dies, IFHTSE 2005. Pula, pp. 11-19
[12] Leskovšek, V.; Kalin, M.; Vižintin, J. Influence of deep-cryogenic treatment on wear resistance of vacuum heat-treated HSS. // Vacuum, 80, (2006), pp. 507-518. https://doi.org/10.1016/j.vacuum.2005.08.023
[13] Leskovšek, V.; Ule, B. Improved vacuum heat-treatment for fine-blanking tools from high speed steel M2. // Journal of Material Processing Technology 82, (1998), pp. 89-94. https://doi.org/10.1016/S0924-0136(98)00023-5
[14] Cajner, F.; Landek, D.; Šolić, S.; Cajner, H.; Leskovšek, V. Effect of deep cryogenic treatment on tribological properties of PM S390 MC high speed steel. // Proceedings "New challenges in heat treatment and surface engineering", Conference in Honour of prof. Božidar Liščić, Dubrovnik - Cavtat, Croatia, 09-12 June 2009.
[15] Hirotsu, Y.; Nagakura, S. Crystal structure and morphology of the carbide precipitated from martensitic high carbon steel during the first stage of tempering. // Acta Metallurgica, 20, 4(1972), pp. 645-655. https://doi.org/10.1016/0001-6160(72)90020-X
[16] Han, K.; van Genderen, M. J.; Böttger, A.; Zandbergen, H. W.; Mittemeijer, E. J. Initial stages of Fe-C martensite decomposition. // Phil. Mag. A, 81, 3(2001), pp. 741-757. https://doi.org/10.1080/01418610108212169
[17] Tyshchenko A. I.; Theisen W.; Oppenkowski A.; Siebert, O.; Razumov, N.; Skoblik, A. P.; Sirosh, V. A.; Petrov, Yu. N.; Gavriljuk, V. G. Low-temperature martensitic transformation and deep cryogenic treatment of a tool steel. // Materials Science and Engineering A 527, (2010), pp. 7027-7039. https://doi.org/10.1016/j.msea.2010.07.056

Authors' contacts:

Sanja ŠOLIĆ, PhD, Assistant Professor
University North, Department of Mechanical Engineering
Ul. 104. brigade 3, 42000 Varaždin, Croatia
E-mail: ssolic@unin.hr

Zdravko SCHAUPERL, PhD, Full Professor
University of Zagreb,
Faculty of Mechanical Engineering and Naval Architecture
Ivana Lučića 5, 10000 Zagreb, Croatia
E-mail: zdravko.schauperl@fsb.hr

Matjaž GODEC, PhD, Assistant Professor, director
Institute for Metals and Technology
Lepi pot 11, 1000 Ljubljana, Slovenia
E-mail: matjaz.godec@imt.si

Vlado TROPŠA, PhD, Assistant Professor
University North, Department of Mechanical Engineering
Ul. 104. brigade 3, 42000 Varaždin, Croatia
E-mail: vlado.tropsa@unin.hr

ISSN 1846-6168 (Print), ISSN 1848-5588 (Online)
ID: TG-20171123184728

Original scientific paper

INVESTIGATION ON THE EFFECTS OF PROCESS VARIABLES ON COPPER EXCHANGE ON NaX IN A BATCH STIRRED REACTOR

Sandra SVILOVIĆ, Ivona HORVAT, Marija ĆOSIĆ, Renato STIPIŠIĆ

Abstract: The aim of this work was to determine the effects of anion type (A), time (*t*), impeller off-bottom clearance (C/H) and solute concentration (*c*) on copper exchange on zeolite NaX in a batch stirred reactor. The experiments were carried out at constant temperature (300 K) and at the same impeller speed (250 rpm). The amount of exchanged copper at examined conditions was measured by UV/Vis spectrophotometer. In order to find the optimal process conditions for copper exchange on the basis of experimental data, Taguchi's method for experimental design were used, applying larger-the-better approach. Beside the optimum experimental conditions this method allowed to define the influence of each process variable on the process conducted. Applied method has shown that the highest copper exchange is achieved at increased solute concentration, when sulphate anion was used, and impeller is positioned at standard position (C/H =0.33). It was also found that solute concentration and anion type have more pronounced impact on process investigated than impeller position and process duration (c > A > c/H > t). For the optimum experimental condition, kinetic data for copper exchange were obtained and tested using the Elovich and the Ritchie kinetic models.

Keywords: batch reactor; ion exchange kinetics; optimisation; zeolite

1 INTRODUCTION

Zeolites are a very promising support for design and preparation of environmentally friendly catalysts. Among others, copper exchanged zeolites are also used as catalysts and could be used for selective ammonia oxidation, carbon monoxide oxidation at low temperatures, toluene removal, wet peroxide oxidation of phenol, etc. [1-4]. Zeolite NaX is a microporous, crystalline solid with a well-defined three-dimensional silica-alumina structure and extra-framework exchangeable sodium cation. It is the synthetic form of naturally occurring aluminosilicate mineral faujasite.

The Taguchi method uses a specifically fashioned orthogonal array consisting of controllable parameters and their variation levels in order to optimise process conditions. For quality assessment this method could use three types of signal to noise (*S/N*) ratio: smaller-the-better, nominal-the-best, and larger-the-better [5]. The advantage of Taguchi method is assessment of optimal experimental conditions with the least number of experiments. Already, this method has been used for process optimization for heavy metal sorption [5-9].

The stirred tank batch reactor is still the most widely used reactor type in the laboratory. It is used for variety of objectives including homogenizing single or multiple phase in terms of concentration of components, physical properties, and temperature. In the solid-liquid system mixing needs to ensure suspension of solid particle and appropriate conditions for mass and heat rate transfer in the solid-liquid interface. Fluid flow pattern in stirred vessel may have considerable effect on the mentioned process outcomes. Flow patterns in the reactor mainly depend upon impeller geometry. When impeller with flat blades is used, the radial flow inside the vessel is generated. In that case, fluid stream is discharged towards the vessel wall and it divides; one portion flows downward along wall and back to the centre of impeller from below, while another portion flows upward toward liquid surface and back to the impeller from above. Fluid flow pattern in stirred reactor, beside the impeller type, depends on impeller off-bottom clearance and impeller size as well [10, 11].

The aim of this work was to investigate the influence of anion type, time, impeller off-bottom clearance and solute concentration on copper exchange on zeolite NaX in order to find optimal process conditions. Process kinetics, at optimal process conditions, is investigated as well.

2 MATERIALS AND METHODS

2.1 Materials

Zeolite NaX (Sigma-Aldrich) was crushed and sieved to obtain particles between 0.071 and 0.090 mm. Solutions containing Cu^{2+} were prepared using the appropriate weight of $CuSO_4 \cdot 5H_2O$, $CuCl_2 \cdot 2H_2O$ and $Cu(NO_3)_2 \cdot 3H_2O$. The initial concentrations of copper solutions were checked by the Perkin Elmer Lambda 25 UV/Vis spectrophotometer.

2.2 Taguchi method

In this study, experiments were planed according to Taguchi's L9 orthogonal array, which has nine rows corresponding to the number of experiments and four columns corresponding to the controllable factors, Tab. 1. In this study, anion type (A), time (*t*), impeller off-bottom clearance (*C*/*H*) and concentration of copper solution (*c*) were chosen as controllable factors and their effect on the amount of copper retained on zeolite was investigated. All the selected factors, Tab. 2, had three testing values, represented as level 1, 2 and 3.

In this work larger-the-better characteristic was used:

$$\frac{S}{N_{\mathrm{LB}}} = -10 \cdot \log \frac{\sum_{i=1}^{n} \frac{1}{y_i}}{n} \tag{1}$$

where S/N represent signal-to-noise ratio, subscript LB is larger the better, n is the number of repetition (three) under the same experimental conditions, and y is a measurement result, i.e. amount of copper retained on the zeolite NaX.

Table 1 Design of experiments

Test	Factor			
	Anion	Time	Impeller off-bottom clearance	Concentration
1	1	1	1	1
2	1	2	2	2
3	1	3	3	3
4	2	1	2	3
5	2	2	3	1
6	2	3	1	2
7	3	1	3	2
8	3	2	1	3
9	3	3	2	1

Table 2 Controllable factors and associated levels

Factor	Level 1	Level 2	Level 3
Anion type (/)	Sulphate	Chloride	Nitrate
Time (min)	50	30	10
Impeller off- bottom clearance (/)	0.2	0.33	0.46
Solution concentration (mmol/l)	5	10	15

The amount of copper retained on the zeolite, q_t, was calculated as:

$$q_t = \frac{(c_0 - c_t)\cdot V}{m} \tag{2}$$

where c_0 is the initial concentration of copper solution (mmol/l), c_t is the concentration of copper solution at time t (mmol/l), V is the volume of solution (l) and m is the mass of zeolite (g).

The next step in Taguchi method is calculation of average S/N_{LB} ratio of each controllable factor at level i, denoted as S/N_{FL}, in order to determine the optimal conditions:

$$\frac{S}{N_{FL}} = \frac{\sum_{j=1}^{n_{Fi}} \left[\left(\frac{S}{N_{LB}} \right)_i^F \right]_j}{n_{Fi}} \tag{3}$$

where $\left(S/N_{LB}\right)_j^F$ represents S/N_{LB} ratio for factor F on the level i, the superscript j is the j^{th} appearance of the i^{th} level [5]. For the 9 tests, each level for every factor appears 3 times.

2.3 Kinetic models

The Ritchie model is expressed as [12]:

$$q_t = q_e \left[1 - \left(\frac{1}{1 + k_2 t} \right) \right] \tag{4}$$

where q_e is the amount of copper exchanged in equilibrium – maximum capacity (mmol/g), t is time (min) and k_2 is the rate constant of the Ritchie second-order kinetic model (g/mmol min).

The Elovich model is presented as [13]:

$$q_t = \frac{1}{b} \cdot \ln(1 + a \cdot b \cdot t) \tag{5}$$

where a and b are the constants.

2.4 Experimental procedure

Experiments for Taguchi method were carried out in a stirred batch reactor. The glass reactor with the internal diameter of $T = 12$ cm was equipped with four baffles placed at 90° around the vessel periphery. The solution height, H, was equal to internal vessel diameter ($T = H$). The suspension, 1.3 l of copper solution and 5 g of zeolite, was stirred using straight blade turbine, SBT (Fig. 1). Impeller diameter was $d = 6.5$ cm, and its position, i.e. impeller off-bottom clearance (C/H) was varied in range from 0.20 to 0.46 (Tab. 2). As a source of copper, three different solutions with three initial concentrations (Tab. 2) were used. In order to enable comparison of experiments data all studies were performed at the same temperature ($T = 300$ K), zeolite particle size ($d_P = 0.071$-0.090 mm) and at the same impeller speed ($N = 250$ rpm). At defined time (Tab. 2) the samples were taken from the reactor. Prior to the analysis with UV/Vis spectrophotometer, the samples were centrifuged and filtrated.

Figure 1 Straight blade turbine, SBT

Experiment for kinetic investigation was carried out in the same reactor at optimum process conditions defined using Taguchi method. Sampling intervals for this study were chosen according to the ion exchange rate. In the beginning of the process, the ion exchange rate is quite high so the sampling was done more often; later, as the exchange rate decreases, frequency of sampling is decreased as well.

3 RESULTS AND DISCUSSION

One of the goals of this investigation was to find the optimum experimental conditions which provide the highest copper exchange using the lager-the-better quality characteristic. The results for S/N_{LB} ratios, calculated by Eq. (1), along with the amount of copper retained on zeolite (Eq. (2)), are shown in the Tab. 3.

Table 3 Results of experimental part of Taguchi design and S/N_{LB} ratios

Experiment	q_t (mmol/g)	S/N_{LB}
1	1.227	1.777
2	1.603	4.099
3	1.592	4.039
4	1.514	3.603
5	0.688	-3.248
6	0.980	-0.175
7	1.341	2.549
8	1.615	4.163
9	1.027	0.231

The results show that amount retained is in the range from 0.688 to 1.615 mmol/g and S/N_{LB} ratio in the range from −3.248 to 4.163 depending on the controllable factors. From these S/N_{LB} ratios related S/N_{FL} ratios and ranges for each controllable factor were calculated and shown in Tab. 4. Range was used to determine the impact of the controllable factors on the amount of copper retained on zeolite. It was calculated as the difference between the highest and the lowest S/N_{FL} value for each factor. The largest range implied the most effective factor. In this study, the concentration was found to be the most effective factor and it is followed by anion type, impeller position and the time. It could be seen that with increase of the initial concentration there is the increase in the amount of copper retained on zeolite. This is the result of increase in the driving force, which is the concentration of the solution [14]. The impact of the impeller position could be explained by flow patterns generated by the impeller. Generally, the overall fluid flow pattern in the vessel with an SBT impeller consists of two circulation loops and is characterized by a high shear level. [15, 16] As was first observed by Nienow [17], when impeller is set close to the vessel bottom, this "double-loop" flow pattern transforms to "single-loop", i.e. axial flow pattern. This transition occurred at C/H=0.2, where low impeller off-bottom clearance led to flow compression and ultimately to transformation of radial to axial flow pattern. On the other hand, when impeller was set to the highest investigated clearance (C/H=0,46), due to the relative vicinity of the surface, fully developed radial flow caused a slight air intake. This obviously decreased the zeolite surface available for ion exchange and resulted in the lowest S/N_{LB} value. The effect of anion might be explained by the change in Si/Al ratio of zeolite NaX during the exchange [18-20].

Table 4 S/N_{FL} ratios and contribution of each controllable factor

	Factor			
	A	t	C/H	c
Level 1	3.305	2.643	1.921	−0.413
Level 2	0.059	1.671	2.644	2.157
Level 3	2.314	1.365	1.113	3.935
Range	3.246	1.278	1.531	4.348
pC (%)	29.98	4.53	5.28	60.21
Rank	2	4	3	1

Also, the statistical evaluation of factor importance was made using the percentage of contribution (pC) (Tab. 4). Comparing these results with the range results it could be seen that previously obtained order of significance is confirmed. Therefore, every controllable factor, considering the obtained range and pC, was associated with the rank. Factor which has a rank 1 should be utilized first and so on.

From Tab. 4, the optimum operating conditions (highest S/N_{FL} value) could be evaluated and for the present study these conditions are as follows: A1, t1, C/H2, c3 that is solution of $CuSO_4 \cdot 5H_2O$, 50 min for contact time, of-bottom clearance of 0.33 and concentration 15 mmol dm^{-3}.

These process properties, and the same temperature, zeolite particle size and impeller speed, as for Taguchi design, were used for kinetic study. Results obtained in this experiment were fit to the Elovich and Ritchie kinetic model (Fig. 2).

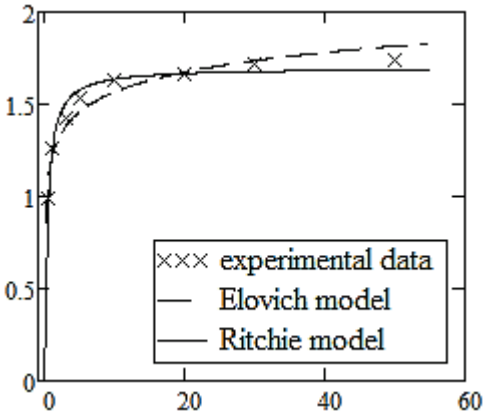

Figure 2 Kinetic data

As it can be seen from Fig. 2, the copper exchange on zeolite NaX better fits with the Ritchie model than the Elovich indicating that tested process is a second-order reaction.

4 CONCLUSION

The effect of anion type (A), time (t), impeller off-bottom clearance (C/H) and solute concentration (c) on copper exchange on zeolite NaX in a batch stirred reactor was studied. According to the Taguchi design analysis, optimal copper exchange is achieved when sulphate anion was used (A1), after 50 minutes (t1), when the impeller is positioned at standard position (C/H2), and at the highest copper concentration (c1). Moreover, the effect of investigated variables was found and in this investigation solute concentration and anion type have more pronounced impact on copper exchange on zeolite NaX than the impeller position and process duration (c > A > C/H > t). For the optimum experimental conditions, kinetic data for copper exchange were obtained and it is found that the Ritchie model describes this data the best.

ACKNOWLEDGEMENT

This work has been fully supported by the Croatian Science Foundation under the project HETMIX (IP-11-2013-8959)

Note: This research was presented at the International Conference MATRIB 2017 (29 June - 2 July 2017, Vela Luka, Croatia).

5 REFERENCES

[1] Jabłońska M., Palkovits R., Copper based catalysts for the selective ammonia oxidation into nitrogen and water vapour – Recent trends and open challenges, Appl. Catal. B Environ., Vol. 181(2016) 332-351.

[2] Tkachenko O. P., Greish A. A., Kucherov A. V., Weston K. C., Tsybulevski A. M., Kustov L. M., Low-temperature CO oxidation by transition metal polycation exchanged low-silica faujasites, Appl. Catal. B Environ.,Vol. 179 (2015) 521-529.

[3] Romero D., Chlala D., Labaki M., Royer S., Bellat J-P., Bezverkhyy I., Giraudon J-M., Lamonier J-F., Removal of Toluene over NaX Zeolite Exchanged with Cu^{2+}, Catal., Vol. 5 (2015) 1479-1497.

[4] Maduna Valkaj K., Katović A., Zrnčević S., Catalytic Properties of Cu/13X Zeolite Based Catalyst in Catalytic Wet Peroxide Oxidation of Phenol, Industrial & Eng. Chem. Res., Vol. 50 (2011) 4390-4397.

[5] Yen H. Y., Li J. Y., Process optimization for Ni(II) removal from wastewater by calcined oyster shell powders using Taguchi method, J. Environ. Menage., Vol. 161 (2015) 344-349.

[6] Yen H. Y., Lin C. P., Adsorption of Cd(II) from wastewater using spent coffee grounds by Taguchi optimization, Desalin. Water Treat., Vol. 57 (2016) 11154-11161.

[7] Özdemir U., Özbay B., Özbay I., Veli S., Application of Taguchi L_{32} ortogonal array design to optimize copper biosorption by using *Spaghnum moss*, Ecotoxicol. Environ. Saf., Vol. 107 (2014) 229-235.

[8] Nagpal G., Bhattacharya A., Singh N. B., Taguchi's Optimizing Technology for Removal of As(III) from Aqueous Solution by Khangar, Asian J. Chem., Vol. 28 (2016) 814-818.

[9] Salahandish R., Ghaffarinejad A., Norouzbeigi R., Rapid and efficient lead (II) ion removal from aqueous solutions using Malva sylvestris flower as a green biosorbent, Anal. Methods, Vol. 8 (2016) 2515-2525.

[10] Kaćunić A., Akrap M., Kuzmanić N., Effect of impeller type and position in a batch cooling crystallizer on the growth of borax decahydrate crystals, Chem. Eng. Res. Des., Vol. 91 (2013) 274-285.

[11] Kresta S.M., Wood P.E., The mean flow field produced by a 45 ◦ pitched-blade turbine: changes in the circulation pattern due to bottom clearance, Can. J. Chem. Eng. Vol., 71 (1993) 42-53.

[12] Ritchie A. G., Alternative to Elovich equation for the kinetics of adsorption of gasses on solids, Chem. Soc. Faraday Trans., Vol. 73 (1977) 1650-1653.

[13] Dávilla-Rangel J. I., Solache-Ríos M., Sorption of cobalt by two Mexican clinoptilolite rich tuff zeolitic rocks and kaolinite, J. Radioanal. Nucl. Chem., Vol. 270 (2006) 465-471.

[14] Kardag D., Koc Y., Turan M., Armagan B., Removal of ammonium ion from aqueous solution using natural Turkish clinoptilolite, J. Hazard. Mater. B, Vol. 136 (2006) 604-609.

[15] Kuzmanić N., Akrap M., Kovačević A., An experimental investigation into the complete drawdown of floating solids in dual-impeller stirred vessels, J. Chem. Eng. Japan Vol. 39 (2006) 932-939.

[16] Rewatkar V.B., Joshi J.B., Effect of impeller design on liquid phase mixing in mechanically agitated reactors. Chem. Eng. Comm., Vol. 102 (1991) 1-33.

[17] Nienow, A.W., Suspension of solid particles in turbine agitated baffled vessels, Chem. Eng. Sci. Vol. 23 (1968) 1453-1459.

[18] Abu-Zied, B. M., Cu^{2+}- acetate exchanged X zeolites: Preparation, characterization and N_2O decomposition activity, Micropor. Mesopor. Mater., Vol. 139 (2011) 59-66.

[19] Benaliouche, F., Boucheffa, Y., Ayrault, P., Mignard, S., Magnoux, P., NH_3-TPD and FTIR spectroscopy pf pyridine adsorption studies for characterization of Ag- and Cu-exchanged X zeolites, Micropor.Mesopor. Mater., Vol. 111 (2008) 80-88.

[20] Hammoudi, H., Bendenia, S., Marouf-Khelifa, K., Marouf, R., Schott, J., Khelifa, A., Effect of the binary and ternary exchanges on crystallinity and textural properties of X zeolites, Micropor. Mesopor. Mater., Vol. 113 (2008) 343-351.

Authors' contacts:

Sandra SVILOVIĆ, PhD, Associate professor
University of Split, Faculty of Chemistry and Technology
Ruđera Boškovića 35, 21000 Split, Croatia
Tel: 021/329-431, e-mail: sandra@ktf-split.hr

Ivona HORVAT, student
University of Split, Faculty of Chemistry and Technology
Ruđera Boškovića 35, 21000 Split, Croatia

Marija ĆOSIĆ, PhD, Assistant professor
University of Split, Faculty of Chemistry and Technology
Ruđera Boškovića 35, 21000 Split, Croatia
Tel: 021/329-453, e-mail: akrap@ktf-split.hr

Renato STIPIŠIĆ, Senior lecturer
University of Split, Faculty of Chemistry and Technology
Ruđera Boškovića 35, 21000 Split, Croatia
Tel: 021/329-467, e-mail: stipisic@ktf-split.hr

ISSN 1846-6168 (Print), ISSN 1848-5588 (Online)
ID: TG-20171123185409

Original scientific paper

STRAIN DIAGRAMS OF CROSS-SECTION OF REINFORCED CONCRETE BENDING ELEMENTS

Anatolii KOVROV, Aleksei KOVTUNENKO, Nina VYSOCHAN

Abstract: The article is dedicated to the construction of the "bending moment – curvature" diagrams for rectangular cross-sections of reinforced concrete bending elements. Assumptions and equilibrium equations used in the construction of diagrams are given in the article. The algorithm for the construction of the "bending moment – curvature" diagram is shown. Diagrams constructed by the proposed algorithm are compared with experimental data and with the results obtained by the methods proposed by other authors. The equations for determination of key points of linearized "bending moment – curvature" diagrams for cross-section with different reinforcement ratio are proposed.

Keywords: bending moment; curvature; diagram; reinforced concrete; strain

1 INTRODUCTION

Determination of the stress-strain state of reinforced concrete bending elements using the deformation theory is regulated by the current normative documents [1, 2] of Ukraine. In this case, to describe the diagram of deformation of concrete it is recommended to use the formula:

$$\frac{\sigma_c}{f_{cd}} = \frac{k\,\varepsilon_c/\varepsilon_{c1} - \left(\varepsilon_c/\varepsilon_{c1}\right)^2}{1+\left(k-2\right)\varepsilon_c/\varepsilon_{c1}} \tag{1}$$

or

$$\sigma_c = f_c \sum_{k=1}^{5} a_k \left(\frac{\varepsilon_c}{\varepsilon_{c1}}\right)^k. \tag{2}$$

The works of L. Mailyan [3], I. Prokopovich [4], A. Kovrov [5] and other scientists [6÷9] are devoted to the development of methods for determining the stress-strain state of rod-shaped reinforced concrete elements on the basis of the deformation model.

It is necessary to use the "bending moment – curvature" diagrams that fully take account of the work of materials and which can be used in practical analysis to more fully take into account the processes occurring in statically indeterminate reinforced concrete structures with changing loads up to destruction.

The aim of this work is to study the influence of the degree of reinforcement on the "bending moment – curvature" diagrams of the cross-sections of reinforced concrete bending elements and the development of a practical methodology for their construction.

2 BASIC ASSUMPTIONS

The following assumptions are accepted in the paper to describe the stress-strain state of reinforced concrete bending elements:

1) Bernoulli's conjecture (the hypothesis of flat sections) is considered valid – the deformations vary linearly with respect to the cross-sectional height.
2) There is cohesion between the reinforcement and the surrounding concrete, such that the deformations in the reinforcement and concrete are equal.
3) The dependence of "stress-strain" upon compression of concrete is described, in accordance with the proposals of A. Bambura [6], using the Eq. (2).
4) The relationship between stresses and strains upon tension of concrete is described using the Prandtl diagram.
5) The relationship between stresses and strains in tension and compression of reinforcement is described using the Prandtl diagram.
6) Resistance of the design section is considered exhausted when deformations of the extreme compressed concrete fiber or tension reinforcement reach the limit values, respectively, ε_{bu} and ε_{su}.

Equilibrium equations having the following form can be written for the cross-section of the reinforced concrete bending element:

$$\sum X = 0:$$
$$b\left[f_{cd}\sum_{k=1}^{5}\frac{a_k}{k+1}\frac{\varepsilon_c^{k+1}}{\aleph\,\varepsilon_{c1}^k} - f_{ctd}\left(\frac{\varepsilon_{ctu1}}{\aleph} - \frac{\varepsilon_{ct1}}{2\aleph}\right)\right] + \tag{3}$$
$$+ E_s\left(A_{sc}\varepsilon_{sc} - A_{st}\varepsilon_{st}\right) = 0,$$

$$\sum m = 0:$$
$$b\left[f_{cd}\sum_{k=1}^{5}\frac{a_k}{k+2}\frac{\varepsilon_c^{k+2}}{\aleph^2\varepsilon_{c1}^k} + \frac{f_{ctd}}{2}\left(\frac{\varepsilon_{ctu1}^2}{\aleph^2} - \frac{\varepsilon_{ct1}^2}{3\aleph^2}\right)\right] + \tag{4}$$
$$+ E_s\left[A_{sc}\varepsilon_{sc}\left(\frac{\varepsilon_c}{\aleph} - a_{sc}\right) + A_{st}\varepsilon_{st}\left(d - \frac{\varepsilon_c}{\aleph}\right)\right] - M = 0$$

where $\aleph$ – a beam curvature; b – a cross-section width; d – effective depth of a cross-section; a_{sc} – distance from the

most compressed face to the center of gravity of the compressed reinforcement; ε_c, ε_{sc}, ε_{st} – strain of the most compressed concrete fiber, compression reinforcement layer and tension reinforcement layer, respectively; A_{sc}, A_{st} – area of the compression and tension reinforcement layer, respectively.

3 CONSTRUCTION OF THE "BENDING MOMENT – CURVATURE" DIAGRAMS BY STEP ITERATION METHOD

The authors propose the following algorithm for determining the stress-strain state of rectangular cross-sections of reinforced concrete bending elements with increasing load up to the limit state with the construction of the "bending moment – curvature" diagram:

1) The initial data for the construction of the "bending moment-curvature" diagram for the rectangular section of reinforced concrete bending elements are as follows:
- design values of compressive f_{cd} and tensile f_{ct} strength of concrete;
- design value of modulus of elasticity of concrete E_{cd};
- ultimate compressive ε_{c1}, ε_{cu1} and tensile ε_{ct1}, ε_{ctu1} strain of concrete;
- design value of reinforcement strength f_y;
- design value of modulus of elasticity of reinforcement E_s;
- ultimate strain of reinforcement f_y/E_s and ε_{ud};
- dimensions of cross-section h and b;
- area of compression and tension reinforcement A_s and A_s';
- values of concrete covers for tension and compression reinforcement a and a';

1) Strain of the extreme tensile fiber $\varepsilon_{bt} = \Delta\varepsilon_{bt}$ and curvature $\aleph$ of the bending element is set in the first stage of work of the cross-section of the reinforced concrete bending element, in accordance with the proposals of L. Maillian [3]. It is assumed that $\Delta\varepsilon_{bt} = 0.05\varepsilon_{btu}$, and curvature of bending elements is proposed $\aleph = 2\varepsilon_{ct}$.
2) Strain of the extreme compressed fiber ε_c, strain of the compressive ε_{sc}, and the tensile reinforcement ε_s are determined from the accepted values of strain of the extreme tensile fiber and the curvature of the element based on the similarity of the triangles on the strain diagram of the cross-section and are substituted into Eq. (3).
3) If the equation of equilibrium (3) is not satisfied, then it is necessary to clarify the curvature and repeat the calculation on points 3 and 4 until the specified accuracy is reached. In this case, if the left side of Eq. (3) is greater than zero, then the curvature at the subsequent iteration is assumed $\aleph_{i+1} = 0.9999\aleph_i$. If the left side of the equation is less than zero, then the height of the compressed zone at the subsequent iteration is assumed $\aleph_{i+1} = 1.0001\aleph_i$.
4) The value of the bending moment perceived by the cross-section for a given strain of the extreme tensile fiber of concrete is determined by formula (4).
5) At the next step, strain of the extreme tensile fiber of concrete is increased. The calculation of points 2...6 is repeated until the strain of the extreme tensile fiber of concrete reaches the ultimate value.
6) The crack is formed in the section after the deformations of the extreme tensile fiber of concrete have reached the ultimate value. Strain of the extreme compressed fiber is increased for further construction of the diagram, in accordance with the proposals of L. Maillian [3].
7) Strain of the compressive ε_{sc} and the tensile reinforcement ε_s are determined from the accepted values of strain of the extreme compressed fiber and the curvature of the element based on the similarity of the triangles on the strain diagram of the cross-section and are substituted into Eq. (3).
8) If the equation of equilibrium (3) is not satisfied, then it is necessary to clarify the curvature and repeat the calculation on points 8 and 9 until the specified accuracy is reached. In this case, if the left side of Eq. (3) is greater than zero, then the curvature at the subsequent iteration is assumed $\aleph_{i+1} = 0.9999\aleph_i$. If the left side of the equation is less than zero, then the height of the compressed zone at the subsequent iteration is assumed $\aleph_{i+1} = 1.0001\aleph_i$.
9) The value of the bending moment perceived by the cross-section for a given strain of the extreme compressed fiber of concrete is determined by Eq. (4).
10) The calculation of points 8...10 is repeated until the strain of the extreme compressed fiber of concrete or tensile reinforcement reaches the ultimate value.

The program for determining the stress-strain state of rectangular cross-sections of reinforced concrete bending elements using the constructed "bending moment – curvature" diagrams was developed in the computer mathematics system MATLAB in accordance with the above algorithm.

Let us compare the "bending moment – curvature" diagrams, constructed from experimental data, to the formulas SNiP 2.03.01-84* "Concrete and reinforced concrete structures" [8], to the practical method based on I. Prokopovich's proposals, and the proposed method.

In the experiments of R. Asaad [9], studies were carried out with the beam of the following characteristics: dimensions of the cross-section $b \times h = 12 \times 20$ cm, strength of concrete $f_c = 18.5$ MPa, tension reinforcement 2Ø28 of class A-400 with area $A_s = 9.852$ cm^2, compression reinforcement 1∅6 of class A-400 with area $A_s' = 0.338$ cm^2, reinforcement ratio $\mu = 4.83$ %. "Bending moment – curvature" diagrams are shown in Fig. 1.

In the experiments of Chin Kim Dam [10], studies were carried out with the beam of the following characteristics: dimensions of the cross-section $b \times h = 10 \times 16$ cm, strength of concrete $f_c = 21.2$ MPa, tension reinforcement 2∅12 of

class A-400 with modulus of elasticity $E_s = 2.05 \times 10^5$ MPa and yield strength $f_y = 490$ MPa, area $A_s = 2.26$ cm^2, reinforcement ratio $\mu = 1.67$ %. "Bending moment – curvature" diagrams are shown in Fig. 2.

A statistical estimate of the distribution of the ratio of theoretical and experimental curvatures is given in Tab. 1.

Table 1 Statistical estimate of the distribution of the ratio of theoretical and experimental curvatures

	Experiment of R. Asaad	Experiment of Chin Kim Dam
Sample mean M_x	0.9502	0.9942
Sample variance S_x	0.0944	0.1136
Selective coefficient of variation v_x	0.0994	0.1142
Confidence interval (P=0.95)	0.8847	0.9299
	1.0156	1.0585

4 CONSTRUCTION OF LINEARIZED "BENDING MOMENT – CURVATURE" DIAGRAMS

The type of diagrams for different sizes of cross-sections, strength of concrete and reinforcement of reinforced concrete elements is studied using the proposed algorithm for constructing the "bending moment – curvature" diagrams for cross-sections of reinforced concrete bending elements.

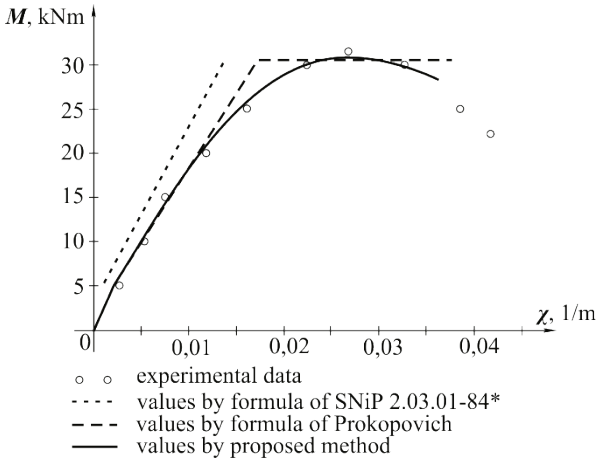

Figure 1 "Bending moment – curvature" diagrams for experimental beam of R. Asaad [9]

A family of "bending moment – curvature" diagrams for a rectangular section with dimensions 200 × 400 mm from concrete with strength of $f_c = 15$ MPa reinforced by reinforcement of class A-400 with yield strength of $f_y = 390$ MPa and the modulus of elasticity $E_s = 2 \times 10^5$ MPa with a change of reinforcement ratio in the range from 0.315 % to 2.58 % is shown on Fig. 3.

A family of "bending moment – curvature" diagrams for a rectangular section with dimensions 200 × 400 mm from concrete with strength of $f_c = 20$ MPa constructed with the help of a program compiled in the computer mathematics system MATLAB is shown in Fig. 4.

For practical purposes, it is convenient to use linearized deformation diagrams.

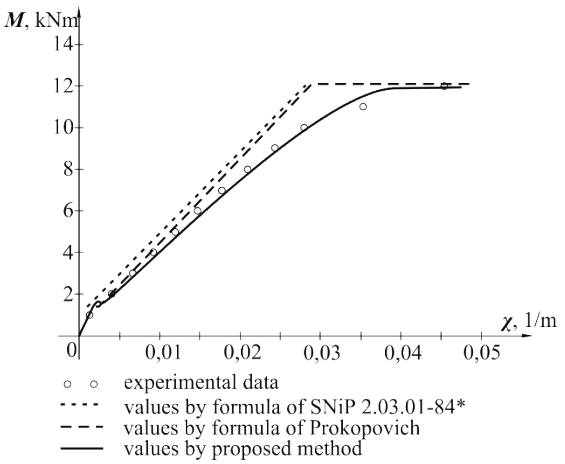

Figure 2 "Bending moment – curvature" diagrams for experimental beam of Chin Kim Dam [10]

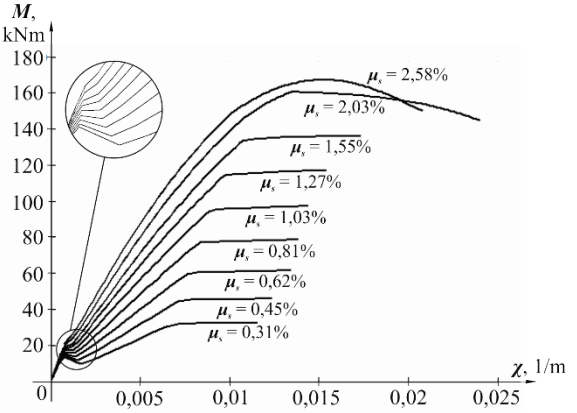

Figure 3 "Bending moment – curvature" diagrams with a change of reinforcement ratio ($f_c = 15$ MPa)

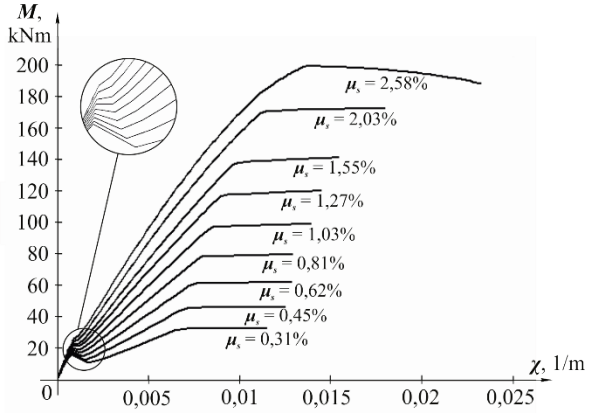

Figure 4 "Bending moment – curvature" diagrams with a change of reinforcement ratio ($f_c = 20$ MPa)

Studies in the families of the "bending moment – curvature" diagrams shown in Fig. 3 and Fig. 4 carried out by the authors allowed to conditionally distinguishing the following three characteristic types of linearized diagrams:

1. For weakly reinforced sections (Fig. 5)

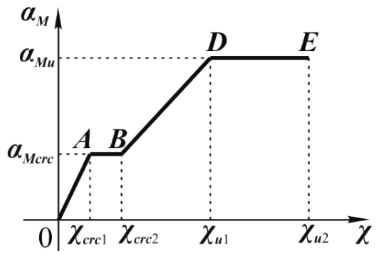

Figure 5 "Bending moment – curvature" diagram for weakly reinforced section

2. For normally reinforced sections (Fig. 6)

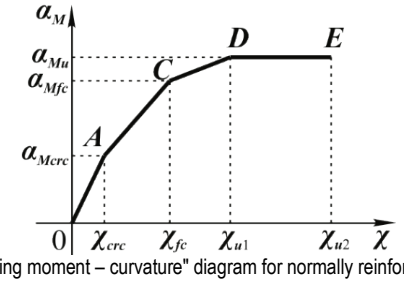

Figure 6 "Bending moment – curvature" diagram for normally reinforced section

3. For heavily reinforced sections (Fig. 7)

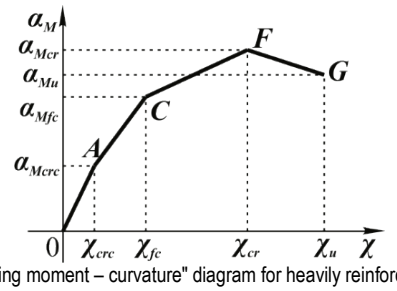

Figure 7 "Bending moment – curvature" diagram for heavily reinforced section

Each of these types of diagrams has characteristic points associated with the physical processes that occur during the deforming process of the bending elements.

It is recommended to reduce the equilibrium Eqs. (3) and (4) to the dimensionless form to exclude the necessity of solving the problem of constructing a diagram for each section. To this end, we divide the above equations by $f_{cd}bh$ and $f_{cd}bh^2$, respectively. As a result, we get:

$$\sum_{k=1}^{5}\frac{a_k}{k+1}\frac{\varepsilon_c^{k+1}}{\chi\varepsilon_{c1}^{k}}-\varphi_{ct}\left(\frac{\varepsilon_{ctu1}}{\chi}-\frac{\varepsilon_{ct1}}{2\chi}\right)+ +\varphi_s\left(\mu_{sc}\varepsilon_{sc}-\mu_{st}\varepsilon_{st}\right)=0, \tag{5}$$

$$\sum_{k=1}^{5}\frac{a_k}{k+2}\frac{\varepsilon_c^{k+2}}{\chi^2\varepsilon_{c1}^{k}}+\frac{\varphi_{ct}}{2}\left(\frac{\varepsilon_{ctu1}^2}{\chi^2}-\frac{\varepsilon_{ct1}^2}{3\chi^2}\right)+ +\varphi_s\left[\mu_{sc}\varepsilon_{sc}\left(\frac{\varepsilon_c}{\chi}-\xi_{sc}\right)+\mu_{st}\varepsilon_{st}\left(\xi_{c0}-\frac{\varepsilon_c}{\chi}\right)\right]- -\alpha_M=0 \tag{6}$$

where $\chi=\aleph h$ – curvature reduced to the section height (reduced curvature); $\varphi_{ct}=f_{ctd}/f_{cd}$; $\varphi_s=E_s/f_{cd}$; $\mu_{sc}=A_{sc}/(bh)$ – compressive reinforcement ratio; $\mu_{st}=A_{st}/(bh)$ – tensile reinforcement ratio; $\xi_{sc}=a_{sc}/h$ – the relative height of the concrete cover for compressed reinforcement; $\xi_{c0}=h_0/h$ – the relative effective depth of section; $\alpha_M=M/\left(f_{cd}bh^2\right)$ – bending moment reduced to dimensionless form (reduced bending moment).

The point **A** in the given diagrams corresponds to the beginning of the formation of a crack in the cross-section. Strain of the extreme tensile fiber of concrete reaches the value ε_{ctu1}. The following equation for determining the reduced curvature is obtained by substituting the strains of the extreme compressed fiber of concrete, compressed, and tensile reinforcement, expressed through strain of the extreme tensile fiber of concrete, into Eq. (5) and performing equivalent mathematical transformations:

$$A_1\chi^6+A_2\chi^5+A_3\chi^4+A_4\chi^3+A_5\chi^2+A_6\chi+A_7=0, \tag{7}$$

where $A_1=10a_5$; $A_2=12\left(a_4\varepsilon_{c1}-5a_5\varepsilon_{ctu1}\right)$;

$A_3=15\left(a_3\varepsilon_{c1}^2-4a_4\varepsilon_{c1}\varepsilon_{ctu1}+10a_5\varepsilon_{ctu1}^2\right)$;

$A_4=20\left(a_2\varepsilon_{c1}^3-3a_3\varepsilon_{c1}^2\varepsilon_{ctu1}+6a_4\varepsilon_{c1}\varepsilon_{ctu,1}^2-10a_5\varepsilon_{ctu1}^3\right)$;

$A_5=30\{a_1\varepsilon_{c1}^4-2a_2\varepsilon_{c1}^2\varepsilon_{ctu1}+3a_3\varepsilon_{c1}^2\varepsilon_{ctu1}^2-4a_4\varepsilon_{c1}\varepsilon_{ctu1}^3+ +5a_5\varepsilon_{ctu1}^4+2\varphi_s\varepsilon_{c1}^5\left[\mu_{sc}\left(1-\xi_{sc}\right)+\mu_{st}\left(1-\xi_{c0}\right)\right]\}$;

$A_6=-60\varepsilon_{ctu1}\left[a_1\varepsilon_{c1}^4-a_2\varepsilon_{c1}^3\varepsilon_{ctu1}+a_3\varepsilon_{c1}^2\varepsilon_{ctu1}^2- -a_4\varepsilon_{c1}\varepsilon_{ctu1}^3+a_5\varepsilon_{ctu1}^4+\varphi_s\varepsilon_{c1}^5\left(\mu_{sc}+\mu_{st}\right)\right]$;

$A_7=\varepsilon_{ctu1}^2\left(30a_1\varepsilon_{c1}^4-20a_2\varepsilon_{c1}^3\varepsilon_{ctu1}+15a_3\varepsilon_{c1}^2\varepsilon_{ctu1}^2- -12a_4\varepsilon_{c1}\varepsilon_{ctu1}^3+10a_5\varepsilon_{ctu,1}^4\right)- -30\varphi_{ct}\varepsilon_{c1}^5\left(2\varepsilon_{ctu1}-\varepsilon_{ct1}\right).$

It is necessary to substitute in Eq. (6) the curvature value obtained from Eq. (7) and the strain of the extreme compressed fiber of concrete, compressed, and tensile reinforcement to determine the reduced bending moment of cracking.

The horizontal section AB in the diagram shown in Fig. 5 corresponds to the development of a crack in the cross-section with an invariable value of the bending moment. The following system of equations for the unknown strain of the extreme compressed fiber of concrete and reduced curvature is obtained by substituting the strains of the compressed and tensile reinforcement, expressed through strain of the extreme compressed fiber of concrete, into Eqs. (5) and (6) and after equivalent mathematical transformations:

$$\begin{cases} B_{1,1}\varepsilon_c^6+B_{1,2}\varepsilon_c^5+B_{1,3}\varepsilon_c^4+B_{1,4}\varepsilon_c^3+B_{1,5}\varepsilon_c^2+ +B_{1,6}\chi^2+B_{1,7}\varepsilon_c\chi+B_{1,8}=0; \\ B_{2,1}\varepsilon_c^7+B_{2,2}\varepsilon_c^6+B_{2,3}\varepsilon_c^5+B_{2,4}\varepsilon_c^4+B_{2,5}\varepsilon_c^3+ +B_{2,6}\chi^3+B_{2,7}\varepsilon_c^2\chi+B_{2,8}\varepsilon_c\chi^2+ +B_{2,9}\alpha_M^{crc}\chi^2+B_{2,10}=0; \end{cases} \tag{8}$$

where $B_{1,1}=10a_5$; $B_{1,2}=12a_4\varepsilon_{c1}$; $B_{1,3}=15a_3\varepsilon_{c1}^2$;
$B_{1,4}=20a_2\varepsilon_{c1}^3$; $B_{1,5}=30a_1\varepsilon_{c1}^4$;
$B_{1,6}=-60\varphi_s\varepsilon_{c1}^5\left(\mu_{sc}\xi_{sc}+\mu_{st}\xi_{c0}\right)$; $B_{1,7}=60\varphi_s\varepsilon_{c1}^5\left(\mu_{sc}+\mu_{st}\right)$;
$B_{1,8}=-30\varphi_{ct}\varepsilon_{c1}^5\left(2\varepsilon_{ctu1}-\varepsilon_{ct1}\right)$; $B_{2,1}=60a_5$; $B_{2,2}=70a_4\varepsilon_{c1}$;
$B_{2,3}=84a_3\varepsilon_{c1}^2$;
$B_{2,4}=105a_2\varepsilon_{c1}^3$; $B_{2,5}=140a_1\varepsilon_{c1}^4$;
$B_{2,6}=420\varphi_s\varepsilon_{c1}^5\left(\mu_{sc}\xi_{sc}^2+\mu_{st}\xi_{c0}^2\right)$;
$B_{2,7}=420\varphi_s\varepsilon_{c1}^5\left(\mu_{sc}+\mu_{st}\right)$;
$B_{2,8}=-840\varphi_s\varepsilon_{c1}^5\left(\mu_{sc}\xi_{sc}+\mu_{st}\xi_{c0}\right)$; $B_{2,9}=-420\varepsilon_{c1}^5$;
$B_{2,10}=70\varphi_{bt}\varepsilon_{c1}^5\left(3\varepsilon_{ctu1}^2-\varepsilon_{ct1}^2\right)$.

Point C on the diagrams shown in Fig. 6 and 7, corresponds to the reaching the ultimate value ε_{c1} by strain of the extreme compressed fiber of concrete. The equation for determining the unknown reduced curvature is obtained by substituting the strain of compressed and tensile reinforcement, expressed through strain of the extreme compressed fiber of concrete, into Eq. (5) and performing equivalent mathematical transformations:

$$C_1\chi^2+C_2\chi+C_3=0, \tag{9}$$

where $C_1=-60\varphi_s\left(\mu_{sc}\xi_{sc}+\mu_{st}\xi_{c0}\right)$;
$C_2=60\varphi_s\varepsilon_{c1}(\mu_{sc}+\mu_{st})$;
$C_3=\varepsilon_{c1}\left(30a_1+20a_2+15a_3+12a_4+10a_5\right)-$
$-30\varphi_{ct}\left(2\varepsilon_{ctu1}-\varepsilon_{ct1}\right)$

It is necessary to substitute in Eq. (6) the reduced curvature value obtained from Eq. (9) and the strain of the compressed and tensile reinforcement to determine the value of the reduced bending moment corresponding to the point C.

Point D on the diagrams shown in Fig. 5 and 6, corresponds to the reaching the ultimate value f_y/E_s by strain of the tensile reinforcement. The equation for determining the unknown reduced curvature is obtained by substituting the strain of the extreme compressed fiber of concrete and compressed reinforcement, expressed through strain of tensile reinforcement, into Eq. (5) and performing equivalent mathematical transformations:

$$D_1\chi^6+D_2\chi^5+D_3\chi^4+D_4\chi^3+D_5\chi^2+D_6\chi+D_7=0, \tag{10}$$

where $D_1=10a_5\xi_{c0}^6$; $D_2=12\xi_{c0}^5\left(a_4\varepsilon_{c1}-5a_5\varepsilon_{s0}\right)$;
$D_3=15\xi_{c0}^4\left(a_3\varepsilon_{c1}^2-4a_4\varepsilon_{c1}\varepsilon_{s0}+10a_5\varepsilon_{s0}^2\right)$;
$D_4=20\xi_{c0}^3\left(a_2\varepsilon_{c1}^3-3a_3\varepsilon_{c1}^2\varepsilon_{s0}+6a_4\varepsilon_{c1}\varepsilon_{s0}^2-10a_5\varepsilon_{s0}^3\right)$;
$D_5=30\Big[\xi_{c0}^2\left(a_1\varepsilon_{c1}^4-2a_2\varepsilon_{c1}^3\varepsilon_{s0}+3a_3\varepsilon_{c1}^2\varepsilon_{s0}^2-\right.$
$\left.-4a_4\varepsilon_{c1}\varepsilon_{s0}^3+5a_5\varepsilon_{s0}^4\right)+2\varphi_s\mu_{sc}\varepsilon_{c1}^5\left(\xi_{c0}-\xi_{sc}\right)\Big]$;
$D_5^{II}=30\xi_{c0}^2\left(a_1\varepsilon_{c1}^4-2a_2\varepsilon_{c1}^3\varepsilon_{s0}+3a_3\varepsilon_{c1}^2\varepsilon_{s0}^2-\right.$
$\left.-4a_4\varepsilon_{c1}\varepsilon_{s0}^3+5a_5\varepsilon_{s0}^4\right)$;
$D_6=-60\varepsilon_{s0}\Big[\xi_{c0}\left(a_1\varepsilon_{c1}^4-a_2\varepsilon_{c1}^3\varepsilon_{s0}+a_3\varepsilon_{c1}^2\varepsilon_{s0}^2-\right.$
$\left.-a_4\varepsilon_{c1}\varepsilon_{s0}^3+a_5\varepsilon_{s0}^4\right)+\varphi_s\varepsilon_{c1}^5\left(\mu_{sc}+\mu_{st}\right)\Big]$;
$D_6^{II}=-60\Big[\varepsilon_{s0}\xi_{c0}\left(a_1\varepsilon_{c1}^4-a_2\varepsilon_{c1}^3\varepsilon_{s0}+a_3\varepsilon_{c1}^2\varepsilon_{s0}^2-\right.$
$\left.-a_4\varepsilon_{c1}\varepsilon_{s0}^3+a_5\varepsilon_{s0}^4\right)+\varphi_{sy}\varepsilon_{c1}^5\left(\mu_{st}-\mu_{sc}\right)\Big]$;
$D_7=\varepsilon_{s0}^2\left(30a_1\varepsilon_{c1}^4-20a_2\varepsilon_{c1}^3\varepsilon_{s0}+15a_3\varepsilon_{c1}^2\varepsilon_{s0}^2-\right.$
$\left.-12a_4\varepsilon_{c1}\varepsilon_{s0}^3+10a_5\varepsilon_{s0}^4\right)-30\varphi_{ct}\varepsilon_{c1}^5\left(2\varepsilon_{ctu1}-\varepsilon_{ct1}\right)$.

here $\varphi_{sy}=f_{cd}/f_{yd}$.

The values of the coefficients D_5^{II} and D_6^{II} are used in constructing the linearized diagram shown in Fig. 6. The ultimate value of the reduced bending moment for diagrams shown in Fig. 5 and 6 is determined by substituting in Eq. (6) the reduced curvature value obtained from Eq. (10) and the strain of the extreme compressed fiber of concrete and compressed reinforcement.

The horizontal section DE on the diagrams shown in Fig. 5 and 6 corresponds to the formation of a conditional plastic hinge in the cross-section (an increase in the curvature at a constant value of the bending moment until destruction). The criterion for failure element is the achievement of ultimate values ε_{cu1} and ε_{sud} respectively by strain of extreme compressed fibers of concrete or tensile reinforcement. The ultimate value of reduced curvature is determined by solving one of the following equations in accordance with the failure criterion:

- in case of failure due to rupture of tensile reinforcement:

$$E_1^s\chi^6+E_2^s\chi^5+E_3^s\chi^4+E_4^s\chi^3+E_5^s\chi^2+E_6^s\chi+E_7^s=0, \tag{11}$$

where $E_1^S=10a_5\xi_{c0}^6$; $E_2^S=12\xi_{c0}^5\left(a_4\varepsilon_{c1}-5a_5\varepsilon_{sud}\right)$;
$E_3^S=15\xi_{c0}^4\left(a_3\varepsilon_{c1}^2-4a_4\varepsilon_{c1}\varepsilon_{sud}+10a_5\varepsilon_{sud}^2\right)$;
$E_4^S=20\xi_{c0}^3\left(a_2\varepsilon_{c1}^3-3a_3\varepsilon_{c1}^2\varepsilon_{sud}+6a_4\varepsilon_{c1}\varepsilon_{sud}^2-10a_5\varepsilon_{sud}^3\right)$;
$E_5^S=30\Big[\xi_{c0}^2\left(a_1\varepsilon_{c1}^4-2a_2\varepsilon_{c1}^3\varepsilon_{sud}+3a_3\varepsilon_{c1}^2\varepsilon_{sud}^2-\right.$
$\left.-4a_4\varepsilon_{c1}\varepsilon_{sud}^3+5a_5\varepsilon_{sud}^4\right)+2\varphi_s\mu_{sc}\varepsilon_{c1}^5\left(\xi_{c0}-\xi_{sc}\right)\Big]$;
$E_6^S=-60\Big[\varepsilon_{sud}\xi_{c0}\left(a_1\varepsilon_{c1}^4-a_2\varepsilon_{c1}^3\varepsilon_{sud}+a_3\varepsilon_{c1}^2\varepsilon_{sud}^2-\right.$
$\left.-a_4\varepsilon_{c1}\varepsilon_{sud}^3+a_5\varepsilon_{sud}^4\right)+\varepsilon_{c1}^5\left(\varphi_s\mu_{sc}\varepsilon_{sud}+\varphi_{sy}\mu_{st}\right)\Big]$;
$E_7^S=\varepsilon_{sud}^2\left(30a_1\varepsilon_{c1}^4-20a_2\varepsilon_{c1}^3\varepsilon_{sud}+15a_3\varepsilon_{c1}^2\varepsilon_{sud}^2-\right.$
$\left.-12a_4\varepsilon_{c1}\varepsilon_{sud}^3+10a_5\varepsilon_{sud}^4\right)-30\varphi_{ct}\varepsilon_{c1}^5\left(2\varepsilon_{ctu1}-\varepsilon_{ct1}\right)$;

- in case of failure due to crushing of compressed concrete:

$$E_1^C\chi+E_2^C=0, \tag{12}$$

where $E_1^C = 60\varphi_{sy}\varepsilon_{c1}^5\left(\mu_{sc}-\mu_{st}\right)$;

$$E_2^C = \varepsilon_{cu1}^2\left(30a_1\varepsilon_{c1}^4 + 20a_2\varepsilon_{c1}^3\varepsilon_{cu1} + 15a_3\varepsilon_{c1}^2\varepsilon_{cu1}^2 + 12a_4\varepsilon_{c1}\varepsilon_{cu1}^3 + 10a_5\varepsilon_{cu1}^2\right) - 30\varphi_{ct}\varepsilon_{c1}^5\left(2\varepsilon_{ctu1}-\varepsilon_{ct1}\right).$$

The point F in the diagram shown in Fig. 7 corresponds to the maximum value of the reduced bending moment perceived by the cross-section. Deformation of the extreme compressed concrete fiber is also an unknown value in determining the values of the reduced curvature and the reduced bending moment corresponding to the point F. In this connection, the two equilibrium equations must be supplemented by the equation obtained from the extreme condition of the reduced bending moment:

$$\frac{\mathrm{d}\alpha_M}{\mathrm{d}\chi} = 0. \tag{13}$$

The derivation of an additional equation from the extremality condition (13) requires cumbersome mathematical transformations due to the existence of a relationship between the values of strain of the extreme compressed fiber of concrete and the reduced curvature that are entered into Eq. (6). In this connection, the determination of the parameters corresponding to point F is proposed to be performed by using the step-iteration method. For this, it is necessary to specify a series of values of strain of the extreme compressed fiber of concrete for which the condition $\varepsilon_{c1} < \varepsilon_c < \varepsilon_{cu1}$ is satisfied, and substitute them in the equilibrium Eq. (5). The following equation for determining the values of curvature corresponding to the given values of strains of the extreme compressed fiber of concrete is obtained as a result of equivalent transformations:

$$F_1\chi_i^2 + F_{2(i)}\chi_i + F_{3(i)} = 0, \tag{14}$$

where $F_1 = -60\varphi_s\varepsilon_{c1}^5\mu_{st}\xi_{c0}$;

$$F_{2(i)} = 60\varepsilon_{c1}^5\left(\varphi_{sy}\mu_{sc} + \varphi_s\mu_{st}\varepsilon_{c(i)}\right);$$

$$F_{3(i)} = \varepsilon_{c(i)}^2\left(30a_1\varepsilon_{c1}^4 + 20a_2\varepsilon_{c1}^3\varepsilon_{c(i)} + 15a_3\varepsilon_{c1}^2\varepsilon_{c(i)}^2 + 12a_4\varepsilon_{c1}\varepsilon_{c(i)}^3 + 10a_5\varepsilon_{c(i)}^2\right) - 30\varphi_{ct}\varepsilon_{c1}^5\left(2\varepsilon_{ctu1}-\varepsilon_{ct1}\right).$$

The values of the reduced bending moments corresponding to the accepted values of strains of the extreme compressed fiber of concrete are determined by substituting in Eq. (6) the values of reduced curvature determined as a result of solving of Eq. (14).

The maximum value of the reduced bending moment and the corresponding value of the reduced curvature are selected from a series of values of the reduced curvature and reduced bending moment obtained with the assumed values of strain of the extreme compressed fiber of concrete for plotting the point F.

The point G in the diagram in Fig. 7, corresponds to the achievement of the ultimate reduced curvature with a decrease of the reduced bending moment perceived by the cross-section. The value of reduced curvature corresponding to point G is determined by solving Eq. (14) with strain of the extreme compressed fiber of concrete $\varepsilon_c = \varepsilon_{cu1}$. The obtained value of reduced curvature is substituted into Eq. (6) to determine the value of the reduced bending moment.

Equations of equilibrium (5) ÷ (14) allow us to construct linearized "bending moment – curvature" diagrams in the reduced values for reinforced concrete bending elements of rectangular cross-section with arbitrary dimensions. The bending stiffness of a reinforced concrete element of rectangular cross-section at any stage of the section work can be determined, according to the accepted designations, by the formula:

$$B_M = \frac{M}{\aleph} = \frac{\alpha_M}{\chi} f_{cd} b h^3. \tag{15}$$

5 CONCLUSION

The "bending moment – curvature" diagrams, constructed according to the step-iteration method based on the complete material strain diagrams, describe the work of reinforced concrete bending elements with sufficient accuracy. The sample mean of the ratio of the theoretical values of the curvatures to the experimental values is from 0.95 to 1.01.

The type of the "bending moment – curvature" diagrams constructed for cross-sections of reinforced concrete bending elements depends on the ratio of reinforcement and strength of concrete.

The equations that allow determining the key points of the linearized "bending moment – curvature" diagrams of strain of rectangular cross-section of the reinforced concrete bending elements have been proposed.

Note: This research was presented at the International Conference MATRIB 2017 (29 June - 2 July 2017, Vela Luka, Croatia).

6 REFERENCES

[1] EN 1992, Eurocode 2: Design of concrete structures. Part 1: General rules and rules for buildings. December 2004.
[2] DSTU B V.2.6-156: 2010: Concrete and reinforced concrete structures of heavy concrete. Design rules, Ministry for Regional Development and Building of Ukraine, Kyiv, 2011. (in Ukrainian)
[3] Maillian, L.: Resistance of reinforced concrete statically indeterminate beams to force impacts, Publishing house of Rostov University, Rostov-On-Don, 1989. (in Russian)
[4] Prokopovich, I.; Yaremenko, A.; Balduk, P.: About the construction of dependencies between stresses and strains of the nonlinear creep theory, News of universities: Civil engineering and architecture, No. 1 (1985) 8-9. (in Russian)
[5] Kovrov, A.; Chaikovsky, R.; Siniukina, T.: To the analysis of regularities of deformation of cross-sections of continuous

reinforced concrete beams, Newsletter of OSACEA, No. 27 (2007) 178-183. (in Russian)
[6] Yaremenko, A.; Kovrov, A.: Siniukina, T.: About the practical way to determine the stiffness of reinforced concrete beams, Newsletter of OSACEA, No. 20 (2005) 389-394. (in Russian)
[7] Bambura, A.: Experimental foundations of applied deformation theory of reinforced concrete, The dissertation of the ScD, Kyiv, 2005. (in Ukrainian)
[8] SNiP 2.03.01-84* "Concrete and reinforced concrete structures", Gosstroy of the USSR (in Russian)
[9] Asaad, R.: Development of methods for analysis of statically indeterminate reinforced concrete beams, taking into account the descending branch of deformation, Abstract of the dissertation of the PhD, Tashkent, 1984. (in Russian)
[10] Chin Kim Dam: Influence of a long-term high-level load on the deformability and bearing capacity of reinforced concrete beams, The dissertation of the PhD, Odessa, 1985. (in Russian)

Authors' contacts:

Anatolii KOVROV, PhD, Professor
Odessa State Academy of Civil Engineering and Architecture,
Strength of Materials Department
65026, Ukraine, Odessa, Didrikhsone St., 4
E-mail: akovrov@inbox.ru

Aleksei KOVTUNENKO, PhD, Assistant Professor
Odessa State Academy of Civil Engineering and Architecture,
Strength of Materials Department
65026, Ukraine, Odessa, Didrikhsone St., 4
E-mail: kovtunenko.aleks@mail.ru

Nina VYSOCHAN, Research Assistant
Odessa State Academy of Civil Engineering and Architecture,
Strength of Materials Department
65026, Ukraine, Odessa, Didrikhsone St., 4
E-mail: ninokli@mail.ru

ISSN 1846-6168 (Print), ISSN 1848-5588 (Online)
ID: TG-20170912134323

Original scientific paper

THE PERFORMANCE OF THE DC MOTOR BY THE PID CONTROLLING PWM DC-DC BOOST CONVERTER

Erol CAN, Hasan Hüseyin SAYAN

Abstract: This paper presents the PID controlling direct current (DC) to the direct current boost converter feds DC motor which has a 3.68 kW and 240 V of DC voltage input on its characteristics. What is first formed is the boost converter mathematical model at the design stage. Secondly, a mathematical model of the DC motor is created so that the boost converter with the machine can be established and modeled at the Matlab Simulink. The PID controller is considered for arranging a pulse width modulation for a boost converter switch because the needed voltage is provided for a DC motor. After that, the PID controlling direct current (DC) to a direct current boost converter running the DC motor is implemented at the Matlab Simulink. In addition to that, the only constant source running the DC motor is simulated at the Matlab Simulink. The DC motor operated by the PID controlling converter that has a low input voltage is compared to the DC motor operated by the high constant DC voltage. A low voltage input converter controlling the DC motor has a high performance according to the high constant DC source running the DC motor.

Keywords: DC-DC converter; DC motor; PID control; step-sinus pulse width modulation

1 INTRODUCTION

Many researchers deal with the speed control of the DC machine since DC motors are controlled over a wide range with stable and linear characteristics. DC motors are preferred at the industrial working areas because of the stable speed and stable load performance [1÷3]. In addition to that, sometimes dc energy on systems may be inadequate although direct voltage sources are needed for the operation of DC motors. The DC-DC converters are considered good selection for supplying the load when the direct current sources are not sufficient. So, the DC-DC converters are very important at the DC energy regulation, generation systems and power applications. Some control techniques have to be used for the increase performance of the power circuit using DC sources [4÷8].The PID control techniques have been applied for the controlling of some power systems [9÷10]. In the study, the PID control using the step sinus pulse width modulation (SSPWM) DC-DC boost converter is unlike the similar studies [11÷13]. The DC-DC boost converter of the mathematical model for the system first part is designed so that the DC-DC boost converter can increase a low-level DC voltage (150 V) to a high-level value (520 V). After that, a mathematical model of the DC motor for the system second part is created to perform at the Matlab Simulink. For the regulation of the low DC voltage, the PID control is applied from the output speed of the DC motor to the switch of DC-DC converter after the converter is connected to the DC motor as in Fig. 1. The DC motor with the DC-DC boost converter, the DC motor with the constant DC source are modeled at the Matlab Simulink for the observation and the comparison of output performances, which are toques, rotor speeds, and currents. The DC-DC boost converter drives DC motor with 150 V on a closed-loop with the PID control, while the constant DC source runs the DC motor by 240 V on an open-loop which is uncontrolled. The running DC motor with a DC-DC converter on a closed-loop control has the demanded results such as high settlement current and torques, even though the running DC motor with the constant DC source has high voltage on an open-loop control.

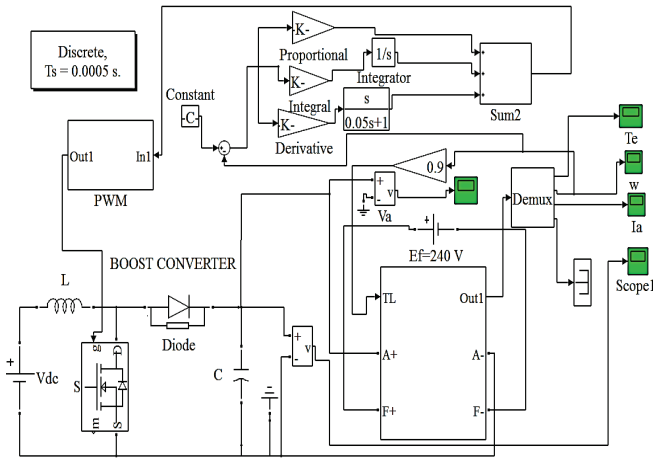

Figure 1 PID controlling the DC-DC boost converter running the DC motor

2 BOOST CONVERTER

Fig. 2 shows the power converter which operates to raise a direct voltage. Firstly, the power circuit of the mathematical model is obtained by the relation between the input and output voltage equations when the MOSFET switch that is an active component is operating the passive components such as inductor, resistance and capacitor. In the equations, V_g is the value of input voltage, V_L is the value of inductance voltage, and i_L is the value of inductance current, R is the resistive load, C is the capacitor for converter output voltage, and D is the duty time for the switches.

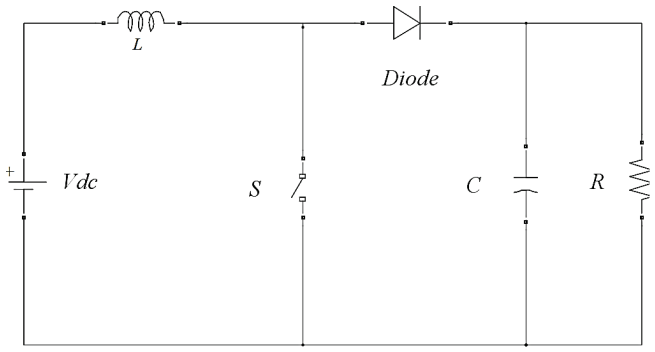

Figure 2 Boost converter circuit model

For the equation of state space, the form of equations and the relations between the current of inductance and the voltage of output have to be formed to a $\dot{x} = \boldsymbol{A}x + \boldsymbol{B}u$ form.

For $S = ON$

$$V_g = VL \tag{1}$$

$$\frac{\mathrm{d}i_L}{\mathrm{d}t} L = V_g \tag{2}$$

$$i_L = \frac{V_g}{L} \tag{3}$$

$$\dot{V} = \frac{I_z}{C} \tag{4}$$

The variables obtained in the above shown equations are shown in the matrix form as follows.

$$\begin{bmatrix} i \\ \dot{V} \end{bmatrix} = \underbrace{\begin{bmatrix} 0 & 0 \\ 0 & 0 \end{bmatrix}}_{DA_{on}} \begin{bmatrix} I \\ V \end{bmatrix} + \underbrace{\begin{bmatrix} \frac{D}{L} & 0 \\ 0 & \frac{D}{C} \end{bmatrix}}_{DB_{on}} \begin{bmatrix} V_g \\ I_z \end{bmatrix} \tag{5}$$

For $S = OFF$

$$V_g = VL + V_c \tag{6}$$

$$\frac{\mathrm{d}i_L}{\mathrm{d}t} L = V_g - V_c \tag{7}$$

$$\frac{\mathrm{d}i_L}{\mathrm{d}t} = \frac{V_g - V_c}{L} \tag{8}$$

$$i = \frac{V_g}{L} - \frac{V_c}{L} \tag{9}$$

$$\dot{V} = \left(I - \frac{V}{R} + I_z \right) \frac{1}{C} \tag{10}$$

$$\dot{V} = \frac{I}{C} - \frac{V}{RC} + I_z \frac{1}{C} \tag{11}$$

$\boldsymbol{A}$ and $\boldsymbol{B}$ matrix are calculated to form the state space which has the required variables for the boost converter. – $\boldsymbol{A}$ as the given Eq. (12), and $\boldsymbol{B}$ as given Eq. (13).

$$\boldsymbol{A} = DA_{\text{on}} + (1-D)A_{\text{off}} \tag{12}$$

$$\boldsymbol{B} = DB_{\text{on}} + (1-D)B_{\text{off}} \tag{13}$$

Eqs. (14) and (15) show the matrixes on the final form:

$$\boldsymbol{A} = (D-1) \begin{bmatrix} 0 & -\frac{1}{L} \\ -\frac{1}{C} & -\frac{1}{RC} \end{bmatrix} \tag{14}$$

$$\boldsymbol{B} = \begin{bmatrix} \frac{D}{L} & 0 \\ 0 & \frac{1}{C} \end{bmatrix} \tag{15}$$

3 DESIGN OF THE PULSE WIDTH MODULATION

The pulse width modulation technique is widely considered for the motors drive and different loads drive at the some studies [15÷20]. The paper deals with the modulation technique. The technique is that the step-sinus pulse width modulation (SSPWM) showed in Fig. 3 controls the switch of the DC-DC converter. SSPWM is formed when two different triangles compare to the step sinus signals. The switching times can be are determined with triangular similarity, because the steps of sinus signal increase the b unit lengths on the vertical and different the k unit lengths on the horizontal, as shown in Fig. 3. The creating voltage on loads is calculated as analytic because the interactions of steps with the triangles form similar triangles. Every formed triangle has a different size in all formed triangles. Pulse widths are produced because the similar triangle rules are shaped in the half period ($T/2$). Pulse widths are shown in Fig. 4 as similar triangles. D_f is the first pulse width, D_a is the average pulse width, and n is the pulse number.

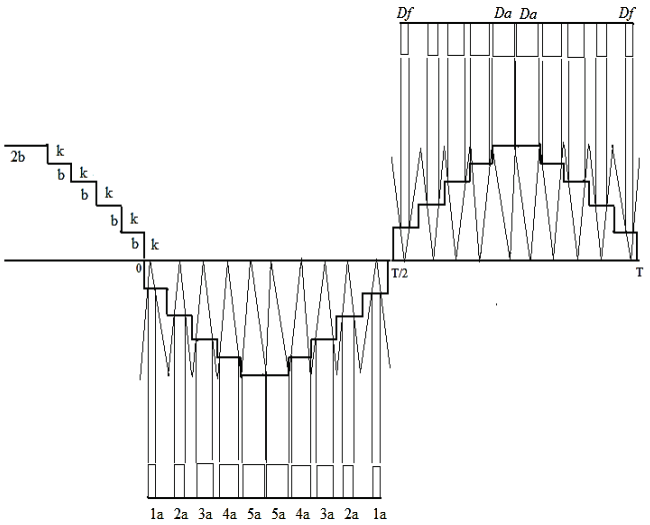

Figure 3 (a) Steps compared with the triangles, (b) formed triangles

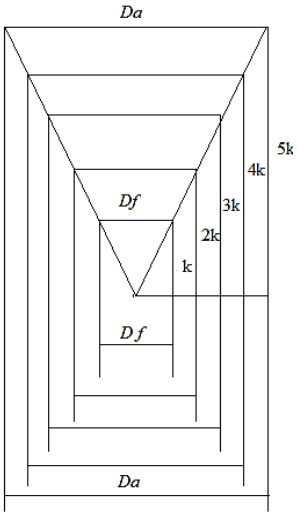

Figure 4 Formed triangles

The PWM switching voltages producing current signals are shown for inductive loads (L) in the PWMs in Fig. 5.

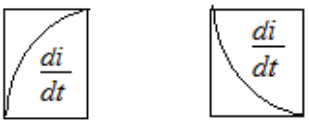

(a) (b)

Figure 5 (a) PWM producing current in between $T/2$ and T, (b) PWM producing current in between 0 and $T/2$

The size changes of the SSPWMs are 1a, 2a, 3a, 4a, 5a in the period of $T/2$ as shown in Fig. 6.

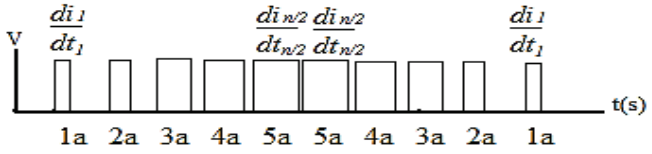

Figure 6 A linear increases of the PWM signals is created in the comparison of the results

While controlling switch, the step sinus pulse width modulation provides the total current for the inductive load (L) in Fig. 6 as in the Eq. (16).

$$\frac{\mathrm{d}i}{\mathrm{d}t} = L \cdot \left(\frac{\mathrm{d}i_1}{\mathrm{d}t_1} + \frac{\mathrm{d}i_2}{\mathrm{d}t_2} + \ldots + \frac{\mathrm{d}i_{n/2}}{\mathrm{d}t_{n/2}} + \frac{\mathrm{d}i_{n/2}}{\mathrm{d}t_{n/2}} + \ldots + \frac{\mathrm{d}i_2}{\mathrm{d}t_2} + \frac{\mathrm{d}i_1}{\mathrm{d}t_1} \right) = 2L \sum_{k=1}^{n/2} \frac{\mathrm{d}i_k}{\mathrm{d}t_k} \quad (16)$$

If two triangles are used to produce SSPWM for every step in the horizontal size of the steps which are increased for 2b, two same SSPWMs are created on every step as in Fig. 7.

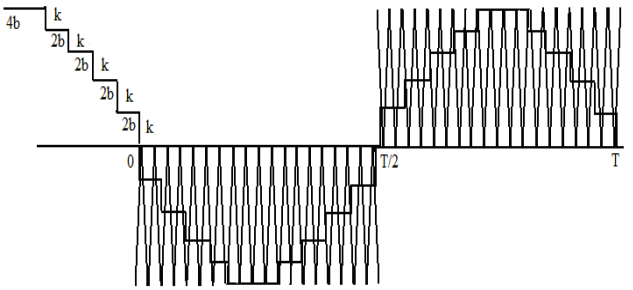

Figure 7 A linear increases of the angular PWM signals is created in comparison of the results

The width changes for the SSPWMs are 2× (1a, 2a, 3a, 4a, 5a) in the period of $T/2$ as shown in Fig. 8.

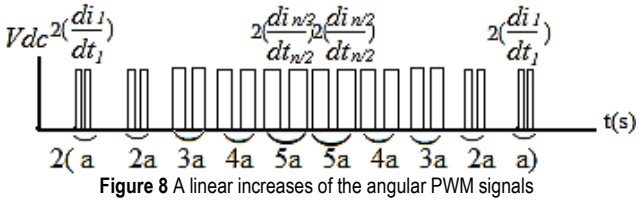

Figure 8 A linear increases of the angular PWM signals

The angular step sinus pulse width modulation produces the total current of the equation in Fig. 6 as in the Eq. (17) for inductive loads.

$$\frac{\mathrm{d}i}{\mathrm{d}t} = 2L \cdot \left(\frac{\mathrm{d}i_1}{\mathrm{d}t_1} + \frac{\mathrm{d}i_2}{\mathrm{d}t_2} + \ldots + \frac{\mathrm{d}i_{n/2}}{\mathrm{d}t_{n/2}} + \frac{\mathrm{d}i_{n/2}}{\mathrm{d}t_{n/2}} + \ldots + \frac{\mathrm{d}i_2}{\mathrm{d}t_2} + \frac{\mathrm{d}i_1}{\mathrm{d}t_1} \right) = 4L \sum_{k=1}^{n/2} \frac{\mathrm{d}i_k}{\mathrm{d}t_k} \quad (17)$$

The switching times create a total alternating voltage according to the step sinus pulse width modulation on a period of $T/2$. The switch times increase from D_f to D_a. The increases are linear because of the similar triangle rules because comparison of steps and triangles are arranged for creating triangular similarity as in Fig. 4. There are n pulses in a period of $T/2$. Therefore, the pulses are added as Eq. (18).

$$\left(\frac{D_f + D_a}{2} \right) \cdot n \quad (18)$$

4 DC MOTOR DESIGN

The DC motor's mathematical model implements a separately created DC machine. The model has certain parameters. The resistance of armature is R_a in ohms and the inductance of armature is L_a in henries. The resistance of field is R_f in ohms and the inductance of field is L_f in henries. The field armature's mutual inductance is L_{af} in henries. The total inertia of the DC machine is J in kg·m². The total friction coefficient of the DC machine is B_m in $N{\cdot}m{\cdot}s$. The total Coulomb friction torque constant of the DC

machine is T_f in N·m. KE is the voltage constant and w is the machine speed in rad/s. The armature current is i_a in ampere. The field current is i_f in ampere, the electrical torque is T_e in Nm. The field terminal exists between (F+, F−) with the inductance L_a and resistance R_a in the series. The armature circuit is constructed between the A+ and A− which contain the inductance L_a and the resistance R_a in the series with a counter-electromotive force E calculated as the Eq. (19).

$$E = K_E w \tag{19}$$

E is proportional to the field current $\dot{I}_f$ in a separately created DC machine model and K_E is calculated as the Eq. (20)

$$E = L_{af} \dot{I}_f \tag{20}$$

The mechanical part is described as the Eq. (21).

$$J \frac{\mathrm{d}w}{\mathrm{d}t} = T_e - T_L - B_m w - T_f \tag{21}$$

The state space equation is formed for the machine speed w as the Eq. (23).

$$\frac{J}{B_m} \frac{\mathrm{d}w}{\mathrm{d}t} - w = T_e - T_L - T_f \tag{22}$$

$$\dot{w} = \frac{T_e - T_L - T_f}{Js - B_m} \tag{23}$$

The DC machine model of the Matlab Simulink is shown in Fig. 9 according to the created mathematical equations.

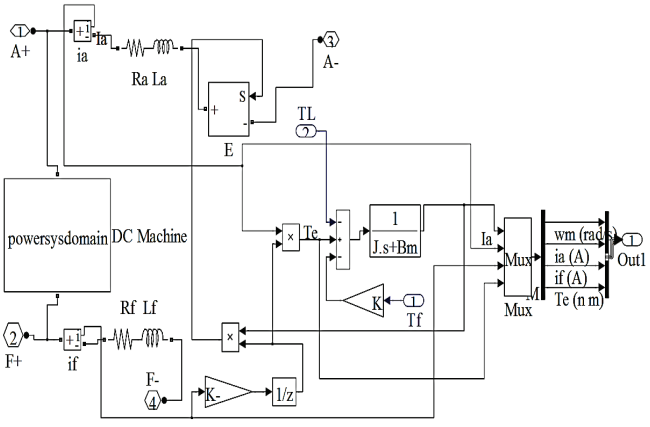

Figure 9 DC machine model of the Matlab Simulink

The DC machine model of the Matlab Simulink is given in Fig. 9 according to the created mathematical models. The PID control is considered to obtain a better result while running the system. The differential form of the PID controller is in the Eq. (24). The Laplace form of the PID controller is in the Eq. (25). K_p is the proportional gain. K_i is the integral gain. K_d is the derivational gain.

$$u(t) = K_p e(t) + K_i \int e(t)\,\mathrm{d}t + K_d \frac{\mathrm{d}e}{\mathrm{d}t} \tag{24}$$

$$K_p + \frac{K_i}{s} + K_d s = \frac{K_p s^2 + K_p s + K_i}{s} \tag{25}$$

If the proportional gain, integral gain and derivational gain are applied to the DC motor equation, the Eq. (26) and Eq. (27) are formed as follows:

$$\dot{w} = K_p + \frac{K_i}{s} + K_d s \frac{T_e - T_L - T_f}{Js - B_m} \tag{26}$$

$$\dot{w} = \frac{K_p (Js^2 - B_m s) + K_i (Js - B_m) + K_d s^2 (T_e - T_L - T_f)}{Js^2 - B_m s} \tag{27}$$

5 EXPERIMENTAL RESULTS

The applications of the PID controlling DC motor on the closed-loop control and the constant DC source feeding the DC motor on an open-loop control are performed in the Matlab Simulink. The armature of the DC motor with the constant DC source is worked with 520 V while the armature of the DC motor with DC-DC converter is performed with 150 V at the closed-loop control as shown in Fig. 10.

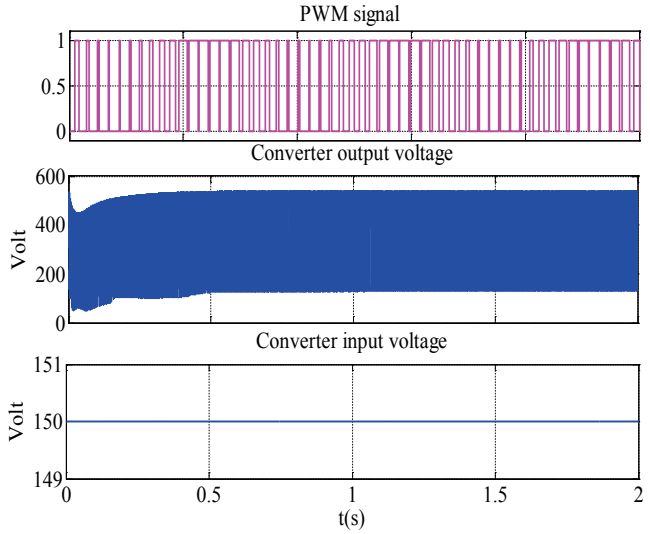

Figure 10 PID controlling the DC-DC converter of input, output voltages and the PWM signal

The speed of the DC motor which has 0.9 N·m of load can reach 115 rad/s (1100 rpm), while 240 V of the constant direct voltage source runs the DC motor as uncontrolled, which is an open-loop control as shown in Fig. 11. The speed of the DC motor which has 0.9 N·m of load reaches 145 rad/s (1385 rpm) on a closed- loop control, while 150 V of direct voltage feeding the converter runs the DC motor as

shown in Fig. 11. The PID controlling of the DC-DC converter achieves a high performance on the speed of the DC motor although the converter has low voltage according to the constant DC source.

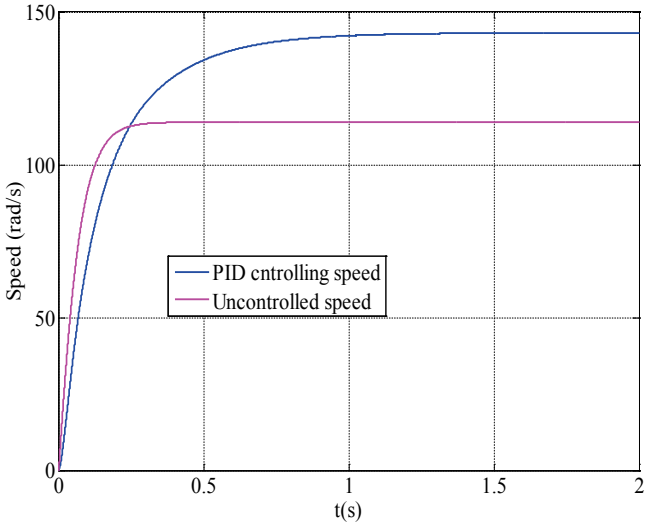

Figure 11 PID controlling the DC-DC boost converter and the constant DC source running the speed of the DC motors

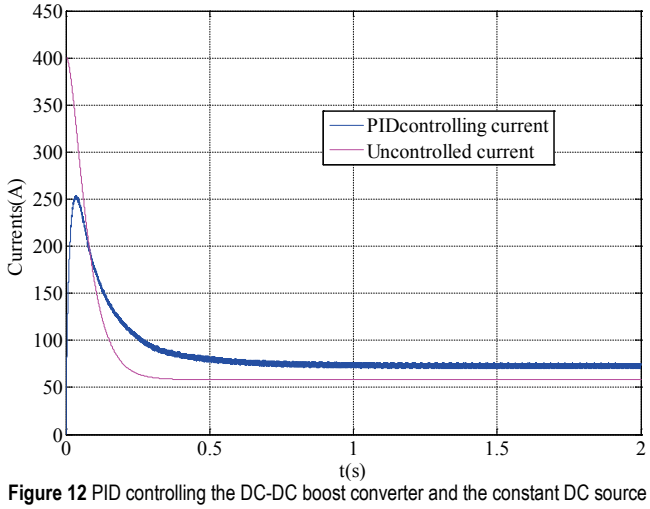

Figure 12 PID controlling the DC-DC boost converter and the constant DC source running the currents of the DC motors

After 240 V of the constant direct voltage running the DC motor as in an open loop control in Fig. 12, a settling current value of the DC motor can reach 62 A on 0.3 s while a starting current of the DC motor obtains a peak current value such as 400 A on 0.05 s. 150 V of the direct voltage feeding the power converter with, the DC motor runs on a closed-loop with a PID control. A settling current of the DC motor can reach 72 A on 0.1 s while the DC motor reaches 400 A of the peak current value on 0.5 s as in Fig. 12. Although the converter has a lower input voltage which is 150 V as opposed to the constant DC source of 240 V, the DC motor with the DC-DC converter achieves a high performance on a settling current of the DC motor in a closed-loop control.

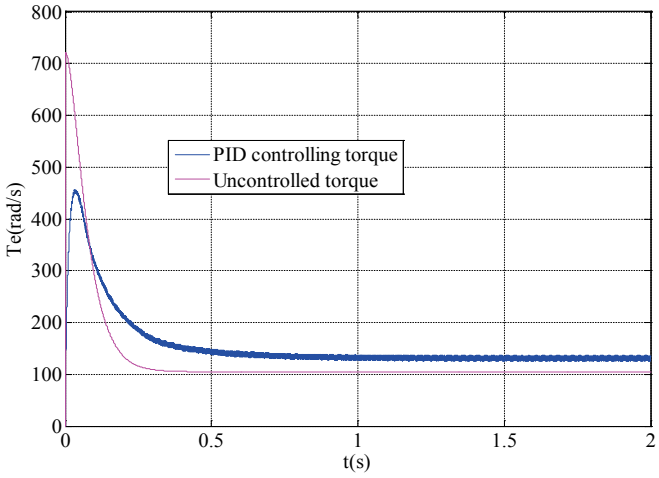

Figure 13 PID controlling DC-DC boost converter and a constant DC source running the torques of the DC motors

After 240 V of the constant direct voltage source runs the DC motor on open-loop control in Fig. 13, a settling torque of the DC motor can remain such as 105 Nm on 0.05 s while the maximum starting torque reaching 720 N·m on 0.3 s. When the 150 V of direct voltage feeding the DC-DC boost converter runs the DC motor with the PID controlling as in Fig. 13, a settling torque of the DC motor can reach 143 N·m on 0.1 s after 450 N·m of the maximum starting torque. The PID controlling DC-DC converter achieves high performance on the settling torque of the DC motor even though the input of the converter has a low input voltage according to the constant DC source which is 240 V.

The values of the used parameters are shown in Tab. 1 for the system constructed.

Table 1 Values of the used parameters

Parameter	Values	Parameter	Values
L_{af}	1.8 H	*Converter input* V_{dc}	150 V
L_a	0.012 H	L	0.1 mH
R_a	0.6 Ω	C	0.001 mF
R_f	240 Ω	K_p	0.002
L_f	120 H	K_i	0.001
B_m	0.2 N·m·s	K_d	0.001
J	0.5 km²	TL	0.9 N·m
T_s	0.0001 s	*Converter output* V_{dc}	550 V

6 CONCLUSION

The DC motor and the DC-DC boost converter mathematical model were formed so that the PID controlling converter connecting the DC motor could be constructed at the Matlab Simulink. The PID controlling DC-DC boost converter driving the DC motor and a constant DC source driving the DC motor are simulated in the Matlab Simulink for the comparison of output performances after the formed mathematical model. The results are analyzed in this study after the system is performed. for the current and torque and speed of the DC motor, the DC motor which has a PID controlling DC-DC boost converter does a better performance on a closed-loop than a constant DC source

running the DC motor on an open-loop according to the results.

7 REFERENCES

[1] Sen, P. C. Thvristorised dc drives. // Wiley Eastern Ltd 1979

[2] Thadiappan, K.; Bellamkonda, R. A fast-response DC motorspeed control system. // IEEE Transactions on Industry Applications, vol. IA-10, no. 5, September/October 1974, pp. 843-851.

[3] Sheel, S.; Chandkishore, R.; Gupta, O. Speed control of DC driveusing MRAC technique. // International Conference on Mechanical and Electrical Technology, 10-12 September, 2010, Singapore, pp. 135-139

[4] Borage, M.; Tiwari, S.; Bhardwaj, S.; Kotaiah, S. A full-bridge dc–dc converter with zero-voltage-switching over the entire conversion range. // IEEE Trans Power Electron. 2008 Jul; 23(4):1743-1750.

[5] Wai, R. J.; Lin, C.Y.; Duan, R. Y.; Chang, Y. R. High efficiency DC-DC converter with high voltage gain and reduced switch stress. // IEEE Trans Ind Electron. 2007; 54(1):354-364.

[6] Mao, H.; Rahman, O. A.; Batarseh, I. Zero-voltage-switching dc–dc converters with synchronous rectifiers. // IEEE Trans Power Electron. 2008 Jan; 23(1):369-378.

[7] Thammasiriroj, Y.; Warit, et al. Nonlinear Model Based Single-Loop Control of Interleaved Converters for a Hybrid Source System. // ECTI Transaction on Electrical Engineering, Electronics, and Communications 15.1 (2017): 19-31.

[8] Ai, J.; Mingyao, L. Ultra-Large Gain Step-Up Coupled Inductor DC-DC Converter With Asymmetric Voltage Multiplier Network for a Sustainable Energy System. // IEEE Transactions on Power Electronics (2016).

[9] Sheel, S.; Gupta, S. Advanced techniques of PID controllertuning–development of a toolbox. // First International conference on Control, Instrumentation and Mechatronics CIM '07 at Persada Johor, Malaysia.

[10] Kha, N. B.; Ahn, K. K. Position control of Shape Memory Alloyactuators by using self-tuning Fuzzy PID controller. // First IEEE Conference on Industrial Electronics and Applications, 2006, Singapore, pp. 1-5.

[11] Thadiappan, K.; Bellamkonda, R. A fast-response DC motorspeed control system. // IEEE Transactions on Industry Applications, vol. IA-10, no. 5, September/October 1974, pp. 843-851.

[12] Guan, E. Y. et al. Fundamental modulation: Multi-pattern scheme with an entire range of modulation indices for multilevel cascaded converter. // Proc. IEEE Ind. Electron. Appl. Conf., 2006, pp. 1-6.

[13] Williams, J. Narrow-band analyzer (Thesis or Dissertation style). // Ph.D. dissertation, Dept. Elect. Eng., Harvard Univ., Cambridge, MA, 1993.

[14] Chiasson, J.; Tolbert, L. M.; Mckenzie, K. J.; Du, Z. Control of amultilevel converter using resultant theory. // IEEE Trans. Control Syst. Technol., vol. 11, no. 3, pp. 345-354, May 2003.

[15] Wilkinson, J. P. Nonlinear resonant circuit devices (Patent style), U. S. Patent 3 624 12, July 16, 1990.

[16] Kerem, A.; Aksoz, A.; Saygin, A.; Yilmaz, E. N. Smart grid integration of micro hybrid power system using 6-switched 3-level inverter. // In Smart Grid and Cities Congress and Fair (ICSG), 2017 5th International Istanbul (pp. 161-165). IEEE.

[17] Can, E.; Sayan, H. H. PID and fuzzy controlling three phase asynchronous machine by low level DC source three phase inverter/PID i neizrazito upravljanje trofaznim asinhronim motorom pomocu trofaznog izmjenjivaca slabe istosmjerne struje. // Tehnicki vjesnik-Technical Gazette, 23, 3(2016): 753-761.

[18] Can, E.; Sayan, H. H. SSPWM three phase inverter design and experimented on unbalanced loads. // Tehnički vjesnik-Technical Gazette, 23, 5(2016): 1239-1244.

[19] Saygin, A.; Aksoz, A.; Yilmaz, E. N. A different model of WECS connected to smart grid through matrix converter. // In Smart Grid Congress and Fair (ICSG), 2016 4th International Istanbul (pp. 1-5). IEEE. (2016, April).

[20] Can, E.; Sayan, H. H. Different Mathematical Model for the Chopper Circuit. // Tehnički glasnik-Technical Journal, (2016), 10(1-2), 13-15.

[21] Can, E.; Sayan, H. H. The increasing harmonic effects of SSPWM multilevel inverter controlling load currents investigated on modulation index. // Tehnički vjesnik-Technical Gazette, 24, 2(2017). https://doi.org/10.17559/TV-2015102013462

Authors' contacts:

Dr. Erol CAN, Assistant Professor
Department of Aircraft Airframe Powerplants,
School of Civil Aviation, Erzincan University, Erzincan, Turkey
E-mail: can_e@hotmail.com

Dr. H. Hüseyin SAYAN, Associate Professor
Department of Electrical and Electronics Engineering,
Faculty of Technology, Gazi University, Ankara, Turkey
E-mail: hsayan@gazi.edu.tr

ISSN 1846-6168 (Print), ISSN 1848-5588 (Online)
ID: TG-20171019175235

Original scientific paper

NUMERICAL INVESTIGATION OF THE INFLUENCE OF TIP CLEARANCE AND ROTOR-STATOR INTERACTION ON CENTRIFUGAL PUMP PERFORMANCE AND CAVITATION

Cong LIU

Abstract: The influence of tip clearance on pump performance and the impact of the rotor-stator interaction on cavitation are investigated by numerical means, respectively. Firstly, the SST model is employed in numerical anaylsis, and the numerical investigation of the pump performance based on a different turbulence model is compared with the experimental data. Secondly, the pump performance at different tip clearances is investigated, and the numerical results indicate that the smaller tip clearance the better performance of keeping the head stable at a low mass flow rate. Thirdly, as the NPSH-Head curves are computed at different tip clearances, the conclusion can be drawn that the smaller the tip clearance, the stronger the capability of preventing cavitation. Lastly, the effect of the rotor-stator interaction on cavitation is performed at a design case, when the φ = 9°, the volume fraction of cavitation is maximum, however, when the φ = 120°, the volume fraction of cavitation is minimum. Besides, the blade loading is studied at a corresponding φ value. When the φ = 44°, the blade loading is minimum, however, when the φ = 120°, the blade loading is maximum. The cavity all appears from the leading edge to the 20% chord length for a different φ value, which indicates that the cavitation zone grows along the normal direction of the suction surface.

Keywords: cavitation; radial pump; rotor-stator interaction; tip clearance

1 INTRODUCTION

The radial diffuser pump is favoured for applications in a wide range of industrial domains, such as power plants, papermaking, chemical production, and so on. It is necessary to maintain a gap between the blade tip and the stationary shroud to ensure the relative motion. However, a channel is formed for water to leak because of the gap, which will contribute to a tip leakage flow, and the flow not only has a significant effect on the head and efficiency, but may also lead to cavitation. Cavitation can cause the deterioration of pump performance, noise, vibration and wall erosion, etc. [1], which are all undesirable phenomena.

The effect of tip clearance on suction performance at different flow rates in a mixed flow pump has been investigated by Yo Han Jung, et al. [1]. For large tip clearance, the head breakdown happened earlier at the design and high flow rates, but the area size of the cavitation at different tip clearances and flow rates was not examined. The unsteady cavitation flows in the centrifugal pump was studied by Wang Jian [2] by using the improved turbulence model to predict the cavitation inception, shedding off and collapse procedures, however, the tip clearance is not considered. Some experiments [3] are conducted by changing the tip gap sizes to investigate the correlation between the cavitation inception number and tip leakage vortex in an axial flow pump. The tip leakage vortex structure and cavitation patterns in an axial flow pump are revealed by the author using an experimental and improved numerical method [4, 5].

The influence of different viscosity and incompressible gas content on cavitation in a centrifugal pump was presented by Wen-Guang Li [6], who found that the NPSHr was more easily impacted by incompressible gas content. Besides, the impact of different temperature was investigated by other researchers through an experiment and simulation [7÷10].

The impact of rotor-stator interaction on the head in a centrifugal pump is studied by Feng Jianjun [11] by using PIV and LDV, but cavitation is not considered. The experimental and numerical investigation of the processing of helical vortex in a conical diffuser with a rotor–stator interaction was carried out by A. Javadi [12]. The flow unsteadiness generated in a swirl apparatus was analysed, but the influence of rotor-stator interaction on cavitation was according to him not present.

In this paper, the performance of pump at different flow coefficients was compared between the experiment and simulation to verify the correctness of the numerical method firstly. Secondly, the effect of tip clearance on pump performance was obtained with three different tip sizes. The cavitation model was employed to get the NPSH-H curve at different tip clearance sizes and the impact of rotor-stator interaction on the volume fraction of cavitation was investigated. Lastly, the blade loading was examined and compared under different relative circumferential positions between the rotating impeller and stationary diffuser.

2 GOVERNING EQUATIONS AND THE CAVITATION MODEL

Cavitation in a pump is treated differently from the thermal phase change, because the cavitation process is too quick at the interface to be modified for the assumption of thermal equilibrium. In highly simplified cavitation models, mass transfer is only driven by mechanical effects, in other words, by the liquid-vapour pressure differences rather than the thermal. In this paper, the Rayleigh-Plesset model is implemented as an interphase mass transfer model. For the cavitation flow, the homogeneous multiphase model is normally used, so each fluid component is assumed to have the same velocity and pressure. The governing equations in

the homogeneous multiphase and the Rayleigh-Plesset equation are as follows.

Continuity Equations

$$\frac{\partial}{\partial \mathrm{t}}\left(r_\alpha \rho_\alpha\right)+\nabla\cdot\left(r_\alpha \rho_\alpha U_\alpha\right)=S_{MS\alpha}+\sum_{\beta=1}^{N_p}\Gamma_{\alpha\beta}. \tag{1}$$

Where N_p is the total number of the phase, the volume fraction of each phase is denoted by r_α, $\alpha = 1$ to N_p. The user specified mass sources are described by $S_{MS\alpha}$, and $\Gamma_{\alpha\beta}$ is the mass flow rate per unit volume from phase β to phase α. This term only occurs when the interphase mass transfer happens. In this study, as neither the mass sources nor the interphase mass transfer exist, and the total number of the phase is 2, the equation can be simplified as follows:

$$\frac{\partial}{\partial \mathrm{t}}\left(r_\alpha \rho_\alpha\right)+\nabla\cdot\left(r_\alpha \rho_\alpha U_\alpha\right)=0. \tag{2}$$

Momentum Equations

$$\frac{\partial}{\partial t}\left(\rho U\right)+\nabla\cdot\left(\rho U\otimes U_\alpha-\mu\left(\nabla U+\left(\nabla U\right)^T\right)\right)=S_M+\nabla p. \tag{3}$$

Where $\rho=\sum_{\alpha=1}^{N_p} r_\alpha\rho_\alpha$, $\mu=\sum_{\alpha=1}^{N_p} r_\alpha\mu_\alpha$. Obviously, the equation is essentially a single phase transport with variable density and viscosity, and the interphase transfer terms have all been cancelled out. Due to the external body forces, S_M describes the momentum sources; considering the radius of the pump impeller is small, the momentum sources term can be ignored.

Cavitation Model

The Rayleigh-Plesset model is implemented to model the cavitation in the centrifugal pump. It provides the basis for the rate equation controlling vapour generation and condensation. This equation describes the growth of a gas bubble in the pump and is as follows:

$$R_B\frac{\mathrm{d}^2R_B}{\mathrm{d}t^2}+\frac{3}{2}\left(\frac{\mathrm{d}R_B}{\mathrm{d}t}\right)^2+\frac{2\sigma}{\rho_w R_B}=\frac{p_\mathrm{v}-p}{\rho_w}. \tag{4}$$

Where R_B represents the bubble radius, p is the pressure in the water surrounding the bubble, ρ_w is the density of water, and the surface tension coefficient between the water and water vapour is described by σ, p_v is the saturation vapour pressure of water at the temperature, and it is has the following empirical formula:

$$p_v=p_k\exp\left\{\left(1-\frac{T_K}{T}\right)\left[a+\left(b-cT\right)\left(T-d\right)^2\right]\right\}. \tag{5}$$

Where $p_K = 22.13$ MPa, $T_K = 647.31$ K, $a = 7.21379$, $b = 1.152\times10^{-5}$, $c = -4.787\times10^{-9}$, $d = 483.16$. In this paper, $T = 25$ °C, hence p_v can be calculated and it is 3229Pa.

Neglecting the surface tension between the water and water vapour and the second order terms, which only have a significant effect on the rapid bubble acceleration, the equation can be reduced to:

$$\frac{\mathrm{d}R_\mathrm{B}}{\mathrm{d}t}=\sqrt{\frac{2}{3}\frac{p_v-p}{\rho_w}}. \tag{6}$$

The corresponding rate of the change of bubble volume and mass are derived as follows:

$$\frac{\mathrm{d}V_\mathrm{B}}{\mathrm{d}t}=\frac{\mathrm{d}}{\mathrm{d}t}\left(\frac{4}{3}\pi R_B^3\right)=4\pi R_B^2\sqrt{\frac{2}{3}\frac{p_v-p}{\rho_w}} \tag{7}$$

$$\frac{\mathrm{d}m_\mathrm{B}}{\mathrm{d}t}=\rho_v\frac{\mathrm{d}V_\mathrm{B}}{\mathrm{d}t}=4\pi R_B^2\rho_v\sqrt{\frac{2}{3}\frac{p_v-p}{\rho_w}}. \tag{8}$$

If the bubble number per unit volume is denoted by N_B, the volume fraction of vapour, r_v, can be expressed as:

$$r_v=V_BN_B=\frac{4}{3}\pi R_B^3N_B. \tag{9}$$

The total interphase mass transfer rate per unit volume is:

$$\dot{m}_{wv}=N_B\frac{\mathrm{d}m_B}{\mathrm{d}t}=\frac{3r_v\rho_v}{R_B}\sqrt{\frac{2}{3}\frac{p_v-p}{\rho_w}}. \tag{10}$$

Assuming bubble growth, namely vaporization, the expression can be generalized to contain condensation as follows:

$$\dot{m}_{wv}=F\frac{3r_v\rho_v}{R_B}\sqrt{\frac{2}{3}\frac{\left|p_v-p\right|}{\rho_w}}\mathrm{sgn}\left(p_v-p\right). \tag{11}$$

Where F is an empirical factor that may differ between condensation and vaporization, the reason is that the rate of vaporization is usually much faster than that of condensation. A number of studies have shown that vaporization is firstly initiated at nucleation sites, which is why the bubble radius R_B is replaced by the nucleation site radius R_nuc for simulating purposes. As the volume fraction of vapour increases, accordingly, the nucleation site density must decrease because of less liquid. For vaporization, r_v in the equation is replaced by $r_\mathrm{nuc}(1-r_v)$, where r_nuc is the volume fraction of the nucleation sites, which is why the equation for the vaporization progress is given:

$$\dot{m}_{wv}=F\frac{3r_\mathrm{nuc}(1-r_v)\rho_v}{R_B}\sqrt{\frac{2}{3}\frac{\left|p_v-p\right|}{\rho_w}}\mathrm{sgn}\left(p_v-p\right). \tag{12}$$

The Rayleigh–Plesset cavitation model adopted by CFX is validated by Bakiretal [13] and requires the following values of the two-phase flow parameters, which are appropriate for most cavitation simulations [14, 15]. The parameters are listed as follows: R_{nuc} = 1 μm, r_{nuc} = 5×10^{-4}, F_{vap} = 50, F_{cond} = 0.01.

3 SIMULATION PROCEDURE

3.1 Physical model

A radial diffuser pump with the specific speed of n_s = 82.5 is researched in this paper. The pump of flow rate, head and rotational speed are Q_d = 0.0045 m^3/s, H_d = 7 m and n_d = 1450 rpm, respectively, at a design point. The diameter of the impeller inlet and outlet are 0.08 m and 0.1505 m, the absolute flow angle is 80 degrees, and the blade number of impeller is 6. Correspondingly, 0.155 m and 0.19 m are the inlet and outlet diameters of the diffuser, the absolute flow angle is 60 degrees and the blade number of the diffuser is 9. The view of the pump is shown in Fig. 1, and Tab. 1 presents the specifications of the pump.

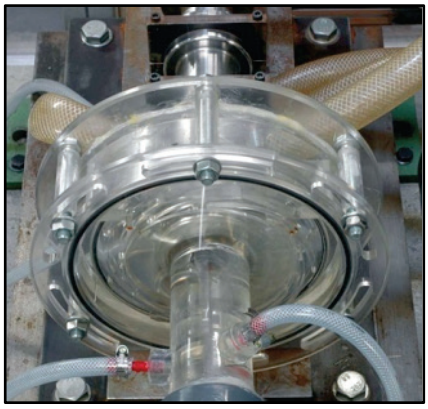

Figure 1 The view of the pump

Table 1 Specifications of the pump

Impeller parameters	Value
Number of blade Z_i	6
Impeller inlet diameter d_1 (m)	0.08
Impeller exit diameter d_2 (m)	0.1505
Absolute flow angle α_i (°)	80
Blade inlet angle β_{1i} (°)	17.9
Blade outlet angle β_{2i} (°)	22.5
Blade span b_i (m)	0.0127
Diffuser parameters	
Number of vanes Z_d	9
Diffuser inlet diameter d_3 (m)	0.155
Diffuser outlet diameter d_4 (m)	0.19
Absolute flow angle α_d (°)	60
Vane inlet angle β_{1d} (°)	171
Vane outlet angle β_{2d} (°)	160.3
Vane span b_d (m)	0.014
Design operating conditions	
Impeller rotational speed n (rpm)	1450
Specific speed n_s	82.5
Flow rate Q_d(m^3/s) Q_d (m^3/s)	0.0045
Delivery head H_d (m)	7

3.2 Computational model and boundary conditions

With the assumption that the flow is in the incompressible steady state, the internal flow of the pump is simulated by using the CFX software. Because of the rotation of the impeller, the MRF (multiple frame of reference) is selected, and the interface type between the impeller outlet and diffuser inlet adopts the frozen rotor model. The geometry of the pump to be modelled includes two impeller blade passages and three diffuser blade passages, because the frozen rotor model requires the pitch ratio at the interface between the impeller and diffuser to be 1 for as much as possible, as it considers the accuracy and reliability of the numerical result. The Counter Rotating Wall is adopted by the shroud of the impeller, and the blade wall and hub are set to a no slip boundary. Besides, the diffuser is stationary. Periodic boundaries are used to enable only 1/3 of the section of the full pump geometry to be modelled.

Three turbulence models are compared with the experimental data. The data carried out by the k-ω based on SST (Shear Stress Transport) model has a better agreement with the results of the experiment than the others, as shown in Fig. 2, which is why the k-ω based on the SST model is employed to solve the three-dimensional steady Reynolds-averaged equations.

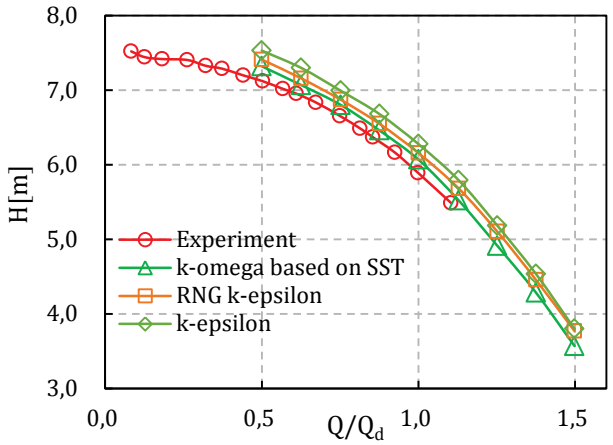

Figure 2 Head rise of the experimental and computational results

3.3 Mesh generation and independence verification

The high resolution structured hexahedral mesh has been generated for a computational domain by using the ANSYS Turbo Grid 17.0 with an ATM (Automatic Topology and Meshing) option (see Fig. 3(a)). Near a no-slip wall, viscosity has a large effect on the transport processes, and there are strong gradients in the dependent variables. Besides, the SST model requires a high resolution of the boundary layer of more than 10 points, which is why an O-Grid is built and refined to satisfy the requirements for the surrounding of the blades [16]. The wall-normal mesh resolution unit y^+ is defined as [17]

$$y^+ = u^* y/\nu,\ u^* = \sqrt{\tau_w/\rho},\ \tau_w = \mu\left(\frac{\partial u}{\partial y}\right), \quad (13)$$

where u^* is the friction velocity and τ_w is the wall shear stress. The mean value of y^+ is controlled below 10 in the surrounding of the impeller blade and diffuser vane when using the SST, and the mesh resolution is acceptable, while an H-Grid is applied for the passage. The detailed mesh information near the leading and trailing edges of the impeller blades and diffuser vanes are enlarged in Fig. 3(b), 3(c), respectively.

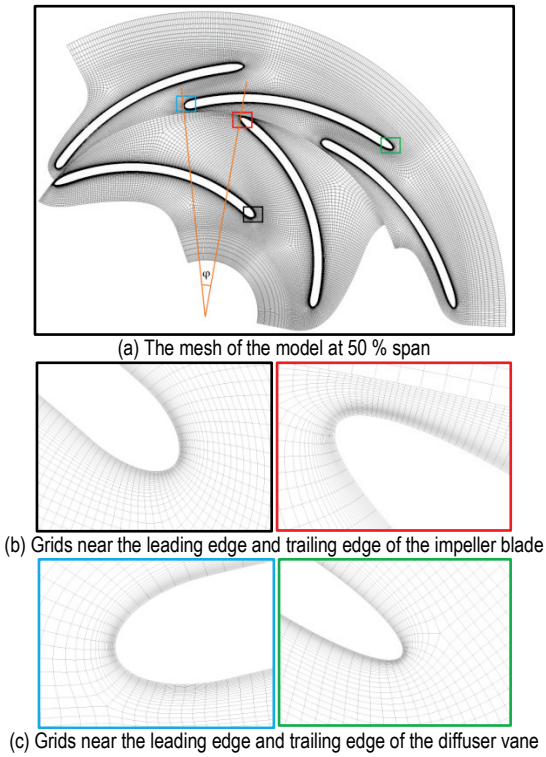

(a) The mesh of the model at 50 % span

(b) Grids near the leading edge and trailing edge of the impeller blade

(c) Grids near the leading edge and trailing edge of the diffuser vane

Figure 3 The mesh of the computational domain

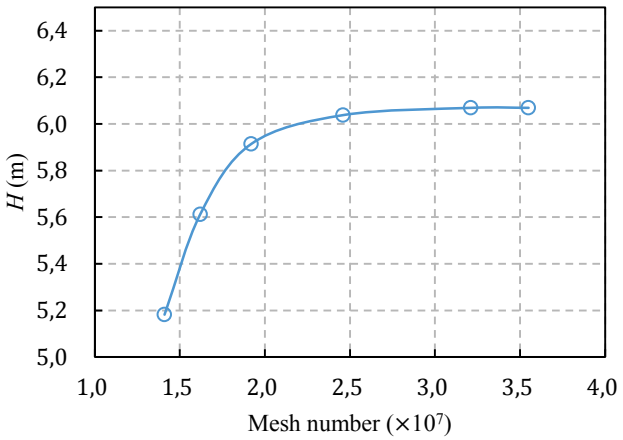

Figure 4 Independence verification of the mesh number

To eliminate the effect of the mesh number upon the numerical results, the independence verification of the mesh is carried out with six different numbers of the mesh. When the mesh number exceeds 3.21×10^7, as shown in Fig. 4, the numerical results remain almost unchangeable. Thus, the mesh number of 3.21×10^7 meets the requirement of calculating accuracy and is selected in this study.

3.4 Solutions

The high resolution option was chosen for the advection scheme and turbulence numerics. The results implementing the first order scheme will be used as the initial value of the high resolution scheme in case the scheme is not robust. When the RMS (root mean square) residual value is less than 10^{-4}, and the volume flow rate difference between the inlet and outlet reaches 10^{-5} simultaneously, the calculation will be terminated and considered to have converged.

In this paper, the effect of three different tip clearance sizes on the performance of the pump and cavitation will be studied, as shown in Tab. 2, 0.6 mm, 1.3 mm and 2.0 mm, respectively. Besides, the influence of a relative circumferential position between the rotating impeller and stationary diffuser on cavitation is obtained.

Table 2 Numerical simulate cases

Simulation case	Tip clearance size
Case 1	0.6 mm
Case 2	1.3 mm
Case 3	2.0 mm

4 RESULTS AND DISCUSSIONS

4.1 The effect of variation in tip clearance on pump performance without cavitation

Fig. 5 provides the performance of the pump at different tip clearances and a different mass flow rate. The figure exhibits that the head of the pump decreases as the tip clearance increases. Keeping the head in view, when the mass flow rate is less than 1, the rate of the head increase will decrease with the decrease of tip clearance. Moreover, at the same mass flow rate, the increase of the head from the tip clearance of 2.0 mm to 1.3 mm is less than from 1.3 mm to 0.6 mm. However, when the mass flow rate is more than 1, the relation is not remarkable, but the head of all tip clearances decreases as the mass flow rate increases.

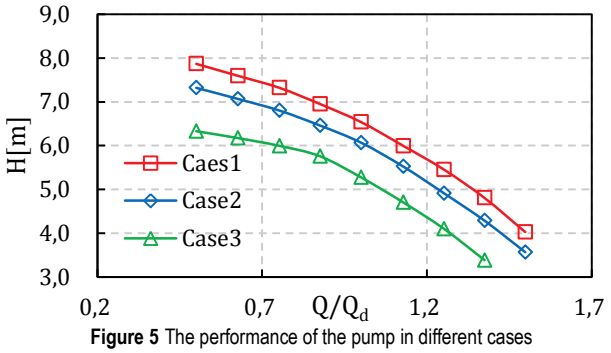

Figure 5 The performance of the pump in different cases

From the results of the simulation, what can be observed is the characteristic that a smaller tip clearance has a better performance of keeping the head stable than a

bigger tip clearance at low mass flow rate. However, it is extraordinarily difficult to keep a clearance of less than 0.5 mm, so the size of tip clearance is limited.

4.2 The effect of variation in tip clearance on pump cavitation performance at a design mass flow rate

Fig. 6 shows pump cavitation performance in the form of curves, which is a chart of the head vs. NPSH (Net Positive Suction Head) at a design mass flow rate under different tip clearances, where NPSH is defined as the pressure differential between the liquid total pressure of the pump inlet and the saturated vapour pressure at a pumping temperature [18]. The NPSH is illustrated by [19].

$$NPSH = \frac{P_{\text{tin}} - P_v}{\rho_l g} \tag{14}$$

As shown in Fig. 6, for a part of the simulation, the degradation in the NPSH vs. head curves with the reduction of the pump inlet total pressure is not significant. This is due to the fact that the pump inlet total pressure is significantly high to impede cavitation, namely, the normalized pressure rise through the pump is almost constant. However, with the pump inlet pressure dropping progressively, the incipient cavitation will emerge but will have little impact on the performance of the pump. Until the blade passage has enough blockage due to the vapour, the performance will rapidly degrade.

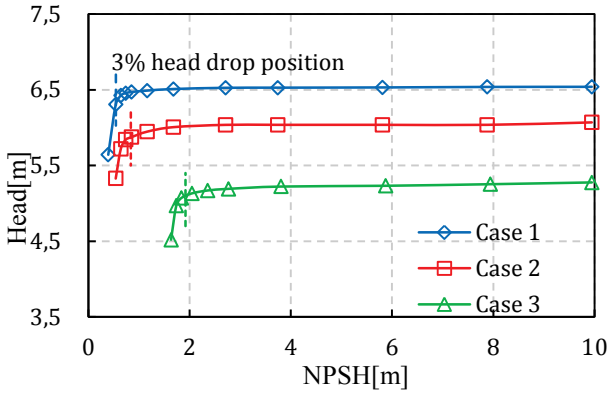

Figure 6 The drop curves of the NPSH vs. head at a design mass flow rate under different tip clearances

As the tip clearance decreases, the head breakdown corresponding to the 3 % head drop emerges at a smaller NPSH value, which demonstrates that the smaller the tip clearance, the stronger the capability of preventing cavitation. However, the relationship between the increase of the tip clearance and enhancement of the capability of preventing cavitation is nonlinear.

4.3 The effect of rotor-stator interaction on cavitation

The transient blade row modelling and cavitation model were employed to investigate the influence of the relative circumferential position between the rotating impeller and stationary diffuser on cavitation. The rotating angle φ indicated the relative circumferential position between the rotating impeller and stationary diffuser, and $\varphi = 0$ degree is defined when the prescribed impeller blade trailing the edge approaches the designated diffuser vane leading the edge (Fig. 3(a)).

In order to analyse the effect of rotor-stator interaction on cavitation, the volume fraction of cavitation (VFC) is defined below.

$$VFC = \frac{V_c}{V_p} \times 100\%, \tag{15}$$

where V_c is the volume of zone, whose pressure is below 3229Pa. V_p is the total volume of the computational domains.

Fig. 7 shows the relation of VFC and the head with φ at a 3 % head drop point of the case 2. The head profiles at $\varphi = 0$ degree show a very good periodicity for each 120 degrees, obviously, within the circumferential range of 360 degrees. The average of the head under the condition of the unsteady is equal to the steady, which validates the expected flow correctness for the numerical simulation.

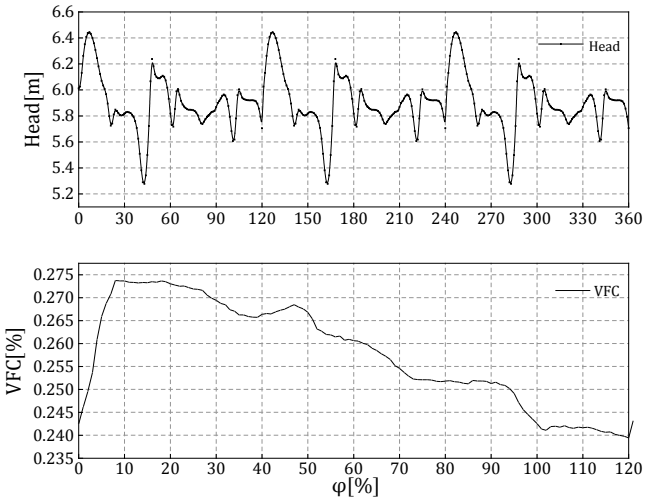

Figure 7 Head and VFC compared with different φ at a 3 % head drop point of the case 2

As Fig. 7 shows, the head has relative fluctuation amplitude of about 8÷10 % with the impeller position φ. Both the head and VFC have extreme points at the same φ value. However, the VFC shows the trend of falling down. When $\varphi = 9°$, VFC reaches the maximum value, about 0.27 %, and correspondingly, the head also achieves the maximum value, about 6.45 m. As the impeller rotates, the head reaches the minimum value, about 6.43 m, at $\varphi = 44°$. When the VFC reaches the minimum value, about 0.24 %, at $\varphi = 120°$, the head reaches the minimum value, about 5.7 m.

4.4 The blade loading at different φ values

The static pressure on the suction and pressure that surfaces at a 50 % span was estimated for different φ values at a 3 % head drop point of the case 2. The variation of the static pressure is shown in Fig. 8.

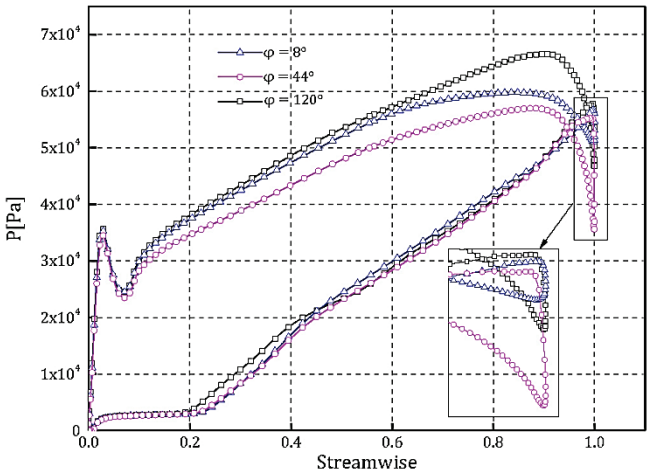

Figure 8 The blade loading at different φ values at a 3 % head drop point of the case 2

The blade loading is represented by the area inside the curve, which indirectly represents the work done by the impeller. It is observed that the static pressure variation is affected by the relative position of the rotor and stator. The lowest pressure emerges on the suction side around the leading edge and almost keeps its constant value, which is equal to the vapour pressure, and then it rapidly increases. Because the cavitation bubble develops along the blade suction side within the constant pressure region, the cavity zone corresponds to this region. In fact, the cavity appears from the leading edge to the 20 % chord for different φ values, which indicates that the cavitation zone grows along the normal direction of the suction surface. As for the blade loading, when φ = 120°, the blade loading reaches a maximum, and the VFC is at its minimum value.

5 CONCLUSIONS

A simulation was carried out for the mass flow parameter ranging from 0.5 to 1.5 at a design speed using different turbulence models, and the k-ω based on the SST turbulence model was chosen eventually. Then the numerical data was compared with the experimental data. The influence of three different tip clearances on the performance of the pump were researched; the smaller tip clearance the better performance of keeping the head stable, but the size of tip clearance is limited. The pump cavitation performance on different tip clearances were studied by using the cavitation model, and the conclusion is that the smaller the tip clearance, the stronger the capability of preventing cavitation. Lastly, transient blade row modelling was employed to examine the relation between the cavitation and rotor-stator interaction. When φ = 9°, the VFC reached a maximum value, while the minimum value achieved was at φ = 120°. Meanwhile, the blade loading was also estimated, and when the blade loading reaches a maximum at φ = 120°, the VFC is at its minimum value. The cavity appears from the leading edge to the 20 % chord length, indicating that the cavitation zone grows along the normal direction of the suction surface.

6 REFERENCES

[1] Yo Han Jung, Young Uk Min, and JinYoung Kim, 2014, "Effect of tip clearance on suction performance at different flow rates in a mixed flow pump", ASME US-European Fluids Engineering Division Summer Meeting.

[2] Jian Wang, Yong Wang, Houlin Liu, Haoqin Huang, Linglin Jiang, (2015) "An improved turbulence model for predicting unsteady cavitating flows in centrifugal pump", International Journal of Numerical Methods for Heat & Fluid Flow, Vol. 25 Iss: 5, pp. 1198-1213.

[3] Laborde, R., Chantrel, P., and Mory, M., 1997, "Tip Clearance and Tip Vortex Cavitation in an Axial Flow Pump", ASME J. Fluids Eng., 119(3), pp. 680–685.

[4] Zhang D, Shi W, Pan D, Dubuisson M. Numerical and Experimental Investigation of Tip Leakage Vortex Cavitation Patterns and Mechanisms in an Axial Flow Pump. ASME.J. Fluids Eng.2015;137(12):121103-121103-14.

[5] Desheng Zhang and Weidong Shi. Study on Unsteady Tip Leakage Vortex Cloud Cavitation in an Axial Flow Pump Using an Improved Numerical Method. ASME/JSME/KSME 2015 Joint Fluids Engineering Conference. No. AJKFluids2015-33010, pp. V001T33A001; 14.

[6] Li W. Modeling Viscous Oil Cavitating Flow in a Centrifugal Pump. ASME.J. Fluids Eng.2015; 138(1):011303-011303-12.

[7] Hirschi, R., Dupont, P., Avellan, F., Favre, J. N., Guelich, J. F., and Parkinson, E., 1998, "Centrifugal Pump Performance Drop Due to Leading Edge Cavitation: Numerical Predictions Compared With Model Tests", ASME J. Fluids Eng., 120(4), pp. 705–711.

[8] Wursthorn, S., and Schnerr, G. H., 2001, "Numerical Investigation of Performance Losses in a Centrifugal Pump Due to Cavitation", ZAMM, 81(Suppl. S3), pp. S579-S580.

[9] Coutier-Delgosha, O., Patella, R. R., Rebound, J. L., Hofmann, M., and Stoffel, B., 2004, "Experimental and Numerical Studies in a Centrifugal Pump with Two-Dimensional Curved Blades in Cavitating Condition", ASME J. Fluids Eng., 125(6), pp. 970-978.

[10] K David Huang, Sheng-Chung Tzeng, Wei-Ping Ma, Effects of anti-freeze concentration in the engine coolant on the cavitation temperature of a water pump, Applied Energy, Volume 79, Issue 3, November 2004, pp. 261-273.

[11] Feng, J; Benra, F; Dohmen, H. Unsteady Flow Visualization at Part-Load Conditions of a Radial Diffuser Pump: by PIV and CFD. Journal of Visualization. 12, 1, 65-72, 2009. ISSN: 13438875.

[12] Javadi, A. et al. Experimental and Numerical Investigation of the Precessing Helical Vortex in a Conical Diffuser, With Rotor-Stator Interaction. Journal of Fluids Engineering. 138, 8, 1, Aug. 2016. ISSN: 00982202.

[13] F. Bakir, R. Rey, A.G. Gerber, T. Belamri and B. Hutchinson, Numerical and Experimental Investigations of the Cavitating Behavior of an Induce, Int J Rotating Machinery, Vol. 10, pp. 15-25, 2004.

[14] Tang, F., and Li, J. W., 2010, Numerical Simulation of Rotating Cavitation in a Liquid Hydrogen Pump Inducer,

Proceedings of the 13th Asian Congress of Fluid Mechanics, Dhaka, Bangladesh.
[15] Ding, H., Visser, F. C., Jiang, Y., and Furmanczyk, M., 2011, Demonstration and Validation of a 3D CFD Simulation Tool Predicting Pump Performance and Cavitation for Industrial Applications, ASME J. Fluids Eng., 133(1), p. 011101.
[16] Bardina, J. E., Huang, P. G. and Coakley, T. J., Turbulence Modeling Validation Testing and Development, NASA Technical Memorandum 110446, 1997.
[17] Javadi, A; et al. Experimental and Numerical Investigation of the Precessing Helical Vortex in a Conical Diffuser, With Rotor-Stator Interaction. Journal of Fluids Engineering. 138, 8, 1, Aug. 2016.
[18] Li W. Modeling Viscous Oil Cavitating Flow in a Centrifugal Pump. ASME. J. Fluids Eng. 2015; 138(1):011303-011303-12. doi:10.1115/1.4031061.
[19] Brennen, C. E., 1994, Hydrodynamics of Pumps, Oxford University Press, Oxford.

Author's contacts:

Cong LIU,
Xuhai College, China University of Mining and Technology,
No. 1 Jinshan East Road, Quanshan District
221000 Xuzhou, Jiangsu Province, China
Tel./Fax: +8615152101093
E-mail: 511070388@qq.com

ISSN 1846-6168 (Print), ISSN 1848-5588 (Online)
ID: TG-20171101183657

Original scientific paper

LIGHT PERMANENCE WRAP PRINTS PRODUCED WITH CMYK UV INKJET INKS

Ana LEŠIĆ, Igor MAJNARIĆ, Damir MODRIĆ, Marko MORIĆ, Ivana BOLANČA MIRKOVIĆ

Abstract: Nowadays, Inkjet technology has become one of the most widespread printing technologies in car industry (car wrapping = printing and wrapping the whole vehicle or a part of a vehicle in printed foil). Printed wrap foils are, after the wrapping process, exposed to the same conditions as a lacquered vehicle: intensive sunlight, high and low temperatures, rainfall, snow, ice, particles or bugs that the vehicle encounters while driving, etc. In this paper we tested different types of wrapping foils (Orajet, 3M Scotchcal and 3M Controltac) and solvent inkjet inks to investigate the influence of different types of wrap foils on the real reproduction of UV ink jet coloured imprints, as well as their stability fluctuations during ageing. The inkjet prints age faster under the influence of UV light (Xenon lamp in SolarBox) in a period of 240 hours. The results show that the 3M Scotchcal foil has the best CMYK stability.

Keywords: car wrap foil; Inkjet printing technology; light permanence; UV curing inks

1 INTRODUCTION

When selecting materials, a wide number of processes and factors decide about the quality and performance of the final product. When considering car wrapping, the following parameters determine the quality and technical requirements: foil manufacturers, vehicles, printing offices and distributors of all those technologies that are a contact point between the manufacturers and brand owners.

When working with foils, cutting is a very important step in the production. E-cut foils are specially developed for cutting machines (e-cut refers to electronic cutting – with a computer controlled cutting knife and with the purpose of getting different kinds of precisely cut shapes). E-cut foils can be classified into non-transparent (or opaque) and transparent (or translucent) foil types. Depending on the application, there are also other types of wrapping foils: foils for glass decorating, Di-Noc films and protective films. [1]

1.1 Wrapping foils

During the nineties of the 20th century, the revolution in foil application occurred. The reason for that was the possibility of personalized printing by acceptable prices, the development of highly productive foil cutters, inkjet printers that use inks resistant to outdoor influences and the development of self-adhesive foils. The most popular producers of foils on the market today are the following: 3M, Grafityp, APA, Avery Dennison and Arlon. Apart from the standard glossy foils (white and coloured), it is possible to print on mat and chrome foils. One of the popular classifications is given by the quality of production. Based on that classification, there are **premium foils** (the best quality), **intermediate foils** (medium quality) and **foils for promotional purposes**. [2]

One special category includes foils for interior decoration and special foils for glass application, where the Di-Noc foils are a typical representative of that category, mostly used in architecture, for walls.

The most important classification of foils is the one by structure, that is, the number of materials that the foil is made of: **cast foils** (usually made from vinyl) and **calendered foils** (mostly made from PVC). All the layers of foils have similar thickness. The final layer is usually used for fixing the ink in the printing process (Figure 1).

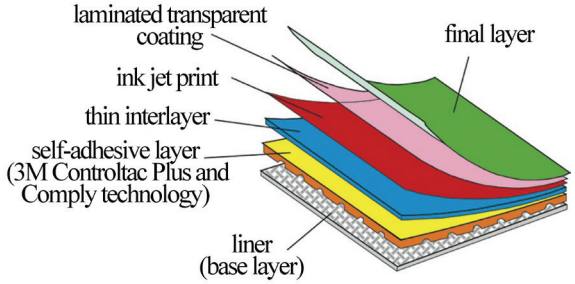

Figure 1 Basic construction of a wrapping printable foil with the 3M Controltac and Comply technology [3, 4]

1.1.1 Production of foils

Cast foils are made by mixing all the ingredients together and pouring them in a liquid aggregate condition on the paper carrier. This process produces a film which has the thickness of 1-2 mm. It is a durable, flexible, adaptable and dimensionally stable film that holds the inkjet colour very well. Such foils are ideal for wrapping complex surfaces such as those on vehicles, where a slick finish is expected. Calendered foils are made by applying the molten mixture through the mould, after which the mixture is passed through a series of calendering rolls.

By rolling and stretching, thick layers of foil (usually 3-4 mm thick) are produced with uniform properties. This results in a somewhat less dimensionally stable and less adaptable coating foil which will exhibit shrinkage when exposed to heat. However, such wrapping foils are cheaper and more resistant to scratching. [5, 6]

1.1.2 Adhesives

A typical wrap foil is coated with a solvent-based adhesive layer (an adhesive that is activated by stronger contact of a silicone squeegee). [7, 8]

There are different types of adhesives. The most common are: PA (Pressure-Activated Adhesive) that is activated by increased pressure and heat, SP (Strong Pressure Adhesive) that is activated by high pressure, and PSA (Pressure Sensitive Adhesive) that is activated by low pressure. In some of these adhesive layers, the Comply Adhesive Technology can also be found. This is actually a film with air ducts through which air is exfoliated during the cladding (to remove even the smallest air bubbles). This technology solved a problem that would otherwise require a decollation of the foil part and re-bonding, which in some cases causes the film to deform, which would then become unusable. [9, 10]

1.2 Inkjet printing technology

The Inkjet printing technique implies NIP printing systems (Non Impact Printing). This means that liquid ink apply through micro size nozzles directly on printing substrate (without contact with imaging unit). The assumption for dripping is correct Weber number (must be greater than W_k>12).[3] Inkjet printing techniques can be divided into two basic categories: Continuous Inkjet and Discontinued (or DoD - Drop On Demand) Inkjet. In Continuous Inkjet, the binary and multiple dropout systems differ, while in DOD Inkjet there are three different ways of forming droplets: Piezo Inkjet, Thermal Inkjet and Electrostatic Inkjet.

1.2.1 UV inkjet inks

UV and LED UV inks provide high thicknesses of application regardless of the thickness of the printing substrate. The composition of this color consists of: pigments (15%), prepolymers (20-35%), monomers and oligomers (10-25%), photoinitiators (5-10%) and additives (1-5%). One of the most important UV ink components are certainly photoinitiators. By absorbing UV light from the appropriate source, they enhance the polymerization processes, thus initiating the drying process itself.

1.2.2 UV electromagnetic radiation

The UV region includes only a small part of the electromagnetic radiation spectrum and is expressed in wavelengths measured in nanometers (1 nm = 10^{-9} m). The UV wavelengths are extremely short and range between 200 and 380 nm and have been shown to be the most suitable for UV ink and varnish drying. The UV spectrum is divided into three possible subregions with different UV drying characteristics: UVC, UVB and UVA electromagnetic waves. The UVC ranges from 200 to 280 nm. Such high UV radiation energy provides instant drying and is most often used for surface UV drying of inks and coatings. The UVB ranges from 280 to 315 nm. The light in this wave range penetrates deeper into the layer of ink film, i.e. this UV radiation (with longer wavelengths) allows a better drying of the medium printed ink layers. The UVA ranges from 315 to 380 nm. This type of UV rays is the closest to the visible part of the spectrum. It can reach deep layers of highly pigmented colors and ensure the drying of thick layers of lacquer.

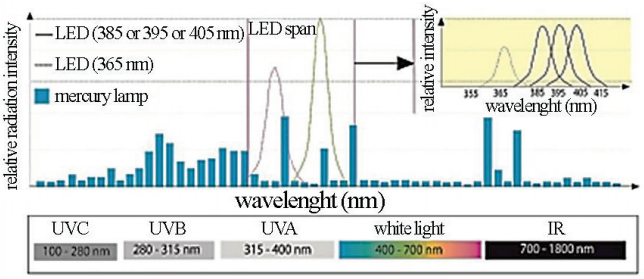

Figure 2 Radiation spectrum of typical UV sources

1.2.3 UV ink drying

UV light sources are mostly called UV lamps. They are usually made up of quartz glass tubes that contain mercury. The body of the lamp is constructed of high-quality quartz glass which passes at least 90% of generated UV rays. The quartz lamp body must be resistant to the internal temperature exceeding 1100°C, while the temperature on the surface of the lamp is about 900°C. In order to avoid damage to the surface of the lamp, an adequate cooling system must be installed.

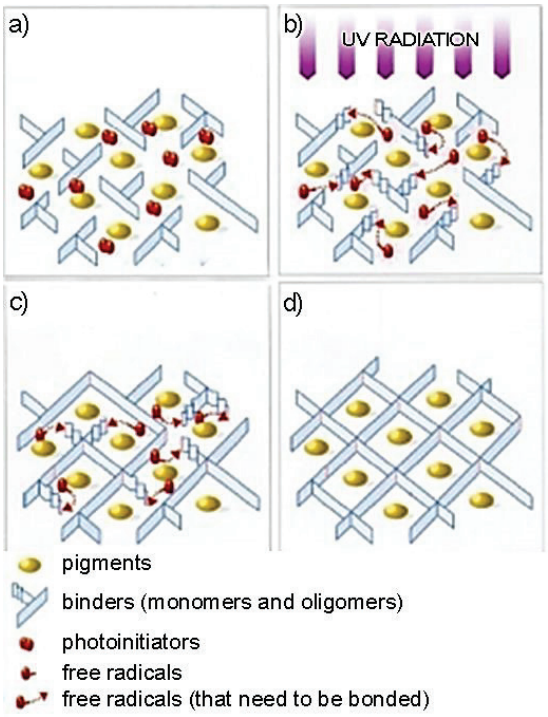

Figure 3 UV ink polymerization process: a) wet coating (liquid or viscous), b) UV radiation, ink is still liquid, c) the photoincitiators are bonding and macro-molecules are formed, d) final stage: all molecules are linked except the pigments

In the case of UV drying, the printing ink film polymerizes and completely dries as soon as radiation arrives. The UV drying method, however, requires special printing ink containing a binder and additional photoinitiators. The photoinitiators are active at the wavelengths between 365 and 415 nm, which results in a solidification process. This cross-linked reaction of UV-dyeing and varnish takes place for one second.

2 EXPERIMENT

For the experiment purposes, a CMYK test form with a 0-100% rasterton value – RTV (with a 10% step) was made. A PDF document was then made and sent to Roland's RIP Versa Works. The printed form was printed on a Roland LEC 300 (with UV ink). Three experimental wrap films were used for printing: 3M Scotchcal, 3M Controltac and Orajet.

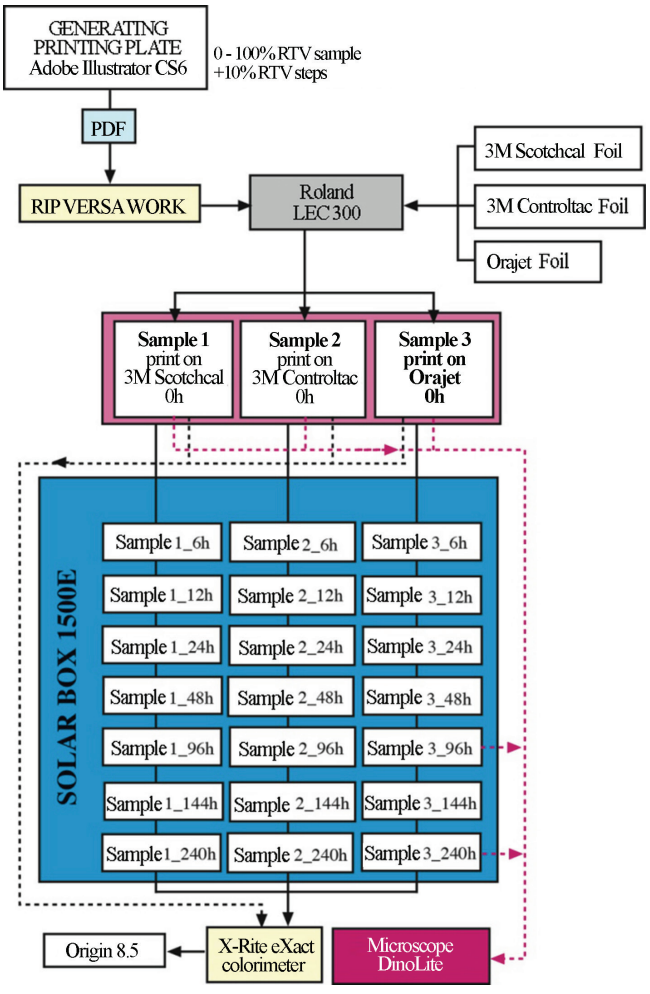

Figure 4 Scheme of the performed experiment

After the printing, a null measurement followed. It included the measurement of colorimetric values of typical fields with 20% and 100% RTV with the X-Rite eXact spectrophotometer. Thereafter, a set of three previously measured samples was subjected to fast aging in the SolarBox 1500E chamber on a 280 × 280 mm bracket that was adapted to the dimensions of the aging chamber. The aging conditions in the chamber were pre-defined: 50 °C temperature and 550 W/m^2 radiation, in time periods of 6h, 12h, 24h, 48h, 96h, 144h and 240h.

The measured results were analyzed in the Origin 8.5 program, where the results depicting the value of the change in coloration (ΔE_{00}) were shown in the graphs, depending on the aging time (fields with 20% and 100% RTV values were analysed). [11, 12]

3 RESULTS AND DISCUSSION

The aging process of the printed foil is a process of atmospheric influence (temperature, relative humidity, insolation, etc.) over a longer period of time. Since the changes in coloration during the aging process can be caused by changes in the substrate itself, it was necessary to determine how much the substrates themselves change (Figure 4).

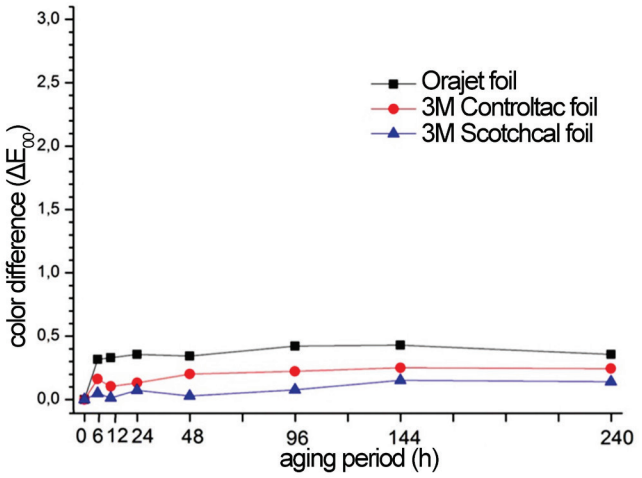

Figure 5 Differences in the colouring of white wrap foils within 240 hours

For all three foils it can be said that they are very stable and that during the aging process (after the period of 240h) no apparent changes (seen by the naked eye) have been observed. However, from Figure 4, it is obvious that the biggest changes occurred on the Orajet foil and that the least changes occurred on the 3M Scotchcal foil. The utmost changes occurred at the beginning of experimental aging (after 6h in the chamber), and their numerical values are the following: ΔE_{Orajet}=0.31, $\Delta E_{Controltac}$=0.16 and $\Delta E_{Scotchcal}$=0.05. During the 240-hour period, no color changes occurred, and the values at t=240h are: ΔE_{Orajet}=0.35, $\Delta E_{Controltac}$=0.24 and $\Delta E_{Scotchcal}$=0.14.

UV inkjet ink is dried by polymerization that starts with the exposure to ultraviolet electromagnetic radiation. Due to the short drying time, the print has a relatively thick layer of ink, which does not diminish over time. Moreover, such inkjet ink is much more resistant to atmospheric conditions than solvent inks because the other contain a high percentage of solvents.

Figures 5, 6, 7 and 8 show the results of the measured CMYK surfaces printed with 20% (bright tones) and 100% RTV (full tones). [13, 14]

Figure 5a shows the differences in the colouring of cyan UV inkjet ink, measured on 20% RTV fields. The largest changes in ΔE_{00} were achieved after t=240h ($\Delta E_{Scotchcal}$=0.37, $\Delta E_{Controltac}$=0.76 and ΔE_{Orajet}=1.02). The difference in full tone colouration (Figure 5b) abruptly changed after the first six hours, after which the colour differences reached the following values: Scotchcal ΔE_{144h}= 0.95, Controltac ΔE_{40h}= 0.41 and Orajet ΔE_{240h}= 0.91. As it was expected, the highest changes occurred on the PVC Orajet foil, and the smallest on the vinyl 3M Scotchcal foil.

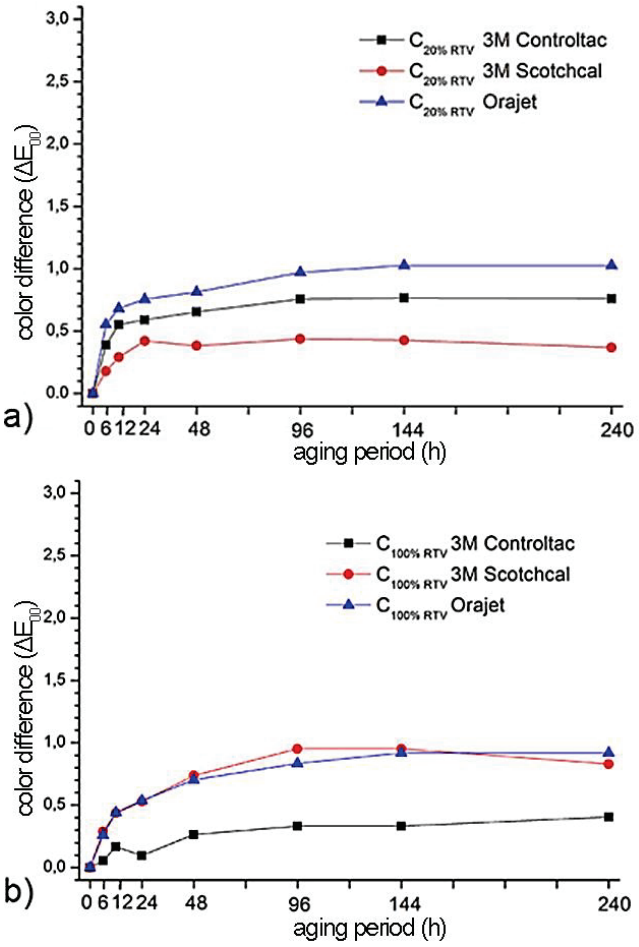

Figure 6 Changes in the cyan UV inkjet colours after 0h and 240h; a) ΔE_{00} for 20% RTV fields; b) ΔE_{00} for 100% RTV fields

For magenta full tones (Figure 6a) it can be seen that the results for the 3M Scotchcal and Orajet foils are almost identical. The only differences appear after 240 hours, when the change on the 3M Scotchcal foil is lesser than the one on the Orajet foil (difference between the two is ΔE=0.05). At this point, the resulting colour changes are: $\Delta E_{Scotchcal}$=0.57 and ΔE_{Orajet}=0.62. The largest deviations are visible on the magenta prints on the 3M Controltac foil ($\Delta E_{Controltac}$=0.68).

The results of colour changes for the fields with 20% RTV (Figure 6b) show a trend that, when increasing the aging time period, the measured values on the Orajet and 3M Controltac foils equalize (they overlap after 240h). At that point, the differences in colouring were: ΔE_{Orajet}=0.73, $\Delta E_{Controltac}$=0.72. The measured values for the 3M Scotchcal foil are the lowest in the same time measured, and reach the value $\Delta E_{Scotchcal}$=0.50. Such colour changes remain the same even after the period between 48 and 96 hours of aging.

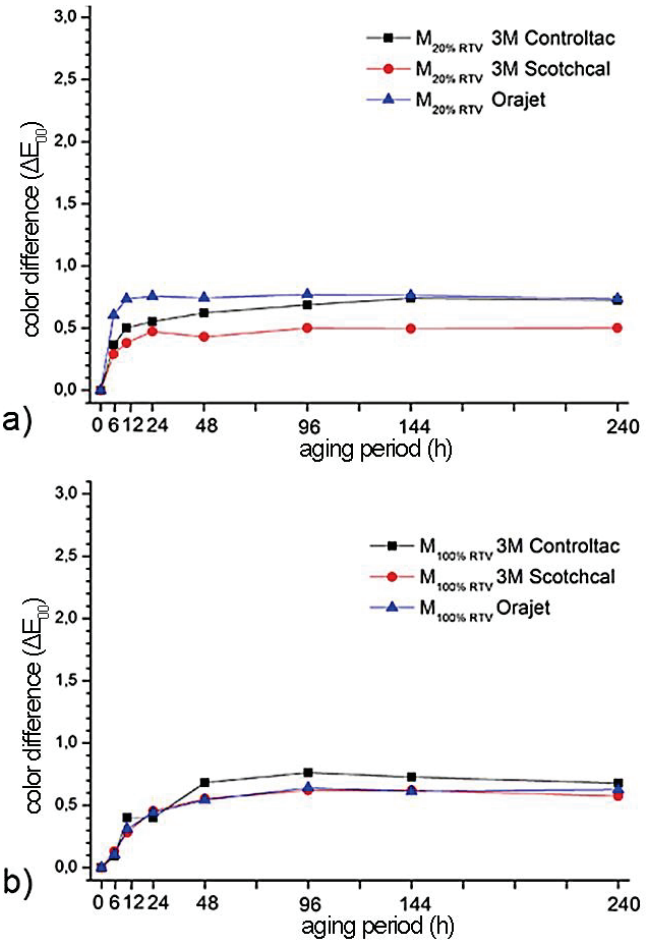

Figure 7 Changes in the magenta UV inkjet colours after 0h and 240h; a) ΔE_{00} for 20% RTV fields; b) ΔE_{00} for 100% RTV fields

On the yellow fields with 100% ink coverage (Figure 7b), the colour differences vary linearly to a period of 144h. From that moment on, the changes are constant. Therefore, after the t=144h, the colour differences are: $\Delta E_{Scotchcal}$=0.36, $\Delta E_{Controltac}$=0.42 and ΔE_{Orajet}=0.43, and after 240h, ΔE_{Orajet}=0.47. On the screened fields, the results are similar (Figure 7b). That means that during aging, the yellow prints on the 3M Controltac foil have changed the least. However, at the end of the experiment (t=240h), all values were equalized ($\Delta E_{Scotchcal}$=0.43, $\Delta E_{Controltac}$=0.41 and ΔE_{Orajet}=0.43). Such changes are minimal, but it is to be expected that, with the increase of the aging time period, the changes could increase too.

By analysing the full tonal field printed with black UV ink (Figure 8b), it is apparent that the differences have over time approximately linearly increased. After the period of 240h, the values of ΔE_{00} were: $\Delta E_{Scotchcal}$=0.76, $\Delta E_{Controltac}$=0.76 and ΔE_{Orajet}=1.64. Thus, these are the ones with the biggest changes in coloring if compared to other experimental results. It is especially important to point out the value curve for the Orajet foil that shows an exceptional tendency to increase the color difference value. On a graph that shows the color change results for the 20% RTV black field (Figure 8a), a non-characteristic change in color difference is observed after the first six hours of aging (ΔE_{Orajet}=2.78).

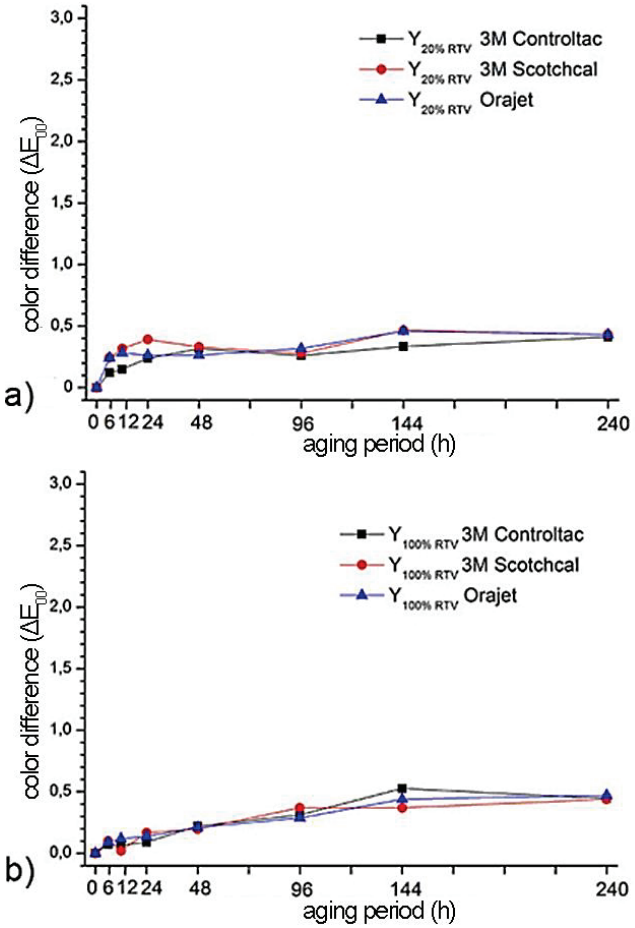

Figure 8. Changes in the yellow UV inkjet colours after 0h and 240h; a) ΔE_{00} for 20% RTV fields; b) ΔE_{00} for 100% RTV fields

Further aging will cause much less changes which are the following after t=240h: $\Delta E_{Scotchcal}$=0.28, $\Delta E_{Controltac}$=0.39 and ΔE_{Orajet}=3.03. This value for the Orajet wrap foil exceeds the limit of tolerance and is visible to the naked eye. The black UV ink on the Orajet substrate should, therefore, not be used for practices where the print would be exposed to aging conditions, because it would show a marked difference in coloration in a very short time. A possible solution to such a problem would be additional varnish or the application of an additional protective layer by special laminating.

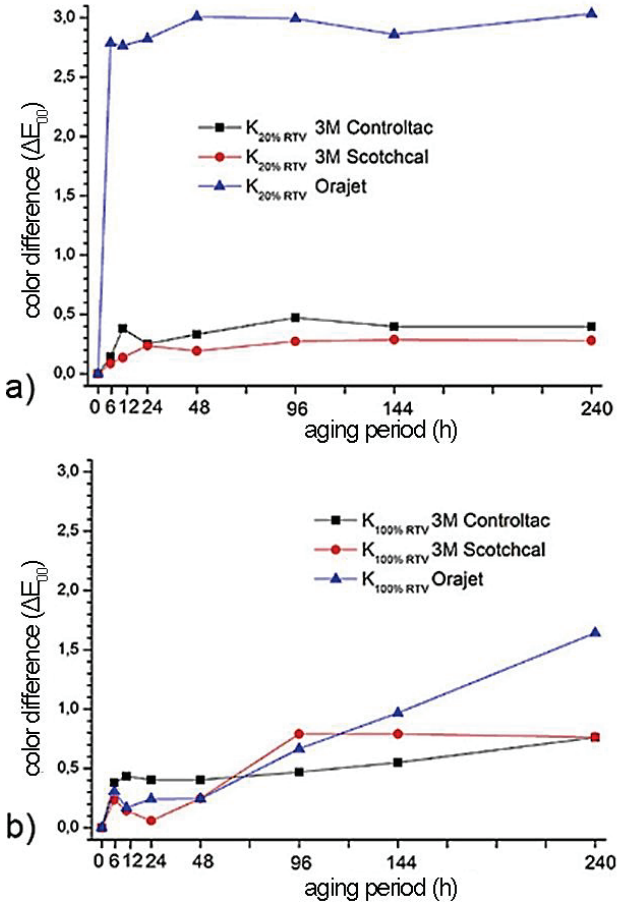

Figure 9. Changes in the black UV inkjet colours after 0h and 240h; a) ΔE_{00} for 20% RTV fields; b) ΔE_{00} for 100% RTV fields

4 CONCLUSION

In the analysis of experimentally aged wrap printing substrates, we found no significant changes in the colorimetric values during the period of 240 hours. Such changes are not visible to the human eye. By colorimetric measurements, it was found that the largest changes are exhibited on the Orajet foil ($\Delta E_{Orajet\text{-}240h}$=0.35), and the lowest on the 3M Scotchcal foil ($\Delta E_{Scotchcal\text{-}240h}$=0.14). Moreover, colour difference curves do not show a tendency of growth over time, and all three foils retained satisfactory colorimetric properties after a longer aging period.

When analysing the UV inkjet print, it is concluded that each process colour behaves differently. On cyan prints, after six hours, larger changes took place, which over a period of 240h increased to a maximum of $\Delta E_{240\text{-}6h}$=0.3. Due to low production costs, the biggest changes were, as expected, on the Orajet foil, and the smallest on the 3M Scotchcal foil. However, all changes do not exceed the value of ΔE=1. Magenta prints were almost identically changed on the Orajet and 3M Scotchcal foils, on fields with 100% RTV, while the biggest differences for the 20% RTV fields were noticed on the 3M Controltac foil. All changes did not exceed the value ΔE=1 until the end of experimental aging.

The yellow colour has shown the slightest change in colouring. Overall differences do not exceed the value of ΔE=0.5, and the values are approximately the same for the prints on all three foils on fields with 20% and 100% RTV. The black colour demonstrated the largest changes. Full-tone fields exhibit a linear growth tendency throughout the experiment. The maximum value is $\Delta E_{Orajet\ 20\%\ RTV}$=3.03. After the initial change at t=6h, this curve demonstrates an approximately stable growth gradient. The black UV prints were the only that after a very short time (6 hours of aging) showed a big difference in coloration, $\Delta E_{Orajet\ 20\%}$=3.03. This difference is clearly visible, which is why the black UV ink is not recommended for use in practice (especially for small RTV values).

The 3M Scotchcal foil has, in most cases, shown the best and the most stable results in measurements. The majority of the measured colour differences show a value lesser than ΔE=0.5 for all CMYK colours on the 3M Scotch cal foil (even the black UV ink on 20% RTV fields).

5 REFERENCES

[1] Print – magazin 6/2, Obljepljivanje vozila (6.2015), 44.
[2] http://multimedia.3m.com/mws/media/451422O/sell-sheet-for-7725-and-7125.pdf (Accessed: 16.7.2016)
[3] Majnarić I., Osnove digitalnog tiska, Sveučilište u Zagrebu, Grafički fakultet Zagreb, (2015), 21-25
[4] Wrap magazine 1/1, (1.2016), 42-45.
[5] http://www.tekra.com/resources/tek-tip-white-paper/tek-tip-cast-vs-calendered-vinyl, Tek tip - cast vs calendered vinyl (Accessed: 16.7.2016)
[6] Wrap Magazin, Folije – osnova kvalitetnog wrap-a, 1/1, (1.2016), 20.
[7] http://multimedia.3m.com/mws/media/253349O/instruction-bulletin-and-application-guide.pdf (Accessed: 20.7.2016)
[8] http://multimedia.3m.com/mws/media/731671O/product-bulletin-1080-series.pdf (Accessed: 16.7.2016)
[9] http://multimedia.3m.com/mws/media/664607O/product-bulletin-80.pdf (Accessed: 16.7.2016)
[10] https://kpmfusa.com/history-of-vehicle-wrap/ - History of vehicle wrap (Accessed: 20.4.2016)
[11] http://multimedia.3m.com/mws/media/1002230O/instruction-bulletin-5-5.pdf (Accessed: 14.7.2016)
[12] http://arlon.com/Objects/Documents/Tech%20Manuals_Guides/Vehicle%20Wrap%20Removal %20Guide-2014.pdf (Accessed: 14.7.2016)
[13] Možina K., Medved T., Rat, B., Bračko S., Influence of Light on Typographic and Colorimetric Properties of Ink Jet Prints, Journal of Imaging Science and Technology 54(6), 2010. 060403-1
[14] Bolanča, I., Bolanča Z., Lozo B., Influence of digital prints ageing on process recycling of waste paper, REWAS'04, Global symposium on recycling, waste treatment and clean technology, vol. II. (2004)

Authors' contacts:

Ana LEŠIĆ, mag. ing. techn. graph.
Lašćinska 6, 10 000 Zagreb, Croatia
(+385) 99 2544464, lesic.ana1@gmail.com

Dr. Sc. Igor MAJNARIĆ, Asisstant Professor
Faculty of Graphic Arts, University of Zagreb
Getaldićeva 2, Zagreb, Croatia
(+385) 01 237 10 80, majnaric@grf.hr

Dr. Sc. Damir MODRIĆ, Associate Professor
Faculty of Graphic Arts, University of Zagreb
Getaldićeva 2, Zagreb, Croatia
(+385) 01 237 10 80, damir.modric@grf.hr

Mr. Sc. Marko MORIĆ
Intergrafika, Bistranska 19, 10000 Zagreb,
Croatia
(+385) 01 3639 987, marko.moric@akd.hr

Dr. Sc. IVANA BOLANČA MIRKOVIĆ, Associate Professor
Faculty of Graphic Arts, University of Zagreb
Getaldićeva 2, Zagreb, Croatia
(+385) 01 237 10 80, ibolanca@grf.hr

ISSN 1846-6168 (Print), ISSN 1848-5588 (Online)
ID: TG-20171030080153

Original scientific paper

SEEPAGE PROTECTION OF IRRIGATION CANALS USING HORIZONTAL DIRECTIONAL DRILLING

Aleksandr MENEYLYUK, Anatoliy PETROVSKIY, Aleksandr BORISOV, Aleksey NIKIFOROV

Abstract: The paper is dedicated to the development of methods of waterproofing curtains arrangement for seepage protection of irrigation canals. The analysis of the informational sources in the field of seepage protection of irrigation canals has been conducted together with the use of horizontal directional drilling and the bentonite usage. The innovative technology of such works is proposed. The gist of the innovative technology is the combination of horizontal directional drilling and waterproofing bentonite-containing mortar injection. The laboratory experiments of the protective curtain arrangement are conducted. Bentonite powder concentration per unit of volume of hardening mortar, discharge pressure (supply) of injection mortar, and duration of mortar supply are chosen as the most influencing technological factors. Soil filtration coefficient is selected as the most important indicator. It is concluded that the combination of values of low bentonite powder concentration and relatively high discharge pressure allows obtaining lowest soil filtration coefficient values.

Keywords: bentonite; horizontal directional drilling; irrigation canals seepage; soil filtration coefficient; waterproofing curtain

1 INTRODUCTION

Analysis of the problems arising from the underground loss of water in the irrigation canals of the southern regions showed that the scale of the impact and the need for financial and technical resources are playing a dominant role in conservation of water resources intended for the reclamation of arid regions. The arrangement of waterproofing curtains can be used to protect irrigation water from losses during transportation through extended channels. Numerous methods help to build such curtains, but their analyses showed low economic and environmental performance. According to this, the elaboration of innovative seepage protection technology is relevant. The present study has a social significance, as it will allow to provide the population with timely supply of water intended for reclamation.

2 THE AIM AND TASKS OF THE STUDY

The aim of the study is to determine the optimum operating parameters of the waterproofing curtain arrangement for irrigation canals seepage protection by processing and analyzing experimental statistical dependency of soil filtration coefficient from the studied factors. In keeping with this purpose, the following research objectives were formulated:

- Analyze the informational sources in the areas of protection from irrigation water loss, usage of horizontal directional drilling, binders for anti-filtration injection mortar.
- Work out the conception of innovative technology.
- Develop the methodology for laboratory research of anti-filtration underground shields and construct the appropriate laboratory bench.
- Carry out the laboratory research of arrangement of waterproofing curtain by horizontal directional drilling with varying technological parameters of mortar injection.
- Build and analyze the experimental statistical dependencies of curtain filtration coefficient from technological factors by regression analysis of laboratory results with the help of "Compex" software.
- Determine the technological parameters of waterproofing curtain arrangement in which an optimal value of soil filtration coefficient is obtained.

3 ANALYSIS OF INFORMATION SOURCES

Different research shows that methods of water management in different countries can be significantly improved. The developed water management scenarios [1] showed that water, which could be used in the agricultural land expansion, can be saved by 43÷52 % (4.7÷5.7 billion m^3). The findings indicate that average technical, allocative, and overall economic efficiency of irrigation water use in the Northern China are 0.35, 0.86 and 0.80, respectively [2]. According to [3], the loss of water by the seepage from unlined canals in India generally varies from 0.3 to 7.0 m^3/s per 100 m^2 of wetted surface.

Ukraine is also suffering from non-effective water management techniques. There are lengthy irrigation canals in Ukraine (Tab. 1). According to studied sources [4], there are problems with underflooding of agricultural territories due to seepages of irrigation canals. This proves that the problem of reduction of irrigation canals in Ukraine, as well as in the whole world, is an urgent problem.

Scientists of Iran have suggested that the installation of a grout curtain in hydraulic projects can be rational, based on the reviewing many types of waterproofing methods regarding cost, feasibility and safety factors [5]. Measurements showed that irrigation water loss rates, while influenced by soil texture, were even more strongly influenced by the condition and composition of channel

banks [6]. It is concluded [3] that the seepage loss from canals is governed by hydraulic conductivity of the subsoil, canal geometry, and water depth relative to the canal bed. According to that, the method of reducing the water seepage by injection of surrounding soil with bentonite-containing mortar can be effective from the technical point.

Fundamental research suggests several methods for the reduction of seepage losses of irrigation canals. One of them is lining of canal banks [7]. The annual groundwater recharge in the irrigated areas can be reduced by approximately 50 % by concrete lining of irrigation canals banks [8]. Still, researches confirm, that large losses from canals have been identified, even when the canal is lined [9]. It is shown [10] that the seepage flow can go both through canals with impervious lining on their sloping sides and canals in which the impervious lining is located on the bottom of the canal and the sides are unlined. Moreover, lining is an extremely expensive procedure.

Table 1 Irrigation canals of Ukraine [11]

Canals and waterways of Ukraine	Years of erection	Length, km	Height difference of the canal end points, m
Dnepr-Donbas Canal (the 1st stage of construction)	1970-1982	263	68.3
Dnepr-Donbas Canal (the 2nd stage of construction)	1980-1997 (unfinished)	171	68.3
Dnepr-Ingulets Canal	1978-1988	150.5	55.5
Dnepr-Krivoy Rog Canal	1957-1961	41.3	83.8
Inguletsky Canal	1951-1963	53.5	57
Kakhovsky Canal	1980	130	24
North Crimean Canal	1957	400.4	100
Seversky Donets-Donbass Canal (the 1st stage of construction)	1928-1930	131.6	200
Seversky Donets-Donbass Canal (the 2nd stage of construction)	1949-1954	123.3	200

The results of the research, conducted by the Iranian and British scientists, showed that the random reinforcement of soils with fiber can be an effective technique in controlling the seepage velocity and seepage force [12].

The two most known methods for determining losses from irrigation canals (inflow-outflow and ponding test) are quite expensive and time-consuming [13]. Several relatively inexpensive methods can be used for search and location of seepage places of irrigation canals, for example electromagnetic induction system [13], acoustic Doppler current profilers [14, 15].

Thus, it can be suggested, that it is very useful and economically effective to locate the place of the loss and liquidate it. For this, the combination of horizontal directional drilling and injection with waterproofing mortar can be used.

As a result of the analysis of Ukrainian sources on the subject, it can be concluded that the existing methods of the waterproofing curtain arrangement are not effective for the localization of irrigation water loss [16, 17, 18, 19, 20]. In recent years, several attempts were made to develop an efficient technology for similar works [21], but the use of horizontal directional drilling (HDD) technology for groundwater protection shields can be more promising from an economic or technological perspective.

Horizontal directional drilling technology is described in many sources, for example, in [22]. It can be used for laying and rehabilitation of underground communications, wells setting with different configurations in the soil column. The arrangement of such wells will allow to use them as a way of supplying an injectable solution into the desired region of underground space. Such an injection at the appropriate technological modes will make it possible to form waterproofing curtain at the place of water seepage.

The operation, which increases the complexity of work on HDD, is the installation of equipment in a specially constructed pit [23]. Placement of the drilling rig on the earth surface can reduce labor costs and cash cost per arrangement of horizontal directional wells.

During the arrangement of curved shape wells, it is important to ensure the stability and accuracy of the drilling head move in the soil column. To that end, you can use special nozzles, technological modes of drilling [24].

The aforementioned confirms the possibility of the waterproofing curtain arrangement under the irrigation canals by drilling directional wells, pulling the injector into them followed by injecting of a hardening solution.

For effective shielding device it is important to choose a binder having hydrophobic properties. Bentonite can be considered as an effective tool for the waterproofing curtain arrangement [25]. Its use is possible mixed with larger fraction material [26, 27]. Glue properties of bentonite can be used for curtain arrangement, preventing the spread of radioactive substances [28]. Moreover, bentonite due to its low dispersion may be used as binder in the injectable solutions [29, 30].

4 THE CONCEPTION OF INNOVATIVE TECHNOLOGY

Innovative technology will provide a method for underground curtain arrangements under structures. Using this method will not only reduce the complexity and cost of projects, but will also shorten the time of production.

The problem is solved by the method of the construction of a waterproofing curtain. The horizontal, sloping or curved injection wells are created starting from the surface of the earth. The wells are pumped by injected mortar. After setting, this mortar forms a shield.

The scheme of works on the underground curtain arrangement is shown in the figures: Fig. 1 shows a vertical section through the axis of the pilot well when it is created; Fig. 2 - the same, when the injector is drawn into it; Fig. 3 -

the same, when the mortar is injected; Fig. 4 - cross-section of a curtain A-A.

The multi-step drilling process is outlined in Fig. 1 as follows. A number of parallel wells (6) are drilled in the ground (5) under irrigation canal (1) from the ground surface (2) curvilinear to the base of the canal (4). The injector (7) is pulled after completion of drilling the well (6) (Fig. 2). Then, the dilator (10) and the head with a hinge driving force (swivel) (11) are attached to the drill rod (9) instead of the drill bit (8), the swivel (11) is attached to the injector (7). Drilling rig (3) draws the injector (7) in the well (6) according to project trajectory, wherein the swivel (11) rotates with the drill rod (9) not transmitting rotational movement to the injector (7). Injection mortar is fed from the supply line (12) to the injector (7), which is drawn in by the traction device (13) (Fig. 3).

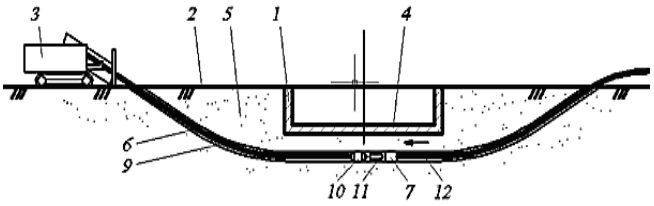

Figure 1 The pilot well drilling

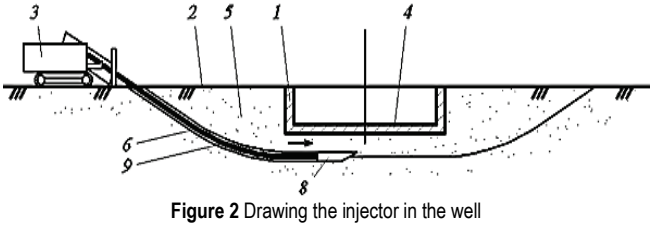

Figure 2 Drawing the injector in the well

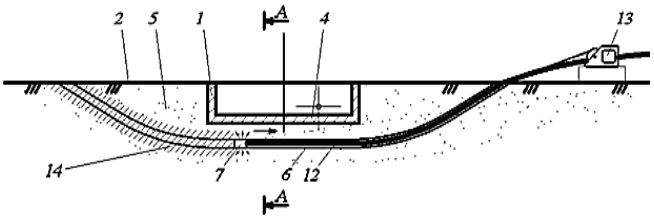

Figure 3 Injection of hardening mortar into the well

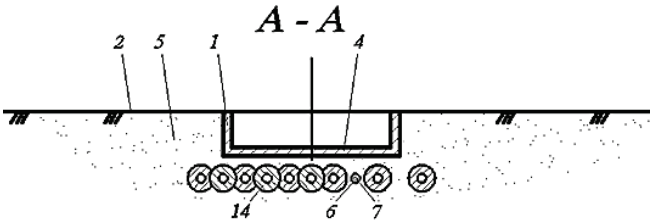

Figure 4 Cross-section A-A of the underground shield

The distance between the wells is assigned depending on the radius of mortar distribution and should not exceed two radii of distribution zone (Fig. 4). Soil injection is produced by hardening compounds, which are selected according to the permeability of rocks based on viscosity and time of mortar setting. After hardening of the mortar the waterproofing curtain (14) is formed in the ground. The curtain is bent over the underground part of the building.

5 OVERALL METHODOLOGY OF THE STUDY

To simulate the injection process described above, the laboratory bench (Fig. 5) has been created. It simulates the section perpendicular to the axis of the well, wherein the injectable solution is distributed at various places away from the injection source.

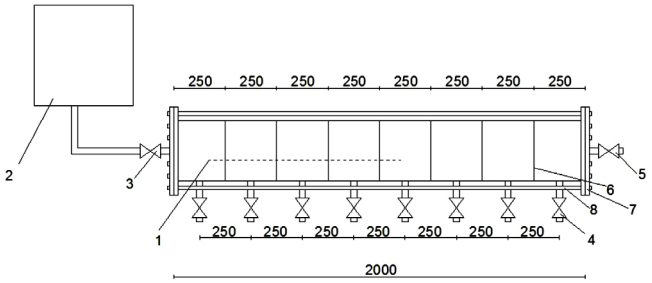

Figure 5 Scheme of laboratory test bench for injections: 1 - the cylindrical tank of the laboratory bench; 2 - the pump with pressure gauge for supplying the solution to the tank; 3 - crane for solution supplying; 4 - taps to indicate the filling tube with solution; 5 - tap for output of the solution; 6 - threaded joint sections; 7 - flanged end cap; 8 - metal ties to seal threaded connections.

Since the main feature of impervious screen is its impermeability to water, it was decided to select a soil filtration coefficient as a key indicator. This indicator represents the filtration rate when the pressure gradient is equal to unity, and is measured in 'm/day' or 'cm/sec'. Determination of filtration coefficient was carried out using the SPETSGEO device [31]. According to the normative documents [32], minimum allowances of filtration coefficient values were established in which the reliability of impervious properties can be considered as sufficient (Tab. 2). It is assumed that the curtain has reliable impervious properties when the value of filtration coefficient is less or equal to 0.3 m/day.

Three factors were chosen as having the greatest impact on the key indicator: X_1, X_2, and X_3.

- X_1 - bentonite powder concentration per unit of volume of hardening mortar, which changes a soil filtration property. This factor is important because the bentonite-containing mortar prevents the penetration of water through injected ground. Considering this, the concentration of the bentonite should be sufficient to form the shield, which has a maximum capacity of impermeability. However, there is a limiting factor - viscosity of the injection mortar, which affects the penetration of material into the gaps between the fine particles of a sandy ground. According to sources considered [33, 34], the permissible viscosity for clay and cement mortars is between 26 and 43 sec. The viscosity was determined by viscometer "Marsh Funnel" with volume of 1000 ml.
- X_2 - discharge pressure (supply) of injection mortar in the base soil. Discharge pressure affects the range of injection mortar spread in soil. This factor is very

important in economic terms, as modern industrial pumps can achieve more than 100 bar pressures, at the same time allowing you to increase the distance between the horizontally drilled wells, which can reduce the cost of the project.

- X_3 - the duration of mortar supply, by which a curtain is formed. Time factor could allow establishing a direct proportional relationship between the injection time and the concentration of active substances which affects the properties of impervious soil shield.

6 METHODOLOGY OF LABORATORY BENCH INJECTION

Test process included the following steps:

1) Preparing the lab bench to the tests.
2) Filling a cylindrical tank of the test bench by sand and preparing for the injection.
3) The injection process with the specified parameters.
4) Technological break.
5) Definitions of the filtration coefficient, fixing the results.

Preparation of the laboratory bench for testing included lubrication of threaded joints, tank installation in vertical position to be filled with sand, as well as preparation of materials, tools and instruments used in the test. Characteristics of sand used to fill the bench are shown in Tab. 3.

Filling of the cylindrical tank of the laboratory bench was carried out in an upright position with layer-wise sand compaction. Sealing was carried out by ramming. Thus, the achieved density was close to the density of sandy soil under natural conditions. After filling the pipe tank was brought to the horizontal position.

Table 2 The division of soils according to the permeability degree

Soil type	Soil filtration coefficient (meter/day)
waterproof	< 0.005
nearly waterproof	0.005…0.30
moderately waterproof	0.30…3
weakly waterproof	3…30
non-waterproof	>30

The following requirements were identified while formulating research problems of selection of injectable solution components:

- components should have waterproof properties or capable of forming a stable waterproof structure;
- environmental safety components of the composition;
- convenience throughout the work (good miscibility, convenience when measured proportions, and so on).

Characteristics of bentonite, used in injection mortar, are shown in Tab. 4.

Preparation of the mortar took place in a separate container immediately prior to injection. Measured amounts of the components were poured into the tank and were stirred by means of a mixer into a homogeneous mortar.

Table 3 Physical properties of sand to be injected during laboratory experiments

#	Name of the characteristic	Value of indicator	
1	Grain composition: total balances on sieve, % 2.5 mm 1.25 mm 0.63 mm 0.315 mm 0.14 mm has passed through a sieve of 0.14 mm	 14.5 % 25.0 % 20.0 % 31.25 % 8.25 % 0.1 %	 14.5 % 39.5 % 59.5 % 90.75 % 9.0 % -
2	The content of grains measuring more than 10.0 mm, must not exceed % by weight	0.5	
3	The content of grains larger than 5.0 mm should not exceed % by weight	5.5	
4	Gradation factor	2.0	
5	Pulverized, clay particles, %	1.0	
6	Bulk density, kg/m^3	1420	
7	Humidity, %	2	
8	Clay in lumps	no	

Table 4 Physical properties of bentonite

#	Name of the property	Unit of measurement	Value
1	The content of montmorillonite (XRD analysis)	%	>80
2	Swelling Index (ASTM D 5890)	ml/gr^2	> 24
3	Water loss (ASTM D 5891)	ml	> 18

During injection, the mortar was periodically stirred in order not to change the solution concentration.

Injection of mortar was happening with the defined technological parameters: a certain pressure and a predetermined time. Crane located opposite the point of the mortar injection remained open throughout the experiment until the moment when the mortar passed through the laboratory bench and did not start to flow through it.

7 METHODS OF DETERMINATION OF SOIL FILTRATION COEFFICIENT BY THE SPETSGEO DEVICE

The sequence of determination of soil filtration coefficient:

1) Fill the tube 1 (Fig. 6) with the tested sandy soil.
2) Fill the tube with the sand producing layers.
3) Fill the measuring cylinder with water, turn it over the tube and set the top cover so that its neck would be placed above the ground surface on approximately 0.5÷1 mm.

As such, the measuring cylinder maintains a constant water level above the sample. As a result of the infiltration of water through the sample, the level goes down, the air bubble breaks in a graduated cylinder and the corresponding amount of water is put out of it. By this the water gradient is achieved, its numerical value is equal to one and the pressure is equal to the length of filtration path.

If after installation large air bubbles break into the cylinder, it indicates that the neck of the cylinder is located too far from the ground surface. In this case, the measuring cylinder has to be pushed a little deeper in order to let only small air bubbles to rise through the water, following one after the other at the same distance.

1) After reaching the specified mode, measure the scale of water level in the cylinder (1), start the stopwatch and fix the second level after a certain time (50÷100 seconds for medium-grained sand, 250÷500 seconds for clay sand).
2) Repeat the test several times, record observations, and calculate the average value of the soil filtration coefficient for them. Determination of soil filtration coefficient was carried out according to the formula of [31],

$$k = \frac{Q}{T \times F'}, \quad \text{cm/s} \tag{1}$$

where: Q - volume of water filtered during the time T, cm^3; T - filtration time, s; F - area of the tube section, cm^2.

SPETSGEO device for determination of the soil filtration coefficient is shown on Fig. 6.

8 METHODOLOGY OF STATISTICAL ANALYSIS OF EXPERIMENTAL DATA

As part of the experimental laboratory research it is most convenient to follow a special plan, or a planning matrix, defined as:

$$N = 2^n, \tag{2}$$

where: N - number of experiments, sufficient to describe the response functions within the studied factor space; n - number of variable factors that determine the process.

In the calculations of this research assessment of the impact factors, it has been decided to obtain the response function of the second degree, where: Y - a function of hail; B_i - regression coefficients; X_i - variable factors.

Table 5 Matrix of varying researched factors

#	Factor's indication	−1	0	+1
1	X_1	10 gr/l	40 gr/l	70 gr/l
2	X_2	2.027 bar	3.040 bar	5.066 bar
3	X_3	10 min	60 min	110 min

For reliable results, it has been decided to take a 15-point symmetrical plan "B3" with repetition of experiments at each point not less than 3 times. Matrix of varying the technological parameters of injection (investigated factors) is shown in Tab. 5. The coding of factors value was made as follows: the medium value of each factor was marked as "0", the minimal as "−1" and the maximal - as "+1".

Despite the fact that for a complete experiment with three factors, which vary on 3 levels, it is required to conduct 27 tests, the optimal experimental planning allows to take only 15 tests. This will still keep the same research accuracy.

Calculation of experimental statistical model was performed taking into account the adopted experimental error. Two-way risk was set at a typical level of 10 % (α = 0.1). After that the testing was conducted to determine the difference of calculated coefficient estimates from zero. The Gauss's criterion was used for this calculation. Coefficient estimates, which were acknowledged as indistinguishable from zero, were consistently excluded from the experimental statistical model. After this model with all significant coefficient estimates was tested for adequacy by the Fisher test. If this criterion was not critical for a given risk value, the model was assumed to be correct for engineering solutions and analysis. Calculation of the coefficients and statistical analysis of experimental statistical model was performed using the dialogue system COMPEX-99, which was developed in the Odessa State Academy of Civil Engineering and Architecture [35].

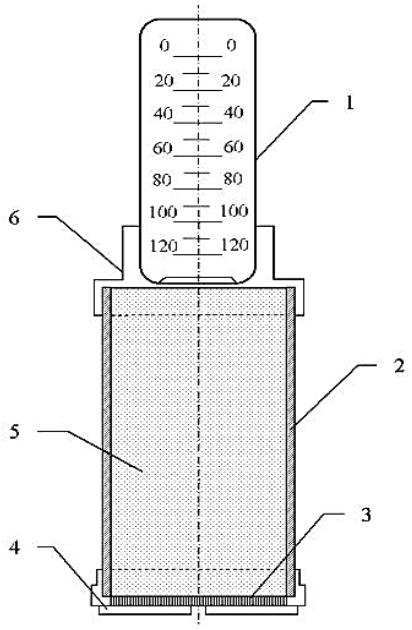

Figure 6 SPETSGEO device for determination of soil filtration coefficient: 1 - the glass measuring cylinder with a scale division 1 cm^3; 2 - the major tube; 3 - bedplate, which is attached on the lower part of the cylinder; 4 - the bottom cover; 5 - the cavity that is filled with soil; 6 - the top cover.

9 METHOD OF SELECTION OF THE INJECTABLE MORTAR COMPOSITION

Selection of an injectable mortar composition determined the most suitable concentration of the solution components. Preparation of the sample solution and determination of the viscosity was conducted in accordance

with the study plan and predetermined binder concentration. When mixing the solution, the sequence of components addition was respected. Mixing occurred as long as the sediment at the bottom of the tank did not disappear.

$$Y_j = B_0 + B_1X_1 + B_{11}X_1^2 + B_{12}X_1X_2 + B_{13}X_1X_3 + \\ + B_2X_2 + B_{22}X_2^2 + B_{23}X_2X_3 + B_3X_3 + B_{33}X_3^2. \quad (3)$$

Determination of the mortar viscosity was performed using Marsh funnel viscometer according to the procedure [36] (see Fig. 7).

The algorithm of composition selection is a sequence of the following actions:

1) Prepare the sample of the solution.
2) Hold funnel vertically plugging the outlet with a finger, pour the solution into the funnel through a sieve (sieve filters out large particles, which may stall the outlet funnel).
3) Quickly remove finger from the outlet, and immediately start the countdown.
4) Enable solution to emerge from the Marsh funnel into a graduated container.
5) Record the time in seconds that it took for the solution to leave the funnel.

Figure 7 Viscometer "Marsh Funnel"

Table 6 The plan and the results of experimental laboratory studies

№	Actual value of factors			Coded value of factors			Soil filtration coefficient (SFC), meter per day
	X_1	X_2	X_3	X_1	X_2	X_3	
	Bentonite powder concentration, grams per liter	Discharge pressure of mortar, bar	Duration of mortar supply, min	Bentonite powder concentration	Discharge pressure of mortar	Duration of mortar supply	
1	2	3.040	4	5	6	7	8
1	70	5.066	110	1	1	1	0.37114
2	70	5.066	10	1	1	−1	0.26929
3	70	2.027	110	1	−1	1	0.21114
4	10	5.066	110	−1	1	1	0.07526
5	70	2.027	10	1	−1	−1	0.40124
6	10	5.066	10	−1	1	−1	0.08985
7	10	2.027	110	−1	−1	1	0.80065
8	10	2.027	10	−1	−1	−1	0.36041
9	70	3.040	60	1	−0.33	0	0.34387
10	10	3.040	60	−1	−0.33	0	0.29899
11	40	5.066	60	0	1	0	0.15554
12	40	2.027	60	0	−1	0	0.08977
13	40	3.040	110	0	−0.33	1	0.14669
14	40	3.040	10	0	−0.33	−1	0.17049
15	40	3.040	60	0	−0.33	0	0.04775

10 THE RESULTS OF EXPERIMENTAL STUDIES

Tab. 6 presents the experimental data. The columns 2 and 5, 3 and 6, 4 and 7 show actual and coded values of studied value respectively. The value of soil filtration coefficient, shown in the table, can be obtained at the distance of 2 meters or less from the source of the mortar. The dependency of soil filtration coefficient on technological factors (bentonite powder concentration, discharge pressure and duration of mortar supply) is shown in the equation 1. Points in this formula mark the factor impact estimations, deemed indistinguishable from zero.

Fig. 8 shows the ranking of the degree of variable factors influence on the indicator.

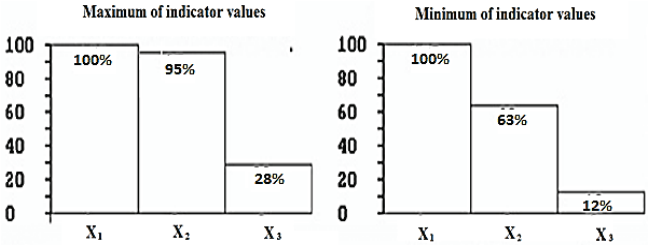

Figure 8 Ranking the impact of variable factors on the indicator (soil filtration coefficient)

The greatest influence on the filtration coefficient in the area of maximum indicator values has two factors in approximately the same degree: the concentration of

bentonite powder and discharge pressure of mortar. At the same time, the duration of mortar supply does not play such a significant role in the change of the indicator. In the area of minimum indicator values, where the dependencies are the most significant from the perspective of results implementation, the degree of influence of the discharge pressure decreased slightly. The degree of the time factor influence in the considered factor space has decreased to the limits that are not significant from an engineering point of view.

$$SFC\ (\text{m/day}) = 0.105 \bullet + 0.212 X_{12} + 0.123 X_1 X_2 - \\ - 0.064 X_1 X_3 - 0.087 X_2 + \bullet + \bullet + \bullet + \bullet \quad (4)$$

These rankings can be interpreted as follows:

- Bentonite concentration in the mortar plays the most important role for the following reasons: the conditions of the experiments carried out have enabled the most complete way to explore this relationship in the selected factor space, which is confirmed by the nature of the graph shown in Fig. 9; composition of the mortar does play a major role in the arrangement of protective shields.
- From a physical point of view, the degree of influence of pressure on impervious properties is quite high, as the supply pressure of the mortar directly affects the amount of bentonite injected into the soil.
- Duration of mortar supply factor is not significant from an engineering point of view on the change of the monitoring indicator within the selected experimental conditions.

Fig. 9 shows graphs of the indicator from each of variable factors.

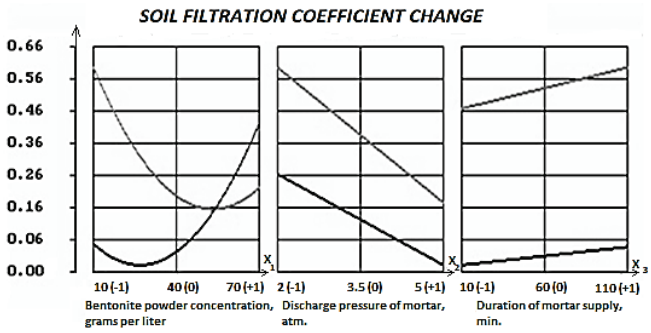

Figure 9 Indicator of dependence on the factors (dark lines and curves show dependence on each of the studied factors in the area of minimum indicator value, light lines – in the area of maximum value).

The nature of the graph of the soil filtration coefficient from bentonite concentration can be interpreted as similar to parabolic. In this case, the extreme point of this curve is vividly shown and is within X_1 = (−0.4, −0.5) in the minimum indicator area, whereas it is within X_1 = (0.6, 0.7) in the maximum zone. It can be said that for the conditions studied in the experiments, it was possible to identify the optimal conditions for bentonite powder concentration. When translating into full-scale parameters, the most effective mortar in the minima zone would contain the amount of bentonite within 22÷25 grams per liter, in the area of the maxima – 58÷61 g/l.

The dependence of soil filtration coefficient from the discharge pressure of mortar is inversely proportional. The angle of the line to the horizontal is sufficiently sharp, therefore we can assume that the data points belong to the parabolic nature of the curve with a peak, not included in considered factor space. In this case, used pressure values are not the highest possible from a technical point of view and may be adjusted upward during the further study.

The effect of duration of mortar supply on the indicator value is directly proportional. Limits of soil filtration coefficient changes are quite small for time variation, so you can conclude that the dependency, which follows from the obtained data, is not enough meaningful from an engineering point of view. However, under natural conditions, long duration of injection will undoubtedly affect the soil filtration coefficient of the waterproofing curtain to the reduction. The reason for this discrepancy may be due to imperfect experimental conditions.

Nature of the dependence obtained in the zone of high and low values of indicator are close. It should be noted that dependences obtained in the zone of the low values of indicator must be taken as highly significant. This is due to the ultimate goal of the experiments which is to determine the conditions under which the soil filtration coefficient of the waterproofing curtain will meet the specified conditions for water-proof resistance.

Fig. 10 shows the descending ranking values of soil filtration coefficient obtained during laboratory tests. By this ranking, the conditions, which are the most suitable for low values of indicator, can be analyzed.

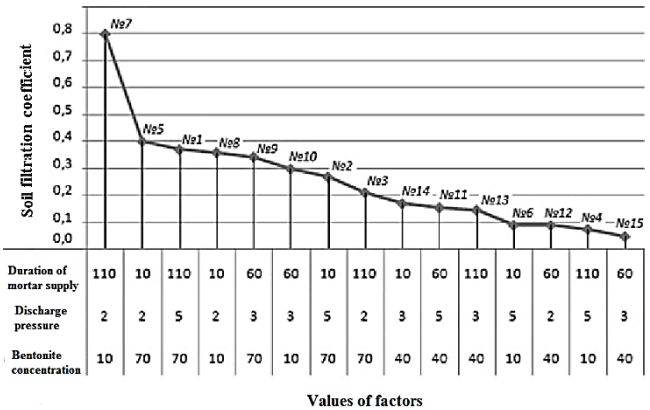

Figure 10 Graph of soil filtration coefficient values (ranked in descending order)

Five experiments were conducted, in which a mortar containing 40 grams of bentonite per liter was used. The majority of the experiments were carried out at the operating discharge pressure of X_2 = 2.027÷3.040 bar. These experiments showed the lowest filtration value. Also, low values of filtration coefficient are determined in the experiments, in which the combination of low concentrations of bentonite (or the low viscosity of mortar) and relatively high discharge pressure were used. The

experiments, in which a high viscosity and low discharge pressure of mortar were used, showed slightly higher values of soil filtration coefficient. Finally, the least favorable were the combination of high contents of bentonite in mortar and high discharge pressure; small saturation of bentonite powder and a low pressure of mortar. Inconsistencies of experiments ranking can be attributed to the account of the corrective impact of duration of mortar supply.

Fig. 11 shows the effect of the bentonite powder concentration and discharge pressure on the filtration rate of the waterproofing curtain while the duration of mortar supply is fixed on the level X_3 = 10 min. This level was selected to avoid errors in the calculation of the dependency.

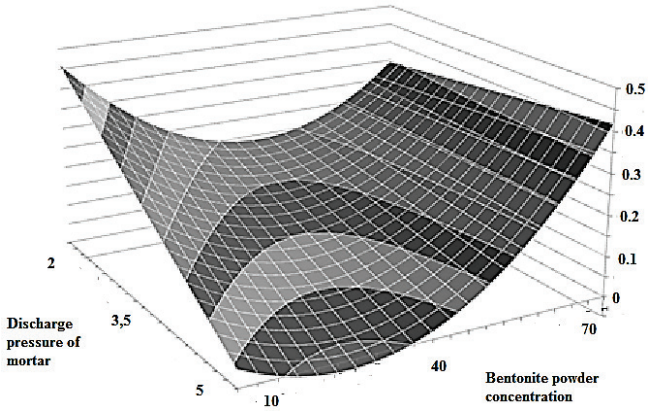

Figure 11 Change of the soil filtration coefficient of the waterproofing curtain under the influence of the bentonite powder concentration and discharge pressure when fixing the duration of mortar supply at X_3 = 10 min

Analysis of the graph shows that the dependence of the indicator on the concentration of bentonite is close to a parabolic arch. The effect of the discharge pressure of mortar supply is inversely proportional: minimum zone of soil filtration coefficient is formed at the highest pressures. Thus, in the case of short-term injection, the maximum pressure should be followed with the optimal concentration of bentonite in mortar at about 22÷25 grams per liter, with the least 43÷46 grams per liter, and less viscous mortar is more effective. The soil filtration coefficient is equal to 0.023 meters per day and 0.194 meters per day respectively to the parameters indicated. Thus it can be concluded that the value of discharge pressure effects the level of bentonite concentration in terms of lowest soil filtration coefficient values obtained.

11 CONCLUSIONS

1) The analysis of information sources showed high actuality of search for method of underground waterproofing curtain arrangement for irrigation canals seepage protection, low economic and technical efficiency of existing methods. Use of horizontal directional drilling and mortar, prepared with the use of bentonite, could be effective for such work.
2) The developed technique and research equipment allows determining the filtration coefficient of sand injected under different technology parameters.
3) The results of experimental studies allowed creating graphs and polynomial equations that define patterns of the impact of technological regimes and composition of an injectable solution on impervious properties of the shield.
4) Bentonite concentration in the injection mortar and the discharge pressure of mortar have the biggest impact on the index. Duration of mortar supply does not noticeably affect the indicator for the chosen experimental conditions.
5) The combination of values of low bentonite powder concentration (or the low viscosity of mortar) and relatively high discharge pressure allows to obtain lowest soil filtration coefficient values.
6) The optimum soil filtration coefficient value is equal to 0.023 meters per day, and is achieved at a bentonite powder concentration equal to 22-25 grams per liter and the discharge pressure of mortar – to 5.066 bar. It will allow building a reliable underground curtain with the distance between wells at 2 meters.

11 REFERENCES

[1] H. Mostafa and N. Fujimoto, Water saving scenarios for effective irrigation management in Egyptian rice cultivation, Ecological Engineering, pp. 11-15, 2014.
[2] J. Tang, H. Folmer and J. Xue, Technical and allocative efficiency of irrigation water use in the Guanzhong Plain, China, Food Policy, pp. 43-52, 2015.
[3] Bureau of Indian Standards, Measurement of Seepage Losses from Canals, IS:9452 (Part I & II), 1980, New Delhi: (Bureau).
[4] V. Kovalchuk, System management of irrigated areas water regime for protection against flooding, Kiev: Ukrainian Institute of Water Problems and Land Reclamation, 2016.
[5] A. Uromeihy and G. Barzegari, Evaluation and treatment of seepage problems at Chapar-Abad Dam, Iran, Engineering Geology, pp. 219-228, 2007.
[6] M. Kahlown and W. Kemper, Seepage losses as affected by condition and composition of channel banks, Agricultural Water Management, pp. 145-153, 2004.
[7] P. G. Nicholson, Soil Improvement and Ground Modification Methods, Hawaii: Butterworth-Heinemann, 2015.
[8] K. Meijer, E. Boelee, D. Augustijn and I. van der Molen, Impacts of concrete lining of irrigation canals on availability of water for domestic use in southern Sri Lanka, Agricultural Water Management, pp. 243-251, 2006.
[9] E. Wachyan and K. Rushton, Water losses from irrigation canals, Journal of Hydrology, pp. 275-288, 1987.
[10] A. Mirnateghi and J. Bruch Jr., Seepage from canals having variable shape and partial lining, Journal of Hydrology, pp. 239-265, 1983.
[11] Canals of Ukraine, 11 December 2016. Available: http://www.photoukraine.com/russian/articles?id=26.
[12] A. Estabragh, A. Soltani and A. Javadi, Models for predicting the seepage velocity and seepage force in a fiber reinforced silty soil, Computers and Geotechnics, pp. 174-181, 2016.

[13] D. Pognant, D. Canone and M. Previa, Using EM Equipment to Verify the Presence of Seepage Losses in Irrigation Canals, Procedia Environmental Sciences, pp. 836-845, 2013.
[14] K.-D. Kinzli, M. Martinez, R. Oad, A. Prior and D. Gensler, Using an ADCP to determine canal seepage loss in an irrigation district, Agricultural Water Management, pp. 801-810, 2010.
[15] C. A. Martin and T. K. Gates, Uncertainty of canal seepage losses estimated using flowing water balance with acoustic Doppler devices, Journal of Hydrology, pp. 746-761, 2014.
[16] A. Adamovich, Grouting and grout curtain in the hydropower construction (Zakreplenie gruntov i protivofil'tracionnye zavesy v gidrojenergeticheskom stroitel'stve), Moskow: Jenergiya, 1980.
[17] A. G. Alimov, Antifiltration protection of canals and reservoirs (Protivofil'tracionnaja zashhita kanalov i vodoemov), Gidrotehnicheskoe stroitel'stvo, pp. 36-42, 2008.
[18] J. M. Ammosova, Soil protection against chemical pollution (Ohrana pochv ot himicheskih zagrjaznenij), Moskow: MGU, 1989.
[19] V. F. Val'kov, K. S. Kazeev and S. I. Kolesnikov, Soil Ecology: a textbook for university students (Jekologija pochv : uchebnoe posobie dlja studentov vuzov), Rostov-na-Donu: UPL RGU, 2004.
[20] V. Zadgenidze, Protecting areas from flooding (Zashhita territorij ot podtoplenija. Praktikum: metod. posob.), Odessa: OGASA, 2005.
[21] A. Chernuhin and A. Galinskij, Application of the method "a diaphragm underground wall" for the localization of radioactive waste disposal points (Primenenie sposoba "stena v grunte" dlja lokalizacii punktov zahoronenija radioaktivnyh othodov, Stroitel'noe Proizvodstvo, pp. 7-10, 1997.
[22] E. Skonberg, C. E. Tammi, A. M. Desilets, V. Srivastava and J. M. Evans, Horizontal Directional Drilling Best Management Practices Manual, New York: GRI, 2002.
[23] T. Zayed and M. Mahmoud, Data acquisition and factors impacting productivity of Horizontal Directional Drilling (HDD), Tunnelling and Underground Space Technology, pp. 63-72, 2013.
[24] F. Hungerford and T. Ren, Directional drilling in unstable environments, International Journal of Mining Science and Technology, pp. 397-402, 2014.
[25] C. Imbert and M. V. Villar, Hydro-mechanical response of a bentonite pellets/powder mixture upon infiltration, Applied Clay Science, pp. 197-209, 2006.
[26] M. Villar, Infiltration tests on a granite/bentonite mixture: Influence of water salinity, Applied Clay Science, pp. 96-109, 2006.
[27] L. Xu, W. Ye, B. Chen, Y. Chen and Y. Cui, Experimental investigations on thermo-hydro-mechanical properties of compacted GMZ01 bentonite-sand mixture using as buffer materials, Engineering Geology, pp. 46-54, 2016.
[28] J. Vaunat and A. Gens, Analysis of the hydration of a bentonite seal in a deep radioactive waste repository, Engineering Geology, pp. 317-328, 2005.
[29] M. Holmboe, S. Wold and T. Petterson, Effects of the injection grout Silica sol on bentonite, Physics and Chemistry of the Earth, pp. 1580-1589, 2011.
[30] L. P. Chegbeleh, S. M. Yidana, M. Nishigaki and F. Achampong, Comparative study on the application of ethanol–bentonite slurry and salt–bentonite slurry as effective injection materials for barrier sealing, Applied Clay Science, pp. 40-45, 2014.
[31] Soils. Laboratory methods for determining the filtration coefficient (State Standard of the USSR - Grunty. Metody laboratornogo opredelenija kojefficienta fil'tracii - GOST 25584-90), 1990. Available: http://www.gosthelp.ru/text/GOST2558490GruntyMetodyla.html.
[32] Soils. Classification (Grunti. Klasifikacija - State Standard of Ukraine - DSTU B V.2.1-2-96 (GOST 25100-95)), 1996. Available: http://normativ.com.ua/types/tdoc353.php.
[33] A. Chapovskij, Laboratory work on soil science and soil mechanics (Laboratornye raboty po gruntovedeniju i mehanike gruntov), Moskow: Nedra, 1975.
[34] A. Churakov, Production of special works in hydraulic engineering (Proizvodstvo special'nyh rabot v gidrotehnicheskom stroitel'stve), Moskow: Stroyizdat, 1976.
[35] V. Voznesenskij, T. Ljashenko and B. Ogarkov , Numerical methods for solving construction and technological problems on a computer (Chislennye metody reshenija stroitel'no-tehnologicheskih zadach na JeVM), Kiev: Vyshha shkola, 1989.
[36] Soils. Laboratory tests. General provisions (State Standard of Ukraine - Grunti. Laboratorni viprobuvannja. Zagal'ni polozhennja - DSTU B V.2.1-3-96 (GOST 30416-96)), 1996. Available: http://online.budstandart.com/ua/catalog/ doc-page?id_doc=4079.

Authors' contacts:

Aleksandr MENEYLYUK
Doctor in technical sciences, Full professor, Head of Department of Technology of building industry, Odesa State Academy of Civil Engineering and Architecture, ORCID ID: 0000-0002-1007-309X,
E-mail: pr.mai@mail.ru

Anatoliy PETROVSKIY
PhD (technical sciences), professor, doctoral student, Odesa State Academy of Civil Engineering and Architecture,
E-mail: san-one@te.net.ua

Aleksandr BORISOV
PhD (technical sciences), Associate Professor, Odesa State Academy of Civil Engineering and Architecture,
E-mail: komar9@mail.ru

Aleksey NIKIFOROV (corresponding author)
Master (technical sciences), postgraduate student, Odesa State Academy of Civil Engineering and Architecture, ORCID ID: 0000-0001-7002-7055, tel. (fax) +38(066)-33-09-054, Postal address: 2 (ap. 1), Kartamyshevsky Ln, Odessa, Ukraine, 65091
E-mail: aleksey-nikiforov@mail.ua

ISSN 1846-6168 (Print), ISSN 1848-5588 (Online)
ID: TG-20171123183818

Preliminary communication

THE INFLUENCE OF CONSTRUCTION AND PROCESS DESIGN ON IMBIBITIONAL PROPERTIES OF "WATERPROOFING − LIMESTONE SHELL" SYSTEM

Nina DMITRIEVA, Oleg POPOV, Anna HOSTRYK

Abstract: Absorption capacity and water absorption as the main factors determining the strength and adhesion of waterproofing with stone have not been sufficiently studied. The need to establish this characteristic of the stone is due to the difference in the behavior of its porous system in the dry state and after absorbing moisture from the volume of water and the solution. The article presents a solution to the problem of increasing the effectiveness of waterproofing plastering systems by selecting the optimal technological factors: the type of material, the number of layers and the time of full water saturation.

Keywords: imbibitional properties; limestone shell system; mastic waterproofing; plastering waterproofing

1 INTRODUCTION

In the modern world, most people prefer to live in houses with good ecological characteristics. This promotes the use of natural building materials, with excellent environmental qualities. One of such material is limestone-shell.

Since several thousand years, buildings and structures have been constructed from this material [1]. Today, many of them are monuments of architecture. In the last century, the issue of preserving monuments of cultural heritage, including Odessa, was sharply raised. In the official list of monuments of town-planning and architecture of Odessa, 700 buildings and structures were added. Only 31 % of them are in good technical condition and do not require major repairs and restoration. The remaining 69 % of monuments of cultural heritage require, to different extents, major repairs, restoration or replacement of structures and building elements.

Based on the results of the processing of technical and design documentation from the archival data of the housing and communal services and design organizations, buildings and structures that are made of bond shell - limestone or have constructional structural parts from this building material, make up 26 %.

The reasons for damaging the waterproofing course are most often the following: non-compliance with the technology of the waterproofing device; low quality of the material; change in groundwater table; incorrectly chosen type of waterproofing; low adhesion bond strength; works on the base with excessively high humidity; violation of the dosage of waterproofing components; deformation caused by the displacement of the individual building elements relative to each other, etc. Moreover, the practice of building management shows that the destruction of open joints, and consequently the disruption of the continuity of waterproofing, is one of the main reasons for premature deterioration of structures, increased costs for repair, and restoration work and deterioration of the operational characteristics of the building. The damages of the waterproofing system are the most common cause of failure of subsurface structures [2].

Thus, one of the topical problems of the building complex is the problem of destruction of shell - limestone structures due to the absence or damage of waterproofing.

One of the factors affecting the durability of the structure, shell-limestone in particular, is the effect of moisture; namely, alternate moistening and drying of the material, regardless of the temperature regime. This is especially true for materials with a capillary - porous structure. Evaporation of moisture from the structure occurs by drying, first from large, and then from smaller pores of capillaries.

It is assumed that for some period in completely air-dried conditions, the evaporation of free capillary and absorbed-bound water from the body of the structure is possible. At the same time, the wedging forces play out on the structure, and as a result, considerable shrinkage stress appears in the material.

With increasing relative humidity of the surrounding air, the material is again moistened, the cracks are unfolded. The rate of destruction of stone structures under the influence of stress, shrinkage and bulging depends on the intensity of moistening and drying [1].

Figure 1 Mayakovsky Street 5

One can give enough examples of such buildings in the historic center of Odessa; several of them are shown in Fig. 1÷3.

Figure 2 Pushkinskaya Street 20

Figure 3 Kanatnaya Street 39

The study of the influence of constructive technological solutions of the system "waterproofing limestone-shell" will increase the protection from the effects of capillary rise and water absorption, providing reliable and durable operation of buildings and structures from shell limestone.

The following authors studied the absorption characteristics of shell-limestone: Komyshev A. V., Eremenok P. L., Izmailov Yu. V., Figarov A. G., Orujev F. M., Tursunov N. T., Shcherbina S. N. Scientific works of scientists such as Shilina A. A., Lukinsky O. A., Khomenko V. P., Leonovich S. N. were scientific and theoretical basis of waterproofing research conducted by Karapuzov E. K, Soha V. G., et al. However, the absorption characteristics of the "waterproofing - limestone-shell" system of the limestone-shell of the Odessa deposit have been little researched.

To a great extent, the main factor determining the formation of the strength of the mortar durability and the strength of adhesion in the bond is the suction capacity, determining the ability of the stone to absorb moisture out of the green mortar. The necessity in establishing this characteristic of the stone is due to the difference in the behavior of its pore system upon the absorption of moisture from the volume of water and from the mortar [7].

According to the results of the analysis given in [8], one of the rational methods of the waterproofing system is plaster waterproofing with the use of dry mixtures and cold mastics.

The pre-selected samples were weighed to determine the weight and volume in the dry state before the application of the waterproofing mixture itself, and marked with the number of the series and the direction of bedding of the stone structure.

Waterproofing mixture of dry powders was prepared by gradually adding them to the water under constant agitation until it turned into a viscous mass, which was applied with a spatula. The material was applied according to the experimental design in one, two and three layers on a dry and wet surface of the sample. To prevent coating during application, the direction of each subsequent layer was perpendicular to the previous layer. The thickness of the layers did not exceed 1÷2 mm to prevent the formation of cracks. Mastic was applied by brush. Each subsequent layer was applied only after the previous one had dried completely.

The process of applying plaster and mastic waterproofing are shown in Figs. 4÷5

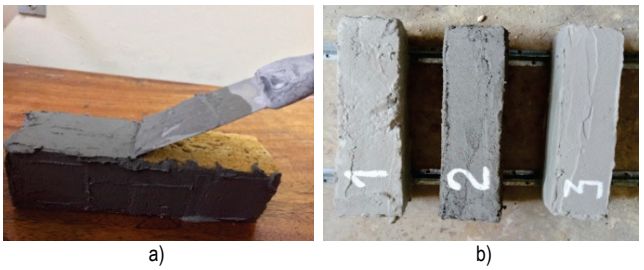

a) b)

Figure 4 Application of waterproofing on the basis of dry mixes

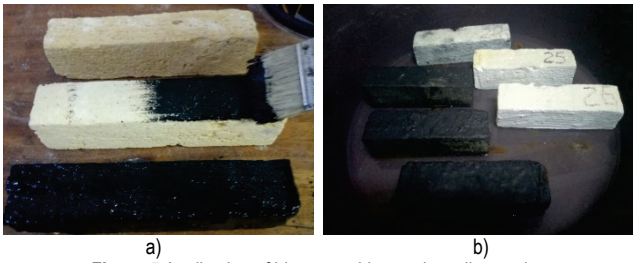

a) b)

Figure 5 Application of bitumen-rubber and acrylic mastics

The essence of the investigation was the determination of the impact of structural and technological solutions on the absorption properties of the system "waterproofing - limestone-shell".

2 RESULTS OF EXPERIMENTS

The investigation of the intensity of the suction capacity was determined by the amount of water in grams absorbed in 1, 2, 3 minutes by one dm^2 of the air-dry stone surface and treated with a certain kind of waterproofing (according to the experiment's plan) immersed in water at a depth of 5 mm, 10 mm and 15 mm.

The graph of Figs. 6÷10 is constructed according to the results of the investigation of the water absorption of limestone-shell not treated with waterproofing composition.

Based on the results of the studies, graphs of the dependence of the water absorption coefficient of the "waterproofing - limestone-shell" system on variability factors are constructed, Figs. 11÷19.

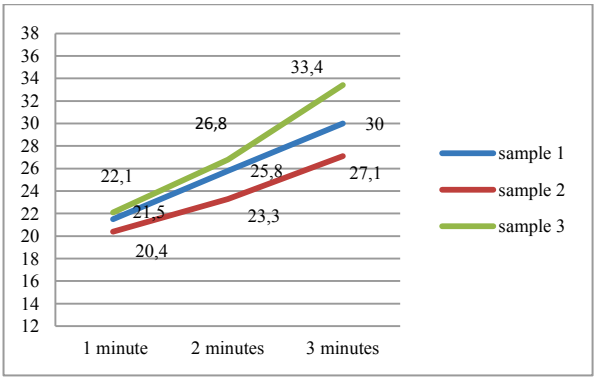

Figure 6 Determination of the water absorption coefficient of limestone-shell rock, "Gidrozit".

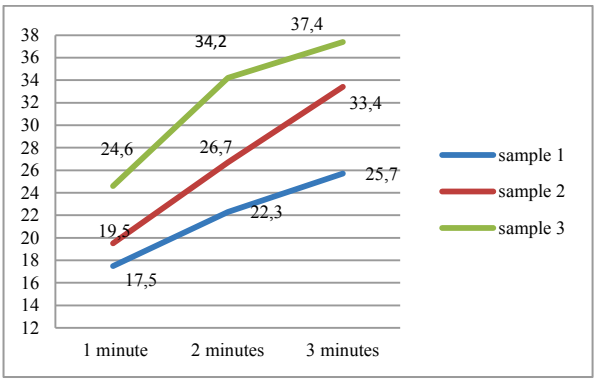

Figure 7 Determination of the water absorption coefficient of limestone-shell rock, "Siltek V-30".

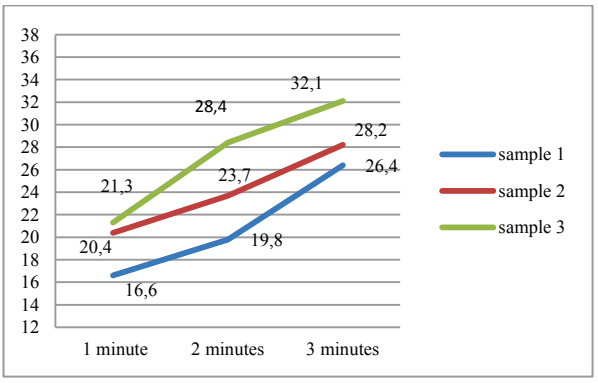

Figure 8 Determination of the water absorption coefficient of limestone-shell rock, "Ceresit CR 65".

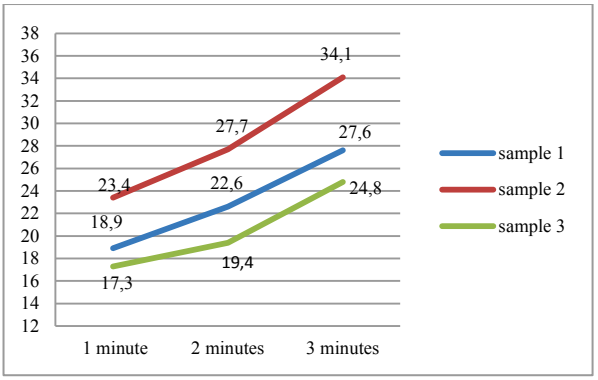

Figure 9 Determination of the water absorption coefficient of limestone-shell rock, mastic "AQUASTOP".

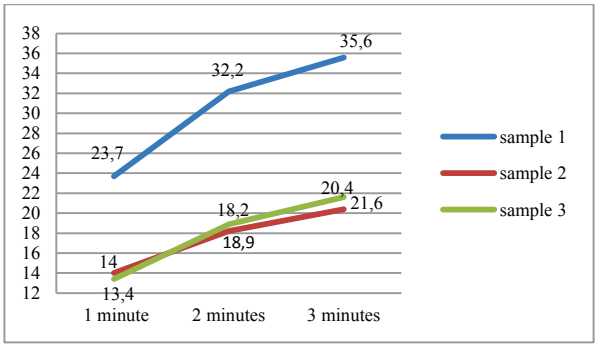

Figure 10 Determination of the water absorption coefficient of limestone-shell rock, Bitumen-rubber mastic.

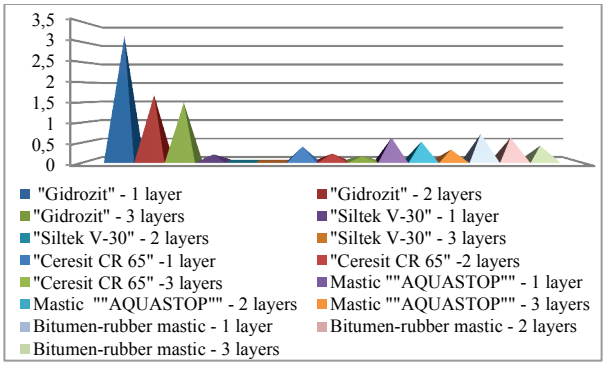

Figure 11 Values of water absorption of the "waterproofing-limestone-shell" system immersed in water by 5 mm, 1 minute.

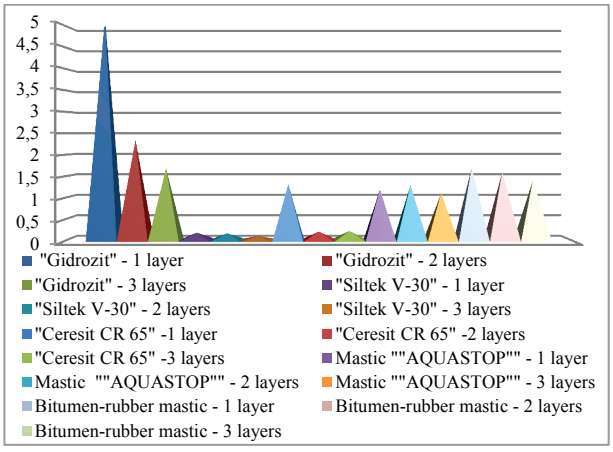

Figure 12 Values of water absorption of the "waterproofing-limestone-shell" system immersed in water by 5 mm, 2 minutes.

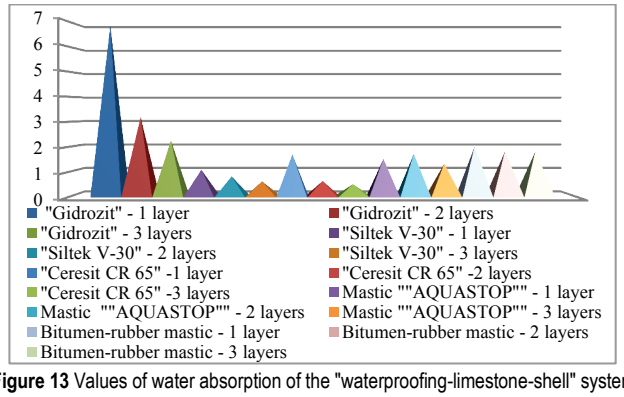

Figure 13 Values of water absorption of the "waterproofing-limestone-shell" system immersed in water by 5 mm, 3 minutes.

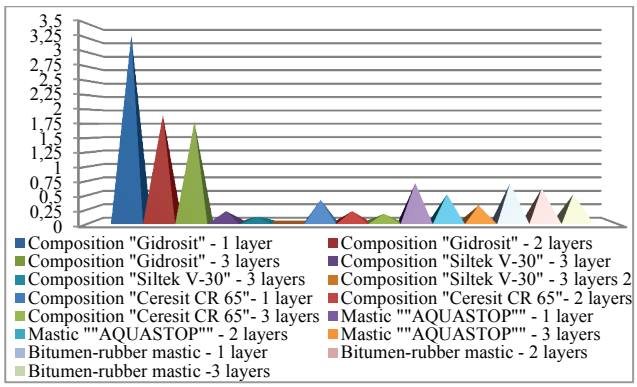

Figure 14 Values of water absorption of the "waterproofing-limestone-shell" system immersed in water by 10 mm, 1 minute.

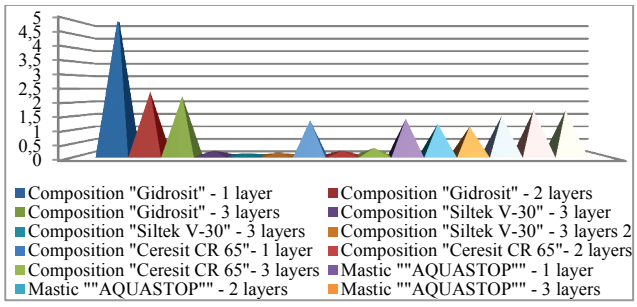

Figure 15 Values of water absorption of the "waterproofing-limestone-shell" system immersed in water by 10 mm, 2 minutes.

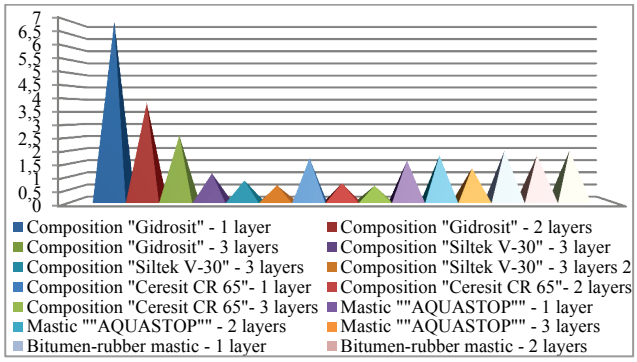

Figure 16 Values of water absorption of the "waterproofing-limestone-shell" system immersed in water by 10 mm, 3 minutes.

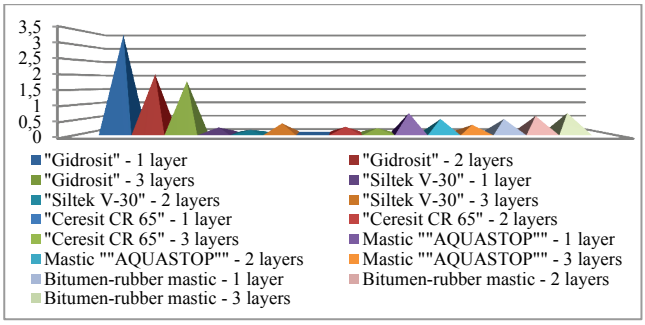

Figure 17 Values of water absorption of the "waterproofing-limestone-shell" system immersed in water by 15 mm, 1 minute.

The water absorption increases with increasing time from 1 to 3 minutes. At the same time, the water absorption depends on the type of material and the number of layers of their application.

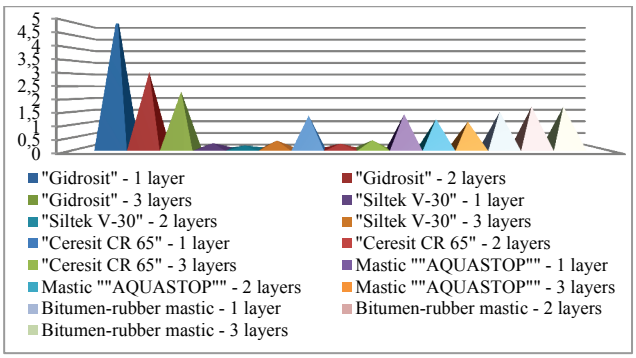

Figure 18 Values of water absorption of the "waterproofing-limestone-shell" system immersed in water by 15 mm, 2 minutes.

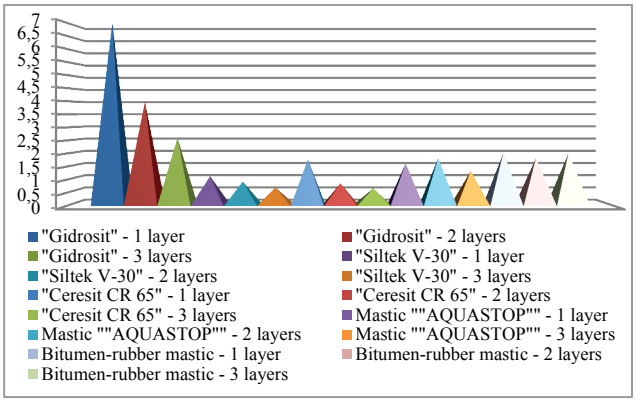

Figure 19 Values of water absorption of the "waterproofing-limestone-shell" system immersed in water by 15 mm, 3 minutes.

The directionality of the stone layers relative to the surface and its composition impact on the value of the suction capacity of the stone. The suction of moisture from the solution along the layers of rock is more intense than in the direction perpendicular to the bedding. The maximum value of the suction capacity for the stone of a given deposit is affected by the type of material that showed the minimum water retention capacity. These are samples processed by the composition "Hydrozit". For example, when immersed at a depth of 5 mm, treated in one layer with this composition, the samples showed water absorption: after 1 minute - 3.19 g; after 2 minutes - 5.25 g; after 3 minutes - 6.94 g. An increase in the immersion depth of the samples shows that the water absorption rate of samples treated with a layer increases by 0.16 g, by immersion at 10 mm and by 0.2 g -by immersion at 15 mm.

Varying the depth of immersion did not affect the water absorption rates of specimens treated with AQUASTOP mastic.

According to the comparative analysis, the initial intensity of water absorption of limestone-shell rock decreases with the installation of waterproofing systems, depending on the type of material and the number of layers.

This indicates a decrease in the intensity of water absorption compared to the initial intensity of limestone and waterproofing systems (3 layers of application), which is: Hydrosite - 4.96 times; Siltek V-30 - 63.4 times, Ceresit CR 65÷68.3 times; Mastics: "AQUASTOP" - 19 times; Bitumen-rubber mastic (BRM) - 12 times.

When comparing the parameters of the processed samples with one layer and three layers, it was found that the decrease in water absorption after 3 minutes is: Hydrozit ÷3.08 times; Siltek V-30 - 1.8 times, Ceresit CR 65 - 3.6 times; Mastics: "AQUASTOP" -in 1.15 times; Bitumen-rubber mastic (BRM) - in 1.1 times.

At the initial intensity, the structure of limestone-shell rock also has an impact. In most cases, the pores of limestones are of various shapes - micro-and macro capillaries of variable cross-section. The larger the diameter of the bulk of the capillary pores of the stone, the higher the value of its initial water absorption intensity. Results of the tests of the intensity of capillary suction capacity of the rock are constructed in Figs. 20÷28.

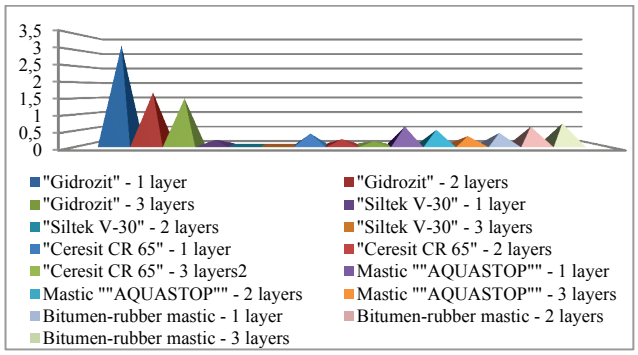

Figure 20 Intensity of capillary suction capacity of the rock submerged in water at 5 mm, 1 minute.

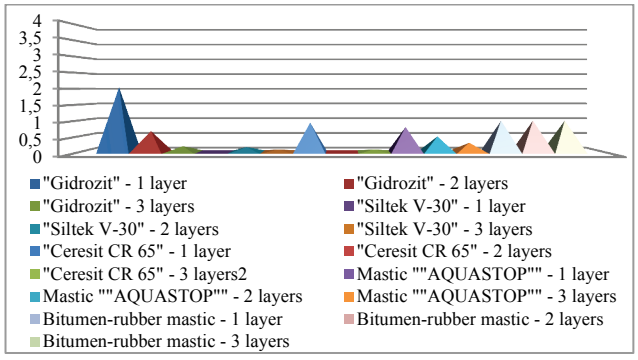

Figure 21 Intensity of capillary suction capacity of the rock submerged in water at 5 mm, 2 minutes.

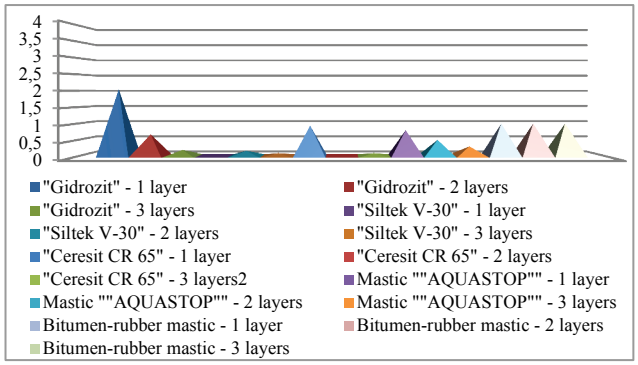

Figure 21 Intensity of capillary suction capacity of the rock submerged in water at 5 mm, 3 minutes.

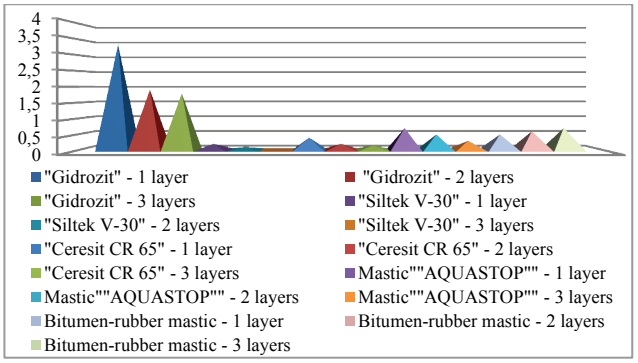

Figure 23 Intensity of capillary suction capacity of the rock submerged in water at 10 mm, 1 minute.

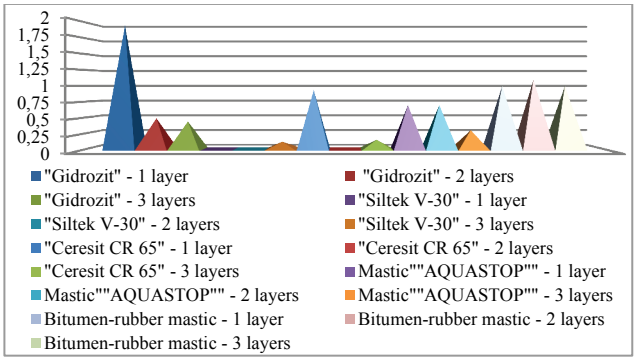

Figure 24 Intensity of capillary suction capacity of the rock submerged in water at 10 mm, 2 minutes.

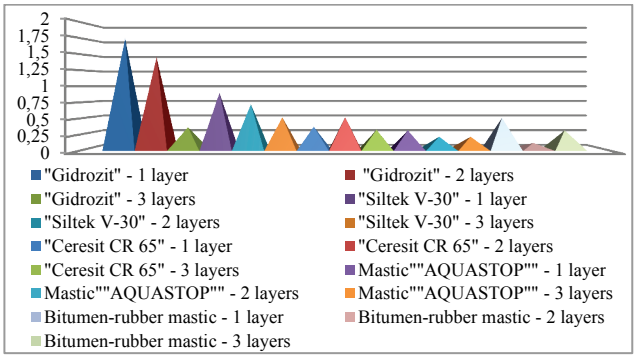

Figure 25 Intensity of capillary suction capacity of the rock submerged in water at 10 mm, 3 minutes.

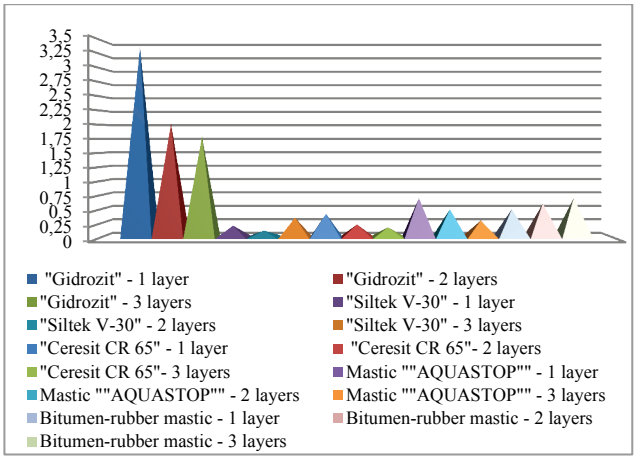

Figure 26 Intensity of capillary suction capacity of the rock submerged in water at 15 mm, 1 minute.

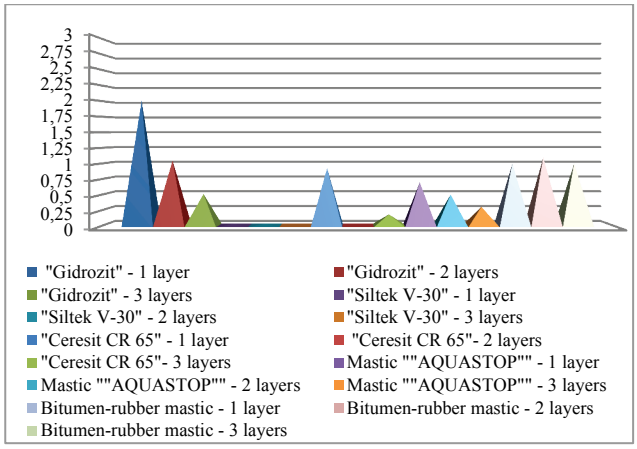

Figure 27 Intensity of capillary suction capacity of the rock submerged in water at 15 mm, 2 minutes.

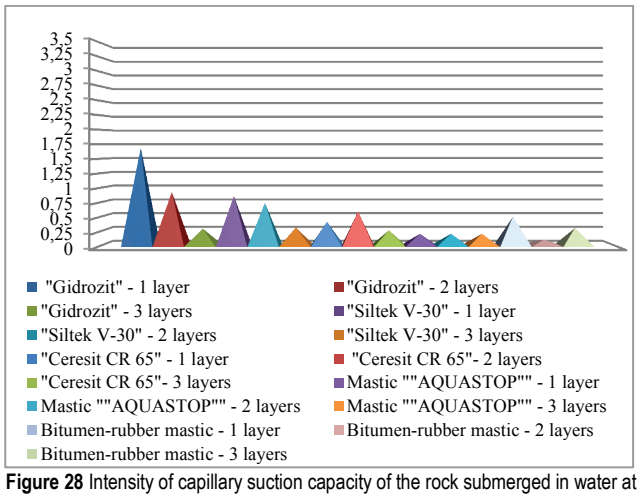

Figure 28 Intensity of capillary suction capacity of the rock submerged in water at 15 mm, 3 minutes.

The minimum value of water absorption (0.47 g) was shown by a series of samples No. 9 treated with Ceresit CR 65 in 3 layers after 3 minutes. At the same time, samples of the No. 6 series, treated with Siltek V-30 in 3 layers, showed a minimum of this value during the first 2 minutes (0÷0.09 g).

As the research results show, in most cases the suction intensity decreases after the elapse of time, except the Siltek V-30 waterproofing system (series of samples No. 4, 5, 6). As can be seen in the graph, the intensity of absorption increases at the third minute, regardless of the depth of immersion, and with increasing the number of layers of waterproofing, the intensity of the suction capacity decreases.

3 CONCLUSION

1) The effect of technological parameters of waterproofing on the capillary suction of the treated structure is studied.
2) The indicator of water absorption intensity of the system "waterproofing-limestone shell", limestone-shell was determined.
3) The indicator of the intensity of capillary suction capacity is determined.
4) The analysis of the obtained data is carried out.

Note: This research was presented at the International Conference MATRIB 2017 (29 June - 2 July 2017, Vela Luka, Croatia).

4 REFERENCES

[1] Zarubina, L. P. Waterproofing of constructions, building and structures. / BHV-Petersburg, 2011.
[2] Vuytsik, P. Mechanical methods of horizontal waterproofing at historical buildings. // Building materials. 9(2006), pp. 58-59.
[3] Tsuvarev, M. A. Watreproofing of the underground structures by plaster solutions. // Tsuvarev M. A. – M.: Stroiizdat, 1988, 64 p.
[4] Kizima, V. P.; Yakivchuk, V. V.; Liul'chyk, O. V. Insulation and waterproofing works in construction. / Ternopil: Pidruchnyky i posibnyky, 2010, 256 p.
[5] The construction technology / By V. C. Chernenko, M. G. Yermolenko. -K.: Vyscha shkola,2002.
[6] http://centro-pol.ru/pronikayushhaya-gidroizolyaciya.html
[7] Polyakov, S. V. Izmailov, Yu. V.; Konovodchenko, V. I.; Orudzhev, F. M.; Polyakov, N. D. stonework with sawn limestones, Chisinau, 1973.
[8] Dmitrieva, N. V.; Hostryk, A. N. The analysis of methods of the waterproofing repairat constructions with limestone-shell. // DigestOSACEA, 4(2015).

Authors' contacts:

Oleg POPOV, PhD, Associate Professor (Corresponding author)
Odessa State Academy of Civil Engineering and Architecture
Razumovska str., 32/.41, 65091, Odessa, Ukraine
+380503339753 / oleg.a.popov@gmail.com

Nina DMITRIEVA, PhD, Associate Professor
Odessa State Academy of Civil Engineering and Architecture
Gaidar str., 35/6, 65070, Odessa, Ukraine

Anna HOSTRYK, PhD student
Odessa State Academy of Civil Engineering and Architecture
Dykovskaya str., 14/24, 65029, Odessa, Ukraine

ISSN 1846-6168 (Print), ISSN 1848-5588 (Online)
ID: TG-20171026150948

Preliminary communication

AN EMPIRICAL ANALYSIS OF OVERHEAD COST MANAGEMENT IN THE CZECH CONSTRUCTION INDUSTRY

Lucie HERMANOVÁ, Tomáš HANÁK

Abstract: Overhead costs are considered to be an important part of cost management in companies. This research aims to address the ways in which overhead costs are managed in the specific environment of construction. The Czech Republic is selected as the study area in order to give answers to several research questions. Data collected through a web-based survey among 112 respondents are evaluated e.g. in relation to the use of various costing methods, frequency of costing updates or in relation to the companies' competitiveness. The results presented in this paper have an ambition to serve not just as a contribution to the current body of knowledge, but the managerial implications resulting from the analysis performed and the ensuing discussion could be helpful especially for practitioners, i.e. the cost managers responsible for estimating the products/works/services properly, and they could also contribute to maintaining and improving companies' position on the market.

Keywords: company; construction; management; overhead costs; survey

1 INTRODUCTION

Alongside time and satisfaction, costs are among the principal performance indicators for construction projects [1]. Costs are crucial both for the client and the contractor: the client wishes to get the final output of a construction project at the lowest possible cost, while the contractor is motivated to satisfy the client and get an adequate profit. Therefore, on the one hand, the contractor is motivated to negotiate a reasonable contract price, and on the other hand, he seeks to reduce his own costs in order to maximize profit. The calculation of the unit price of production consists of the direct cost calculation plus the overhead costs (OHC) and profit [2].

The amount of direct costs is dependent on the scope of works, unit prices of materials, wage tariffs and costs of machinery usage, and can be easily planned in a detailed way. However, a proper allocation of overhead costs to individual contracts is a challenging issue. Taking into consideration that OHC can be considered as a factor of the company's competitiveness [3], it is obvious that overhead costs should be managed adequately in order for the company to remain eligible to participate in tenders with acceptable prices.

OHC are defined by Janani et al. [4] as costs that are not a component of the actual construction work but support the main work. Accordingly, administration staff wages, the depreciation of fixed assets or acquisition and operation of IT and mobile devices are among the typical OHC items.

An accurate estimation of OHC should be supported by a detailed cost accounting enabling the required analysis. From a theoretical perspective, different approaches have been presented to support the OHC estimation, e.g. approaches based on neural networks [5, 6], ABC approach [7] or earned value [8]. OHC management should also take account of the fact that some cost items are of a variable or fixed nature, i.e. are or are not, respectively, dependent on the volume of production. This issue was addressed by Banker et al. [9], who claim that OHC are not driven by production volume but by transactions resulting from production complexity.

Taking into consideration that the construction process is usually accompanied by a high level of uncertainty and complexity, and that a high number of stakeholders are involved [10], the company should also consider whether all the works will be implemented using its own capacity, or if employing subcontractors is more advantageous. Taking into consideration that subcontractors and general contractors have an important influence on the functioning of a construction company [11], the decision to outsource will also influence the extent of overhead costs in a particular contract.

Based on a review of appropriate literature, it can be said that OHC is a focus for many researchers, especially in terms of construction projects. For example, Chan has explored the principal factors affecting construction project overhead expenses [12], Becker et al. addressed the predictability of construction project outcomes through the intentional management of indirect construction costs [13] and Plebankiewicz and Lesniak presented their research on defining and calculating overhead costs and profit by Polish contractors [14].

The issue of OHC management becomes more important especially in the highly competitive environments such as tenders using electronic reverse auctions [15]. At a high price pressure, i.e. where it is no longer possible to reduce direct costs, OHC represent potential additional room for a tender price reduction.

1.1 Research aim

Based on the literature, it can be reasonably claimed that OHC management counts among the important managerial tasks in the construction sector companies. Therefore, the present research aims to contribute to the current body of knowledge by performing an investigation

within the Czech construction sector in order to analyse the selected managerial practices relating to OHC management in companies.

1.2 Research questions

Following the above-defined research aim, three research questions were formulated.

- The selection of a suitable costing method can be considered an important prerequisite enabling proper OHC evaluation. As there are several methods available, the first research question seeks to establish the most frequently used costing method.
  RQ1: Which is the most frequently used costing method?
- Updating OHC calculation is important in relation to providing outputs that reflect the current state of the company. It might be interesting to find out whether the size of the company affects the frequency of OHC calculation updating.
  RQ2: Is the size of the company affecting the frequency of OHC calculation updating?
- OHC can be divided into several subcategories to provide more detailed evidence and cost management.
  RQ3: Do companies use OHC sub-categories?

2 METHODOLOGY

A web-based survey was used to collect the data in the studied area representing companies active in the Czech construction sector. Data was collected from April 2015 to May 2016. The content of the survey is divided into three sections containing 16 questions. The first section concerns the general information about the surveyed companies (e.g. the scope of business, number of employees, place of business and the length of the company's existence on the market). The information provided in Section 1 ensures that the respondents are relevant to the study population. The number of employees has been used as a variable measuring the size of the company.

The second section examined various aspects relating to OHC management (e.g. the relative significance of OHC, costing methods used, distribution of OHC into sub-categories). The content delivered in Section 2 will allow answering the research questions.

The last section focused on the effect OHC have on the company's competitiveness by asking the respondents whether they agreed with the statement that OHC affect companies' competitiveness (estimated on a 5-point Likert scale). An additional question then examined the significance of OHC in comparison to other factors that influence competitiveness.

3 RESULTS AND DISCUSSION

3.1 Description of the study population

In total, 672 subjects (companies operating on the Czech construction market) were invited by email to participate in this research. From this number, 112 subjects responded appropriately to the survey questions and submitted their answers to the examined topics, representing a 16.7 % rate of response. The majority of respondents (74.1 %) reported 15 years or more of activity on the market. Taking this result into consideration, it can be claimed that the study population represents a valuable sample. Similarly, an overwhelming majority of respondents reported that construction works belong to their core business.

Based on the Commission Recommendation [16], the number of employees was used to measure the size of the company (≤50 a small, ≤250 medium, and >250 large company). Small companies were the most frequent category of respondents, followed by mid-size and large companies (63, 37, and 12 respondents respectively). A description of the sample with respect to the company size is given in Table 1.

Table 1 Distribution of respondents regarding the size of the company

Size of company	Absolute frequency	Relative frequency
Small	63	56.3%
Mid-size	37	33.0%
Large	12	10.7%
Total	112	100.0%

This research faces a similar problem as other studies that take company size into consideration [17]. In particular, this relates to the uneven distribution of respondents within the categories, showing a higher representation of small companies as opposed to large companies.

3.2 OHC significance in a company

Respondents reported the significance of OHC to their company. This significance is assessed as a relative share of OHC on the company's total costs (Eq. (1)).

$$OHC\ significance = \frac{amount\ of\ OHC}{total\ costs} \quad (1)$$

Outputs are presented at 10 % intervals (see Tab. 2). The total of 99 respondents replied to this question while other respondents did not provide this information.

Table 2 Relative share of company OHC on total costs

Relative significance	Relative frequency
0 % - 10 %	28.3%
11 % - 20 %	47.5%
21 % - 30 %	12.1%
31 % - 40 %	7.1%
41 % - 50 %	3.0%
51 % - 60 %	1.0%
61 % - 70 %	0.0%
71 % - 80 %	0.0%
81 % - 90 %	1.0%
91 % - 100 %	0.0%

Almost half of the respondents (47.5 %) reported that OHC represented between 11 % and 20 % of the total company costs. Typically, OHC are between 0% and 30 %,

indicating that OHC are considerably lower than the direct costs. The rate exceeded 50 % only in a couple of cases (2 companies). We attribute this to the fact that these companies focus mostly on delivering services rather than performing works.

3.3 OHC calculation

The next question in Section 2 asked about the companies' approach to OHC calculation. Specifically, companies reported whether they (a) used any specific method for an accurate OHC calculation, (b) used only approximate estimations, or (c) did not use any method or estimation. It was found that half of the population (50.9 %) approached OHC calculation responsibly, 29.5 % at least tried to make an approximate estimation of the costs, while the rest of the population (19.6 %) did not apply any method/estimation to OHC.

The next question inquired about the specific methods used for OHC calculation/estimation based on [18] and [19]. The only respondents who answered "Yes" or "Partially" to the previous question were asked this question. See the details in Fig. 1).

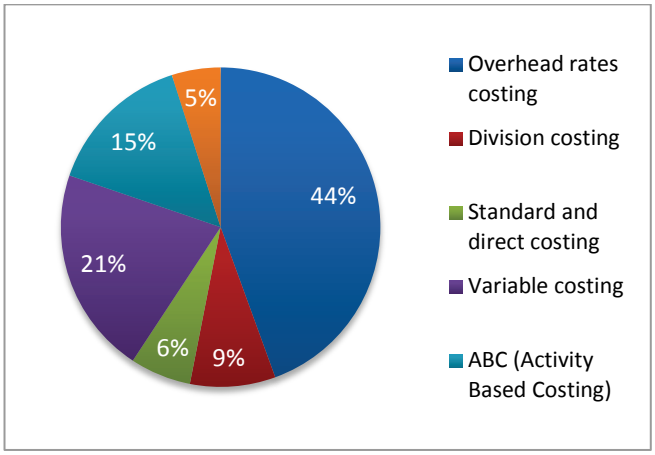

Figure 1 OHC calculation methods usage

Based on the data presented in Fig. 1, RQ1 can be answered as follows: The most frequently used method for OHC calculation in the Czech construction sector is the overhead rates costing method, followed by variable costing and activity based costing (ABC), where almost half of respondents (36 out of 81 respondents answering to this question) use overhead rates costing.

3.3 Updating OHC calculation

Having accurate input data for any calculation is crucial if actual outputs are required. Consequently, RQ2 asked how often such updates are made with respect to the company size (see the data in Tab. 3).

The results clearly show that the majority of the respondents (70 out of 112) update the OHC calculation annually; however, the preference to perform more frequent updates (monthly, quarterly or biannually) was reported in some companies. In total, 14 companies reported that they applied some other approach (no updates or irregular updates performed if some major change in the company occurs). It is very important for companies to apply updates regularly; however, major one-off changes in the company must be taken into account sooner if necessary (e.g. a change of outsourcing policy for the delivery of works by sub-contractors, significant changes in the prices of substantial commodities purchased or a substantial change in the number of employees).

Table 3 Updating OHC calculation

Company size	Updating frequency				
	Monthly	Quarterly	Biannually	Annually	Other
Small	7	5	2	39	10
Mid-size	2	4	5	23	3
Large	1	2	0	8	1

The preference to update annually could be attributed to the fact that at the end of each year, financial statements are prepared and could then serve as an information source for OHC calculation updates.

Concerning RQ2, Table 3 indicates that there is no significant relationship between the OHC updates frequency and the company size. To support this statement, the data were tested using the chi-square test of independence. It should be mentioned that the application of the chi-square test of independence is more suitable if the data are more evenly distributed among the categories. However, the use of chi-square tests is not appropriate if any of the expected frequencies is below 1 or if the expected frequency is less than 5 in more than 20 % of the cells. This is why the categories "monthly", "quarterly" and "biannually" were merged into "more often than once a year" (MOTO) and the category "Other" was omitted. For the adjusted data (the MOTO and Annually categories) taken from Tab. 3, there is just one cell with the expected frequency below 5 (3 in the case of large companies and the MOTO category). From this perspective, the chi-square test of independence can be used. The data were tested with a 5 % significance level. For the chi-square test of independence, the null hypothesis assumes that the examined categorical variables are independent.

For a chi-square value of 0.368 with 2 d.f. (degrees of freedom), the p-value = 0.832. Because $p>0.05$, there is not enough evidence to reject the null hypothesis concerning the independence of the examined variables. Therefore, the results support the assumption that company size does not affect the frequency of OHC calculation updates.

3.4 Details of OHC calculation

RQ3 aimed to establish the level of detail concerning OHC in terms of dividing OHC into sub-categories. Results show that the most frequent approach is to use a general OHC category without any subdivision (54 respondents), followed by the use of two sub-categories (47 respondents) and the use of three sub-categories (5 respondents).

This result is surprising because the two most common software solutions used in the Czech Republic for estimating the price of construction works commonly work with the subdivision of OHC into production OHC and administration OHC (i.e. two sub-categories). It appears that about half of the companies use a more detailed approach to OHC management with two or three sub-categories, while the rest only use one general OHC category. The remaining 6 companies in the sample do not keep track of OHC for calculation purposes.

Few companies reported the use of different OHC rates according to the subject of the contract. This is important because the structure of production OHC in particular can differ significantly, e.g. with regard to water supply systems, buildings or transport infrastructure projects. Therefore, it can be recommended that companies with a diverse portfolio of work/activities apply this approach.

None of the respondents mentioned that the value of the contract was taken into account for OHC management purposes. They do not seem to be concerned with the fact that for small contracts, the relative amount of OHC is higher than for large contracts due to the fixed and variable nature of the individual OHC items. Companies dealing with both large and small contracts (in financial terms) should therefore take this aspect into account in order to implement a corresponding calculation of contract prices.

3.5 OHC and competitiveness

In the final section of the survey, respondents were asked to give their opinion on the statement that OHC affects the company's competitiveness on a 5-point Likert scale where 1 indicates strong agreement and 5 indicates strong disagreement (see Tab. 4).

Table 4 Relation of OHC and competitiveness

Response	Relative frequency
Strongly agree	55.3%
Rather agree	36.6%
Nor agree nor disagree	4.5%
Rather disagree	3.6%
Strongly disagree	0.0%

The data clearly show that an overwhelming majority of respondents (92.0 %) agree with the statement that OHC affect the company's competitiveness. If compared with the data in the Section 3.4, it appears that companies are aware of OHC significance but, simultaneously, they assume that OHC management on a general level (i.e. without the distribution into sub-categories) is sufficient for their purposes.

Finally, respondents were also asked to give their opinion on various competitiveness factors in order to get an idea of the significance they assigned to OHC. The overall management of the company was the most frequently mentioned competitiveness factor, followed by direct costs, manufacturing processes and techniques, with OHC being fourth.

These results confirm that OHC management is one of the key areas for construction companies to pay attention to.

4 CONCLUSIONS

The present research dealt with the issue of OHC management in the construction sector. By using a web-based survey, data from Czech companies were collected and evaluated in order to provide the experts and the professional community with a deeper understanding of various aspects relating to OHC management. In particular, the results revealed the significance of OHC within companies, the companies' approach to OHC calculation, the details thereof and the calculation update frequency. The results confirmed that OHC cannot be omitted as they affect the company's competitiveness on the market and, consequently, its ability to win contracts.

The research also faced several limitations. Firstly, although the study population provided insight into the opinions and practices of 112 private companies, its distribution in terms of company size was not well-balanced. Therefore, an extension of the dataset, especially in the category of mid-size and large companies, could enable a follow-up analysis which could potentially lead to additional interesting findings.

Furthermore, addressing OHC values in greater detail could be of interest. Such approach has the potential to assess the level of the companies' competitiveness in a quantitative way. This is one of the possible future research directions that could contribute to the current state of knowledge in the area of corporate OHC management.

Acknowledgment

The authors wish to express their gratitude to the Project No. LO1408 "AdMaS UP – Advanced Materials, Structures and Technologies", supported by the Ministry of Education, Youth and Sports under the "National Sustainability Programme I", Czech Republic, for an excellent cooperation during the preparation of this paper.

5 REFERENCES

[1] Radujković, M.; Vukomanović, M.; Burcar Dunović, I.: Application of key performance indicators in south-eastern European construction, Journal of Civil Engineering and Management, Vol. 16, No. 4 (2010) 521-530.

[2] Plebankiewicz E.; Lesniak A.; Hromadka V.; Vitkova E.; Kocourkova G.: Estimating the value of public construction works in Poland and the Czech Republic, Scientific Review – Engineering and Environmental Sciences, Vol. 72, No. 2 (2016) 206-219.

[3] Apaviciene R.; Daugliene A.: New classification of construction companies: overhead costs aspect, Journal of Civil Engineering and Management, Vol. 17, No. 4 (2011) 457-466.

[4] Janani, R.; Rangarajan, P. T.; Yazhini S.: A systematic study on site overhead costs in construction industry, International Journal of Research in Engineering and Technology, Vol. 4, No. 10 (2015) 149-151.

[5] ElSawy, I.; Hosny, H.; Razek, M.A.: Neural Network Model for Construction Projects Site Overhead Cost Estimating in Egypt, International Journal of Computer Science Issues, Vol. 8, No. 3 (2011) 273-283.

[6] Juszczyk M., Lesniak, A.: Site Overhead Cost Index Prediction Using RBF Neural Networks, 3rd International Conference on Economics and Management (ICEM 2016), Suzhou, Jiangsu, China, July 2016, 6 p.
[7] Enshassi A.: Investigating the overhead costs in construction projects in Palestine, Journal of Financial Management of Property and Construction, Vol. 13, No. 1 (2005) 35-47.
[8] Globerson, S.: Using the earned value approach for controlling overhead cost in construction projects, Journal of Modern Project Management, Vol. 5, No. 2 (2017) 50-55.
[9] Banker, R. D.; Potter, G.; Schroeder, R. G.: An empirical analysis of manufacturing overhead cost drivers, Journal of Accounting and Economics, Vol. 19, No. (1) (1995) 115-137.
[10] Jajac, N.; Rogulj, K.; Radnic, J.: Selection of the method for rehabilitation of historic bridges - a decision support concept for the planning of rehabilitation projects, International Journal of Architecture Heritage, Vol. 11, No. 2 (2017) 261-277.
[11] Radziszewka-Zielina, E.: The Application of Multi-Criteria Analysis in the Evaluation of Partnering Relations and the Selection of a Construction Company for the Purposes of Cooperation, Archives of Civil Engineering, Vol. 62, No. 2 (2016) 167-182.
[12] Chan, C.T.W.: The principal factors affecting construction project overhead expenses: an exploratory factor analysis approach, Construction Management and Economics, Vol. 30, No. 10 (2012) 903-914.
[13] Becker, T. C.; Jaselskis, E. J.; El-Gafy, M.: Improving predictability of construction project outcomes through intentional management of indirect construction costs, Journal of Construction Engineering and Management, Vol. 140, No. 6 (2014) Article number 4014014.
[14] Plebankiewicz, E.; Lesniak, A.: Overhead costs and profit calculation by Polish contractors, Technological and Economic Development of Economy, Vol. 19, No. 1 (2013) 141-161.
[15] Hanák, T.: Electronic Reverse Auctions in Public Construction Procurement - Empirical Evidence from the Czech Republic, Archives of Civil Engineering, Vol. 62, No. 3 (2016) 47-60.
[16] European Commission. 2003. Commission Recommendation of 6 May 2003 concerning the definition of micro, small and medium-sized enterprises, EUR-lex. http://eur-lex.europa.eu/LexUriServ/LexUriServ.do?uri=OJ:L:2003:124:0036:0041:EN:PDF
[17] Hanák, T.; Šelih, J.: On-line reverse auctions in construction industry, Gradevinar, Vol. 69, No. 9 (2017), in press.
[18] Popesko, B.: Moderní metody řízení nákladů: jak dosáhnout efektivního vynakládání nákladů a jejich snížení. Grada, Praha, 2009.
[19] Synek, M. et al.: Manažerská ekonomika. 5. Aktualizované a rozšířené vydání, Grada, Praha, 2011.

Authors' contacts:

Lucie HERMANOVÁ, MSc.
Brno University of Technology, Faculty of Civil Engineering
Veveří 95, 602 00 Brno, Czech Republic
hermanova.lu@seznam.cz

Tomáš HANÁK, Associate Professor, PhD
Brno University of Technology, Faculty of Civil Engineering,
Institute of Structural Economics and Management
Veveří 95, 602 00 Brno, Czech Republic
Hanak.t@fce.vutbr.cz

ISSN 1846-6168 (Print), ISSN 1848-5588 (Online)
ID: TG-20170705114516

Subject review

IMPLEMENTING TRANSPORT STRATEGIES BASED ON SUSTAINABLE MOBILITY IN THE COUNTY OF VARAŽDIN

Ines GAJSKI, Darja TOPOLŠEK, Tina CVAHTE OJSTERŠEK, Marjan STERNAD

Abstract: Sustainable mobility is one of the key challenges for further transport development and an increasing quality of life in urban areas. The European Union (EU) encourages its member states to develop transport strategies based on sustainable mobility through EU funds and involvement in various projects launched by the EU Initiative. The Republic of Croatia, as a member state, is still not sufficiently involved in the development of these strategies. Considering the division of the state into regions and counties, we examined the European directives related to sustainable mobility, reviewed examples of good practices in the Republic of Slovenia and then we drafted suggestions for introducing such transport strategies into the Development Strategy of the County of Varaždin. Taking into account the nature of a research paper, we used descriptive methods, compilation methods and deductive methods. With a detailed review of the directives and good practices of the current traffic situation in the County of Varaždin, we concluded that the main focus should remain on the development of cycling, public transport and railway as a means of carrying out freight logistics. It has been proven that the County of Varaždin has the potential to develop transport strategies based on sustainable mobility.

Keywords: European Union; sustainable mobility; Sustainable Urban Mobility Plans; the County of Varaždin; transport strategies

1 INTRODUCTION

Today, ecology plays an important role in all sectors of the economy, including traffic and transport development. Because of its increasing importance, The European Union (EU) is investing and requesting from its members to develop and modernize that area in the transport sector. EU directives and laws have clearly determined policies for the development of sustainable mobility in urban areas and their surroundings. All member states must respect these directives and laws. The Republic of Croatia, as an EU member, must adapt to the requirements and directives that the EU imposes as a priority. In this way, the state can develop in the required direction and solve the problems in the prescribed manner.

With the review of the Development Strategy of the County of Varaždin, we have found that sustainable mobility is not included in further development plans. By reviewing the EU directives, as well as the examples of good practices introduced in the municipalities of the neighbouring country Slovenia, we will be able to give clearer suggestions for the introduction of transport strategies based on sustainable mobility into the Development Strategy of the County of Varaždin.

We can see the importance of this research by the amount of directives that the EU imposes as a priority and numerous projects that have been or are still being implemented in order to reduce the adverse impacts of traffic and increase the quality of life for all residents of urban areas. Legislation has been committed to the following areas:

- intelligent transport services;
- road safety;
- "green" vehicles and fuel;
- cycling and motorcycling;
- urban mobility in general;
- environment [1].

With regard to intelligent transport services, the Directive 2010/40/EU of the European Parliament and of the Council was adopted on July 7, 2010. The Directive deals with the framework for the introduction of intelligent transport systems (ITS) in the road traffic area and mentions other modes of transport, associated with the multimodal transfer of information and planning [2]. Following the road traffic policy orientation 2011÷2020, the European Commission has launched the strategy for a safety analysis on national roads. Many examples of good practices, planning and actions for road safety have proven to be valuable for an exchange between the member states. The existence of the strategy for national road safety can be an indicator that traffic safety is an issue on the political agenda. This part of the legislation is divided into two parts. The first part of the analysis relates to the planning of the aspects and format of the strategy and the second part relates to the content of the action plan [3]. The legislation related to vehicles is very extensive. It covers "clean" and energy-efficient vehicles, "clean" fuels (the European alternative fuel strategy), emission standards for light vehicles, carbon dioxide emissions and other greenhouse gas emissions, fuel efficiency and other directives related to vehicles and fuels [1]. Taking into consideration cycling and motorcycling, we reviewed the Regulation 168/2013 which deals with the technical and administrative conditions for all new vehicles, separate parts and component technical units. These include two or three wheeled vehicles and mopeds whose purpose is driving on public roads, including those made in one or more phases and separate technical units, parts and equipment for the construction of such vehicles [4]. On December 17, 2013, the European Commission also announced "The Urban Mobility Package", whose main element is called "Together Towards Competitive and Efficient Urban Mobility". The appendix to this is the concept of sustainable urban mobility plans

(SUMP), urban logistics, access to all urban regulations, the development of ITS and the safety of urban roads [5]. It is also important to mention the Directive 2011/92/EU, which deals with the environmental impacts from public and private projects, including construction and installation works, plans and all other interventions in the natural environment, taking into account the exploitation of mineral resources [6].

The European Platform implements SUMPs and supports competitive sustainable mobility systems in European cities through further development of the SUMP concept and all the tools required for its successful implementation. It also provides a Portal of Mobility Plans for the dissemination of all relevant information and the facilitation of cooperation and coordination between various actions supported by the EU and the ability to exchange experiences, knowledge and contacts [7]. SUMPs represent modern and sustainable plans for urban mobility and transportation, including goals and tasks, a clear implementation plan and long-term vision, assessment of current and future effectiveness, integrated and balanced development of all modes, horizontal and vertical integration, access to participation, monitoring, review, reporting and quality assurance [8]. The most useful and most important tools for sustainable mobility planning are sustainable mobility marketing, SUMP effects measurement, applications of innovative transport measures and sustainable mobility indicators for cities. Funding through the EU can be divided into three categories: financing through the EU cohesion policy, financing through the European Investment Bank and other ways [9]. Numerous projects related to SUMPs have been implemented within the EU. The EU CH4LLENGE project encourages mobility practitioners to improve the traffic planning process and the development of a quality SUMP concept. It addresses the challenges such as participation, collaboration, selecting measures, monitoring and evaluation [10]. The EU BUMP project provides the knowledge and skills needed for successful urban mobility planning in the cities and suburban areas of the partner countries. In addition to this, the EU BUMP project supports cities in developing their own SUMP concepts [11]. The EU Poly-SUMP project refers to the polycentric planning of sustainable urban mobility and is based on the development of such plans for polycentric regions [12]. The EU Tide project is focused on the development of the North Sea region, i.e. the ears under a strong tidal influence, protected by European directives [13]. The EcoMobility-Shift project includes a methodology for measuring performance in urban mobility and making decisions related to the areas that needed to be improved. Shift methodology gives cities support in creating and strengthening their mobility plans and developing action plans for the implementation of integrated urban mobility [14]. From 2011 to 2013, the EU Quest project has developed quality management tools that help small and medium-sized cities in further development of their policies and actions for sustainable mobility [15]. The EU Advance project aims to improve urban transport systems in European cities. The project gives support to cities and municipalities on their path towards a more sustainable urban mobility and assists them in the development of their SUMP concepts [16]. The EU PUMAS project offers solutions to the challenges of sustainable urban mobility through the co-ordination and development of the SUMP concept in the Alpine area [17]. The EU Solutions project offers solutions for the current and future soil and water pollution. The project is searching for new and better solutions, tools, methods and models of support in the land and water protection decisions [18]. The CIVITAS Initiative is a platform for the exchange of ideas and experience in the field of sustainable urban mobility. In some cases, challenges are technical and logistical, while others need extensive citizen involvement to achieve change. Currently, the CIVITAS Initiative has several different projects related to sustainable mobility, categorized into three categories. There are joint projects or demonstration projects, knowledge-based research projects and support projects [19]. The EU Endurance project is helping cities and regions to develop their SUMP concepts through the facilitation of networking, learning and sharing experiences and best practices in all countries [20].

Considering the results achieved in Ljubljana, Maribor and Ljutomer and the examples of good practices not only in the mentioned towns and municipality, but through the entire country, the Republic of Slovenia proved to be extremely successful in this sector.

It is also important to note that the County of Varaždin and the City of Varaždin (main centre of the County of Varaždin) aim to increase the development of bicycle traffic and cycling infrastructure both in the centre of Varaždin and other county towns, as well as in the rural and more distant areas of the county. The city bus station has been repurposed into a fast food restaurant, while the concession for the city bus transport belongs to a company named "Vincek autobusi". The suburban and interurban bus traffic is insufficiently developed, making it difficult to travel from the rural areas of the county. There is also insufficient use of the railway traffic, which could reduce the burden on the urban and suburban roads from freight vehicles. From the aspects of road safety, together with the County of Varaždin Police Administration, the County of Varaždin took concrete measures, which helped the county to achieve significant success in raising the awareness of road and traffic safety.

We are interested in the following: types of EU directives regarding sustainable mobility, how they work in practice and whether sustainable mobility can be included in the Development Strategy of the County of Varaždin. We have set the following hypothesis: The County of Varaždin has a predisposition to accept sustainable mobility based on transport strategies. We will prove the hypothesis by reviewing the current traffic, mobility and transport situation in the County of Varaždin.

2 METHODS

At the very beginning we set the assumptions about the impact of traffic on the Earth's atmosphere, carbon dioxide emissions and the interests of the County of Varaždin. The scientific process began with an overview of the status and

legislation at the EU-wide level. The next step was a presentation of the methods followed by solutions divided into two categories. The first category refers to SUMP in the Republic of Croatia and the Republic of Slovenia. What is reviewed is the current state of sustainable mobility in both states. Next to that, key projects are presented, examples of good practices and future plans. The second category refers to the County of Varaždin itself, where we described the county, demographic situation, traffic development and connectivity. The collected data were analysed and based on that, analyses were provided, as well as the suggestions for the introduction of sustainable mobility based transport strategies into the Development Strategy of the County of Varaždin. The last part covers the conclusions.

As the main sources of legislation we used the Eltis organization website, the aforementioned directives and regulations of the EU, the main websites of the cities and municipalities of the Republic of Slovenia, as well as the main websites of the County of Varaždin and the City of Varaždin. The area of traffic development and connectivity in the County of Varaždin has been defined by a review of the current situation and we contacted the Development Agency North and the County Road Administration, where they referred us to the County of Varaždin Police Administration. By reviewing the current situation and the mentioned contacts, we can more closely define the traffic image of the County of Varaždin and the City of Varaždin. Throughout the research process, we used the description and compilation methods, as well as the deductive method. All collected data were analysed, and based on the analysis, we prepared suggestions for the introduction of sustainable mobility based transport strategies into the Development Strategy of the County of Varaždin.

An overview of the research step by step:

- the first step: a review and presentation of the EU legislation;
- the second step: a review and presentation of the European platform, SUMP and its tools;
- the third step: a review and presentation of the projects implemented in the field of sustainable mobility;
- the fourth step: a presentation of methods and the hypothesis;
- the fifth step: spatial planning in the Republic of Croatia;
- the sixth step: spatial planning in the Republic of Slovenia;
- the seventh step: a description and demographic situation of the County of Varaždin;
- the eighth step: traffic development and connectivity of the County of Varaždin;
- the ninth step: a collected data analysis;
- the tenth step: proposing solutions;
- the eleventh step: conclusions.

3 PRESENTATION OF RESULTS

The results include the SUMP development in the Republic of Croatia and the Republic of Slovenia, as well as an overview of the current situation, traffic development and connectivity in the County of Varaždin. They also include an analysis of the collected data and suggestions for the implementation of sustainable mobility based strategies into the Development Strategy of the County of Varaždin.

3.1 SUMP in the Republic of Croatia

In the Republic of Croatia there is no legal definition of the SUMP concept, a national guidance for its preparation, or a connection with the national sources of funding. However, the state has defined the goals of sustainability and the political support for SUMP, but public participation and the technical capacity for its preparation are very limited. In 2014, a public hearing on the SUMP concept and project was conducted at the Faculty of Transport and Traffic Sciences, where it was found that there is a lack of coordination between the local, county and state level [21]. The current situation in the country is defined as follows:

- according to the data from 2012, there are 336 registered personal cars per 1,000 inhabitants;
- the need to "rejuvenate" the fleets and the use of high-quality fuel for driving;
- the need for catalytic converter vehicles;
- compared to 1990, carbon monoxide emissions decreased by 70 %;
- compared to 1990, nitrogen oxide emissions decreased by 22 %;
- compared to 1990, lead emissions were reduced by 94 %;
- compared to 1990, the number of passenger cars increased by 80.4 %;
- compared to 1990, the number of heavy duty vehicles increased by 2.2 %;
- compared to 1990, the number of light duty vehicles increased by 7.2 %;
- compared to 1990, the number of motorcycles and mopeds increased by 10.2 %;
- compared to 1990, fuel consumption in road traffic increased by 62 %;
- diesel fuel is twice more used than gasoline [22].

In the period from 2012 to 2025, national forecasts foresee a growth in greenhouse-gas emissions caused by traffic. For this purpose, the Transport Development Strategy has been developed, with the aim of developing an efficient and sustainable transport system in the Republic of Croatia. All measures are in line with the EU regulations. The mentioned measures are the following:

- ensuring the interoperability of the system;
- increasing the level of service ability in the transport sector;
- improving energy efficiency;
- financial sustainability assurance;
- security and protection;
- ensuring social and environmental sustainability;
- efficiency ensuring;
- improving accessibility and social inclusion;

- improving the distribution of traffic patterns in favour of public transport;
- improvement of the environmentally acceptable and alternative modes of transport;
- quality service assurance [23].

It is also important to mention the participation of the Republic of Croatia in two EU projects, the Adria.Move IT! and CIVITAS Dyn@mo projects. The Adria.Move IT! project was co-funded by the 2007÷2013 IPA Adriatic CBC Programme. The project brought together the Adriatic coastal towns that have been facing mobility issues due to their specific historical and spatial circumstances. Traffic congestion is the result of the historical heritage of such cities as they were not designed to use cars and were not prepared for a sudden increase in the number of inhabitants during the summer tourist season. The motive to launch the project was a joint development of efficient, environmentally friendly, safe and heathy transport solutions that could stimulate sustainable transport, an increase in the quality of life and the socioeconomic cohesion of the project area. The project is a good example for other Adriatic local authorities. In order to promote sustainable mobility, small pilot projects have been implemented in partner cities, aimed at encouraging cycling and alternative transport channels [24]. CIVITAS Dyn@mo is an ambitious project with a strategic significance for sustainable mobility planning in four dynamic European cities. It includes two leading cities, Aachen in Germany and Gdynija in Poland, and two learning cities, Mallorca in Spain and Koprivnica in Croatia. The mission of this project is to strengthen sustainable mobility through the promotion of non-polluting lifestyles, the fostering of social interaction and co-operation on the basis of new media and the integrated implementation of innovative transport services for citizens of all ages. Strategic objectives of the project are the development of the "Mobility 2.0" system and service through the implementation of 2.0 technologies, solutions for the electric mobility of citizens, the use of new electric and hybrid vehicles and the inclusion of a dynamic citizen dialogue in mobility planning and service improvement. The objectives are divided into four levels, which are the strategic, technical, service and European level [25].

So far several cities have participated in the projects related to SUMP. The cities are Dubrovnik, Umag and Novigrad for the Adria.Move IT! project and Koprivnica for the CIVITAS Dyn@mo and CH4LLENGE projects. Dubrovnik, as a popular tourist resort, faces problems of overcrowding due to the lack of parking spaces, excessive use of cars, traffic congestion and unregulated cycling and pedestrian paths. Within the framework of the IPA Cross-border Cooperation Program and Adria.Move IT! project, a local Mobility Plan was created, modern urban equipment was installed at key locations in the city and outside the centre, bicycle holders were installed at the Sport Centre and near the city core, and all pedestrian paths were renovated and marked. Moreover, Dubrovnik owns a 3.5 km long pedestrian and cycling route that connects the residential and tourist area with the north-western part of the city. This has significantly contributed to the development of the city as a tourist resort. In the city of Umag, there is a cycling path called Umag-Ungarija, which is a 2.5 m wide and 921 m long asphalt road, equipped with traffic and information signalling. In Novigrad, there are two walking and cycling paths over 11 km in length, called the Dalja-Maleda-Pineta-Karpinjan and Kršin-Stancija-Vinjeri-Novigrad paths. Novigrad is thus succeeding in boosting its sustainable mobility, leading to a reduction in the number of motorised vehicles in traffic. We also have to mention a pilot project of the municipality of Lopar, which is about building a pedestrian and cycling trail on the already existing route that connects Sveti Rok and Jamin. The purpose of the project is to reduce the congestion in road traffic, preserve natural resources and limit the use of vehicles [26]. It is important to mention the City of Koprivnica, which, within the CIVITAS Dyn@mo project, has adopted six measures:

- public transport planning;
- sustainable urban transport plan;
- university campus of zero nitrogen oxide emissions;
- low-emission public transport;
- development of sustainable traffic curriculum for the University of Koprivnica;
- common use program for urban electric vehicles [27].

In order to improve the implementation of SUMP and increase sustainable mobility, many pilot studies have been conducted, and their results gave an insight into the themes and their percentage share in the presented sustainable mobility plans. Tab. 1 shows the topics and their percentage share [28].

Table 1 Topics and their percentage share in the sustainable mobility plans of the Republic of Croatia

Topics	%
Walking and cycling	14.1
Public urban transport	13.4
Integrated traffic system	10.8
Parking control	7.2
Delivery in towns	6.2
Compliance of the urban development and land use	6.2
Access Restrictions Schemes (green zone, reduced gas emission zones, congestion charge)	6.2
Compliance with the traffic plans at the county, national and EU levels	5.9
Ways of citizens' and other participants' participation	5.6
Accessibility, social inclusion (young, old, disabled)	5.2
Evaluation procedures, evaluation of the plan	3.9

3.2 SUMP in the Republic of Slovenia

There is no legal provision in the Republic of Slovenia that would force the local authorities to implement SUMP, but in the last decade, a concept has been developed, mainly through the EU projects. The Slovenian experts tested SUMP through three levels, recommended by the EU, such as the size of the city recommended by the EU (+ 100,000), the size of small municipalities and regions. The concept proved to be successful at each level. The SUMP, adjusted

to the regional level, was developed only for the area of Nova Gorica, while all other SUMP concepts were developed for municipalities. Several years ago, the Ministry of infrastructure, responsible for the urban transport, recognized the value of the SUMP concept and supported it on several levels. The priority of the government is the development of a National Platform for Sustainable Mobility. The Ministry of Infrastructure has also established cohesion funds that serve as a source of funding for the development of SUMP in cities and the implementation of all sustainable measures under this concept [29]. The current situation in the country is defined as follows:

- EU access has raised the use of road traffic by 70 %;
- 500 km of railway lines are electrified;
- the ratio between the road freight transport and rail freight transport is 71:29;
- the share of combined transport is 0.8 %;
- more than 75 % of individual travel in the state is performed by personal cars;
- public passenger transport is used in a 25 % share;
- the total length of roads is 85,220.00 km;
- the total length of railway lines is 2,177.50 km;
- road traffic caused 90 % of harmful emissions;
- the number of traffic accidents is around 38,000 per year;
- spatial planning documents are mainly focused on the infrastructure [30].

It is also important to mention integrated traffic planning based on the development of transport strategies. The process of preparing integrated transport strategies involves a sustainable and holistic approach, a clear vision and goals, a focus on achieving measurable goals, an overview of all transport costs and benefits and staff expertise based on the use of measures that have been tested.

There are the so-called guidelines for the development of sustainable urban mobility plans, prepared for Slovenia in line with the experience gained in the preparation of the integrated transport strategies for Ljubljana, which have been implemented within the CIVITAS Elan project and in the development of the integrated transport strategies for the Ljutomer municipality, covering 11 following steps:

- foundation setting;
- defining the process;
- state analysis and scenario design;
- a scheme of a required state;
- defining priorities;
- selecting measures;
- making a performance plan;
- establishment of supervision;
- acceptance of the strategy;
- implementation of the strategy;
- learning from experience [31].

Each of the mentioned steps has certain sub-processes and additional tasks that need to be completed in order to take the step successfully.

Some of the most well-known projects related to SUMP were conducted in Ljubljana, Maribor and Ljutomer. Ljubljana has participated in two CIVITAS projects, Mobilis and Elan. Maribor is the second largest city in Slovenia and has developed a Sustainable Urban Transport Plan. In 2012, the Ljutomer municipality accepted a traffic strategy which was rated as the most successful in Europe [32].

The results of the Mobilis project in Ljubljana have shown that biodiesel is not a competitive and cost-efficient fuel. Public transport buses, adjusted to this fuel, demanded twice more maintenance. Although the results proved to be negative, 20 buses adapted to biodiesel are still in use and Ljubljana, on the basis of the project, has made firm partnerships with the involved institutions [33]. Besides Mobilis, Ljubljana also participated in the Elan project. Within the Elan project, the SUMP upgrading measures were implemented. The project also provided real-time information, transport according to demand, e-ticketing and a public transport portal, green procurement for city fleets and clean plant propulsion [34]. In 2000, Maribor adopted the concept of spatial development with its goals. The goals are a sustainable urban development, establishing links between the rural and urban areas, preserving the environment and improving the quality of life in the town. In 2008, the Municipal Environmental Program was adopted with a detailed action plan for urban mobility and in 2009, a sustainable energy and climate change was mentioned within the local energy concept, which included a detailed action plan for reducing energy consumption in transport [35]. Maribor has set the strategic objectives that it wants to reach by 2020. The city wants to become the leading municipality in Slovenia in terms of sustainable mobility, to limit noise and pollution levels in line with the EU directives, to reduce the number of traffic accidents and injuries by 50 % (period from 2008 to 2013) and balance travel patterns [36]. The city has also been included in the TRAMOB project, which has been successfully implemented in order to reduce the trend of deterioration of the quality and efficiency of mobility [37]. It is also important to mention the municipality Ljutomer. Ljutomer has implemented its integrated transport strategy to address the five challenges in the municipality, which is a shortage of the planning practice, unhealthy travel habits, a drop in the public passenger transport, poor conditions for walking and cycling and a lower quality of life caused by road traffic. Ljutomer has initiated a national project for the establishment of the SUMP, which include the strategic pillars of sustainable mobility planning, integrated promotion of walking, use of the potential for cycling, attractive public transport and optimization of road traffic [38]. The transport strategy was successfully implemented through the Ljutomer municipality.

Ljubljana, Maribor and Ljutomer are some of the examples of how to successfully import sustainable mobility and its aspects into the system. The Republic of Slovenia can boast numerous examples of good practice, not only in the mentioned cities and municipality, but

throughout the country. The following are some of the examples:

- free local transport – Kavalir (Ljubljana);
- free local bus (Velenje, Nova Gorica, Murska Sobota);
- extension of the bus line to the suburbs (Grosuplje and Brezovica);
- a dead end street with pedestrian and cycling passes (Ljubljana);
- two-way passage of cyclists in one-way streets (Ljubljana);
- a narrowing of the carriageway (Ljubljana);
- common traffic space (Ljubljana);
- the so-called pedestrian bus and bike train;
- a connection of a regular and school bus line (Grosuplje);
- free transportation for the elderly (in a region called Obalno-Kraška);
- traffic island (Reteče);
- travellers – Prevoz.org (established at the University of Ljubljana);
- sustainable mobility in Kranjska Gora;
- soft mobility in Bohinj;
- sustainable mobility at the Ski-jumping World Cup (Planica);
- sustainable mobility at the European basketball Championship Eurobasket 2013 [39].

3.3 Information about the County of Varaždin

The County of Varaždin is located in the northwest of the Republic of Croatia and borders with the County of Krapina-Zagorje, the County of Koprivnica-Križevci, the County of Međimurje and the Republic of Slovenia. The county area amounts to 1,261.29 km^2 and includes 302 villages and six cities. Those cities are Varaždin, Ivanec, Lepoglava, Varaždinske Toplice, Ludbreg and Novi Marof. Additionally, the county includes 22 municipalities. The centre of the county is the City of Varaždin and the population of the county is 175,951 inhabitants [40].

3.3.1 Traffic development and connectivity

The County of Varaždin has several important roads, such as the Goričan-Varaždin-Zagreb highway, the state road D-2, also well-known as "Podravska magistrala". Moreover, the fast road Varaždin-Ivanec-Krapina and the fast road in Podravina linking Ormož, Varaždin and Virovitica are being constructed. Regarding railway traffic, 91,751.00 km of railway lines pass through the county. All lines are single-track, without electrification, intended for mixed traffic. The permissible speed varies from 45 to 100 km/h. When all the positive and negative features of the transport infrastructure are summed up, there are some needs in terms of improving road infrastructure for the purpose of passenger safety, modernization in railway traffic and in terms of improving the infrastructure in the public transport [41]. Looking at the City of Varaždin, some of the most important roads are already built. Those roads are an Eastern bypass connecting Hungary and Čakovec, the Western bypass connecting the settlements Gojanec and Hraščica and the Southwestern bypass connecting the settlements Gojanec and Kneginec [42]. It is known that the most common types of transportation in Varaždin are personal vehicles, public transport, bicycles and walking. In the morning hours, there are 5,880 passengers in personal vehicles, 2,450 passengers in public transport, 980 cyclists and 490 pedestrians [43]. The city has solved the potential parking problems by building several large parking locations, including the underground garage at the Capuchin Square, with 446 parking spaces and three other parking locations. The first of the bigger parking spaces is located at the so-called Banus place, the second one is located at the Faculty of Organization and Informatics (building 2) and the third one is located at the Varaždin Cemetery. The city has several electronic devices to display free parking spaces. Varaždin also owns several objects similar to traffic islands, installed to reduce the critical speed and to increase traffic safety.

3.3.2 Mobility of people

The line transport of passengers in Varaždin was conducted by company named "Autobusni promet d.d. ", which ended up in bankruptcy, while the city bus station was converted to a fast food restaurant. Concession for conducting line transportation was taken over by the company named "Vincek autobusi". Regarding the taxi services, in 2014, the Cammeo Group's taxi service arrived in the County of Varaždin. Due to the frequent unadjusted speed and accidents ending with an injured pedestrian, the centre of the city was turned into a pedestrian zone divided into two parts. The narrow part consists of the Street of Ivan Gundulić, King Tomislav Square and Franciscan Square, as the narrow centre of the city; while the wider part is divided into the streets and squares of a broader centre of the city. In 2014, it was decided that riding a bicycle in certain parts of the pedestrian zone would still be permitted, but not faster than a pedestrian walk. Towards the centre of the city, on the Street of Zrinski and Frankopan, near the bus station of the "Autobusni promet Varaždin", is a two-way bicycle path, with a total length of about 100 m. The path is clearly visible and color-separated from the pedestrian path and the carriageway. If the cyclists want to arrive from one part of the city to another, they cannot shorten their journey through the centre because of a strict cycling ban, but have to cycle around the centre, on marked cycling paths. The City of Varaždin, as the so-called "Bicycle Town", in some locations still does not have an adequate cycling infrastructure and the accompanying signalling. Several tourist cycling routes go through the county, but the county still does not have the option of renting bicycles for tourist purposes. Apart from this, the city has several smaller bicycle parking lots, most popular in the Alojzije Stepinac Street. There is no covered parking space for bicycles.

3.3.3 Ecological factors and road safety

No significant exceedance of harmful greenhouse gases has been noted in the County of Varaždin. However, their greatest influence is seen in the urban areas of the county. For the sake of environmental protection, within the strategic objective of environmental protection, the rational space management and infrastructure development, the priority lies in environmental protection, which emphasizes the importance of addressing the problems of the reduced air quality in the county's urban areas [44].

As a result of an increased number of traffic accidents during 2016 and 2017, camcorder boxes for measuring the speed of vehicles were set up at seven locations in the county (mainly near the City of Varaždin). The County of Varaždin Police Administration owns two cameras that are constantly moving from one location to another. According to the data from the County of Varaždin Police Administration, the County of Varaždin is included in the National Road Safety Program which finances the repair of dangerous traffic spots. The police administration has also carried out numerous actions to increase the awareness of safety, such as making a list of children cyclists carrying helmets, placing promotional commercials for wearing reflecting jackets and establishing the Road Safety Council. The Council initiated the pedestrian crossing lighting action. The pedestrian crossing lighting is based on solar cells, LED lamps and battery cells. The Council has also launched a campaign that involves citizens in the making of road safety decisions.

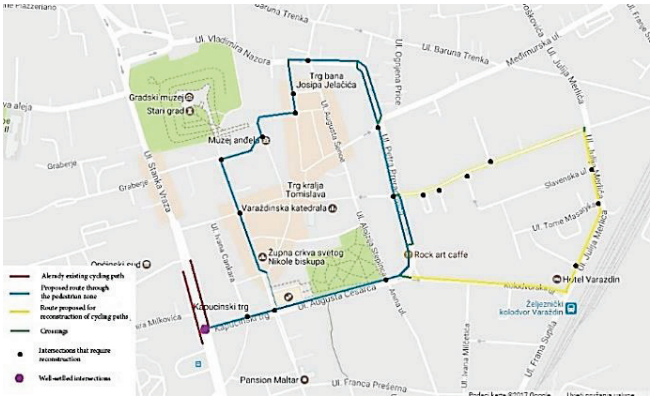

Figure 1 Proposed cycling route through one part of the pedestrian zone in Varaždin

3.3.4 Possible solutions

Regarding the road infrastructure, the County of Varaždin and the City of Varaždin are well equipped. There is a need to work on the development of railway transport for the purpose of freight logistics. This action could reduce the burden on city roads from freight vehicles. Parking problems in the city are well-solved. We propose the construction of traffic islands at some of the critical locations in the county which will also help reduce the number of accidents. For the purpose of the cycling encouragement, recreation and justifying the name "The Bicycle Town", what is proposed is a construction of a two-way cycling route through one part of the pedestrian zone, as well as a reconstruction of the existing cycling paths and a construction of new ones on certain locations. What is also proposed is the import of bicycle rental opportunities at the County of Varaždin Tourist Board. By implementing a two-way cycling route, we believe that the violations of the cycling ban through the centre of the city can be reduced, as well as the travel time from one part of the city to another. Moreover, the quality of life in the city and the pleasure of all Varaždin bikers can be increased. Figure 1 shows the proposed cycling route.

The reconstruction of the city bus station and the implementation of environmentally-friendly bus vehicles for urban traffic are also suggested. In addition to this, we suggest an increase in the number of routes and frequencies in passenger transportation to the suburban villages of the county. Regarding the security that is well-solved in the county, the County of Varaždin Police Administration has put forward several proposals for its increase, such as the changes in the behaviour of traffic participants through the organization of driver awareness campaigns, investments in further development of the infrastructure, a development of safe vehicles and an improvement of medical care. Considering the already set strategic objectives and their priorities, it is necessary to formulate proposals that can be integrated into the existing vision and strategy of the County of Varaždin. It is also necessary to include other participants at the state and county level. At the state level, we recommend including the Ministry of Maritime Affairs, Transport and Infrastructure, project companies and media and other interested groups. At the county level, we recommend the inclusion of the County of Varaždin, the City Council of the City of Varaždin, the Development Agency North, the association "Varaždin bikers", the County of Varaždin Police Administration, the municipal boards of all interested municipalies of the County of Varaždin, the public transport service provider "Vincek autobusi", educational institutions, the Society of the Dystrophic, Cerebral and Polio Invalids and Other Physical Invalids of the City of Varaždin and all other interested groups. The project's holder should be the County of Varaždin authorities, which would conduct interviews with all other interested groups. Five strategic goals have already been set in the Development Strategy of the County of Varaždin. Taking all that into consideration, we propose the introduction of two new strategic goals, as well as the subsequent priorities. The strategic goal 6 is connected to the renewal of the traffic infrastructure. This goal includes two priorities. The first priority is the development of the railway infrastructure and the second priority is the development of a cycling infrastructure and superstructure. The strategic goal 7 is connected to the development and renewal of bus traffic. It also includes two priorities. The first priority is the development of bus traffic in Varaždin and the second priority is the development of intercity bus transport. Measures for both strategic goals should be formed according to the set priorities.

Within the third strategic objective, which is the Environmental Protection and Energy Management, what is proposed is the import of priorities related to the improved greenhouse-gas emissions control and repair of locations exposed to the harmful effects of traffic noise. The EU funds could cover the costs of projects related to sustainable mobility. Some of the money sources can be innovative actions and sustainable urban development that cover and test pilot projects and the trans-European transport networks such as TEN-T which includes interoperable railways and sustainable transport promotions. Some of the money sources are also loans and guaranties from the European Investment Bank (projects over 25,000,000.00 euros), the ELENA program which covers 90 % of the technical costs for the preparation of projects related to renewable energy sources, the JESSICA program which also covers the costs of sustainable development, the European Energy Efficiency Fund, the LIFE program which is a financial instrument for the environmental and climate change actions.

4 CONCLUSION

By reviewing the available literature, it is concluded that the Republic of Croatia is lagging behind the neighbouring Republic of Slovenia with regard to the development of sustainable mobility. It is necessary to mention that significant changes and development efforts in accordance with the EU directives in the case of the Republic of Croatia have only been noticed in the City of Koprivnica which is continuing with the development in this direction. On the other hand, the Republic of Slovenia is actively involved in the development through Ljubljana, Maribor and Ljutomer, and it provides the examples of good practice throughout the country.

Regarding the County of Varaždin, through a review of the Development Strategy of the County of Varaždin and the City of Varaždin, by talking to key stakeholders such as the County Road Administration and the County of Varaždin Police Administration, it is concluded that the County of Varaždin has the predispositions for further development of cycling and for the improvement of conditions for cyclists, which then leads to increased tourism and quality of life. Further development of bus traffic is also much needed. However, all discussions and meetings related to this topic did not bring any positive conclusions. All the presented results and solutions can be linked to the EU directives on clean transport and cycling encouragement. The exception that we did not deal with through reviewing the EU directives is the development of railway traffic, but in the case of the County of Varaždin, the development of railway traffic could save city and county roads from freight vehicles.

These solutions can bring various advantages such as:

- increasing the quality of life in the County of Varaždin;
- encouragement of physical movement;
- reduction of greenhouse gas emissions in the atmosphere;
- increasing the satisfaction of the population;
- facilitating the travel of people from rural areas or distant places;
- reducing congestion caused by personal cars;
- development of the so-called "Healthy Region";
- development of the County of Varaždin in accordance with the EU directives;
- contribution to the development of the entire Republic of Croatia.

Taking all of the above mentioned into account, the strategic goals based on the needs of the County of Varaždin are formed. Moreover, taking into account the logistical side of our research, it is concluded that there is a lack of a more detailed economic analysis, i.e. an overview of all costs that follow the innovations and that need to be done.

Sustainable mobility is the future of a better aggregate functioning, especially in the urban areas.

Acknowledgements

Many thanks to the mentors dr. Marjan Sternad and dr. Darja Topolšek for their leadership and assistance in the writing of the research paper.

We also thank Mr. Miljenko Ernoić from the Development Agency North and Mr. Dejan Radat from the County of Varaždin Road Administration for their help and orientation on the County of Varaždin Police Administration for the purpose of gathering the necessary data.

We thank Mr. Darko Dragičević from the County of Varaždin Police Administration for his quick response, help and co-operation in the collecting of the traffic safety data.

5 REFERENCES

[1] http://www.eltis.org/hr/discover/legislation-polices (Accessed: 31.03.2017)

[2] Towards a roadmap for delivering EU-wide multimodal travel information, planning and ticketing services, (2014). http://www.eltis.org/sites/eltis/files/swd2014194.pdf (Accessed: 01.04.2017)

[3] Road safety planning Good practice examples from national road safety strategies in the EU Non-paper as food for thought and discussions, (2014). http://www.eltis.org/sites/eltis/files/national-road-safety-strategies_en.pdf (Accessed: 02.04.2017)

[4] Regulation (EU) No 168/2013 of the European parliament and of the Council of 15 January 2013 on the approval and market surveillance of two- or three-wheel vehicles and quadricycles, L 60/52. http://www.eltis.org/sites/eltis/files/celex-32013r0168-en-txt.pdf (Accessed: 25.03.2017)

[5] Urban Mobility Package, (2014). http://www.ccre.org/img/uploads/piecesjointe/filename/CEMR_opinion_Urban_mobility_package_EN.pdf (Accessed: 05.04.2017)

[6] Directive 2011/92/EU of the European Parliament and of the Council of 13 December 2011 on the assessment of the effects of certain public and private projects on the environment, L 26/1. http://www.umweltbundesamt.at/fileadmin/site/umweltthemen/UVP_SUP_EMAS/UVP-Gesetz/UVP-RL_kodifiziert_EN_2011.pdf (Accessed: 25.03.2017)

[7] http://www.eltis.org/hr/search/site?f%5B0%5D=im_field_topic%3A432 (Accessed: 24.03.2017)
[8] http://www.eltis.org/hr/mobility_plans/koncept-sump (Accessed: 24.03.2017)
[9] http://www.eltis.org/hr/resources/eu-funding (Accessed: 31.03.2017)
[10] http://www.sump-challenges.eu/ (Accessed: 26.03.2017)
[11] http://www.bump-mobility.eu/en/about-bump.aspx (Accessed: 26.03.2017.)
[12] http://www.poly-sump.eu/home/ (Accessed: 26.03.2017)
[13] http://www.tide-project.eu/ (Accessed: 26.03.2017)
[14] https://ecomobility.org/ecomobility-shift/ (Accessed: 26.03.2017)
[15] http://www.eltis.org/discover/news/quest-project-helps-cities-improve-sustainable-urban-mobility-policies-actions-0 (Accessed: 26.03.2017)
[16] http://eu-advance.eu/index.php?id=40 (Accessed: 26.03.2017)
[17] http://civitas.eu/content/pumas-project-final-conference (Accessed: 26.03.2017)
[18] http://www.solutions-project.eu/project/ (Accessed: 26.03.2017)
[19] http://civitas.eu/mobility-solutions-page (Accessed: 27.03.2017)
[20] http://www.epomm.eu/endurance/index.php?id=2795 (Accessed: 28.03.2017)
[21] http://www.eltis.org/hr/mobility-plans/member-state/croatia (Accessed: 24.04.2017)
[22] http://www.energetika-net.com/vijesti/zastita-okolisa/oneciscenje-zraka-iz-cestovnog-prometa-13358 (Accessed: 24.04.2017)
[23] Buhin, D. (2015). Održiva mobilnost u ruralnim područjima. https://zir.nsk.hr/islandora/object/fpz%3A220/datastream/PDF/view (Accessed 24.04.2017)
[24] http://dalmatiaaeterna.hr/2014/02/adria-move-it-project/ (24.04.2017)
[25] http://civitas.eu/content/dynmo (Acessed: 24.04.2017.)
[26] http://dalmatiaaeterna.hr/2014/02/adria-move-it-project/ (Accessed: 24.04.2017)
[27] http://koprivnica.hr/projekti-grada/civitas-dynmo/ (Accessed: 24.04.2017)
[28] Planovi održive urbane mobilnosti – SUMP, (2014). http://www.fpz.unizg.hr/zgp/wp-content/uploads/2015/02/Zbornik-Planovi-odrzive-urbane-mobilnosti-SUMP-Zagreb-lipanj-2014-ISBN-978-953-243-067-7-.pdf (Accessed: 26.04.2017.)
[29] http://www.eltis.org/hr/node/44126 (Accessed: 24.04.2017)
[30] Trajnostna mobilnost. http://www.focus.si/files/Publikacije/trajnostna_mobilnost.pdf (21.04.2017)
[31] Trajnostna mobilnost za uspešno prihodnost, (2012). http://www.trajnostnamobilnost.si/Portals/0/publikacije/TM_Brosura_FINAL_Civitas.pdf (Accessed: 13.04.2017)
[32] http://www.kc-sump.eu/hr/sump-u-nasoj-regiji/sump-u-sloveniji/ (Accessed: 20.04.2017)
[33] Sustainable Urban Transport – case stories from 5 CIVITAS Mobilis cities. http://civitas.eu/sites/default/files/sustainable20urban20transport20-20case20stories20from20520civitas20mobilis20cities.pdf (Accessed: 20.04.2017)
[34] Innovative cities before and after CIVITAS. http://civitas.eu/sites/default/files/Results%20and%20Publications/CIVITAS_ELAN_final_brochure.pdf (Accessed: 20.04.2017)
[35] Information about sustainable urban transport plan (SUTP) for Maribor. http://www.energap.si/uploads/Sustainable%20urban%20transport%20plan%20for%20Maribor.pdf (Accessed: 20.04.2017)
[36] www.southeast-europe.net/document.cmt?id=843 (Accessed: 20.04.2017)
[37] http://www.smartcitymaribor.si/en/Projects/Smart_Mobility/TRAMOB_Measures_for_sustainable_mobility/ (Accessed: 20.04.2017)
[38] Prometna strategija občine Ljutomer, (2012). http://kc-sump.eu/wordpress/wp-content/uploads/2015/01/prometna-strategija-ljutomer.pdf (Accessed: 21.04.2017)
[39] Trajnostna mobilnost v praksi, (2016). http://www.cipra.org/sl/publikacije/zbornik-dobrih-praks-trajnostna-mobilnost-v-praksi/Trajnostna-mobilnost-v-praksi.pdf/inline-download (Accessed: 21.04.2017)
[40] http://www.varazdinska-zupanija.hr/%C5%BEupanija/opce-informacije/ (Accessed: 26.04.2017)
[41] Županijska razvojna strategija Varaždinske županije 2011. – 2013., (2010). http://www.varazdinska-zupanija.hr/repository/public/upravna-tijela/gospodarstvo-eu/zrs/2211-zupanijska-razvojna-strategija-final.pdf (Accessed: 27.04.2017)
[42] Strategija razvoja Grada Varaždina do 2020. godine, (2016). http://varazdin.hr/upload/2016/12/strategija_razvoja_grada_varazdina_do_2020_godine_584e471f6dd4f.pdf (Accessed: 27.04.2017)
[43] Generalni urbanistički plan grada Varaždina, (2006). http://varazdin.hr/upload/gup/tekst/GUP_Varazdina.pdf (Accessed: 5.06.2017)
[44] Izvješće o stanju okoliša Varaždinske županije za razdoblje od 2010. do 2013. godine, (2014). http://www.varazdinska-zupanija.hr/repository/public/upravna-tijela/poljoprivreda/zastita-okolisa/dokumenti/izvjesce-o-stanju-okolisa.pdf (Accessed: 28.04.2017)

SYMBOLS AND ABBREVIATION

EU	European Union
SUMP	Sustainable Urban Mobility Plans
ITS	Intelligent Transport Systems
TEN-T	Trans-European Transport Network

Authors' contacts:

Ines GAJSKI, (student)
University of Maribor, Faculty of Logistics
Mariborska cesta 7, 3000 Celje, Slovenia
ines.gajski@student.um.si

Tina CVAHTE OJSTERŠEK, Research Assistant
University of Maribor, Faculty of Logistics
Mariborska cesta 7, 3000 Celje, Slovenia
tina.cvahte@um.si

Darja TOPOLŠEK, PhD, Associate Professor
University of Maribor, Faculty of Logistics
Mariborska cesta 7, 3000 Celje, Slovenia
darja.topolsek@um.si

Marjan STERNAD, PhD, Assistant Professor
University of Maribor, Faculty of Logistics
Mariborska cesta 7, 3000 Celje, Slovenia
marjan.sternad@um.si

ISSN 1846-6168 (Print), ISSN 1848-5588 (Online)
ID: TG-20……..

14pt
14pt

ARTICLE TITLE ONLY IN ENGLISH (Style: Arial Narrow, Bold, 14pt)

14pt

Ivan HORVAT, Thomas JOHNSON (Style: Arial Narrow, Bold, 11pt)

11pt
11pt

Abstract: Article abstract contains maximum of 150 words and is written in the language of the article. The abstract should reflect the content of the article as precisely as possible. TECHNICAL JOURNAL is a trade journal that publishes scientific and professional papers from the domain(s) of mechanical engineering, electrical engineering, civil engineering, multimedia, logistics, etc., and their boundary areas. This document must be used as the template for writing articles so that all the articles have the same layout. (Style: Arial Narraw, 8pt)

10pt

Keywords: keywords in alphabetical order (5-6 key words). Keywords are generally taken from the article title and/or from the abstract. (Style: Arial Narraw, 8pt)

10pt
10pt

1 ARTICLE DESIGN
(Style: Arial Narrow, Bold, 10pt)

10pt

(Tab 6 mm) The article is written in Latin script and Greek symbols can be used for labelling. The length of the article is limited to eight pages of international paper size of Letter (in accordance with the template with all the tables and figures included). When formatting the text the syllabification option is not to be used.

10pt

1.1 General guidelines
(Style: Arial Narrow, 10pt, Bold, Align Left)

10pt

The document format is Letter with margins in accordance with the template. A two column layout is used with the column spacing of 10 mm. The running text is written in Times New Roman with single line spacing, font size 10 pt, alignment justified.

Article title must clearly reflect the issues covered by the article (it should not contain more than 15 words).

Body of the text is divided into chapters and the chapters are divided into subchapters, if needed. Chapters are numbered with Arabic numerals (followed by a period). Subchapters, as a part of a chapter, are marked with two Arabic numerals i.e. 1.1, 1.2, 1.3, etc. Subchapters can be divided into even smaller units that are marked with three Arabic numerals i.e. 1.1.1, 1.1.2, etc. Further divisions are not to be made.

Titles of chapters are written in capital letters (uppercase) and are aligned in the centre. The titles of subchapters (and smaller units) are written in small letters (lowercase) and are aligned left. If the text in the title of the subchapter is longer than one line, no hanging indents.

10pt

Typographical symbols (bullets), which are being used for marking an item in a list or for enumeration, are placed at a beginning of a line. There is a spacing of 10pt following the last item:

- Item 1
- Item 2
- Item 3

10pt

The same rule is valid when items are numbered in a list:

1. Item 1
2. Item 2
3. Item 3

10pt

1.2 Formatting of pictures, tables and equations
(Style: Arial Narrow, 10pt, Bold, Align Left)

10pt

Figures (drawings, diagrams, photographs) that are part of the content are embedded into the article and aligned in the centre. In order for the figure to always be in the same position in relation to the text, the following settings should be defined when importing it: text wrapping / in line with text.

Pictures must be formatted for graphic reproduction with minimal resolution of 300 dpi. Pictures downloaded from the internet in ratio 1:1 are not suitable for print reproduction because of unsatisfying quality.

10pt

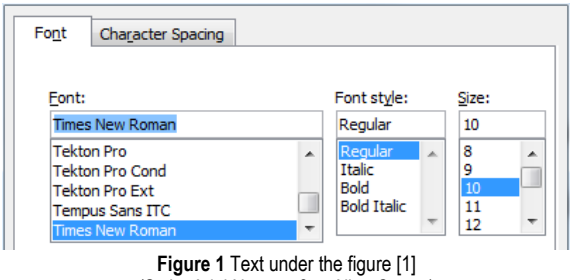

Figure 1 Text under the figure [1]
(Style: Arial Narraw, 8pt, Align Centre)

10pt

The journal is printed in black ink and the figures have to be prepared accordingly so that bright tones are printed in a satisfactory manner and are readable. Figures are to be in colour for the purpose of digital format publishing. Figures in the article are numbered with Arabic numerals (followed by a period).

Text and other data in tables are formatted - Times New Roman, 8pt, Normal, Align Center.

When describing figures and tables, physical units and their factors are written in italics with Latin or Greek letters,

while the measuring values and numbers are written upright.
10pt

Table 1 Table title aligned centre
(Style: Arial Narraw, 8pt, Align Centre)

	1	2	3	4	5	6
ABC	ab	ab	ab	ab	ab	ab
DEF	cd	cd	cd	cd	cd	cd
GHI	ef	ef	ef	ef	ef	ef

10 pt

Equations in the text are numbered with Arabic numerals inside the round brackets on the right side of the text. Inside the text they are referred to with equation number inside the round brackets i.e. ".... from Eq. (5) follows ...." (Create equations with MS Word Equation Editor - some examples are given below).
10pt

$$F_{\text{avg}}(t,t_0)=\frac{1}{t}\int_{t_0}^{t_0+t}F\big(q(\tau),p(\tau)\big)\,\mathrm{d}\tau, \tag{1}$$

10pt

$$\cos\alpha+\cos\beta=2\cos\frac{\alpha+\beta}{2}\cdot\cos\frac{\alpha-\beta}{2}. \tag{2}$$

10pt

Variables that are used in equations and also in the text or tables of the article are formatted as *italics* in the same font size as the text.

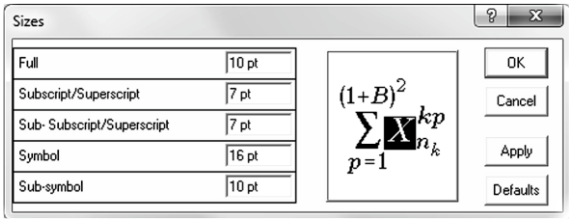

Figure 2 The texts under figures
(Style: Arial Narraw, 8pt, Align Centre)

Figures and tables that are a part of the article have to be mentioned inside the text and thus connected to the content i.e. „ … as shown in Fig. 1…" or „data from Tab. 1…" and similar.
10pt

2 PRELIMINARY ANNOTATION

10pt

Article that is offered for publication cannot be published beforehand, be it in the same or similar form, and it cannot be offered at the same time to a different journal. Author or authors are solely responsible for the content of the article and the authenticity of information and statements written in the article.

Articles that are accepted for publishing are classified into four categories: original scientific papers, preliminary communications, subject reviews and professional papers.

Original scientific papers are articles that according to the reviewer and the editorial board contain original theoretical or practical results of research. These articles need to be written in such a way that based on the information given, the experiment can be repeated and the results described can be achieved together with the author's observations, theoretical statements or measurements.

Preliminary communication contains one or more pieces of new scientific information, but without details that allow recollection as in original scientific papers. Preliminary communication can give results of an experimental research, results of a shorter research or research in progress that is deemed useful for publishing.

Subject review contains a complete depiction of conditions and tendencies of a specific domain of theory, technology or application. Articles in this category have an overview character with a critical review and evaluation. Cited literature must be complete enough to allow a good insight and comprehension of the depicted domain.

Professional paper can contain a description of an original solution to a device, assembly or instrument, depiction of important practical solutions, and similar. The article need not be related to the original research, but it should contains a contribution to an application of known scientific results and their adaptation to practical needs, so it presents a contribution to spreading knowledge, etc.

Outside the mentioned categorization, the Editorial board of the journal will publish articles of interesting content in a special column. These articles provide descriptions of practical implementation and solutions from the area of production, experiences from device application, and similar.
10pt

3 WRITING AN ARTICLE

10pt

Article is written in the English language and the terminology and the measurement system should be adjusted to legal regulations, standards (ISO 80 000 series) and the SI international system of units. The article should be written in third person.

Introduction contains the depiction of the problem and an account of important results that come from the articles that are listed in the cited literature.

Main section of the article can be divided into several parts or chapters. Mathematical statements that obstruct the reading of the article should be avoided. Mathematical statements that cannot be avoided can be written as one or more addendums, when needed. It is recommended to use an example when an experiment procedure, the use of the work in a concrete situation or an algorithm of the suggested method must be illustrated. In general, an analysis should be experimentally confirmed.

Conclusion is a part of the article where the results are being given and efficiency of the procedure used is emphasized. Possible procedure and domain constraints where the obtained results can be applied should be emphasized.
10pt

4 RECAPITULATION ANNOTATION

10pt

In order for the articles to be formatted in the same manner as in this template, this document is recommended for use when writing the article. Finished articles written in MS Word for Windows and formatted according to this

template must be submitted using our The Paper Submission Tool (PST) (https://tehnickiglasnik.unin.hr/authors.php) or eventually sent to the Editorial board of the Technical Journal to the following e-mail address: tehnickiglasnik@unin.hr

The editorial board reserves the right to minor redaction corrections of the article within the framework of prepress procedures. Articles that in any way do not follow these authors' instructions will be returned to the author by the editorial board. Should any questions arise, the editorial board contacts only the first author and accepts only the reflections given by the first author.

10pt

5 REFERENCES (According to APA)

10pt

The literature is cited in the order it is used in the article. Individual references from the listed literature inside the text are addressed with the corresponding number inside square brackets i.e. "… in [7] is shown …". If the literature references are web links, the hyperlink is to be removed as shown with the reference number 8. Also, the hyperlinks from the e-mail addresses of the authors are to be removed. In the literature list, each unit is marked with a number and listed according to the following examples (omit the subtitles over the references – they are here only to show possible types of references):

9pt

[1] See http://www.bibme.org/citation-guide/apa/
[2] See http://sites.umuc.edu/library/libhow/apa_examples.cfm
(Style: Times New Roman, 9pt, according to APA)

10pt

10pt

Authors' contacts:

8pt

Full Name, title
Institution, company
Address
Tel./Fax, e-mail

8pt

Full Name, title
Institution, company
Address
Tel./Fax, e-mail